MULTIPLE INPUT MULTIPLE OUTPUT RADAR THREE DIMENSIONAL IMAGING TECHNIQUE

MA CHANGZHENG

A THESIS SUBMITTED
FOR THE DEGREE OF PHD OF ENGINEERING
DEPARTMENT OF ELECTRICAL AND COMPUTER ENGRINEERING

NATIONAL UNIVERSITY OF SINGAPORE

2014

DECLARATION

I hereby declare that this thesis is my original work
and it has been written by me in its entirety.
I have duly acknowledged all the sources of information
which have been used in the thesis.

This thesis has also not been submitted for any degree
in any university previously.

Ma Changzheng

25 November 2014

Acknowledgments

The author would like to thank his thesis advisor Professor Yeo Tat Soon for his advice, guidance and support; without whom the completion of the work would have been impossible. The author is also very grateful to Professor Yeo for taking time to read the thesis despite his busy schedule.

Apart from his thesis advisor, the author would also like to especially thank Assistant Professor Qiu Chengwei, Associate Professor Chen Xudong, Professor Chen Zhining and Associate Professor Guo Yongxin for their guidance, advice and teachings. The author would also like to thank Dr Tan Hwee Siang for reading and revising the thesis.

The author would also like to express gratitude to the friends and colleagues of the Radar and Signal Processing Laboratory who have helped in one way or another in making his work possible and successful.

The author is also thankful to his family for their support and understanding. Most importantly, the author would like to thank his daughters Vicky, Ellen and Alana. Their innocence and prettiness have encouraged their father to preserve through the hard times.

Contents

Declaration i

Acknowledgement ii

Summary viii

List of Figures x

List of Acronyms xv

1 Introduction 1

1.1 Inverse Synthetic Aperture Radar Imaging Principle 3

1.1.1 Rotation Model of ISAR Imaging 3

1.1.2 Motion Compensation 7

1.2 Interferometric 3D Imaging Technique 8

1.3 Cross Array Based Three Dimensional Imaging Technique . . 10

1.4 Sparse Array Based Three Dimensional Imaging Technique . . 13

1.5 Principle of Multiple Input Multiple Output Radar 15

1.6 Sparse Signal Recovery Algorithm 19

1.7 Objectives and Significance of the Study 21

1.8 My Contributions 23

1.9 Organization of the Thesis 24

1.10 Papers Published/In Preparation 24
1.10.1 Papers Published 24
1.10.2 Papers Submitted 25
1.10.3 Papers in preparation 25

2 3D Imaging Using Colocated MIMO Radar and Single Snapshot Data 26

2.1 Signal Model of Collocated MIMO Radar Imaging 28
2.2 MIMO Radar Structures, Strong Scatterer Selection and Coordinates Transformation 33
2.2.1 Cross-Array MIMO Radar 33
2.2.2 Square-Array MIMO Radar 34
2.2.3 Interferometric MIMO Radar 35
2.2.4 Strong Scatterers Selection 37
2.2.5 Position Computation and Coordinates Transformation 41
2.3 Implementation Consideration 41
2.3.1 Construction of Zero Correlation Zone Codes 41
2.3.2 Pre-shift of Codes and the Effect of DOA Estimation Error 44
2.3.3 Comparison with IFIR radar 46
2.3.4 Discussion on the Realistic Choice of Radar Parameters and the Expected SNR 49
2.4 Simulation results 50
2.4.1 Simulation 1: Comparison of Random Codes to ZCZ Codes 51
2.4.2 Simulation 2: Comparison of Using Cross Array to Square Array 53
2.4.3 Simulation 3: 3D Imaging Using Square Array 54
2.4.4 Simulation 4: Interferometric 3D Imaging 56

2.5 Conclusion 60

3 3D Imaging Using Colocated MIMO Radar and Multiple Snapshots Data 61

3.1 Introduction 61

3.2 Multiple Snapshots MIMO Radar Signal Model 63

3.3 3D Images Alignment, Motion Compensation and Coherent Combination 66

3.4 Point Spread Function Analysis 69

3.5 Computation of Effective Rotation Vector 74

3.6 Simulation Results 76

3.6.1 Simulation 1: Cross-Range Sidelobes Mitigation 77

3.6.2 Simulation 2: 3D Imaging of MIMO Radar Using Multiple Snapshots Signal 79

3.6.3 Simulation3: 3D imaging of a Complex Target 82

3.7 Conclusions 83

4 $\ell_1\,\ell_0$ Norms Homotopy Sparse Signal Recovery Algorithms 86

4.1 Introduction 86

4.2 $\ell_1\,\ell_0$ Norms Homotopy Sparse Signal Recover Algorithm . . . 89

4.2.1 Fundamental of Sparse Signal Recovery 89

4.2.2 Steepest Descent Gradient Projection Method 93

4.2.3 Block $\ell_1\,\ell_0$ Homotopy Algorithm 97

4.3 Comparison with Iterative Shrinkage Threshold Method 101

4.4 Robust Implementation 102

4.5 Simulation Results 105

4.5.1 Simulation 1: One Dimensional General Sparse Random Spikes Signals 105

4.5.2 Simulation 2: Comparison of Real Version and Complex Version $\ell_1\,\ell_0$ Algorithms 107
4.5.3 Simulation 3: Recovery of One Dimensional Random Regular Block Sparse Spikes Signals 109
4.6 Conclusion 113

5 MIMO Radar Imaging Based on $\ell_1\,\ell_0$ Norms Homotopy Sparse Signal Recovery Algorithm 114
5.1 Introduction 114
5.2 Collocated MIMO Radar 3D Imaging Using Linear Equation $\ell_1\,\ell_0$ Homotopy Algorithm 117
5.2.1 Collocated MIMO Radar Signal Model 117
5.2.2 Imaging Based on ℓ_2 Norm Minimization 119
5.2.3 Imaging Based on Combined Amplitude and Total variation Sparse Signal Recovery Algorithm 119
5.2.4 Linear Equation Based Simulation Results 121
5.3 Collocated MIMO Radar 3D Imaging Using Multi-Dimensional Linear Equation $\ell_1\,\ell_0$ Homotopy Algorithm 133
5.3.1 One Dimensional MIMO Radar 2D Imaging 134
5.3.2 Cross-Array MIMO Radar 3D Imaging 138
5.3.3 Square-Array MIMO Radar 3D Imaging 140
5.3.4 Multi-Dimensional Linear Equation $\ell_1\,\ell_0$ Norms Homotopy Sparse Signal Recover Algorithm 144
5.3.5 Multi-Dimensional Linear Equations Based Simulation Results 145
5.4 Distributed MIMO Radar 3D Imaging Using Sparse Signal Recovery Algorithm 147
5.4.1 Distributed MIMO Radar Signal Model 147

5.4.2 Antennas Configuration and Signal Property 151
5.4.3 Simulation of Imaging of a Two Dimensional Circle . . 155
5.5 Conclusion 156

6 Bistatic ISAR Imaging Incorporating Interferometric 3D Imaging Technique 160

6.1 Introduction 160
6.2 The Bistatic Radar Signal Model and BiISAR Imaging Algorithm 162
6.2.1 Special Case 169
6.2.2 Range Migration 169
6.3 Interferometric 3D imaging 170
6.4 Simulation results 173
6.4.1 Simulation 1: Distortion of BiISAR Image 174
6.4.2 Simulation 2: BiISAR Image with Only Rotation Movement 176
6.4.3 Simulation 3: 3D Imaging using Interferometric Technique 177
6.5 Conclusions 179

7 Conclusions and Future Works 181

7.1 Research Purposes and Results 181
7.2 Significance, Limitations and Future Works 183

Summary

Because MIMO radar can form a large aperture and then obtain the 3D image of a target, it has received much attention in recent years. In collocated MIMO radar 3D imaging, the signal model equations derived in this thesis are suitable for slant range target imaging. Under the assumption of orthogonal coding, simple spatial Fourier transform is used to form the 3D image. For real codes, there are auto- and cross-correlations between codes. In order to mitigate sidelobes caused by code correlation, zero correlation zone code has been proposed in this work for use in some special imaging cases, such as for isolated target imaging. But the ZCZ codes in this thesis are not envelope constant, which is not power efficient. The entire image formation procedure combining collocated MIMO radar and ISAR processing is also proposed. It comprises the following steps: single snapshot MIMO radar 3D imaging, 3D images alignment, translational motion compensation, rotation parameters estimation, coherent combination, strong scatterers selection, coordinate transformation and display of 3D image. In this thesis, cyclic correlation is proposed to align the single snapshot 3D images in the cross-range direction and a least-square method is used to estimate the rotation. Compared to the single snapshot case, the method of combining MIMO radar and ISAR processing can improve the SNR and increase the resolution. It should be noted that the system complexity increases for multi-snapshot case.

The strong scatterers on the target are usually sparse compared to the whole imaging area. This property is used to improve the imaging performance. By introducing a sequential order one negative exponential cost function and by varying a parameter, L1 norm and L0 norm homotopy is formed. A new L1 norm and L0 norm homotopy sparse signal recovery algorithm is

proposed. This algorithm is suitable for complex data. The L1 L0 homotopy method is extended to block sparse signal case. This algorithm is superior over many sparse signal recovery algorithms such as OMP, CoSaMp, Bayesian method with Laplace prior, L1-Ls, L1-magic and smoothed L0 norm method, in high SNR and low sparsity case.

Applications of sparse signal recovery algorithm on collocated MIMO radar 3D imaging and distributed MIMO radar 3D imaging are discussed. In order to use the linear equation to describe the imaging system, a very large matrix should be used. This occupies huge memory. A multi-dimensional (tensor) signal model which has a compact expression and occupies less memory is derived. Multi-dimensional signal based L1 norm and L0 norm homotopy sparse signal recovery algorithm is proposed and used in collocated MIMO radar 3D imaging. Compared with FFT method, CS methods are generally computational expensive.

Distributed MIMO radar observes the target from different views, from which the detailed image of the target can be obtained. This is very useful for imaging stealth target because stealth target will scatter electromagnetic energy in several directions and the energy can be easily collected by a distributed radar. From the backscattered beampattern width of a patch on the target, the criterion to decide which antennas can be regarded as being collocated and the antennas that can be regarded as being distributed are obtained. A sequential linear function which describe the scatterers' RCS and the receive signals are obtained.

Bistatic radar, a special case of distributed radar is also studied. For bistatic ISAR (biISAR) imaging, the smear property of biISAR image is derived and an interferometric 3D imaging method is proposed.

List of Figures

1.1 Geometry of Interferometric ISAR 3D Imaging. 4
1.2 Geometry of ISAR Imaging. 9
1.3 Geometry of Antenna Array ISAR Imaging. 10
1.4 Mesh plot and contour plot of 2D FFT of the cross array received signal from discrete frequency pairs $(3, 5)$ and $(15, 14)$. . 12
1.5 Mesh plot and contour plot of 2D FFT of the cross array received signal from discrete frequency pairs$(3, 14)$ and $(15, 5)$. . 12
1.6 Element layout for a sparse array with 64 elements. The aperture is equivalent to that of a 256 elements full 2D square array. 13
1.7 Beam pattern of the 64 elements sparse array, the maximum sidelobes level is -14.5dB. 14
1.8 Spatial spectrum of one range unit using the physical sparse array. 14
1.9 Combined spatial spectrum of the real and the synthetic aperture of the sparse array. Because the time domain information is used, the sidelobes in areas along the combined velocity direction is lower. 15
1.10 One dimensional MIMO array and virtual aperture 17

2.1 Geometry of MIMO radar imaging. 29
2.2 Geometry of the 4 points in the Lemma. 30
2.3 Geometry of cross MIMO array. 34
2.4 Geometry of square MIMO array. 35
2.5 Geometry of Interferometric MIMO array. 36
2.6 Cross range image of a point scatterer in different range cells. 39
2.7 Scatterers in different range and cross range units. 39
2.8 Strong scatterer selection criterion. 40
2.9 The real and imaginary part of a periodic orthogonal sequence for $K = 230$, $\hat{k} = 3$ and $p = 0$. 43
2.10 The periodic auto-correlations and cross correlations of the zero correlation zone codes. 44
2.11 Pre-shift of the codes transmission. 45

2.12 Beam pattern comparison of MIMO radar and IFIR radar. a) receiving array and its beam pattern of IFIR radar. b) virtual array of MIMO radar and it's beam pattern. c) transmitting array and its beam pattern of IFIR radar. d) synthetic beam pattern of transmitting and receiving arrays of IFIR radar. . . 47
2.13 (a)Transmitting beam pattern (dash dot) and receiving beam pattern of IFIR array, (b) Synthetic transmitting-receiving beam pattern. 49
2.14 The implementation flow of 3D imaging. 51
2.15 Geometry of the target and the MIMO array (simulation1). . . 52
2.16 The range and cross range domain target model (simulation 1). 52
2.17 Reconstructed down-range and cross-range image of the target using the ZCZ and random code. (a) contour plot using random codes; (b) contour plot using ZCZ codes; (c) mesh plot using random codes; (d) mesh plot using ZCZ codes (simulation 1) . 53
2.18 Original cross range image of the target (simulation 2). 54
2.19 Contour plot and mesh plot of the reconstructed cross range image using the cross and the square array.(a) for cross-array and contour plot; (b) for square array and contour plot; (c) for cross-array and mesh plot; (d) for square array and mesh plot (simulation 2). 55
2.20 Three different projections and 3D view of the target model (simulation 3). 56
2.21 Projection images on YZ plane for $\delta\zeta$ = 3.5, 4.6, 5.6 and 6 dB corresponding to (a), (b), (c) and (d). The number of false scatterers decrease as the increase of $\delta\zeta$. Small scatterers have high probability be canceled with the increase of $\delta\zeta$ (simulation 3). 57
2.22 Three different projections and 3D views of the image obtained by the MIMO array for $\delta\zeta$ = 6dB (simulation 3). 57
2.23 Projection of the target on the range and cross-range plane (simulation 4). 59
2.24 Three different projections and 3D view of the image obtained by the MIMO interferometric array (simulation 4). 59

3.1 The image of the target is cross-range wrapped. 67
3.2 Beam pattern of linear MIMO array, ISAR and combined MIMO array and ISAR. 70
3.3 Synthetic aperture and linear MIMO array for a $\mathbf{w}$ along the linear array. 70
3.4 Beam pattern of (a) uniform linear MIMO array, (b) ISAR with $\mathbf{w}$ along $[1, -1, 0]$ direction, and (c) combined MIMO array and ISAR. 71
3.5 Synthetic aperture and MIMO array for an arbitrary rotation speed perpendicular to n_0. 72

3.6 Beam pattern of (a) uniform square MIMO array, (b) ISAR with $\mathbf{w}$ along $[1, 0, 0]$ direction, and (c) combined MIMO array and ISAR. 73
3.7 Beam pattern of (a) uniform square MIMO array and (b) combined MIMO array and ISAR with $\mathbf{w}$ along $[1, -1.2, -2.2]$ direction. 74
3.8 The total procedure of MIMO radar 3D imaging. 77
3.9 (a) Original 2D image of the target, (b)Reconstructed 2D image using one snapshot signals and (c) Reconstructed 2D image using multiple snapshots signals (simulation 1). 78
3.10 Contour plot of reconstructed 2D image using single and multiple snapshots signals (simulation 1). 79
3.11 Three different projections and 3D view of the target model (simulation 2). 80
3.12 Wrapped, unwrapped and real cross distance. (a) along the X axis, (b) along the Y axis (simulation 2) 81
3.13 Three different projections and 3D views of the image obtained by one snapshot MIMO array for δv=32 dB and $\delta\zeta$ = 6dB (simulation 2). 81
3.14 Three different projections and 3D views of the image obtained by multiple snapshots MIMO array for δv=32 dB and $\delta\zeta$ = 6dB (simulation 2). 82
3.15 Three different projections and 3D view of the target model (simulation 3). 83
3.16 Three different projections and 3D views of the image obtained by MIMO array using one snapshot signal (δv=32 dB and $\delta\zeta$ = 6dB, simulation 3). 84
3.17 Three different projections and 3D views of the image obtained by MIMO array using multiple snapshots signals (δv=32 dB and $\delta\zeta$ = 6dB, simulation 3). 84

4.1 (a) Mesh plot and (b) contour plot of two dimensional $\ell_{1/2}$ norm . 89
4.2 (a) Mesh plot and (b) contour plot of two dimensional function $2 - e^{-|x|} - e^{-|y|}$. 91
4.3 Shrinkage function for (a)CoSaMp, (b) Soft shrinkage ($t^* = 1$), (c) $\ell_1\,\ell_0$ ($\sigma = 2$, $\mu = \sigma/2$), (d) $\ell_1\,\ell_0$ ($\sigma = 1$, $\mu = \sigma/2$). 103
4.4 Computation costs of different methods. 107
4.5 Minimum mean absolute value errors for different methods, different $p = K/M$ and different SNRs, (a) SNR=20dB, (b) SNR=25dB, (c) SNR=30dB, (d) SNR=35dB (simulation 1) . . 108
4.6 Correct position estimation frequencies for different methods, different $p = K/M$ and different SNRs, (a) SNR=20dB, (b) SNR=25dB, (c) SNR=30dB, (d) SNR=35dB (simulation 1). . 108

4.7 Minimum mean absolute value errors for different SNRs and p for real version and complex version $\ell_1\,\ell_0$ algorithms, (a) SNR=20dB, (b) SNR=25dB, (c) SNR=30dB, (d) SNR=35dB (simulation 2). 110

4.8 Correct position estimation frequencies for different SNRs for real version and complex version $\ell_1\,\ell_0$ algorithms, (a) SNR=20dB, (b) SNR=25dB, (c) SNR=30dB, (d) SNR=35dB (simulation 2). 110

4.9 Computation costs of different methods (simulation 3). 111

4.10 Minimum mean absolute value errors for different methods, different block sparsity and different SNRs, (a) SNR=20dB, (b) SNR=30dB, (c) SNR=40dB, (d) SNR=100dB (simulation 3). . 112

4.11 Correct position estimation frequencies for different methods, different block sparsity and different SNRs, (a) SNR=20dB, (b) SNR=30dB, (c) SNR=40dB, (d) SNR=100dB (simulation 3). . 112

5.1 (a) Original image of the target. Reconstructed image using (b)ℓ_1-magic; (c) OMP algorithm; (d) CoSaMp ($k = 21$, $addK = k$); (e) $\ell_1 - \ell_s$ ($\lambda = 20$); (f) Bayesian method with Laplace prior; (g) Smoothed ℓ_0 algorithm and (h) GP-SOONE($\ell_1\,\ell_0$). 123

5.2 Reconstructed image using SOONE-CATV cost function and diagonal loading gradient projection optimization method for $\zeta = 0.1, 0.2, 0.3$ and 0.4 (from top to bottom) and $\sigma_J = 0.05, 0.1, 0.2$ and 0.5 (from left to right). 124

5.3 The original image of the target in simulation 2 126

5.4 Mesh plot and contour plot of reconstructed images using (a1, a2) ℓ_2 norm minimization, (b1, b2) OMP, (c1, c2) ℓ_1-magic, (d1, d2) Bayesian method with Laplace prior, (e1, e2) Smoothed ℓ_0 algorithm ($\sigma_{min} = 0.05$, $J = 40$, $L = 25$), (f1,f2) ℓ_1-ℓ_s ($\lambda = 2000$), (g1,g2) $\ell_1\,\ell_0$ (GP-SOONE) ($\sigma_{min} = 0.06$, $J = 40$, $L = 25$, $L_0 = 20$ and $L_1 = 20$) and (h1,h2) CoSaMp ($K = 20$, $addK = 1K$) (simulation 2). 127

5.5 (a) Original image of the target. Reconstructed images using (b) ℓ_2 norm minimization, (c) Bayesian method with Laplace prior, (d) OMP, (e) Smoothed ℓ_0 algorithm ($\sigma_J = 0.004, J = 25, L = 40$), (f) $\ell_1\,\ell_0$ (GP-SOONE) ($\zeta = 0$, $\sigma_J = 0.004, J = 25, L = 40, L_0 = 25, L_1 = 8$), (g) CoSaMp (k=40, addK=2k) and (h) ℓ_1-ℓ_s ($\lambda = 81$) (simulation 3). 129

5.6 Reconstructed images using combined amplitude and total variation objective function with SOONE form and gradient projection optimization method for $\zeta = 0.1, 0.2, 0.3$ and 0.4 (from top to bottom) and $\sigma_J = 0.001, 0.002, 0.004$ and 0.006 (from left to right)(simulation 3). 130

5.7 Reconstructed images using 32 and 64 snapshots, (a1,a2)FFT method, (b1,b2) CoSaMp ($k = 5$, $addK = k$), (c1,c2)ℓ_1-ℓ_s, $\lambda = 0.03$, (d1,d2)ℓ_1-magic, (e1,e2) Bayesian method with Laplace prior, (f1,f2) OMP, (g1,g2) Smoothed ℓ_0 algorithm, and (h1,h2) $\ell_1\,\ell_0$ (GP-SOONE)($\zeta = 0$) (simulation 4). 132
5.8 Imaging field division for One Dimensional MIMO array radar. 135
5.9 Imaging field division for cross array MIMO radar. 139
5.10 Imaging field division for Square array MIMO radar. 141
5.11 Rearrangement of reflectivity matrix. 143
5.12 Reconstructed image using multi-dimensional linear equations signal model(simulation 1). 146
5.13 Reconstructed images using cross array MIMO radar multi-dimensional linear equations signal model. (a) minimum ℓ_2 norm method, (b) MD $\ell_1\,\ell_0$ homotopy algorithm, $\varepsilon^2 = 0, \sigma_J = 0.003, J = 25, L = 40, L_0 = 20, L_1 = 20$. 147
5.14 Geometry of distributed MIMO radar. 147
5.15 The point spread function of case (a) where a linear transmitting antenna array is located at (0, -200)km and along the x axis, a receiver is located at (200,0)km. 154
5.16 The point spread function of one transmitter-receiver pair of case (b) where a linear receiving antenna array is located at (0, -200)km and along the x axis, a transmitter is located at (200,0)km. 154
5.17 The cross correlation of case (b) where a linear receiving antenna array is located at (0, -200)km and along the x axis, the two transmitters are located at (200,0)km and $(-153209.8, -128556.5427)$ m, respectively. The signal corresponding to transmitter one at (200,0)km is come from the origin. The signal corresponding to the second transmitter varies with different positions. 155
5.18 Target's image using conventional correlation method. 157
5.19 Reconstructed images using distributed MIMO radar with only one collocated antenna array receiver configuration and complex $\ell_1\,\ell_0$ homotopy sparse signal recovery algorithm. $\sigma_J = 0.005, \varepsilon^2 = 3$. (a) First receiver, (b) Second receiver. 157
5.20 Reconstructed images using distributed MIMO radar and OMP method assuming sparsity of (a)K=4, (b) K=6, (c) K=7, (d) K=9. 158
5.21 Reconstructed image using distributed MIMO radar and complex smoothed ℓ_0 norm method. $\varepsilon^2 = 3$, (a) $\sigma_J = 0.0001$, (b) $\sigma_J = 0.0002$,(c) $\sigma_J = 0.0005$, (d) $\sigma_J = 0.001$. 158
5.22 Reconstructed image using distributed MIMO radar and complex $\ell_1\,\ell_0$ norms homotopy method. $\varepsilon^2 = 3$, (a) $\sigma_J = 0.001$, (b) $\sigma_J = 0.002$,(c) $\sigma_J = 0.005$, (d) $\sigma_J = 0.01$. 159

6.1 Geometry of the bistatic radar and the target. 163

6.2 The bistatic ISAR image of a target ((a) is the target, (b) is the image). 170
6.3 Target model (simulation 1). 174
6.4 ISAR image of monostatic radar on the so called equivalent position (simulation 1). 175
6.5 BiISAR image using bistatic radar (simulation 1). 175
6.6 Reconstructed projection image on XZ plane using interferometric technique (simulation 1). 175
6.7 ISAR image of monostatic radar on the so called equivalent position (simulation 2). 176
6.8 BiISAR image of the bistatic radar (simulation 2). 177
6.9 Three different projected views and the 3-D model of the target (simulation 3). 178
6.10 ISAR image of monostatic radar on the so called equivalent position (simulation 3). 178
6.11 BiISAR image of the bistatic radar (simulation 3). 178
6.12 Three different projected views and the 3-D image of the target using interferometric bistatic radar (simulation 3). 179

List of Acronyms

ISAR	Inverse Synthetic Aperture Radar
MIMO	Multiple Input Multiple Output
RCS	Radar Cross Section
ZCZ	Zero Correlation Zone
DOA	Direction Of Arrival
DFT	Discrete Fourier Transform
IFIR	Interpolated FIR filter
PRF	Pulse Repetition Frequency
BPSK	Bipolar Phase Shift Keying
SL0	Smoothed L0
L1L0	$\ell_1\,\ell_0$ norms homotopy
SDGP	Steepest Descent Gradient Projection
RIP	Restricted Isometry Property
RIC	Restricted Isometry Constant
IST	Iterative Shrinkage Threshold
SVD	Singular Value Decomposition
TV	Total Variation
MAE	Mean Absolute Error
CATV	Combined Amplitude and Total Variation
SOONE	Sequential Order One Negative Exponential function
NP hard	Non-deterministic Polynomial time hard
BL1L0	Block $\ell_1\,\ell_0$
OMP	Orthogonal Matching Pursuit
CoSaMp	Compressive Sampling Matching Pursuit
MDL1L0	Multi-Dimensional $\ell_1\,\ell_0$

Chapter 1

Introduction

Radar is an acronym for radio detection and ranging. It is an active system that transmits a beam of electromagnetic (EM) energy in the microwave region to detect, locate, parameter estimate, image and identify objects. It was developed to detect hostile aircrafts in the beginning of the 20th century. Today, radar is used, for example, in air traffic control, environmental observations, vehicle collision avoidance systems, weather forecasting and ground penetrating applications etc.

Inverse Synthetic Aperture Radar (ISAR) imaging has received much attention in the past three decades [1] [2] [3] [4] [5]. As active radar transmits signals by itself, and electromagnetic wave in microwave band has ability to penetrate cloud and rain, ISAR can image far distance target all day and in all weather conditions. This property makes radar a safer device for long range surveillance. By transmitting wideband signals and using pulse compression technique, high resolution range profile can be obtained. After translational motion compensation, the target can be regarded as rotating around its axis. Scatterers on the target with different cross range positions have different Doppler frequencies. By spectrum analysis, these scatterers can be separated

in the cross range direction, the image of a target (plane, missile) can then be obtained [6] [7]. Resolution in the order of meters can be achieved so far. The property of the ISAR image is that it is a projection of the target on down range cross range plane and the height information is lost. This is inadequate for target identification. In order to overcome this drawback, three dimensional imaging techniques have been proposed. By putting three receive antennas and using interferometric technique, the absolute positions of the scatterers, then the 3D image of the target can be obtained [8] [9] [10]. However, two antennas in one direction can only measure one scatterer's position. If many scatterers have been projected on one ISAR image pixel, interferometric method fails. In order to solve this problem, cross array based three dimensional imaging technique was proposed in [11]. Unfortunately, cross array has high grating lobes. The multiple scatterers in one ISAR pixel should be correctly registered. When cross array is replaced by two-dimensional sparse array, grating lobes can be mitigated although sidelobes are still high. By exploring multiple snapshots signals and coherent processing, the sidelobes can be mitigated [12].

Multiple Input Multiple Output (MIMO) radar transmits multiple coded signals and receives the scattered signals using multiple receive antennas. There are two kinds of MIMO radar configurations: distributed and collocated. For distributed MIMO radar, the distances between antennas are comparable with the distances between the antennas and the target. The antennas observe the target from different directions. Diversity can thus be used to improve target detection performance [13]. For a collocated MIMO radar, the distances between the transmit antennas and the distances between the receive antennas are small and the signals relative to different transmit antennas (or receive antennas) from one scatterer can be considered as coherent, then a large virtual aperture is formed and fine resolution can be achieved [14]. MIMO radar is an

extension of antenna array. Compared with sparse array configuration, with the same number of antennas, MIMO radar has a larger aperture. The use of MIMO configuration to improve radar imaging performance has not been explored. In order to extend the use of MIMO radar to 3D imaging, the collocated and distributed MIMO radar three dimensional imaging algorithm and how the sparse property of the scatterers be used to improve the image quality should be examined. The combination of MIMO radar and ISAR technique to mitigate sidelobes and reduce data collection time should also be discussed.

In the following sections of Chapter one, ISAR imaging technique, cross array based three dimensional imaging technique, sparse array based three dimensional imaging technique, principle of MIMO radar, sparse signal recovery algorithm, my contributions and outline of the thesis are introduced.

In this thesis, a vector is denoted by a small bold letter or two letters with an overhead arrow showing the start and end points, while a matrix, scatterer's position and coordinate system are denoted by capital letters.

1.1 Inverse Synthetic Aperture Radar Imaging Principle

1.1.1 Rotation Model of ISAR Imaging

Usually, for ISAR imaging, the radar is static, while the target moves and forms an inverse synthetic aperture. The geometry of monostatic ISAR imaging is shown in Fig. 1. Certainly, the applications of ISAR imaging techniques are not limited only to the case where the radar is static. ISAR technique can be used for the case where the radar is moving, such as imaging of a target in sky while the radar is located on a moving vehicle.

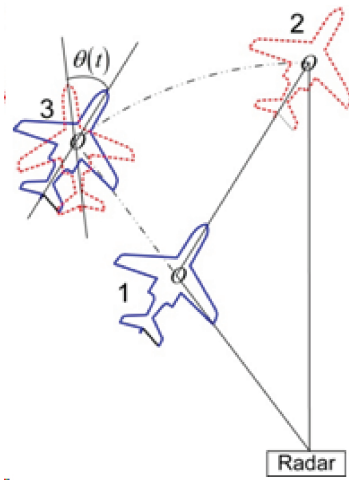

Figure 1.1: Geometry of Interferometric ISAR 3D Imaging.

Let $\hat{\mathbf{n}}$ denote the outwardly directed unit normal to ∂D at $\mathbf{r}^{'}$, where ∂D represents a surface, $\mathbf{r}^{'}$ is located at the surface of the target. In the far field, the physical optics approximation can be used. The induced current J on a conducting surface can be expressed as [15]

$$J(\mathbf{r}^{'}) = \begin{cases} 2\hat{\mathbf{n}} \times H_{inc}(\mathbf{r}') & if \quad \hat{\mathbf{r}} \cdot \hat{\mathbf{n}} < 0 \\ 0 & otherwise, \end{cases} \tag{1.1}$$

where H_{inc} is the incident magnetic field, $\hat{\mathbf{r}}$ is the radar line of sight direction vector.

The vector potential $A(\mathbf{r})$ at $\mathbf{r}$ (the radar observation point) due to the presence of the electric current density $J(\mathbf{r}^{'})$ is [16]

$$A(\mathbf{r}) = \iiint \frac{e^{-jk|\mathbf{r}-\mathbf{r}'|}}{4\pi|\mathbf{r}-\mathbf{r}'|}\mu_0 J(\mathbf{r}')d\mathbf{r}', \tag{1.2}$$

and the scattered magnetic field is

$$H(\mathbf{r}) = \nabla \times \iiint \frac{e^{-jk|\mathbf{r}-\mathbf{r}'|}}{4\pi|\mathbf{r}-\mathbf{r}'|} J(\mathbf{r}')d\mathbf{r}', \tag{1.3}$$

where $k = \frac{2\pi}{\lambda}$ is the wave number, λ is wavelength and μ_0 is the permeability of free space. ∇ operator can be approximated as $-jk\hat{\mathbf{r}}$ in the far field. Because $\hat{\mathbf{r}} \times (\hat{\mathbf{n}} \times H_{inc}) = \hat{\mathbf{n}}(\hat{\mathbf{r}} \cdot H_{inc}) - (\hat{\mathbf{r}} \cdot \hat{\mathbf{n}})H_{inc}$ and $\hat{\mathbf{r}} \cdot H_{inc} = 0$, we have

$$\begin{aligned} H(\mathbf{r}) &= \frac{jk}{2\pi r} \iint_{\hat{\mathbf{r}}\cdot\hat{\mathbf{n}}<0} (\hat{\mathbf{r}} \cdot \hat{\mathbf{n}}) H_{inc}(\mathbf{r}') e^{-jk|\mathbf{r}-\mathbf{r}'|} dS \\ &= \frac{jkH_0}{2\pi r^2} \iint_{\hat{\mathbf{r}}\cdot\hat{\mathbf{n}}<0} (\hat{\mathbf{r}} \cdot \hat{\mathbf{n}}) e^{-j2k|\mathbf{r}-\mathbf{r}'|} dS, \end{aligned} \tag{1.4}$$

where r is the distance between $\mathbf{r}$ and the reference point O' on the target, H_0 is the transmitted magnetic field at $\mathbf{r}$.

The integration in (1.4) can be obtained by discretization of the integration surface. Using the principle of stationary phase, the equation in (1.4) can be approximated as [15]

$$H(\mathbf{r}) = \frac{-jkH_0}{2\pi r^2} \sum_m \alpha_m e^{-j2k|\mathbf{r}-\mathbf{r}'_m|} + o(r^{-2}) \tag{1.5}$$

where the sum is over all points on ∂D at which $\hat{\mathbf{r}} \cdot \hat{\mathbf{n}} = -1$, α_m denotes the contribution to the integral in (1.4) of the local neighborhood $N_{r'_m} \subset \partial D$ of $\mathbf{r}'_m$, where the signals have approximately the same phase. α_m can be regarded as an "effective area" or the reflectivity of a strong scatterer. If the surface near $\mathbf{r}'_m$ is a planar patch and this planar patch is perpendicular to the radar line of sight, α_m is the geometry area. For a sphere, α_m approximates to $\frac{a\lambda}{2}$, where a is the radius of the sphere. $\frac{-jkH_0}{2\pi r^2}$ is known and can be included in α_m for simplicity. For radar imaging, we need to compute the sizes and positions of all patches. After α_m has been estimated, the patch can be established. Compared with the whole surface of the target, there are few surfaces that satisfy $\hat{\mathbf{n}} \cdot \hat{\mathbf{r}} = -1$. So the strong scatterers are sparse.

For monostatic radar, the transmit antenna and the receive antenna are

located at the same site, which can be regarded as the origin of the coordinate system. Scatterers in range direction can be easily separated by transmitting wide band signals. In order to separate two scatterers on the cross range direction, the phase history differences from these two scatterers are critical. Let O denote the reference point on the target, P denote another scatterer. After the phase from P is compensated with the phase from O, the signal from P can be represented as

$$s(t) = \alpha_p e^{-j4\pi(r_p(t)-r_o(t))/\lambda} \tag{1.6}$$

where $r_p(t)$ and $r_o(t)$ are the distances from scatterers P and O to the radar. According to Fig.1.1, after translational motion compensation, the movement of the target is equivalent to that where the target rotates only around its rotation axis with rotation speed of $\omega(t)$. For a short data collection duration, the rotation axis is regarded as static. This is usually called the rotation model of ISAR imaging. The rotation angle is $\theta(t) = \int_0^t \omega(t')dt'$. Assume that the plane perpendicular to the rotation axis is (X,Y), where O is the origin, Y axis is the target line of sight (or the vector from the radar to scatterer O). Denoting $P = (x_0, y_0)$, we have $r_p(t) - r_o(t) \approx x_0 \sin(\theta(t)) + y_0 \cos(\theta(t))$. Assuming the total rotation angle is small, we have $\theta(t) \approx 0$, $\cos(\theta(t)) \approx 1$ and $\sin(\theta(t)) \approx \theta(t)$. Assuming the target's rotation speed is a constant ω_0, then we have $r_p(t) - r_o(t) \approx y_0 + x_0\theta(t) = y_0 + x_0\omega_0 t$. Then equation (1.6) can be approximated as

$$s(t) = \alpha_p e^{-j4\pi x_0\omega_0 t/\lambda} \tag{1.7}$$

where $e^{-j4\pi y_0/\lambda}$ is absorbed into α_p. It can be seen that $s(t)$ is a complex sinusoid function. After inverse Fourier transform, the spectrum of $s(t)$ can

be expressed as

$$S(f) = \frac{1}{T}\int_{-T/2}^{T/2} s(t)e^{j2\pi ft}dt = \alpha_p sinc(T(f - 2x_0\omega_0/\lambda)) \tag{1.8}$$

It can be seen that the peak occurs at $2x_0\omega_0/\lambda$, which is proportional to the cross range coordinate x_0. Because the frequency resolution of $sinc(fT)$ is $\Delta f = \frac{1}{T}$, so the cross range resolution satisfies $2\Delta x\omega_0/\lambda = \frac{1}{T}$, that is $\Delta x = \frac{\lambda}{2\omega_0 T} = \frac{\lambda}{2\Delta\theta}$, where $\Delta\theta$ is the rotation angle of the target.

In the above simplifying approximation, a simple FFT operation can separate scatterers in the cross range direction. However, in actual situations, due to maneuvering of the target, the rotation speed may not be uniform and the rotation axis may be time varying. For non-uniform rotation, linear function was used to approximate the time varying rotation [17]. Then Radon-Wigner transform and other time frequency methods were proposed to form the range instantaneous Doppler image [17], [18]. By using MIMO array, the required synthetic aperture is much less than that in monostatic radar, the uniform rotation approximation is more precise.

1.1.2 Motion Compensation

The processing step of compensation of the phase from O is called motion compensation. An easy way to implement it is to choose an isolated scatterer in the range profile [2]. The selection criterion includes two aspects: (1) the powers of the candidate range units are large; (2) at the same time the variances of the cross range profile of the candidate range units are small (because the smaller the variance, the higher probability that a range unit has only one scatterer). But unfortunately, isolated scatterers are not common [3]. In order to overcome this problem, a weighted minimum least square method was

proposed [19]. In this method, several strong scatterers are selected and their phase histories are extracted. Then the phase history of the target is estimated by the weighted minimum least square method. The drawback of this method is its complexity, because absolute phases need to be computed. If the translational motion has been compensated precisely, the ISAR image will has small entropy. Based on this observation, by searching the phase history and compensating it, the image with minimum entropy corresponds to the case where the motion has been compensated precisely [20]. This method does not depend on the distribution of the scatterers, however it is more computationally expensive.

From above description, we know that ISAR image is a two dimensional projection of a target on Range-Doppler plane. The altitude information perpendicular to this Range-Doppler plane is lost(scatterers with the same range Doppler coordinate but with different altitude coordinates are projected on the same pixel and cannot be separated). This is not suitable for target identification. In order to recover 3D information, 3D imaging algorithms were proposed. These algorithms include monopulse antenna based method, interferometric and antenna array based methods.

1.2 Interferometric 3D Imaging Technique

Interferometric 3D imaging of SAR was first proposed in [21]. By computing the phase difference of a scatterer relative to two different antennas with different height, the altitude information of the scatterer can be obtained and three dimensional map of the terrain is carried out. In ISAR configuration, the interferometric 3D imaging geometry is shown in Fig.1.2, where the target is located on the Y axis, three receive antennas $\mathbf{T}_0$, $\mathbf{T}_1$ and $\mathbf{T}_2$ are located

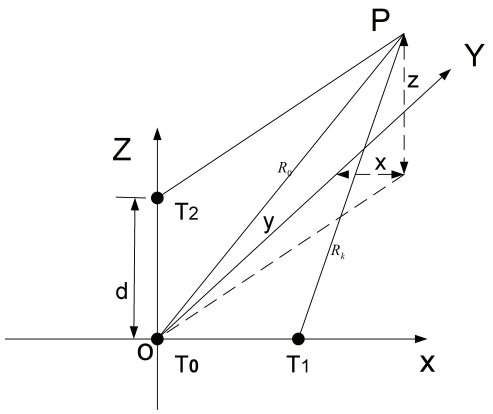

Figure 1.2: Geometry of ISAR Imaging.

on the origin, the X axis and the Z axis, respectively. Antenna $\mathbf{T}_0$ is also the transmit antenna. The x coordinate of scatterer P is related to the phase difference φ_1 between signals received from antenna $\mathbf{T}_0$ and $\mathbf{T}_1$, which can be written as [9] [22] [10]

$$x = \frac{\varphi_1 \lambda r}{2\pi d} \tag{1.9}$$

where d is the distance between antennas $\mathbf{T}_0$ and $\mathbf{T}_1$, $\mathbf{T}_0$ and $\mathbf{T}_2$, r is the distance between the radar and the target. Similarly, the z coordinate of scatterer P is related to the phase difference φ_2 between signals received from antenna $\mathbf{T}_0$ and $\mathbf{T}_2$, which can be expressed as

$$z = \frac{\varphi_2 \lambda r}{2\pi d} \tag{1.10}$$

Because the period of phase is 2π, in order to keep the measured cross range distances unambiguous, the maximum cross range should satisfy

$$x, z \in [-\frac{\lambda r}{2d}, \frac{\lambda r}{2d}] \tag{1.11}$$

In the above equations, the target is assumed to be located in the broadside of the three-antenna plane. In real case, the target may be located in a slant

range. So the equation (1.9) and (1.10) should be revised. In addition, because the image of ISAR is not continuous, phase unwrap technique used in SAR imaging cannot be used. Then the unambiguous distance of interferometric ISAR is limited. Another problem is that if multiple scatterers are projected onto one ISAR image pixel, interferometric technique cannot separate these scatterers. In order to overcome the multiple scatterers' problem, cross array based 3D imaging technique was proposed in [11].

1.3 Cross Array Based Three Dimensional Imaging Technique

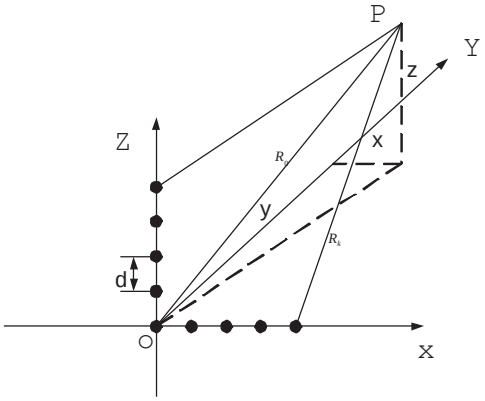

Figure 1.3: Geometry of Antenna Array ISAR Imaging.

The cross array based 3D imaging geometry is shown in Fig.1.3 where the target is also assumed to be located at the broadside of the array.

Assuming that range cell m contains only one isolated scatterer O, after motion compensation using signals from O, the array signal of scatterer P can

be expressed as

$$\mathbf{s}_{px}(t) = e^{-j4\pi\frac{r_p(t)-r_o(t)}{\lambda}} \times \begin{bmatrix} 1 \\ e^{j2\pi\frac{(x_p-x_o)d}{\lambda r}} \\ \vdots \\ e^{j2\pi\frac{(x_p-x_o)(K-1)d}{\lambda r}} \end{bmatrix}, \tag{1.12}$$

$$\mathbf{s}_{pz}(t) = e^{-j4\pi\frac{r_p(t)-r_o(t)}{\lambda}} \times \begin{bmatrix} 1 \\ e^{j2\pi\frac{(z_p-z_o)d}{\lambda r}} \\ \vdots \\ e^{j2\pi\frac{(z_p-z_o)(K-1)d}{\lambda r}} \end{bmatrix}, \tag{1.13}$$

where K is the number of antennas in one axis. The spatial frequencies of the array signal are $f_x = \frac{(x_p-x_o)d}{\lambda r}$ and $f_z = \frac{(z_p-z_o)d}{\lambda r}$. Therefore,

$$x_p = \frac{\lambda r f_x}{d} + x_o, \tag{1.14}$$

and

$$z_p = \frac{\lambda r f_z}{d} + z_o. \tag{1.15}$$

From equations (1.14) and (1.15), what we obtained are $x_p - x_o$ and $z_p - z_o$, which are the cross range distances of the scatterer P relative to the scatterer O. This means that point O is the center of the obtained three dimensional image in the cross range domain.

A question of the above method is registration of scatterers. Assume that there are two scatterers in one ISAR pixel. The two positions in X and Z axis are (x_1, x_2) and (z_1, z_2). Now what are the positions of the two scatterers? (x_1, z_1) and (x_2, z_2) or (x_1, z_2) and (x_2, z_1)?. Let's look at one simulation example. Let the lengths of the two arrays be all 20. Let the two X direction

discrete frequencies be 3 and 15, and the two Z direction discrete frequencies be 5 and 14. The amplitudes of the two scatterers are 1 and 2. One combination of discrete 2D frequencies is $(3, 5)$ and $(15, 14)$. The 2D FFTs of the cross array received signals from $(3, 5)$ and $(15, 14)$ are shown in Fig.1.4. Another combination of discrete 2D frequencies is $(3, 14)$ and $(15, 5)$. The corresponding 2D FFT is shown in Fig.1.5. From the contour plots of the two 2D FFTs, there are little differences. The dominant differences are the amplitudes of the peaks. If the amplitudes of the two scatterers are the same, there is no difference. So ambiguity exists in cross array 3D imaging. Amplitude and rotation axis matched methods were proposed in [11], but the robustness needs to be verified using real data.

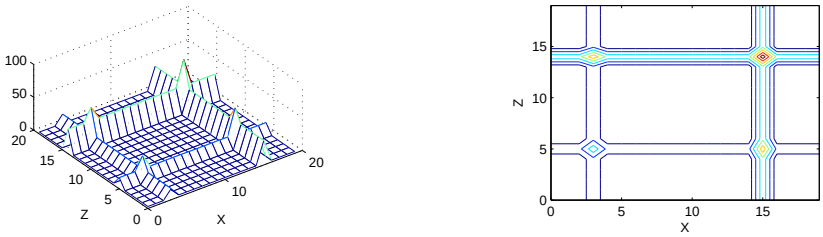

(a) (b)

Figure 1.4: Mesh plot and contour plot of 2D FFT of the cross array received signal from discrete frequency pairs $(3, 5)$ and $(15, 14)$.

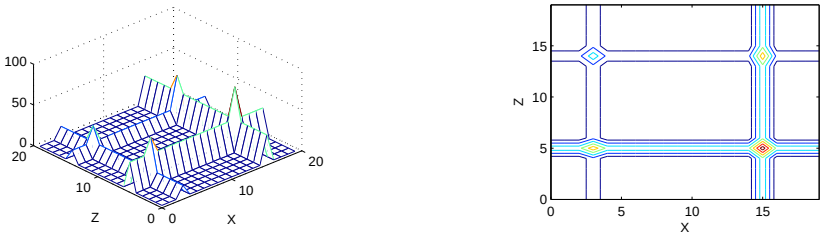

(a) (b)

Figure 1.5: Mesh plot and contour plot of 2D FFT of the cross array received signal from discrete frequency pairs$(3, 14)$ and $(15, 5)$.

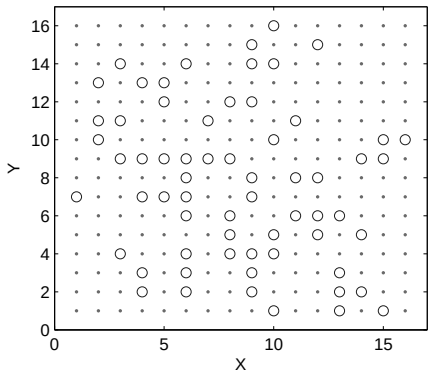

Figure 1.6: Element layout for a sparse array with 64 elements. The aperture is equivalent to that of a 256 elements full 2D square array.

1.4 Sparse Array Based Three Dimensional Imaging Technique

The ambiguity of cross array is due to its non-needle beampattern. If a full two dimensional array is used, this problem is solved. However, the number of antennas increases greatly with the increase of the two dimensional aperture. In order to decrease the number of antennas while keeping the same aperture size, as a tradeoff, sparse array can be used [12]. A two dimensional sparse array is shown in Fig.1.6, where there are only 64 antennas but the aperture is the same as that of 256 antennas. The beampattern is shown in Fig.1.7. There is only one peak, but the sidelobes are also high.

If there are many scatterers in one range cell, the spatial spectrum of these scatterers using sparse array has high sidelobes. Fig.1.8 shows one case of the spatial spectrum where there are only 4 scatterers in one range cell [12]. It is difficult to find the peaks of the 4 scatterers. Usually multiple snapshot signals are received. If the rotation speed of the target is obtained, coherent processing can be used to mitigate the sidelobes and improve the imaging performance. Fig.1.9 shows the spatial spectrum after coherent processing. Sidelobes along

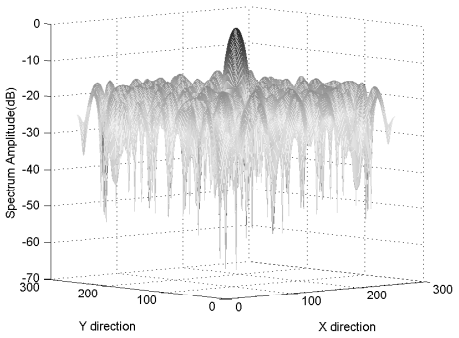

Figure 1.7: Beam pattern of the 64 elements sparse array, the maximum sidelobes level is -14.5dB.

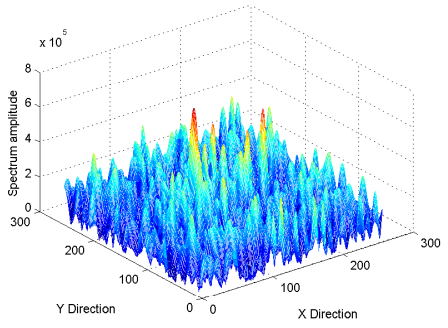

Figure 1.8: Spatial spectrum of one range unit using the physical sparse array.

the direction of rotation speed **w** are mitigated. The high sidelobes is due to the high sidelobes of sparse antenna array beampattern and at the same time there are multiple scatterers. CLEAN technique was used to estimate the position and amplitude of each scatterer [23]. Maximum likelihood estimation was also proposed to estimate the amplitudes and positions of the scatterers and improve the image quality [12]. However, the computational cost is increased.

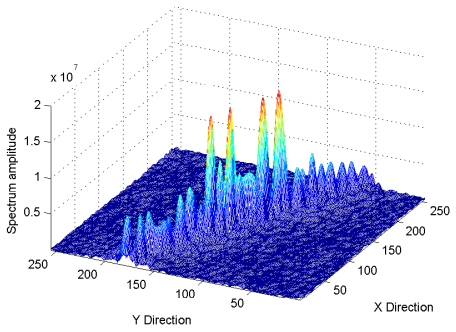

Figure 1.9: Combined spatial spectrum of the real and the synthetic aperture of the sparse array. Because the time domain information is used, the sidelobes in areas along the combined velocity direction is lower.

1.5 Principle of Multiple Input Multiple Output Radar

MIMO radar transmits multiple independent signals from multiple transmit antennas and receives the return signals using multiple receive antennas [24], [13]. There are two different MIMO radar configurations: distributed MIMO radar and collocated MIMO radar. For distributed MIMO radar, as the distances between different antennas are large, the RCS of a target relative to different transmit-receive pairs are different [13]. Thus diversity is used to improve the probability of target detection. For collocated MIMO radar, as the distances between different transmit antennas and the distances between different receive antennas are small, a target or the scatterers on a target can be regarded as coherent relative to different transmitters and receivers. A merit of collocated MIMO radar is that a large virtual aperture can be formed with a small number of antennas. This increases the precision of cross range estimation [14].

Assume that N receive antennas are uniformly located on X axis with inter-element distance of d_r and M transmit antennas are uniformly located

on X axis with inter-element distance of d_t. The signal envelopes $\varphi_m(t), m = 0, \cdots, M-1$ transmitted from different transmit antennas are orthogonal. The signal received from the n^{th} receive antenna after mixing can be expressed as

$$\begin{aligned} s_n(t) = & \alpha_k \sum_{m=0}^{M-1} \varphi_m(t - \tau_m^t - \tau_n^r) e^{-j2\pi f(\tau_m^t + \tau_n^r)} \\ \approx & \alpha_k e^{-j2\pi f(\tau_0^t + \tau_0^r)} \sum_{m=0}^{M-1} \varphi_m(t - \tau_0^t - \tau_0^r) e^{j2\pi f(\frac{m d_t cos(\theta_k)}{c} + \frac{n d_r cos(\theta_k)}{c})} \end{aligned} \tag{1.16}$$

where the relative delays between different antennas are small compared to the duration of codes $\varphi_m(t)$, θ_k is the target's direction of arrival(DOA), α_k corresponds to the target's Radar Cross Section (RCS). The correlation between $s_n(t)$ and $\varphi_m(t - \tau_0^t - \tau_0^r)$ can be expressed as

$$s(n, m) = \alpha_k e^{j2\pi f(\frac{m d_t cos(\theta_k)}{c} + \frac{n d_r cos(\theta_k)}{c})} \tag{1.17}$$

where $e^{-j2\pi f(\tau_0^t + \tau_0^r)}$, as a constant phase term, is omitted. Denote $\mathbf{s} = \text{vec}(s(n, m))$ where vec is the operation of stacking the columns of a matrix on top of each other, $a(n, m) = e^{j2\pi f(\frac{m d_t cos(\theta_k)}{c} + \frac{n d_r cos(\theta_k)}{c})}$ and $\mathbf{a}(\theta_k) = \text{vec}(a(n, m))$, we have

$$\mathbf{s} = \alpha_k \mathbf{a}(\theta_k). \tag{1.18}$$

If d_t and d_r satisfies $d_t = N d_r$, $\mathbf{a}(\theta_k)$ has expression of

$$\begin{aligned} \mathbf{a}(\theta_k) = [1, & \quad e^{j2\pi f \frac{(d_r cos(\theta_k))}{c}}, & \cdots, & \quad e^{j2\pi f(\frac{((N-1) d_r cos(\theta_k))}{c})}, \\ \cdots, & \quad e^{j2\pi f(\frac{m N d_r cos(\theta_k)}{c} + \frac{n d_r cos(\theta_k)}{c})}, & \cdots, & \quad e^{j2\pi f(\frac{(NM-1) d_r cos(\theta_k)}{c})}]^T. \end{aligned} \tag{1.19}$$

It can be seen that $\mathbf{a}(\theta_k)$ is the steering vector of a linear array having MN elements with inter-element distance of d_r. Although there are only $M + N$ elements, a length MN steering vector is obtained, which corresponds to a MN length virtual array. Fig.1.10 shows an example of a MIMO array and

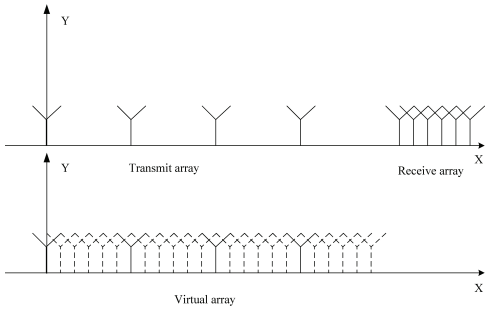

Figure 1.10: One dimensional MIMO array and virtual aperture

the virtual aperture. This means that a higher angular resolution can be obtained using fewer antennas.

MIMO array has been discussed in synthetic aperture radar (SAR) and ultra wide band (UWB) radar imaging [25], [26]. For far field target imaging, a 2D high resolution technique using narrow- and wide- band MIMO radar was proposed in [27], [28], where only one dimensional linear array and imaging of broadside target was discussed. The method to mitigate sidelobes was not discussed. In Chapter 2, a 3D imaging technique using MIMO radar is studied [29]. In this case, the target can be located in the slant range direction. Zero correlation zone (ZCZ) code is designed to mitigate sidelobes.

In the afore-mentioned target imaging methods [27] [28] [29], only one snapshot is used to form the image. Although it avoids motion compensation usually needed in ISAR imaging, it requires a relatively high transmitting energy and induces high sidelobes. Usually, a radar collects multiple snapshots signals. Using these multiple snapshots signals can reduce transmitting power as well as improve cross-range resolution and mitigate sidelobes. In [30] and [31], linear MIMO array in conjunction with ISAR processing was discussed. It is noted that, in these papers, the gaps between virtual antennas are filled with synthetic aperture, and only a 2D image was obtained. The number of codes in the said MIMO array is small and orthogonal property among these

codes is assumed. The target is also assumed to be located on the broadside of the array to show the cross-range resolution improvement. When the rotation axis is perpendicular to the plane formed by the antenna array and the target, the conjunction algorithms were discussed in detail in these two papers. In reality, the rotation axis may not be perpendicular to the said plane. The method needs discussion in detail.

In Chapter 3, two-dimensional MIMO radar and inverse synthetic aperture technique are combined to form a 3D image. The targets can be located in the slant range and can still be imaged. Because the number of codes used in the two-dimensional array is larger than the number of codes used in one dimensional array, the codes cannot be assumed to be orthogonal. One-dimensional range profile cannot be used to align the signal as was done in [30] and [31]. So the processing step is different from [30] and [31]. Furthermore, a direct rotation speed estimation algorithm is proposed, whilst in [30], an iterative algorithm was used, which is computational expensive. Obviously, the SNR is improved with increasing number of snapshots. The most valuable merit using multi-snapshots signals is that the cross-range sidelobes can also be suppressed.

Collocated radar observes the target from one view point. With the development of stealth target, the RCS of a stealth target becomes more and more smaller. But usually, the RCS cannot be small from all view angles. If distributed radar observes the stealth target from multiple viewing angles, the probability of detecting the target could increase. Similarly, distributed imaging radar can obtain more details of a target. Distributed MIMO radar imaging has not been discussed in literature.

1.6 Sparse Signal Recovery Algorithm

Many signals in real world are sparse in the original form or sparse in some transform domains. For radar imaging, according to the derivation of Chapter 1.1, the strong scatterers are located in the reflection faces, noncontinuous places etc, and are sparse. Sparse signal recovery algorithm utilizes the *a prior* information of sparse property of the signal [32] [33]. A linear system with observation noise and model error can usually be expressed as

$$\mathbf{s} = \mathbf{\Psi}\boldsymbol{\alpha} + \mathbf{n}, \tag{1.20}$$

where $\mathbf{n}$ is the observation noise or/and model error. When $\boldsymbol{\alpha}$ is a sparse signal, it can be solved by the following optimization criterion

$$\hat{\boldsymbol{\alpha}} = \arg\min ||\boldsymbol{\alpha}||_{sp} \quad \text{subject to} ||\mathbf{s} - \mathbf{\Psi}\boldsymbol{\alpha}||_2 < \varepsilon, \tag{1.21}$$

where $||\boldsymbol{\alpha}||_{sp}$ expresses the sparse norm of $\boldsymbol{\alpha}$. Sparse property can usually be measured by $\ell_p (0 \leq p \leq 1)$ norm ($||\boldsymbol{\alpha}||_p^p = \sum_{n=1}^{N} \alpha(n)^p$). ℓ_0 norm is the number of non-zero elements of $\boldsymbol{\alpha}$. Although ℓ_0 norm (the number of non-zero elements) is better in describing sparsity of noise free case, sparse learning algorithms based on ℓ_0 norm are computationally expensive because it needs combinational optimization. So algorithms based on ℓ_1 norm (which is a convex function), such as basis pursuit [34], ℓ_1-ℓ_s [35], etc, are more popular. ℓ_1-magic program solves quadratically constrained ℓ_1 minimization by reformulating it as a second-order cone program and uses a log barrier algorithm. However, it is computationally expensive. Hence many simpler algorithms, including the matching pursuit (MP) [36], orthogonal matching pursuit (OMP) [37] are proposed. But the performance is poor for low sparsity case. It has been shown

that the performance using $0 < p < 1$ is better than using $p = 1$ [38] [39] [40]. So constrained ℓ_p norm minimization was solved using steepest descent gradient projection in [38] [39]. But because the derivative of α^p approximates to infinity when α approximates to zero, the step size should be designed carefully.

In order to obtain an approximate ℓ_0 norm solution, a pseudo norm function $F_\sigma(\boldsymbol{\alpha}) = N - \sum_{n=1}^{N} exp(-\frac{\alpha_n^2}{2\sigma^2})$ (Gauss function) was used to replace the ℓ_0 norm in [41]. By varying σ from infinity to zero, a homotopy between ℓ_2 norm and ℓ_0 norm is formed and a smoothed ℓ_0 norm solution is obtained. It has been shown that the smoothed ℓ_0 norm method is two to three orders of magnitude faster than basis pursuit (based on interior-point linear programming solvers) and provides better estimation of the source than matching pursuit method.

A sequential order one negative exponential pseudo norm function

$$G_\sigma(\boldsymbol{\alpha}) = N - \sum_{n=1}^{N} exp(-|\alpha_n|/\sigma)$$

is proposed in this thesis. Compared with the smoothed ℓ_0 norm method, a homotopy between ℓ_1 norm and ℓ_0 norm is formed. This order one negative exponential function has some merits compared to ℓ_p norm and Gaussian function.

Radar imaging is actually a scatterers positions estimation problem. For ISAR imaging, a cross-range position corresponds to a frequency. So frequency estimation methods can be used in ISAR imaging. MUSIC, ESPRIT and matrix pencil methods transform frequency estimation to other problems, such as eigenvalue decomposition, then to avoid griding [42] [43]. The matrix pencil and ESPRIT methods need regular sampling. For irregular sampling, [44] provides atomic norm to process a kind of continuous problems. According

to [44], [45] transforms frequency estimation as a positive semidefinite programming algorithm. The above methods need not to draw grid. Another method to process off-grid problem is to draw a coarse grid and refine (or adjust) the grid gradually [46] [47]. The algorithms of this kind are similar to the conventional CS algorithms. For MIMO imaging, the basis function may not be expressed as a sinusoid. Method of [47] is more suitable for MIMO radar imaging.

Sparse signal recovery algorithm has been used in two dimensional ISAR imaging [48] and shows good performance. But the performance of MIMO radar 3D imaging based on sparse signal recovery algorithm is not discussed. This will be discussed in Chapter 5.

1.7 Objectives and Significance of the Study

According to the literature review, the research gaps for the current study of radar (MIMO radar) imaging are summarized below:

- The beam pattern of sparse array has high sidelobes, which affect the performance of 3D imaging. When maximum likelihood estimation method is used to estimate the parameters of scatterers, the computation complexity increases greatly.

- The current MIMO radar imaging algorithms only discuss linear MIMO array and two dimensional imaging. MIMO radar 3D imaging using multiple snapshots signals has not been discussed.

- The L1-Ls and ℓ_1-magic sparse signal recovery algorithms are computationally expensive while the performance of greedy pursuit algorithms is not satisfactory in some cases. Because the ℓ_0 norm is transited continuously from a non-sparse ℓ_2 norm in smoothed ℓ_0 norm method, there is a

potential to improve the performance by replacing the non-sparse ℓ_2 norm with sparse ℓ_1 norm.

- Distributed MIMO radar observes the target from different directions. This can provide a more detailed image of the target. But the approach has not been studied before.

The main aim of this study was to use MIMO radar configuration to carry out 3D imaging as well as to use the *a priori* sparse distribution of scatterers to design a new sparse signal recovery algorithm to improve radar imaging performance. The specific objectives of this research were to:

- Derive a MIMO radar 3D imaging algorithm such that it can image slant range target. Design transmitting codes such that there are lower sidelobes.
- Propose a MIMO radar 3D imaging procedure that can process multiple snapshots signals. Analyze the performance improvement compared to using single snapshot signal.
- Study distributed MIMO radar signal model and develop 3D imaging algorithm.
- Develop ℓ_1 norm and ℓ_0 norm homotopy sparse signal recovery algorithm and apply the new sparse signal recovery algorithm to MIMO radar 3D imaging.

The results of this present study may have a significant impact on radar applications. This result might help to develop real MIMO radar imaging system operating in all directions. The low power requirement by using multiple snapshots signals makes the transmitter system lighter. Distributed MIMO radar imaging can increases the probability of imaging of stealth targets and should improve the surveillance ability. The proposed ℓ_1 norm and ℓ_0 norm

homotopy sparse signal recovery algorithm could be used in all sparse signal recovery fields, such as image processing, communication, sonar, etc.

1.8 My Contributions

My contributions are mainly on MIMO radar 3D imaging. In collocated MIMO radar 3D imaging, the equations derived in this thesis are suitable for slant range target imaging. Zero correlation zone code is used to mitigate range sidelobes. For cooperating collocated MIMO radar and ISAR processing, the whole imaging procedure is proposed. Cross range direction cyclic correlation is proposed to align the 3D images obtained by using one snapshot signal. A rotation parameter estimation method is proposed and coherent summation of all the collected data is implemented. A ℓ_1 norm and ℓ_0 norm homotopy sparse signal recovery algorithm is proposed. This algorithm is suitable for complex data, while many other algorithms are designed only for real data. The ℓ_1 norm and ℓ_0 norm homotopy method is extended to block sparse signal case and multi-dimensional linear equations case. This algorithm is superior to many sparse signal recovery algorithms such as OMP, CoSaMp [49], L1-Ls, ℓ_1-magic, Bayesian method based on Laplace priori [50] and smoothed ℓ_0 methods in high SNR and high sparsity p. Applications of sparse signal recovery algorithm on collocated MIMO radar 3D imaging and distributed MIMO radar 3D imaging are discussed. For bistatic ISAR imaging, the smear property of biISAR image has been derived and an interferometric 3D imaging method is proposed.

MIMO radar 3D imaging is a new research field. In order to implement imaging, the signals transmitted by different antennas should be kept coherent and the precise position information of different antennas should be known.

Even though these problems are also critical, they are not central to this study, because this thesis focusses only on the discussion of imaging algorithms.

1.9 Organization of the Thesis

The thesis begins with an introduction to the developments of radar imaging in Chapter 1. The contents on Chapter 2 to Chapter 7 are:

Chapter 2: 3D Imaging Using Colocated MIMO Radar and Single Snapshot Data.

Chapter 3: 3D Imaging Using Colocated MIMO Radar and Multiple Snapshots Data.

Chapter 4: $\ell_1\,\ell_0$ Homotopy Sparse Signal Recovery Algorithm.

Chapter 5: MIMO Radar Imaging Based on $\ell_1\,\ell_0$ Homotopy Sparse Signal Recovery.

Chapter 6: Bistatic ISAR Imaging Incorporating Interferometric 3D Imaging Technique.

Chapter 7: Conclusions and Future Works.

1.10 Papers Published/In Preparation

1.10.1 Papers Published

[1]. C. Ma, T. S. Yeo, C. S. Tan, and Z. Liu, "Three-dimensional imaging of targets using colocated mimo radar," *IEEE Trans. Geosci. Remote Sens.*, vol. 49, no. 8, pp. 3009–3021, 2011.

[2]. C. Ma, T. S. Yeo, C. S. Tan, J. Li, and Y. Shang, "Three-dimensional imaging using colocated mimo radar and isar technique," *IEEE Trans. Geosci. Remote Sens.*, vol. 50, no. 8, pp. 3189–3201, 2012.

[3]. C. Ma, T. S. Yeo, Q. Guo and P. Wei, "Bistatic ISAR imaging incorporating interferometric 3-D imaging technique," *IEEE Trans. Geosci. Remote Sens.*, vol. 50, no. 10, pp.3859–3867, 2012.

[4]. C. Ma, T. S. Yeo, C. Chong and T. Zhang, "MIMO Radar 3D Imaging with Improved Rotation Parameters Estimation," *PIERS Proceedings* , Kuala Lumpur, MALAYSIA, pp.214-220, March 27-30, 2012.

[5]. C. Ma, T. S. Yeo, Y. Zhao and J. Feng, "MIMO Radar 3D Imaging Based on Combined Amplitude and Total Variation Cost Function with Sequential Order One Negative Exponential Form,"*IEEE Trans. Image. Processing*, vol. 23, no. 5, pp.2168–2183, 2014.

[6]. Y. J. Chen, Q. Zhang, C. Ma, Y. Luo, T. S. Yeo, "Micro-motion feature extraction of radar target using tracking pulses with adaptive pulse repetition frequency adjustment," *Journal of Applied Remote Sensing.* Accepted for publication.

1.10.2 Papers Submitted

[1]. C. Ma, T. S. Yeo,"Distributed MIMO Radar Imaging Based on ℓ_1 ℓ_0 Norms Homotopy Complex Sparse Signal Recovery," submitted to *IEEE transactions on Image Processing.*

1.10.3 Papers in preparation

[1]. C. Ma, T. S. Yeo,"MIMO radar three dimensional imaging using multiple linear equation model."

[2]. C. Ma, T. S. Yeo,"ℓ_1 ℓ_0 homotopy sparse signal recovery algorithm for arbitrary block signals."

Chapter 2

3D Imaging Using Colocated MIMO Radar and Single Snapshot Data

Inverse Synthetic Aperture Radar (ISAR) imaging has received significant attention in the past three decades [3] [51]. The high range resolution of ISAR is obtained by transmitting large-bandwidth signal while the cross-range resolution is dependent on the rotation of the target relative to the radar. ISAR image is a projected image of the target on the range-Doppler plane. There are a number of shortcomings in ISAR imaging: a) The projected image is two-dimensional, thus could only deliver limited information in target recognition. b) In order to obtain high cross-range resolution, it requires a large relative rotation angle (or long imaging time). However, during this long imaging time, the movement of the target may be time varying, especially for maneuvering targets. The difficulty in motion compensation and scatterers separation often required the use of computationally expensive techniques such as the time frequency imaging method [52] [53].

In order to overcome the first drawback, several three-dimensional imaging methods have been proposed recently [54] [11]. To reduce the imaging time, a microwave radio camera technique was proposed in [5]. There, a 32-element linear antenna array was used to form the 2D image of the target. Only one snapshot is needed. However, in order to form a 3-D image, the one dimensional linear array must be replaced by a 2-D array, thus a large amount of expensive antennas and receivers are required. While sparse array technique can reduce the number of antennas used [55] [12], the MIMO array discussed in this Chapter can significantly reduce the number to a level not achievable in the afore-mentioned methods.

MIMO radar transmits multiple independent signals from multiple antennas and receives the return signals using multiple receive antennas. It has been proven that MIMO array possesses many advantages over conventional phased array [24] [13], including higher degree of freedom as well as higher angular resolution (resulting from its large virtual array). This also means that a high angular resolution can be obtained using fewer antennas (a welcomed cost saving). A 2-D high resolution imaging technique using narrow- and wide- band MIMO radar was proposed in [27] [28]. Unfortunately, the reconstructed cross-range location parameter of each (and every) scatterer is reduced to one half of the real location. A 3-D imaging method using MIMO radar was discussed in [56], where a continuous MIMO array was used to derive the cross-range imaging formula and an approximate phase expression was derived to do phase compensation. We discuss collocated MIMO radar 3D imaging in this Chapter.

In this Chapter, a direct discrete signal model is derived and the precise phase history of a reference point is used to do phase compensation. The scale of the reconstructed image is the same as that of the original target. Three par-

ticular MIMO radar 3-D imaging configurations, namely; cross-array, square-array and interferometric-array, are discussed. Because the pseudo random transmitting codes commonly used have high auto- and cross- correlations, we propose to transmit zero correlation zone codes to mitigate sidelobes in the target range direction to improve the image quality.

Considering that the induced surface current generally is strongest on the target's shinning surface, and that specular reflections produced the strongest radar returns, we propose to use a strong-scatterer selection criterion to mitigate ghost images created by sidelobes and to select strong scatterers for the construction of the target profile.

This Chapter is organized as follows. In Section 2.1, the spatial domain signal model of MIMO radar is derived. Three MIMO radar configurations, coordinate transform and strong scatterers selection criterion are discussed in Section 2.2. Code selection, transmitting strategy, comparison with IFIR radar and some realistic radar parameters are discussed in Section 2.3. Simulation results are shown in Section 2.4.

2.1 Signal Model of Collocated MIMO Radar Imaging

Consider a wideband MIMO radar imaging system with M transmitters and N receivers. We assume that the target is located in the far field and the MIMO radar is equipped with collocated antennas. Therefore, the directions of the target relative to the different transmit antennas and the receive antennas are the same, and the RCS of a scatterer corresponding to different transmit-receive antenna pairs are also the same. The MIMO radar imaging geometry is shown in Fig.2.1.

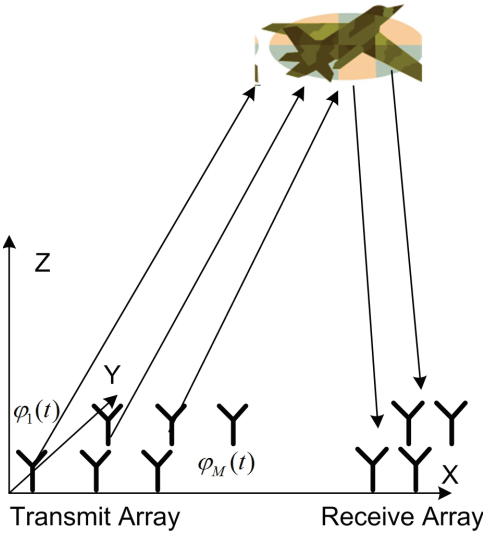

Figure 2.1: Geometry of MIMO radar imaging.

In order to derive clearly, we first introduce a lemma.

Lemma: *O, A, P and Q are four points in space as shown in Fig.2.2 (P and Q are two antennas, O and A are two positions on a target), PO, PA, QO and QA are distances between P and O, P and A, Q and O, and Q and A respectively. PO, PA, QO and QA are much longer than OA and PQ. $\mathbf{n}_0 = \overrightarrow{PO}/PO$ is the line of sight unit vector. We have*

$$QO - PO + PA - QA \approx \frac{(\overrightarrow{OA} - \overrightarrow{OA}^T \mathbf{n}_0 \mathbf{n}_0)^T \overrightarrow{PQ}}{PO} + \frac{\overrightarrow{OA}^T \mathbf{n}_0 PQ^2}{2PO^2}. \tag{2.1}$$

Proof: For expression simplification, we denote $\mathbf{r} = \overrightarrow{PO}$, $r = PO$, $\mathbf{a} = \overrightarrow{OA}$,

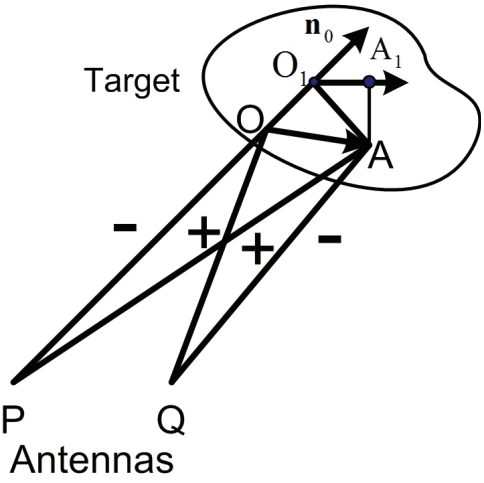

Figure 2.2: Geometry of the 4 points in the Lemma.

$\mathbf{d} = \overrightarrow{PQ}$. *Then*

$$\begin{aligned} & QO - PO + PA - QA \\ = & \tfrac{(\mathbf{r}-\mathbf{d})^T(\mathbf{r}-\mathbf{d})-\mathbf{r}^T\mathbf{r}}{PO+QO} + \tfrac{(\mathbf{r}+\mathbf{a})^T(\mathbf{r}+\mathbf{a})-(\mathbf{r}+\mathbf{a}-\mathbf{d})^T(\mathbf{r}+\mathbf{a}-\mathbf{d})}{QA+PA} \\ = & \tfrac{\mathbf{d}^T\mathbf{d}-2\mathbf{r}^T\mathbf{d}}{PO+QO} + \tfrac{2(\mathbf{r}+\mathbf{a})^T\mathbf{d}-\mathbf{d}^T\mathbf{d}}{QA+PA} \\ = & \tfrac{2\mathbf{r}^T\mathbf{d}(PO+QO-QA-PA)}{(PO+QO)(QA+PA)} + \tfrac{\mathbf{d}^T\mathbf{d}(QA+PA-PO-QO)}{(PO+QO)(QA+PA)} + \tfrac{2\mathbf{a}^T\mathbf{d}}{QA+PA} \\ \approx & \tfrac{-\mathbf{n}_0^T\mathbf{d}\mathbf{a}^T\mathbf{n}_0}{r} + \tfrac{\mathbf{d}^T\mathbf{d}\mathbf{a}^T\mathbf{n}_0}{2r^2} + \tfrac{\mathbf{a}^T\mathbf{d}}{r} \\ \approx & \tfrac{(\mathbf{a}-\mathbf{a}^T\mathbf{n}_0\mathbf{n}_0)^T\mathbf{d}}{r} + \tfrac{\mathbf{d}^T\mathbf{d}\mathbf{a}^T\mathbf{n}_0}{2r^2}, \end{aligned} \tag{2.2}$$

where we use the approximation $PO + QO - QA - PA \approx -2\mathbf{a}^T\mathbf{n}_0$, $(PO + QO)(QA + PA) \approx 4r^2$.

It can also be seen that $\overrightarrow{OO_1} = (\mathbf{a}^T\mathbf{n}_0)\mathbf{n}_0$, $\overrightarrow{O_1A} = \mathbf{a}-(\mathbf{a}^T\mathbf{n}_0)\mathbf{n}_0$ and $\overrightarrow{O_1A_1} = (\mathbf{a}-(\mathbf{a}^T\mathbf{n}_0)\mathbf{n}_0)^T\mathbf{d}/d$. It should be noted that $\overrightarrow{OA}$ and $\overrightarrow{PQ}$ need not be located in a plane. The formula here can be used for any radar and target position configurations.

Let P_m, Q_n denote the positions of the mth transmit antenna and the nth receive antenna respectively, $\mathbf{c}_m$ denote the transmit code of the mth transmit antenna. The code can be phase modulated signal [57]. The baseband transmit

waveform can be expressed as [24]

$$\varphi_m(t) = \sum_{l=0}^{L-1} c_m(l) u(t - lT_0), \tag{2.3}$$

where $u(t) = \begin{cases} 1 & \text{if } -T_0/2 < t < T_0/2, \\ 0 & \text{others.} \end{cases}$, T_0 is the subpulse duration, L is the code length. After demodulating, the received back-scattered signal from scatterer A at receive antenna n can be expressed as

$$\eta_{nA}(t) = \alpha \sum_{m=0}^{M-1} \varphi_m(t - \tau_{mA} - \tau_{nA}) e^{-j\omega(\tau_{mA}+\tau_{nA})}, \tag{2.4}$$

where $\tau_{mA} = P_m A/c$, $\tau_{nA} = Q_n A/c$, ω is the frequency (in radian), α is the signal amplitude, proportional to the square root of the RCS of scatterer A. Assuming that the transmitting codes satisfy $\varphi_m(t) \otimes \varphi_n(t) = \delta_{mn}\delta(t)$, after filtering with φ_m, the signal transmitted from P_m, back scattered from A and received at Q_n can be obtained as

$$\eta_{mnA}(t) = \alpha\delta\left(t - \tau_{mA} - \tau_{nA}\right) e^{-j\omega(\tau_{mA}+\tau_{nA})}. \tag{2.5}$$

$\eta_{mnA}(t)$ can be thought of as received by a virtual antenna formed by the mth transmit antenna and the nth receive antenna. Because $\tau_{mA} + \tau_{nA}$ varies with m and n, the signals of different virtual antennas from the scatterer are not aligned. The $\eta_{mnA}(t)$ for different m and n should be envelope-aligned before coherent processing. If the range profiles at different virtual antennas are similar, by computing the correlations between $|\eta_{mnA}(t)|$ for different m, n, the range profiles can be aligned. The details of envelope alignment can be found in [58]. But if the range sidelobes are high or the SNR is low, the performance of alignment using correlation method is poor. Denote O as the

reference point in the target. If the target line of sight is known, τ_{mO} and τ_{nO} can be computed according to the geometry of the antennas and the target. The transmit instances of the transmit codes can be adjusted according to τ_{mO} and the receive signals can be adjusted according to τ_{nO}. Then, the signals from the target at different virtual antennas are aligned.

With O as the focusing center, the expression $\tau_{mA} + \tau_{nA} - \tau_{mO} - \tau_{nO} \approx 2\overrightarrow{OA}^T\mathbf{n}_0/c$ is independent of the transmit and receive antennas. Then after range alignment, the signals $\eta_{mnA}(t)$ from A for different m and n are located at the same range cell. For clarity in expression, we have omitted the δ function in the following text. After phase compensation with signals from O (unit amplitude), the signal from A can be expressed as

$$\begin{aligned} s_{mnA} &= \eta_{mnA} \times \eta^*_{mnO} \\ &= \alpha exp\left(-j\omega(\tau_{mA} + \tau_{nA} - \tau_{mO} - \tau_{nO})\right) \\ &= \alpha exp\left(jk(P_mO + Q_nO - P_mA - Q_nA)\right). \end{aligned} \tag{2.6}$$

$P_mO + Q_nO - P_mA - Q_nA$ can be expressed as

$$\begin{aligned} & P_mO + Q_nO - P_mA - Q_nA \\ = \; & (P_0A - P_0O + Q_0O - Q_0A) + (P_0A - P_0O + P_mO - P_mA) \\ & +(Q_nO - Q_nA + Q_0A - Q_0O) - 2(P_0A - P_0O) \\ = \; & -2(P_0A - P_0O) + (\mathbf{a} - (\mathbf{a}^T\mathbf{n}_0)\mathbf{n}_0)^T(\overrightarrow{P_0Q_0} + \overrightarrow{P_0P_m} + \overrightarrow{Q_0Q_n})/r \\ & +\mathbf{a}^T\mathbf{n}_0(P_0Q_0^2 + P_0P_m^2 + Q_0Q_n^2)/(2r^2), \end{aligned} \tag{2.7}$$

after applying the lemma introduced earlier. $\mathbf{a}^T\mathbf{n}_0(P_0Q_0^2 + P_0P_m^2 + Q_0Q_n^2)/(2r^2)$ is known and can be compensated. Generally, it is also a small value and can be omitted. Hence s_{mnA} can be expressed as

$$s_{mnA} = \alpha e^{-j2k\mathbf{a}^T\mathbf{n}_0} e^{jk(\mathbf{a}-(\mathbf{a}^T\mathbf{n}_0)\mathbf{n}_0)^T(\overrightarrow{P_0Q_0} + \overrightarrow{P_0P_m} + \overrightarrow{Q_0Q_n})/r}. \tag{2.8}$$

2.2 MIMO Radar Structures, Strong Scatterer Selection and Coordinates Transformation

We introduce in this section three MIMO radar configurations that are suitable to perform 3D imaging.

2.2.1 Cross-Array MIMO Radar

The cross-array MIMO radar structure is as shown in Fig.2.3, where the M transmit antennas and the N receive antennas are uniform linear arrays parallel to the Y and X axis, respectively. The coordinates of P_m and Q_n are $(0, md_y, 0) + P_0$ and $(nd_x, 0, 0) + Q_0$, where d_y and d_x are the inter-element spacings of the transmit array and the receive array, P_0 and Q_0 are two arbitrary points near the origin of the Cartesian coordinate system. The target is in the far field opposite to the 2-D virtual array. Denote $\tilde{\mathbf{a}} = \mathbf{a} - (\mathbf{a}^T\mathbf{n}_0)\mathbf{n}_0$ and $\tilde{\mathbf{a}} = (\tilde{x}, \tilde{y}, \tilde{z})$. Eq. (2.8) can be expressed as (for simplicity, we have omitted the subscript A)

$$s_{mn} = \alpha exp(jk(\tilde{y}md_y + \tilde{x}nd_x)/r), \tag{2.9}$$

where the exponential term $exp(-j2k\mathbf{a}^T\mathbf{n}_0 + jk\tilde{\mathbf{a}}^T\overrightarrow{P_0Q_0}/r)$ has been combined to α. The α can be obtained easily using Discrete Fourier Transform (DFT). Denotes the discrete frequency as $[f_x, f_y]$, then we have

$$f_x = \frac{\tilde{x}d_x}{\lambda r}, \tag{2.10}$$

and

$$f_y = \frac{\tilde{y}d_y}{\lambda r}. \tag{2.11}$$

Translate the frequencies of f_x and f_y to coordinates $\tilde{x}$ and $\tilde{y}$, we have

$$\tilde{x} = f_x\frac{\lambda r}{d_x}, \tag{2.12}$$

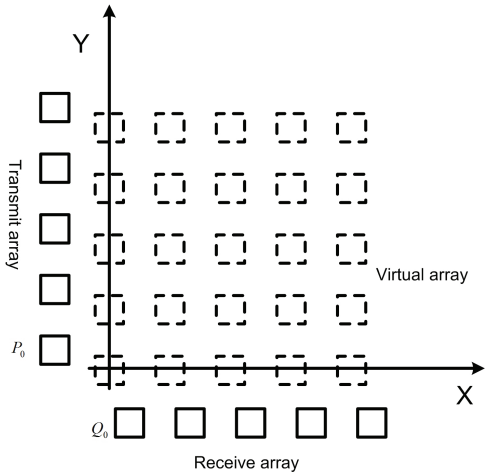

Figure 2.3: Geometry of cross MIMO array.

and

$$\tilde{y} = f_y \frac{\lambda r}{d_y}. \tag{2.13}$$

Because the discrete frequency is limited to $[-\frac{1}{2}, \frac{1}{2}]$, the $\tilde{x}$ and $\tilde{y}$ should be limited to $[-r\frac{\lambda}{2d_x}, r\frac{\lambda}{2d_x}]$ and $[-r\frac{\lambda}{2d_y}, r\frac{\lambda}{2d_y}]$. This is called the unambiguous window [11]. It is clear that while the total number of physical antennas is $M + N$, the freedom to do imaging is MN, which is equivalent to a virtual array of MN antennas. This has greatly reduced the number of antennas. We can see that, irrespective of the positions of the real antennas, the first virtual antenna of the 2-D virtual array is at the origin of the coordinates system.

2.2.2 Square-Array MIMO Radar

The square-array MIMO radar is as shown in Fig.2.4, where the transmit and receive array antennas form two uniform planar arrays. We assume $M = M_1 \times M_2$ and $N = N_1 \times N_2$. The antenna index m and n can be expressed as $m = m_1 + m_2 M_1$ and $n = n_1 + n_2 N_1$, where $0 \leq m_1 < M_1$, $0 \leq m_2 < M_2$, $0 \leq n_1 < N_1$ and $0 \leq n_2 < N_2$. The positions of P_m and Q_n are $(m_1 d_{tx}, m_2 d_{ty}, 0) + P_0$ and $(n_1 d_{rx}, n_2 d_{ry}, 0) + Q_0$. Then we have $\overrightarrow{P_0 P_m} = (m_1 d_{tx}, m_2 d_{ty}, 0)$, $\overrightarrow{Q_0 Q_n} = (n_1 d_{rx}, n_2 d_{ry}, 0)$ and $\overrightarrow{P_0 P_m} + \overrightarrow{Q_0 Q_n} = (m_1 d_{tx} + n_1 d_{rx}, m_2 d_{ty} + n_2 d_{ry}, 0)$. Eq.2.8

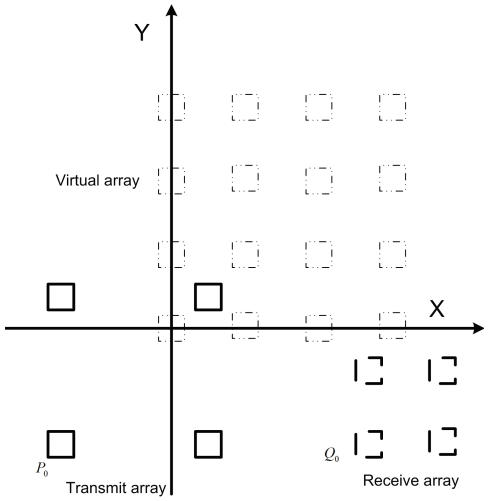

Figure 2.4: Geometry of square MIMO array.

can be expressed as

$$s_{mn} = \alpha e^{jk(\tilde{y}(m_2 d_{ty} + n_2 d_{ry}) + \tilde{x}(m_1 d_{tx} + n_1 d_{rx}))/r}. \tag{2.14}$$

When $N_1 \times d_{rx} = d_{tx}$ and $N_2 \times d_{ry} = d_{ty}$, Eq. (2.14) can be expressed as

$$\begin{aligned} s_{mn} = &\quad \alpha e^{jk(\tilde{y}(m_2 N_2 d_{ry} + n_2 d_{ry}) + \tilde{x}(m_1 N_1 d_{rx} + n_1 d_{rx}))/r} \\ = &\quad \alpha e^{jk(\tilde{y}((m_2 N_2 + n_2) d_{ry}) + \tilde{x}((m_1 N_1 + n_1) d_{rx}))/r}. \end{aligned} \tag{2.15}$$

Denote $\tilde{m} = m_2 N_2 + n_2$, $\tilde{n} = m_1 N_1 + n_1$ and $\tilde{s}_{\tilde{m}\tilde{n}} = s_{mn}$, we have

$$\tilde{s}_{\tilde{m}\tilde{n}} = \alpha exp(jk(\tilde{y} d_{ry} \tilde{m} + \tilde{x} d_{rx} \tilde{n})/r). \tag{2.16}$$

Similar to the cross-array configuration, the α and $(\tilde{x}, \tilde{y})$ can be computed easily using DFT.

2.2.3 Interferometric MIMO Radar

While the cross-array and square-array MIMO radar configurations have reduced the required number of antennas, the interferometric array configuration

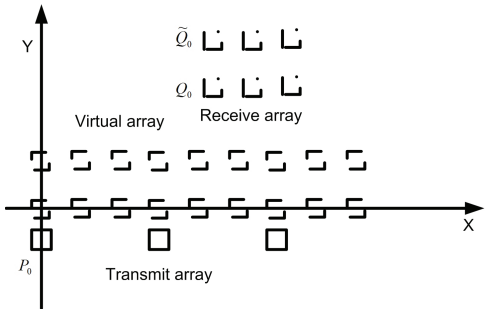

Figure 2.5: Geometry of Interferometric MIMO array.

outlined below can further reduce the required antennas, albeit at a reduced imaging quality. Strictly speaking, the interferometric array configuration is a special case of the square-array. The transmit array consists of only one uniform linear array with M antennas and inter-element distance of d_{tx}, while the receive arrays have two parallel uniform linear arrays, each has N antennas with inter-element distance d_{rx}, as shown in Fig.2.5. Assume that the transmit array is parallel to the X axis, the two receive arrays are also parallel to the X axis and they are all located on the $Z = 0$ plane. The Y coordinates of the first and second receive arrays are $Y_0 - d_{ry}/2$ and $Y_0 + d_{ry}/2$. The transmit array and the two receive arrays form two virtual arrays. Denote Q_n and $\tilde{Q}_n$ as the positions of the first and second receive arrays. The corresponding received signals after phase compensation are denoted as s_{1mn} and s_{2mn}. We have

$$s_{1mn} = \alpha exp(jk\tilde{\mathbf{a}}^T(\overrightarrow{P_0Q_0} + \overrightarrow{P_0P_m} + \overrightarrow{Q_0Q_n})/r), \tag{2.17}$$

and

$$s_{2mn} = \alpha exp(jk\tilde{\mathbf{a}}^T(\overrightarrow{P_0\tilde{Q}_0} + \overrightarrow{P_0P_m} + \overrightarrow{\tilde{Q}_0\tilde{Q}_n})/r). \tag{2.18}$$

Let the transmit and receive arrays' inter-element distances satisfy $Nd_{rx} = d_{tx}$ and denote $\tilde{m} = mN + n$, $s_{1\tilde{m}} = s_{1mn}$, $s_{2\tilde{m}} = s_{2mn}$, we have

$$s_{1\tilde{m}} = \alpha exp(jk\tilde{\mathbf{a}}^T\overrightarrow{P_0Q_0}/r)exp(jk\tilde{x}\tilde{m}d_{rx}/r), \tag{2.19}$$

and

$$s_{2\tilde{m}} = \alpha exp(jk\tilde{\mathbf{a}}^T\overrightarrow{P_0\tilde{Q}_0}/r)exp(jk\tilde{x}\tilde{m}d_{rx}/r). \tag{2.20}$$

The values of $\alpha exp(jk\tilde{\mathbf{a}}^T\overrightarrow{P_0Q_0}/r)$, $\alpha exp(jk\tilde{\mathbf{a}}^T\overrightarrow{P_0\tilde{Q}_0}/r)$ and the coordinate $\tilde{x}$ of the scatterer can be obtained by DFT of the $s_{1\tilde{m}}$ and $s_{2\tilde{m}}$. Denote s_1, s_2 as the DFTs of $s_{1\tilde{m}}$ and $s_{2\tilde{m}}$ on $\frac{\tilde{x}d_{rx}}{\lambda r}$ and let $s = s_1^* s_2$, s can be expressed as (omitting $|\alpha|^2$)

$$s = exp\left(jk\tilde{\mathbf{a}}^T\overrightarrow{Q_0\tilde{Q}_0}/r\right) = exp(jk\tilde{y}d_{ry}/r). \tag{2.21}$$

The $\tilde{y}$ can be obtained by computing the phase ψ of s.

Denote $\psi = k\tilde{y}d_{ry}/r$, we have

$$\tilde{y} = \frac{\psi r}{kd_{ry}}. \tag{2.22}$$

2.2.4 Strong Scatterers Selection

One drawback of MIMO radar is its high range sidelobes. Let the transmit and receive arrays be the same 8×8 square array. The transmitting codes are binary random codes with length of 512. A point target is located in the far field, broadside to the arrays. The three dimensional response of this point scatterer cannot be shown clearly in three dimensional space. A range and cross-range slice through the peak of the response is shown in Fig.2.6. It can be seen that there are strong range and cross-range sidelobes. The strong range sidelobes almost cover the entire range area. The strong cross-range sidelobes are located from -8 to 8, because there are 8 transmitting antennas in one cross-range dimension. The peak values of the strong sidelobes are about -14 to -15 dB. This means that if another scatterer B is located in the strong sidelobes area of scatterer A and if the power of scatterer B is 14 dB lower than that of scatterer A, scatterer B will be submerged. On the other hand, if we allow a high dynamic range, many sidelobes points will be regarded as false

scatterers. We propose to mitigate this problem via the reference processing of some strong scatterers. It is well-known in high-frequency electromagnetic scattering theory that, the returned energy from a target mainly consists of those back-reflected from the shinning (flat) faces of the target. According to Born approximation, multiple bounces can be omitted. This means that there is very likely to have only one strong scatterer in the range units with the same cross-range unit. Denote $R_p = [r_p(1), r_p(2), \cdots, r_p(N)]$ the range profile of cross-range unit p. If R_p has a strong scatterer, there will be a strong peak in R_p, otherwise, there will be many peaks with approximately similar amplitudes (Fig.2.7). According to this phenomenon, we can use the following procedure to select strong scatterers to form 3-D image. Let V_{max} (dB) be the maximum value of $|\alpha|$ (α is the reconstructed reflectivity matrix in the entire imaging area), and the unit is dB. The expected dynamic range of the target is δv dB, which means that scatterers with amplitude belong to $[V_{max} - \delta v, V_{max}]$ are candidate scatterers to form 3-D image. $\delta\zeta$ dB is another threshold to detect the range sidelobe area. Denote v_{max} as the maximum value in R_p. If the second maximum value of another scatter in R_p is larger than $v_{max} - \delta\zeta$, then we conclude the range profile R_p to be a sidelobe range profile, which will not be used to form the final 3-D image. This idea is shown in Fig.2.8. For simplicity, a one-dimensional plot in Fig.2.8 (a) is used to replace a two-dimensional plot.

Let $I = (f_x, f_y, \tau)$ be the two cross-range coordinates and one range coordinate. $max(\cdot)$ is a function computing the maximum value of a matrix and the coordinates of the peak. The strong scatterer selection procedure can be described in the following pseudo codes.

Initializing: $V_{max}, \delta v, \delta\zeta$, $loop = 1$.

while $loop == 1$

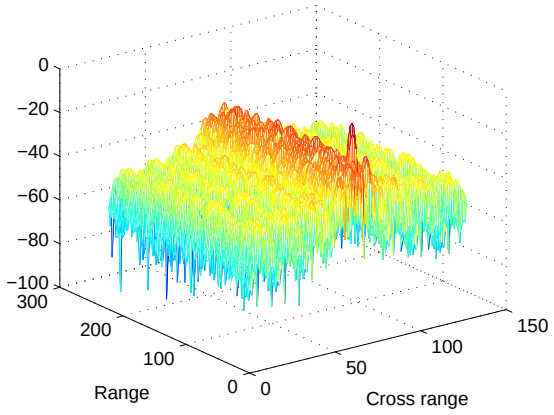

Figure 2.6: Cross range image of a point scatterer in different range cells.

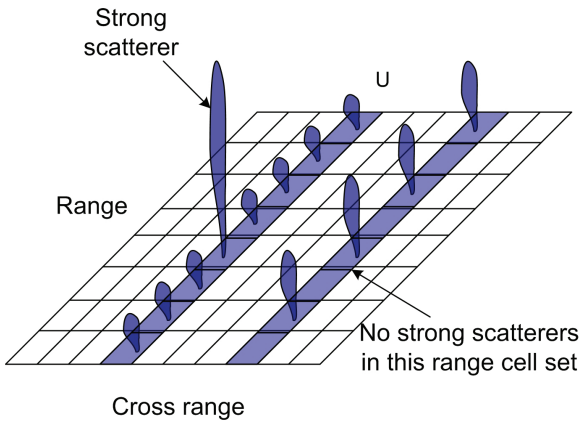

Figure 2.7: Scatterers in different range and cross range units.

$[I, v] = max(|\alpha|)$

if $v > V_{max} - \delta v$ dB

Let the value of $|\alpha|$ in the neighbor of τ(range direction) be zero.

$[\hat{\tau}, \zeta] = max(|\alpha(f_x, f_y, :)|)$

$if \quad v - \delta\zeta > \zeta$ dB

record I and v (strong scatterer)

$else$

cross-range unit (f_x, f_y) is a sidelobe unit

end

Let $|\alpha(f_x, f_y, :)|$ be zero

$else$

$loop = 0$

end

end

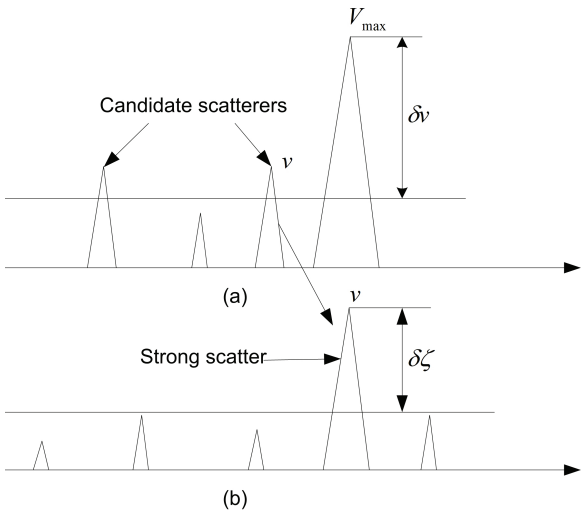

Figure 2.8: Strong scatterer selection criterion.

2.2.5 Position Computation and Coordinates Transformation

For cross-array, square-array and interferometric MIMO radar, the $(\tilde{x}, \tilde{y})$ can be obtained by DFT or by computing the phase difference. However, the obtained $(\tilde{x}, \tilde{y})$ are not the real coordinate of the scatterer A, but the coordinate of $\tilde{\mathbf{a}}$. According to the definition of $\tilde{\mathbf{a}} = \mathbf{a} - (\mathbf{a}^T\mathbf{n}_0)\mathbf{n}_0$, we have $\mathbf{a} = \tilde{\mathbf{a}} + (\mathbf{a}^T\mathbf{n}_0)\mathbf{n}_0$.

Since $\tilde{\mathbf{a}}^T\mathbf{n}_0 = 0$, we obtain $\tilde{z} = \frac{-\tilde{x}n_x - \tilde{y}n_y}{n_z}$. Denote $\hat{r} = \mathbf{a}^T\mathbf{n}_0$, which can be obtained by counting the range unit of the scatterer. We have

$$x = \tilde{x} + \hat{r}n_x, \tag{2.23}$$

$$y = \tilde{y} + \hat{r}n_y, \tag{2.24}$$

$$z = \frac{-\tilde{x}n_x - \tilde{y}n_y}{n_z} + \hat{r}n_z. \tag{2.25}$$

Generally speaking, the reference point O may not be located in the center of the target due to DOA (direction of arrival) estimation error. Then the target may be located just cover the sides of the unambiguous window. Then phase unwrapping should be implemented.

2.3 Implementation Consideration

2.3.1 Construction of Zero Correlation Zone Codes

In Section 2.1 we have assumed that the codes are orthogonal and the matched filtering output is a Dirac function. Actually this is impossible. For random binary codes, the auto-correlations and cross-correlations of the codes have high sidelobes proportional to $1/\sqrt{L}$, where L is the length of the codes. Fortunately, the targets in sky are usually sparsely distributed. We assume that

there are no other targets near the target of interest. In this case, the codes need only to have low sidelobes near the zero time shifts. For example, if the range extent of the target is 50 m, the range resolution of the transmitting signal is 1 m, the length of the code is 100, then the codes need only have low sidelobe values in the area $[-49, 49]$. High level sidelobes in [-99, -50] and [50, 99] do not significantly affect the imaging results. We thus introduce the zero correlation zone codes as follows, which have zero correlations in a zone.

Let K denote the size of the zero correlation zone, $\hat{k}$ be an integer relatively prime to K. Define code $\tilde{c} = [\tilde{c}_0, \tilde{c}_1, \cdots, \tilde{c}_{K-1}]$ as [59]

$$\tilde{c}_k = exp\left(\frac{j\hat{k}\pi(k - K/2 - p)^2}{K}\right), \quad k = 0, 1, \cdots, K-1, \tag{2.26}$$

where p is an arbitrary integer. It has been proven that $\tilde{c}_k$ is a "periodic orthogonal sequence", which means that the periodic correlation $R_{\tilde{c}}(\tau)$ satisfies

$$R_{\tilde{c}}(\tau) = \begin{cases} K & \tau = 0 \\ 0 & 1 \leq |\tau| \leq K-1 \end{cases} \tag{2.27}$$

where $R_{\tilde{c}}(\tau)$ is defined as

$$R_{\tilde{c}}(\tau) = \sum_{k=0}^{K-1} \tilde{c}_k \tilde{c}^*_{k+\tau \ mod \ K}, \quad 0 \leq |\tau| \leq K-1 \tag{2.28}$$

where $k+\tau \ mod \ K$ refers to $k+\tau$ modulo K. The periodic cross correlation is defined in a similar manner.

For $K = 230$, $\hat{k} = 3$, $p = 0$, the real and imaginary part of code $\tilde{c}_k$ are shown in Fig.2.9.

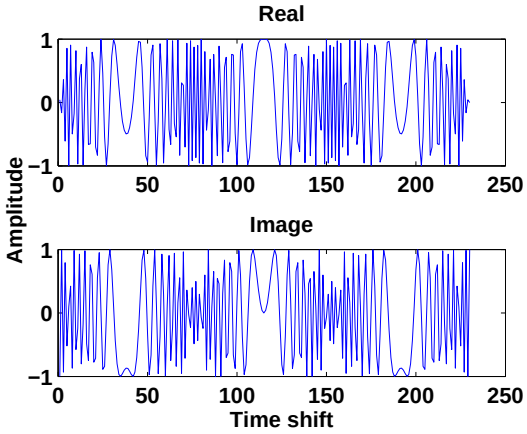

Figure 2.9: The real and imaginary part of a periodic orthogonal sequence for $K = 230$, $\hat{k} = 3$ and $p = 0$.

Denote N as the number of the codes. Define N matrices

$$\mathbf{P}_n = \begin{bmatrix} 0 & 0 & \cdots & 0 \\ \vdots & \vdots & \vdots & \vdots \\ \tilde{c}_0 & \tilde{c}_1 & \cdots & \tilde{c}_{K-1} \\ \vdots & \vdots & \vdots & \vdots \\ 0 & 0 & \cdots & 0 \end{bmatrix}_{N \times K}, \tag{2.29}$$

where $n = 1, \cdots, N$. The elements in each row are zeros except for the n^{th} row.

Let $\mathbf{p}_n = \text{vec}\{\mathbf{P}_n\}$. The N zero correlation zone codes $\{\mathbf{c}_n\}$ with length $L = K \times N$ can be obtained by

$$\mathbf{c}_n = \mathbf{DFT}\{\mathbf{p}_n\}, \quad n = 1, \cdots, N. \tag{2.30}$$

It has been shown in [60] that the periodic auto-correlations of $\mathbf{c}_n$ are zeros in zone $\Omega = [-K+1, -1]\,U[1, K-1]$, while the periodic cross correlations between $\mathbf{c}_n$ and $\mathbf{c}_{n'}(n \neq n')$ are zeros in the entire area. We use the following example to illustrate it. Let $L = 16$, $N = 4$, $K = 4$, $\hat{k} = 3$ and $p = 0$.

Four codes are constructed using the above method. The absolute value of the periodic auto-correlations of the first code and the periodic cross correlations between the first code and the other codes are as shown in Fig.2.10.

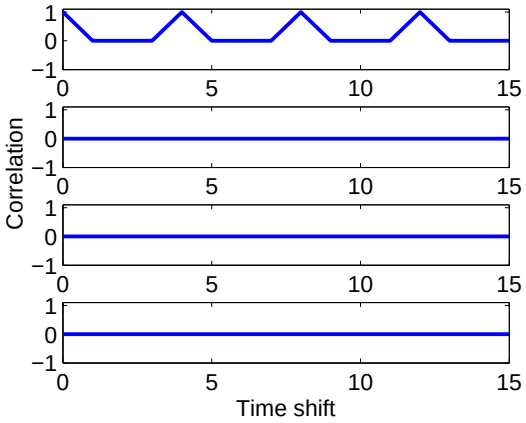

Figure 2.10: The periodic auto-correlations and cross correlations of the zero correlation zone codes.

However, in reality, the correlations of the transmit codes with the receive codes are aperiodic, not periodic. In order to perform periodic correlation, we have to re-define the receive code as $\hat{\mathbf{c}}_n = [c_{n,L-K+1}, \cdots, c_{n,L-1}, c_{n,0}, \cdots, c_{n,L-1}, c_{n,0}, \cdots, c_{n,K-2}]$. In receive filtering, $\hat{\mathbf{c}}_n$ is used to match the received signal. It is clear that at the instant where $\mathbf{c}_n$ matches the middle part of $\hat{\mathbf{c}}_n$ (that is $\mathbf{c}_n$), and sliding through the pre- and post- $K-1$ chips, the aperiodic correlations between $\hat{\mathbf{c}}_n$ and $\mathbf{c}_n$ are periodic correlations between $\mathbf{c}_n$ and $\mathbf{c}_n$. Therefore, the aperiodic zero correlation window is Ω.

2.3.2 Pre-shift of Codes and the Effect of DOA Estimation Error

In the sections considering ZCZ codes, the codes in the code matrix $\mathbf{X}$ are aligned. For imaging slant-range target, the delay differences of the target

relative to different transmit antennas may be much larger than the range resolution. If the codes are transmitted simultaneously, the different transmit codes received at each individual receive antenna are not aligned. If we were to overcome this issue by designing codes with long zero correlations zone, then the increase in the code length will render the codes more Doppler sensitive. Therefore the DOA of the target should be estimated at first, and the transmit instants of the code envelopes should be adjusted such that the signals from different transmit antennas arrive at the target at the same time. This is shown in Fig.2.11.

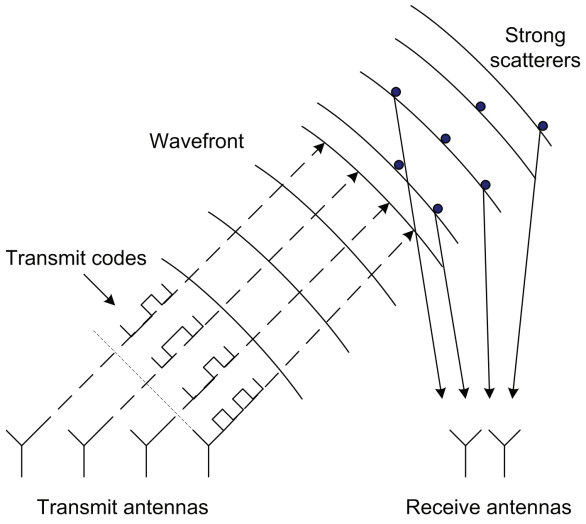

Figure 2.11: Pre-shift of the codes transmission.

The effect of DOA estimation error is analyzed as follows. Denote $\mathbf{n}_1$ as the measured DOA unit vector. Let P_0 be the reference transmit antenna, another transmit antenna is located at $P_1 = P_0 + \mathbf{d}_0$. Relative to P_0, the signal envelope from P_1 should be adjusted by $\frac{\mathbf{d}_0^T \mathbf{n}_0}{c}$ seconds. The real adjustment due to the measured $\mathbf{n}_1$ is $\frac{\mathbf{d}_0^T \mathbf{n}_1}{c}$, the adjustment error is $\frac{\mathbf{d}_0^T (\mathbf{n}_0 - \mathbf{n}_1)}{c}$. Assume that the maximum allowed alignment error is $\frac{1}{5}T$, where T is the chip duration.

Then $\mathbf{n}_0 - \mathbf{n}_1$ should satisfy

$$|\mathbf{d}_0^T(\mathbf{n}_0 - \mathbf{n}_1)| \leq \frac{1}{5}cT = \frac{2}{5}\delta r, \tag{2.31}$$

where δr is the range resolution. For a uniform linear array of aperture D, the width of the beam pattern is about $\frac{\lambda}{D}$. Let θ_0 and θ_1 denote the real and estimated angles. Generally, the angle estimation error, denoted as $\beta\frac{\lambda}{D}$, can be much less than $\frac{\lambda}{D}$. In 2-D case, let $\mathbf{d}_0 = [d_0, 0]$ and $\mathbf{n}_0 = [\cos\theta_0, \sin\theta_0]$. Eq. (2.31) can be written as

$$|d_0(\cos\theta_0 - \cos\theta_1)| \leq \frac{2}{5}\delta r, \tag{2.32}$$

and

$$|d_0 \sin\theta_0 \delta\theta| = |d_0 \sin\theta_0 \beta\frac{\lambda}{D}| \leq \frac{2}{5}\delta r. \tag{2.33}$$

For MIMO linear array, let the inter-element distances of the receive array and the transmit array be d_r and Nd_r, then the maximum d_0 is MNd_r. Eq. (2.33) can be expressed as

$$|MNd_r \sin\theta_0 \beta\frac{\lambda}{D}| \leq |\frac{\beta MNd_r\lambda}{D}| \leq \frac{2}{5}\delta r. \tag{2.34}$$

For a specific MIMO radar configuration, we should first check if Eq. (2.34) is satisfied. If not, we should use a more precise DOA estimation method.

2.3.3 Comparison with IFIR radar

A simpler configuration of multiple-input multiple-output radar, limited to using the same transmitting waveform, is called the Interpolated FIR (IFIR) radar [61]. Assume that there are N receiving antennas with inter-element distance of d_r, and M transmitting antennas with inter element distance of Nd_r. For MIMO radar discussed in the previous sections, the transmitting

codes are the rows of a matrix $\mathbf{C}$, but for IFIR radar, the M transmitting antennas transmit the same code $\mathbf{c}$. Because the transmitting array of IFIR radar is a sparse array, its beam pattern has grating lobes. But since the nulls of the receive beam pattern coincide with the grating lobes, the grating lobes can be canceled [61]. The aperture of the IFIR radar is the same as the collocated MIMO radar. The two radars have the same space resolution. This is shown in Fig.2.12. In this subsection, we compare the output SNR of these two radars. For other comparisons, e.g. clutter and jammer power, please refer to [61].

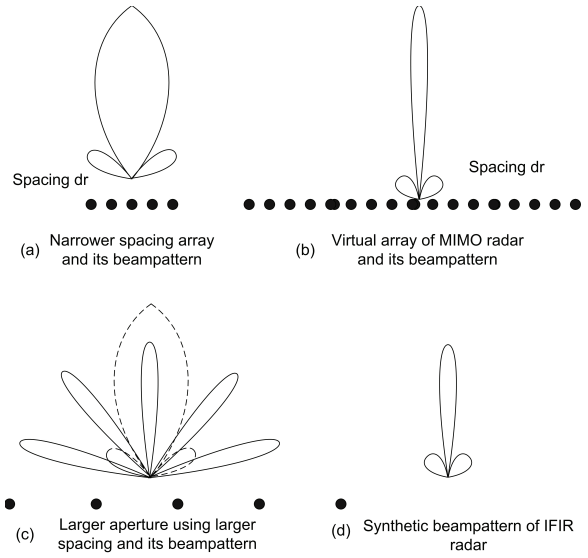

Figure 2.12: Beam pattern comparison of MIMO radar and IFIR radar. a) receiving array and its beam pattern of IFIR radar. b) virtual array of MIMO radar and it's beam pattern. c) transmitting array and its beam pattern of IFIR radar. d) synthetic beam pattern of transmitting and receiving arrays of IFIR radar.

Let Ω be the imaging target area. All antennas of the MIMO array are directional antennas with beam width wider than Ω and are steering toward Ω. For simplicity, we consider only the orthogonal code. Denote $\mathbf{C}_{M\times L}$ as the orthogonal code matrix, $\mathbf{C}\mathbf{C}^H = L\mathbf{I}$. According to Eq. (2.8), the s_{mnA} can be

rewritten as

$$\mathbf{S} = \frac{\sqrt{P_t G_t \alpha A_r L_\alpha}}{4\pi R^2}\mathbf{a}(\theta)\mathbf{b}^T(\theta)\mathbf{C} + \mathbf{Z}, \tag{2.35}$$

where P_t is the power of each transmitter, G_t is the transmit antenna gain, α is the scatterer's RCS, A_r is the effective receive antenna aperture, L_α is the hardware loss, R is the distance, $\mathbf{Z}$ is the noise matrix. $\mathbf{a}(\theta) = [1, \cdots, e^{jk\tilde{\mathbf{a}}^T\overrightarrow{Q_0Q_n}/r}, \cdots]$ and $\mathbf{b}(\theta) = [1, \cdots, e^{jk\tilde{\mathbf{a}}^T\overrightarrow{P_0P_m}/r}, \cdots]$ can be regarded as the steering vectors of the receive array and the transmit array. Denote $P = \frac{P_t G_t \alpha A_r L_\alpha}{(4\pi)^2 R^4}$. After matched filtering, the output of the signal is

$$\alpha = tr(\sqrt{P}\mathbf{a}(\theta)\mathbf{b}^T(\theta)\mathbf{C}\mathbf{C}^H\mathbf{b}^*(\theta)\mathbf{a}^H(\theta)) = \sqrt{P}MNL, \tag{2.36}$$

where $tr(\cdot)$ is the trace of a matrix. The output noise power is

$$\begin{aligned}\sigma^2 &= E\left\{tr(\mathbf{Z}\mathbf{C}^H\mathbf{b}^*(\theta)\mathbf{a}^H(\theta)) \times tr^*(\mathbf{Z}\mathbf{C}^H\mathbf{b}^*(\theta)\mathbf{a}^H(\theta))\right\} \\ &= MNL\sigma_0^2.\end{aligned} \tag{2.37}$$

The SNR is $\frac{MNLP}{\sigma_0^2}$.

For IFIR radar, the received signal is

$$\mathbf{s} = \frac{\sqrt{P_t G_t \alpha A_r L_\alpha}}{4\pi R^2}\mathbf{a}(\theta)M\mathbf{c}^T + \mathbf{Z}, \tag{2.38}$$

The output of the signal after matched filtering is

$$\alpha = \sqrt{P}MNL. \tag{2.39}$$

The output noise power is

$$\sigma^2 = E\{tr(\mathbf{Z}\mathbf{c}^*\mathbf{a}^H(\theta)) \times tr^*(\mathbf{Z}\mathbf{c}^*\mathbf{a}^H(\theta))\} = LN\sigma_0^2 \tag{2.40}$$

So the SNR using IFIR radar is $M\frac{MNLP}{\sigma_0^2}$.

It can be seen that the output SNR of the IFIR radar is M times that of the collocated MIMO radar. However, the beam width of IFIR transmitting and receiving arrays are $\frac{1}{MN}$ and $\frac{1}{N}$. In order to cover all the area, the IFIR radar should scan $(\frac{1}{N}/\frac{1}{MN}) = M$ times. But for MIMO array, it only needs

(a) (b)

Figure 2.13: (a)Transmitting beam pattern (dash dot) and receiving beam pattern of IFIR array, (b) Synthetic transmitting-receiving beam pattern.

transmitting one times. Thus the average SNR of the two methods are the same. Fig.2.13 (a)(b) show an example of $M = 5$ and $N = 3$. The beam pattern of the transmitting array is shown as dash dot line. It can be seen that there are $N = 3$ grating lobes. By adjusting the phase of the receiving weight, three receiving beam patterns are formed. Each aims at the peak of one grating lobe.The final transmitting-receiving beam pattern is shown in Fig.2.13 (b). We can see that it can only receive signals from three beams. In order to receive the entire region's signal, the transmitting array needs scan and transmitting $M = 5$ times.

2.3.4 Discussion on the Realistic Choice of Radar Parameters and the Expected SNR

Imaging radar is usually used following searching and tracking radars to image and identify the target. For a general target such as an airplane, a few tens to one hundred resolution cells in each cross directions is needed to cover the entire target. So a 10×10 transmit array and a 10×10 receive array configuration can satisfy the requirement. Assume that the designed surveillance range is from 50 km to 60 km. The carrier frequency is $f_0 = 35$ GHz. The unambiguous distance is 100 m, which is bigger than the entire length of a typical airplane. The inter-element distances of the receive array and the

transmit array are 4.2875 m and 42.875 m, respectively. The transmit and receive antenna's area is 0.04π. Then the beam pattern angle is about 0.0242 radian and the beam width in the surveillance range is about 1200 m, which is more than sufficient to cover the entire target. The gain of the transmit and receive antenna is about 43.3 dB. The power of each transmit antenna can be less than a hundred watts. The hardware loss factor can be limited to $L_\alpha = 0.8$. Denote $K_b = 1.38 \times 10^{-23}$ J/K be the Boltzmann constant, $T_0 = 290$ K be the environmental temperature, F_n be the noise factor. When the antenna noise temperature equals the environmental temperature, the system noise temperature is $T_s = F_n T_0$. The noise power is $\sigma_0^2 = K_b T_s B_n$, where B_n is the receiver noise band. Since $B_n \approx B_s$, where B_s is the spectral bandwidth of the transmitted signal, according to the derivation in the last subsection, the output SNR after MIMO processing is

$$SNR = \frac{MNLP_t G_t \alpha A_r L_a}{16\pi^2 R^4 K_b F_n T_0 B_s}. \tag{2.41}$$

For the above realistic parameters, a medium SNR value can be obtained.

The MIMO radar 3D imaging process mainly consists of signal separation and cross-range FFT operations. The signal separation requires about $2KLMN$ complex multiplications and the cross-range processing requires K FFT operations (length MN). The computation is easy to implement using modern DSP technique. The whole imaging process is shown in Fig.2.14.

2.4 Simulation results

In the following simulations, we choose $f_0 = 35$ GHz, $B_s = 150$ MHz. $G_t = 43.3$ dB, $A_r = 0.04\pi m^2$, $F_n = 2.5$ dB, $B_n = 150$ MHz, $L_\alpha = 1$ and $R = 50$ km.

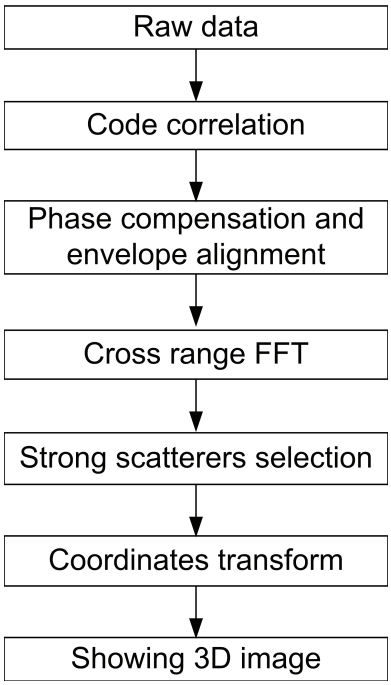

Figure 2.14: The implementation flow of 3D imaging.

2.4.1 Simulation 1: Comparison of Random Codes to ZCZ Codes

In this simulation, we compare the results using random codes and ZCZ codes. Ten transmit antennas each with $P_t = 200$ W and ten receive antennas are arranged as two uniform linear arrays and located in a line as shown in Fig.2.15. The inter-element spacings of the receive array and the transmit array are 4.2857 m and 42.8571 m respectively. The unambiguous distance at the target area is 100 meters. The length of the random binary codes and the ZCZ codes are all 300. A target with 11 scatterers is located on the broadside of the array. Fig.2.16 shows the original image of the target on the down-range and cross-range plane.

The square roots of the RCS of the 11 scatterers are evenly distributed from 1 to 11 meter, then the dynamic range of the target is 21 dB. The SNR of the weakest scatterer after imaging is 11.87 dB. Fig.2.17(a) and Fig.2.17(b)

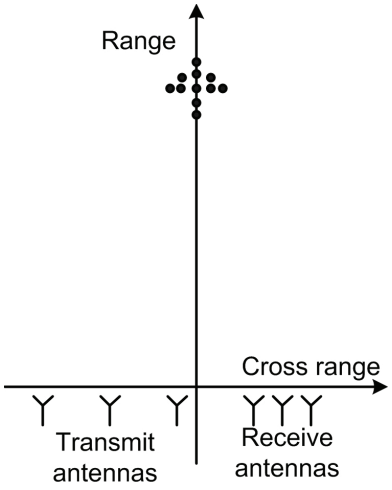

Figure 2.15: Geometry of the target and the MIMO array (simulation1).

show the reconstructed images (contour plot) for transmitting random code and ZCZ codes. Fig.2.17(c) and Fig.2.17(d) are the corresponding mesh plot images. The zero sidelobe range of the ZCZ code is from -29 to 29. It can be seen that the image using random code has high sidelobes near the target area and some weak scatterers are submerged under the sidelobes. But the image using the ZCZ code is better due to its low sidelobe levels in the target zone.

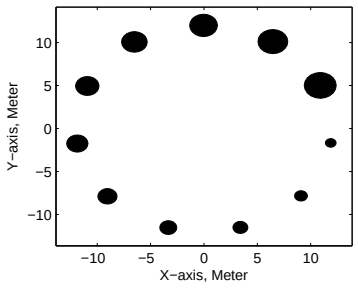

Figure 2.16: The range and cross range domain target model (simulation 1).

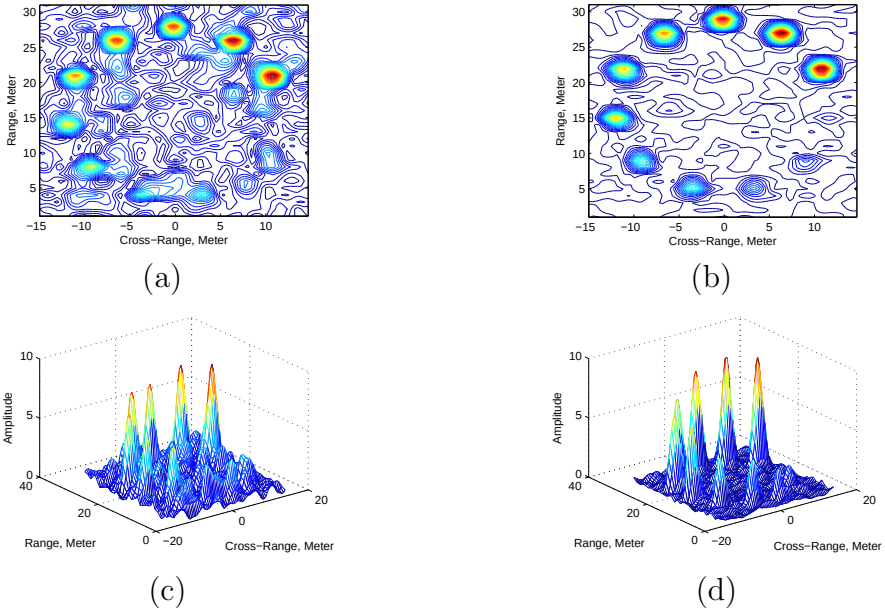

Figure 2.17: Reconstructed down-range and cross-range image of the target using the ZCZ and random code. (a) contour plot using random codes; (b) contour plot using ZCZ codes; (c) mesh plot using random codes; (d) mesh plot using ZCZ codes (simulation 1)

2.4.2 Simulation 2: Comparison of Using Cross Array to Square Array

In this simulation, we compare the difference of using cross MIMO array and square MIMO array. 64 transmit and 64 receive antennas are located on the $Z = 0$ plane. For cross-array, the transmit array and the receive array are along the X and the Y axes respectively and the inter-element distances of the transmit and receive arrays are all 6.6964 m. For the square-array, the inter-element distances of the transmit and receive arrays are 53.5714 m and 6.6964 m respectively. The unambiguous distance at the target area is 64 m. The length of the transmitted random binary codes is 256. For clarity in presentation, the scatterers are located on the broadside, have the same z coordinate and the same RCS of 1 m^2. The transmitting power of each transmitter is 600 W. The theoretical SNR after range and cross range

processing is 32 dB. In this case the effect of sidelobe is more pronounced. Fig.2.18 shows the original image. Fig.2.19 (a) and Fig.2.19 (b) show the 2D contour images of the target in this range cell using cross-array and square-array. Fig.2.19 (c) and Fig.2.19 (d) show the corresponding mesh images. Due to the non-orthogonal property of the codes, the image using cross-array has high sidelobes in the transmit array direction. But in the receive array direction, the sidelobes are mitigated due to coherent array processing of the receive array. For square-array, there are sidelobes in both directions, but their amplitudes are reduced as compared to the cross array case. Generally speaking, using square-array is better than using cross-array.

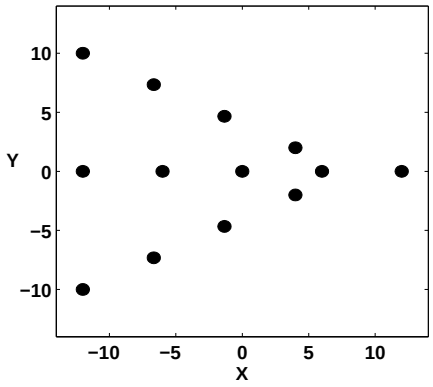

Figure 2.18: Original cross range image of the target (simulation 2).

2.4.3 Simulation 3: 3D Imaging Using Square Array

We show the 3D imaging results in this simulation. The transmit and receive arrays are all 8×8 square arrays with $d_t = 53.5714$ m, $d_r = 6.6964$ m and located on the XY plane. The transmit power for each transmitter is 10 W. The unambiguous distance at the target area is 64 m. The target with 11 scatterers as shown in Fig.2.20(a) is located at the $n_0 = [0.4402, 0.1761, 0.8805]$ direction. The square roots of the RCS of the 11 scatterers are from 1 m to

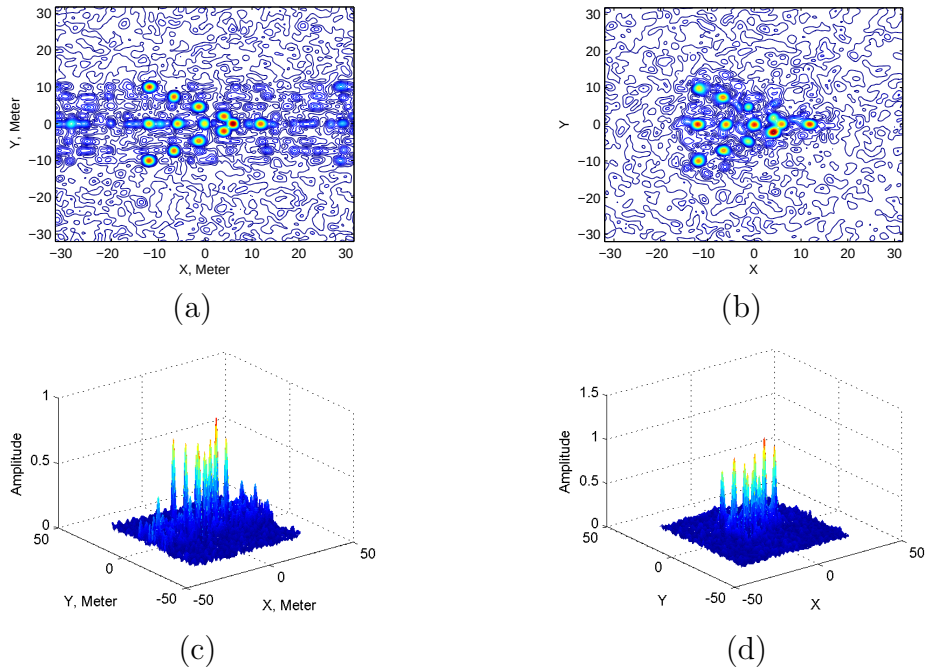

Figure 2.19: Contour plot and mesh plot of the reconstructed cross range image using the cross and the square array.(a) for cross-array and contour plot; (b) for square array and contour plot; (c) for cross-array and mesh plot; (d) for square array and mesh plot (simulation 2).

11 m. The length of the binary random codes is 512. The output SNR of the weakest scatterer is 17.3 dB after processing.

Denote V_{max} as the measured RCS of the strongest scatterer, in order to process high dynamic range target, scatterers with power larger than $V_{max} - 32$ dB are selected as strong scatterers to form the 3D image. The choice of -32 dB is problem related. For all range units with the same cross-range unit, we only selected one strongest unit and denote its power as ζ. If there is other range unit having the same cross-range unit and that the power is larger than $\zeta - \delta\zeta$ dB, then all the range units in this cross-range unit will be regarded as sidelobes units. The reconstructed projection images on the YZ plane for different $\delta\zeta$ are shown in Fig.2.21. The $\delta\zeta$ are selected as 3.52, 4.61, 5.57 and 6.02 dB respectively. If the distance from one estimated scatterer to the real scatterer is larger than 1.5 times resolution, we will then classify

this estimated scatterer as false alarm scatterer. The numbers of false alarm scatterers are 142, 30, 9 and 5 for the above $\delta\zeta$ respectively. It can be seen that with the increase of the $\delta\zeta$, the number of false scatterers decrease, but the smaller (weaker) real scatterers may also be canceled (classified as false alarm). This is a common problem in the trade off between target detection and false alarm in radar. The reconstructed 3D image and the projection images when $\delta\zeta$ = 6dB are shown in Fig.2.22. It can be seen that the 11 scatterers have been reconstructed. The image also includes some false scatterers due to high sidelobes and noise.

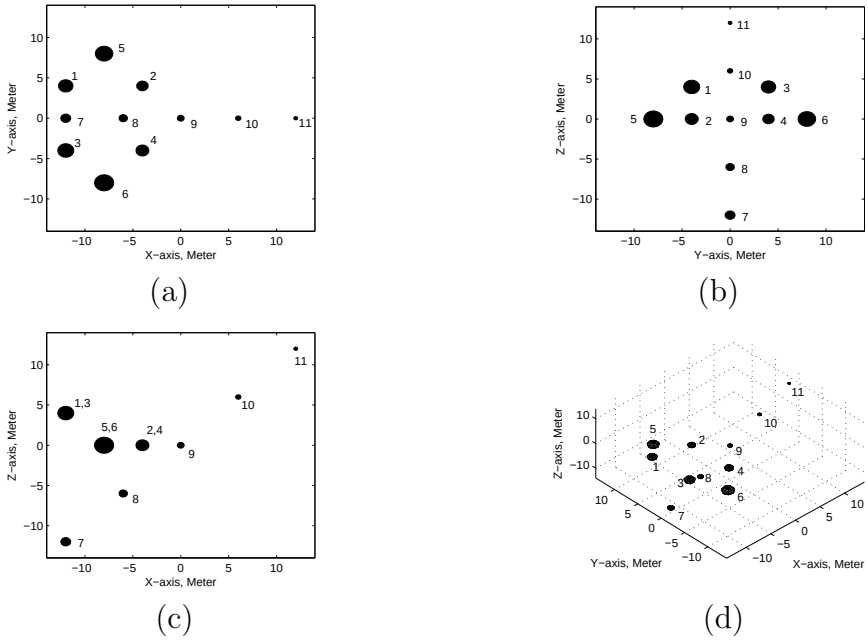

Figure 2.20: Three different projections and 3D view of the target model (simulation 3).

2.4.4 Simulation 4: Interferometric 3D Imaging

In this simulation, we show the 3D imaging results using an interferometric array. The parameters of the target are the same as that in simulation 3. Two uniform linear receive arrays with 10 elements each and one uniform

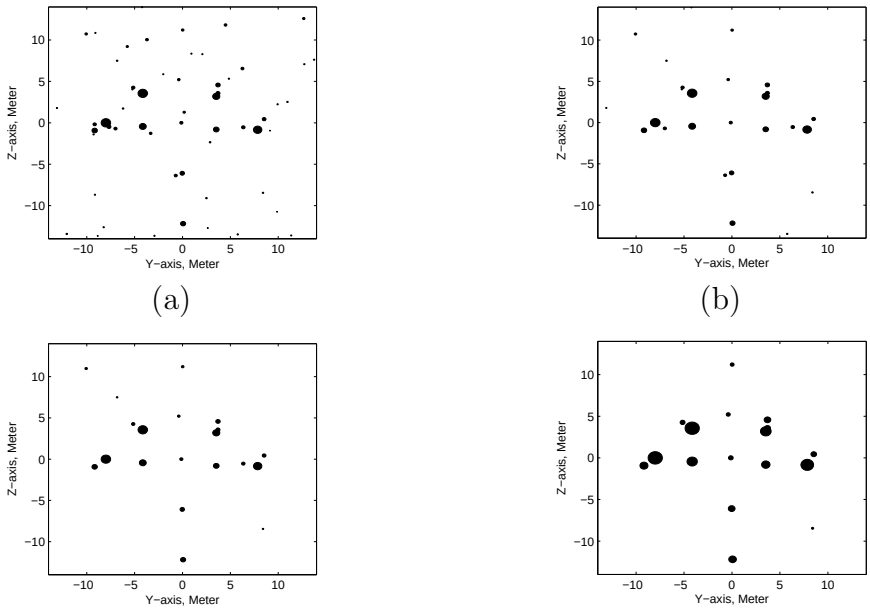

Figure 2.21: Projection images on YZ plane for $\delta\zeta$ = 3.5, 4.6, 5.6 and 6 dB corresponding to (a), (b), (c) and (d). The number of false scatterers decrease as the increase of $\delta\zeta$. Small scatterers have high probability be canceled with the increase of $\delta\zeta$ (simulation 3).

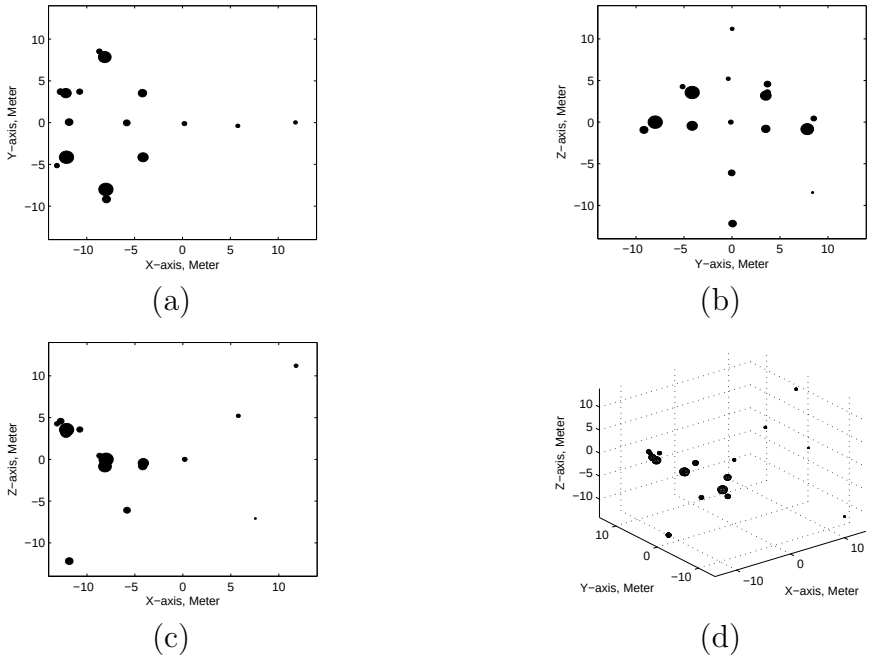

Figure 2.22: Three different projections and 3D views of the image obtained by the MIMO array for $\delta\zeta$ = 6dB (simulation 3).

linear transmit array with 10 elements are located parallel to the Y axis on the $z = 0$ plane, which is similar to Fig.2.5. The inter-element distances of the transmit array and the receive array are 42.8571 m and 4.28571 m respectively. The unambiguous distance is 100 m. The inter-array distance of the two receive arrays is also 4.28571m. Ten ZCZ codes with length 600 are used as the transmit codes. The zero correlation window is from -59 to 59. The target is located in $n_0 = [0.4402, 0.1761, 0.8805]$ direction. The projection of the target on the range and cross-range (the cross-range is the direction of $\mathbf{y}_0 - (\mathbf{y}_0^T \mathbf{n}_0)\mathbf{n}_0$ where $\mathbf{y}_0$ is the unit vector of Y axis) is as shown in Fig.2.23. It is noted that the four scatterers 1, 2, 3 and 4 in Fig.2.20(a) are projected on A and B in Fig.2.23, so the coordinates of scatterers 1, 2, 3 and 4 can not be obtained correctly using interferometric technique. The transmit power of each transmitter is 200 W. The output SNR of the weakest scatterer after processing is 14.88 dB. Denote ζ as the value of the strongest scatterers, then scatterers with value larger than $\zeta - 27$ dB are selected to form the reconstructed 3D image, which is shown in Fig.2.24. Scatterers 1, 2, 3 and 4 have not been reconstructed correctly. The weakest scatterer also has not been reconstructed correctly. There are many false alarm scatterers. Due to the worst-case combination of the scatterer position and the direction of the interferometric array, the resultant radar image has no separation ability in X direction, the quality of the image using interferometric method thus in general is not as good as that of using square MIMO array. But the hardware cost of the interferometric array is low.

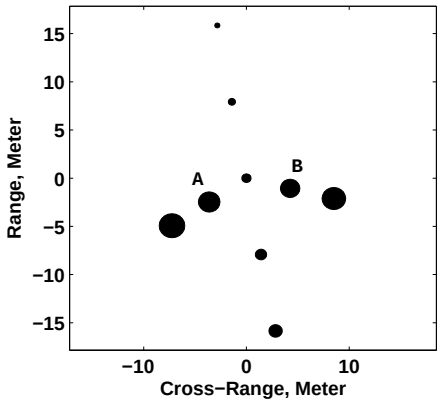

Figure 2.23: Projection of the target on the range and cross-range plane (simulation 4).

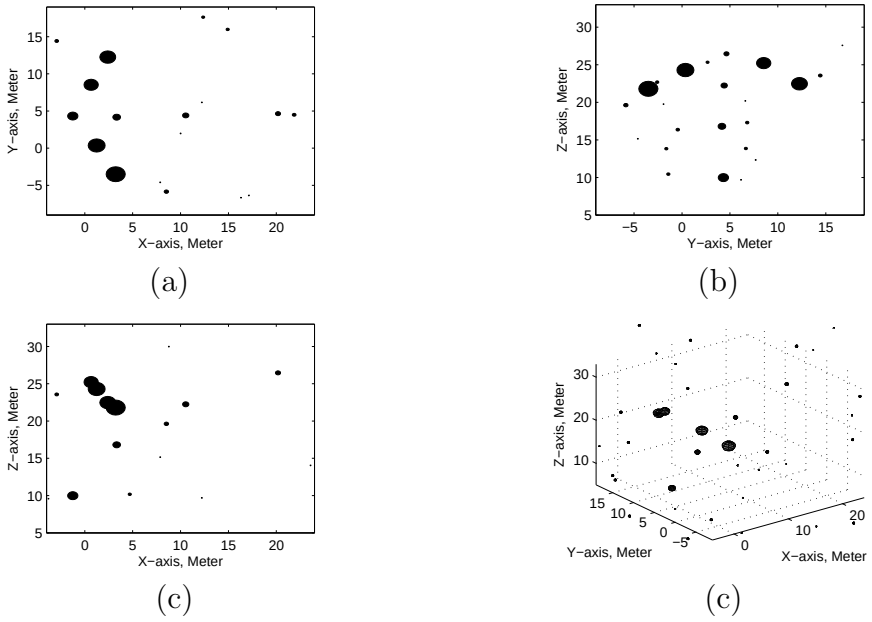

Figure 2.24: Three different projections and 3D view of the image obtained by the MIMO interferometric array (simulation 4).

2.5 Conclusion

The formulae for 3D imaging by collocated MIMO radar have been derived. Three MIMO radar configurations, namely; cross-array, square-array and interferometric array are discussed. For cross-array, sidelobes in the transmit array direction are high, but the sidelobes in the receive array direction are low. For square-array, there are moderate sidelobes in both directions, but their values are lower than that in the cross-array case. For short random codes, the sidelobes will be high. In this case, we made use of only the strongest scatterer within the same cross-range unit to form the 3-D image. A strong scatterers selection criterion is proposed. Codes with zero correlation zone can be used to mitigate the sidelobes in a narrow window. Generally, the length of the ZCZ code should be the multiple of the length of the narrow window and the number of the transmit antennas. But when there is a simultaneous requirement to image a large target area with a large number of transmit antennas, then the resulting long codes will become Doppler sensitive. In this case, ZCZ codes are more appropriate for use in interferometric array where the number of the transmit antennas is not large.

Chapter 3

3D Imaging Using Colocated MIMO Radar and Multiple Snapshots Data

3.1 Introduction

In Chapter 2, only one snapshot is used to form the 3D image. But it requires relatively high transmitting energy and has high sidelobes.

Combining MIMO radar and inverse synthetic aperture technique can reduce transmitting power as well as improve cross-range resolution when compared to mono-static ISAR imaging [30], [31]. In [30] and [31], the authors used linear MIMO array in conjunction with ISAR processing. It is noted that, in these papers, the gaps between virtual antennas are filled with synthetic aperture, and only 2-D image is obtained. The number of codes in the said MIMO array is small and orthogonal property is assumed among these codes. The target is also assumed to be located on the broadside of the array to show the improvement of cross-range resolution. When the rotation axis is

perpendicular to the plane formed by the antenna array and the target, the conjunction algorithms are discussed in detail in these two papers. In reality, the rotation axis may not be perpendicular to the said plane. This also needs to be discussed in detail.

In this Chapter, a two-dimensional MIMO radar and inverse synthetic aperture technique are combined to form the 3D image. Because the number of codes used in the two-dimensional array is larger than the number of codes used in one dimensional array, the codes cannot be assumed orthogonal.In some cases, ZCZC codes may not be suitable to mitigate sidelobes. High sidelobes affect the image quality severely as seen in the last Chapter. Even one-dimensional range profile cannot be used to align the signal as done in [30] and [31]. So the MIMO radar 3D imaging processing steps in this Chapter are different from [30] and [31]. The main work is on how to use multiple snapshots signals to mitigate sidelobes. If the target's rotation vector is known, multiple snapshots signals can be coherently combined to mitigate sidelobes, and even improve cross-range resolution. Using the position information (obtained by MIMO radar using single snapshot signal) and the relative Doppler frequency information (obtained by spectrum analysis of multiple snapshots signal) of some strong scatterers, the relative rotational parameters of the entire rigid-body target is obtained by minimum mean square error method. Compared to the iterative algorithm used in [30], our algorithm is a direct algorithm and computationally cheaper.

This Chapter is organized as follows. In section 3.2, signal model and MIMO radar imaging based on multiple snapshots signal are discussed. 3D images alignment, motion compensation and coherent combination are discussed in section 3.3. The point spread functions for different cases are analyzed in section 3.4 . The estimation method of the rotation parameter is given in

section 3.5. Simulation results are shown in Section 3.6.

3.2 Multiple Snapshots MIMO Radar Signal Model

Taking the square array MIMO radar as an example, multiple snapshots MIMO radar signal model is derived in this section. The antenna position configuration is the same as that shown in Fig.2.4, where the transmit and receive array antennas form two uniform planar arrays. Let P_m, Q_n denote the positions of the mth transmit antenna and the nth receive antenna respectively. Let $\mathbf{c}_m$ denote the transmit code of the mth transmit antenna. The code is also phase-modulated signal [24]. The baseband transmit waveform can be expressed as(same as (2.3))

$$\varphi_m(t') = \sum_{l=0}^{L-1} c_m(l)u(t' - lT_0), \tag{3.1}$$

where T_0 is the subpulse duration, L is the code length, t' is the fast time. Assume that the pre-transmitting time of the mth transmitting signal is T_m. The transmitting signal can be expressed as $\sum_k \varphi_m(t+t'+T_m-kT)e^{j2\pi f(t+t')}$, where T is the pulse repetition duration, f is the carrier frequency, k is the pulse index, t is the slow time. After demodulation, the received back-scattered signal from scatterer A at receive antenna n can be expressed as

$$\begin{aligned}\eta_{nA}(t',t) &= \alpha \sum_{m=0}^{M-1}\sum_{k} \varphi_m(t+t'+T_m-kT-\tau_{mA}(t)-\tau_{nA}(t)) \\ &\quad \times exp(-j2\pi f(\tau_{mA}(t)+\tau_{nA}(t))),\end{aligned} \tag{3.2}$$

where $\tau_{mA}(t) = |P_mA(t)|/c$, $\tau_{nA}(t) = |Q_nA(t)|/c$, α is the signal amplitude, proportional to the square root of the RCS of scatterer A. Let $T_m = \overrightarrow{P_mP_{M-1}}^T\mathbf{n}_0/c \approx \tau_{mA}(t) - \tau_{M-1,A}(t)$, and $R_n = \overrightarrow{Q_nQ_{N-1}}^T\mathbf{n}_0/c \approx \tau_{nA}(t) - \tau_{N-1,A}(t)$. Like in Chapter 2, the receive sampling time are adjusted such that the receive signal envelopes are also approximately aligned. We have

$$\begin{aligned}\eta_{nA}(t',t) &=: \eta_{nA}(t'+R_n,t)\\ &= \alpha\sum_{m=0}^{M-1}\sum_k \varphi_m(t+t'-kT-\tau_{M-1,A}(t)-\tau_{N-1,A}(t))\\ &\quad\times exp(-j2\pi f(\tau_{mA}(t)+\tau_{nA}(t))).\end{aligned} \tag{3.3}$$

Denote $\tilde{\varphi}_m(t')$ as the receive filter and it satisfies $\varphi_n(t')\otimes\tilde{\varphi}_m(t') = \delta_{mn}\delta(t')$. After filtering with $\tilde{\varphi}_m$, the signal transmitted from P_m, back scattered from A and received at Q_n can be obtained as

$$s_{mnA}(t',t) = \alpha\sum_k \delta\left(t+t'-kT-\tau_A(t)\right)\times e^{-j2\pi f(\tau_{mA}(t)+\tau_{nA}(t))}, \tag{3.4}$$

where we denote $\tau_A(t) = \tau_{M-1,A}(t) + \tau_{N-1,A}(t)$ for expression simplicity.

Let O_k be the space center for phase compensation at kth pulse, the corresponding phase is $2\pi f(\tau_{mO_k} + \tau_{nO_k})$. After phase compensation, the phase term is $2\pi f(\tau_{mO_k} + \tau_{nO_k} - \tau_{mA} - \tau_{nA}) = \frac{2\pi}{\lambda}(P_mO_k + Q_nO_k - P_mA - Q_nA)$. According to (2.7), the distance term $P_mO_k + Q_nO_k - P_mA - Q_nA$ can be expressed as (we omit the variable t for simplicity)

$$\begin{aligned}&P_mO_k + Q_nO_k - P_mA - Q_nA\\ \approx\ &-2(P_0A - P_0O_k) + (\mathbf{a}_k - (\mathbf{a}_k^T\mathbf{n}_0)\mathbf{n}_0)^T(\overrightarrow{P_0Q_0} + \overrightarrow{P_0P_m} + \overrightarrow{Q_0Q_n})/r,\end{aligned} \tag{3.5}$$

where $\mathbf{a}_k = \overrightarrow{O_kA}$, $r = P_0O_k$ is the distance from the radar to the reference center.

We assume that the MIMO configuration is square array, and $M = M_1 \times M_2$, $N = N_1 \times N_2$, $N_1 \times d_{rx} = d_{tx}$ and $N_2 \times d_{ry} = d_{ty}$. Denoting $\tilde{m} = m_2 N_2 + n_2$ and $\tilde{n} = m_1 N_1 + n_1$, similar to section 2.2.2, the signal after phase compensation can be expressed as

$$\begin{aligned} & s_{mnA}(t', kT) \\ = \; & \alpha \sum_k \delta\left(t' - \tau_A(kT)\right) e^{-j2\pi f(\tau_{mA}(t)+\tau_{nA}(t)-\tau_{mO_k}-\tau_{nO_k})} \\ = \; & \alpha \sum_k \delta\left(t' - \tau_A(kT)\right) e^{-j\frac{4\pi}{\lambda}(P_0A(t)-P_0O_k)} e^{j\frac{2\pi}{\lambda}\tilde{\mathbf{a}}_k^T(\overrightarrow{P_0Q_0}+\overrightarrow{P_0P_m}+\overrightarrow{Q_0Q_n})/r} \\ = \; & \alpha \sum_k \delta\left(t' - \tau_A(kT)\right) e^{-j\frac{4\pi}{\lambda}(P_0A(t)-P_0O_k)} e^{j\frac{2\pi}{\lambda}\tilde{\mathbf{a}}_k^T\overrightarrow{P_0Q_0}/r} e^{j\frac{2\pi}{\lambda}(\tilde{y}_k d_{ry}\tilde{m}+\tilde{x}_k d_{rx}\tilde{n})/r}. \end{aligned} \tag{3.6}$$

where $\tilde{\mathbf{a}}_k = \mathbf{a}_k - (\mathbf{a}_k^T\mathbf{n}_0)\mathbf{n}_0$ with coordinate $(\tilde{x}_k, \tilde{y}_k, \tilde{z}_k)$.

Because the position of the virtual antenna is at $\overrightarrow{P_0P_m}+\overrightarrow{Q_0Q_n} = (\tilde{n}d_{rx}, \tilde{m}d_{ry}, 0)$, where $0 \le \tilde{n} \le M_1N_1$ and $0 \le \tilde{m} \le M_2N_2$, the signal $s_{mnA}(t', kT)$ can be re-arranged and denoted as $s_{\tilde{m}\tilde{n}A}(t', kT)$, where $\tilde{m}$ and $\tilde{n}$ are in ascending order.

The spatial domain two dimensional Fourier transform (on $\tilde{m}, \tilde{n}$) of $s_{\tilde{m}\tilde{n}A}(t', kT)$ can be expressed as

$$\begin{aligned} & \alpha_A(f_x, f_y, t', kT) \\ = \; & \alpha \sum_k e^{j\pi(M_1N_1-1)(\tilde{f}_{kx}-f_x)} e^{j\pi(M_2N_2-1)(\tilde{f}_{ky}-f_y)} e^{j\frac{2\pi}{\lambda r}\tilde{\mathbf{a}}_k^T\overrightarrow{P_0Q_0}} \\ \times \; & e^{-j\frac{4\pi}{\lambda}(P_0A(kT)-P_0O_k)} \delta\left(t' - \tau_A(kT)\right) \frac{sin(\pi M_1N_1(f_x-\tilde{f}_{kx}))}{sin(\pi(f_x-\tilde{f}_{kx}))} \frac{sin(\pi M_2N_2(f_y-\tilde{f}_{ky}))}{sin(\pi(f_y-\tilde{f}_{ky}))} \\ = \; & \sum_k \tilde{\alpha}(f_x, f_y) e^{-j\frac{4\pi}{\lambda}(P_0A(t)-P_0O_k)} \delta\left(t' - \tau_A(kT)\right) \tilde{\delta}(f_x - \tilde{f}_{kx}, f_y - \tilde{f}_{ky}). \end{aligned} \tag{3.7}$$

where we denote $\tilde{f}_{kx} = \frac{\tilde{x}_k d_{rx}}{\lambda r}$, $\tilde{f}_{ky} = \frac{\tilde{y}_k d_{ry}}{\lambda r}$, $f_x = \frac{n}{M_1N_1}$, $f_y = \frac{m}{M_2N_2}$,

$$\tilde{\delta}(x, y) = \frac{sin(\pi M_1N_1 x)}{sin(\pi x)} \frac{sin(\pi M_2N_2 y)}{sin(\pi y)}$$

and

$$\tilde{\alpha}(f_x, f_y) = \alpha e^{j\pi(M_1N_1-1)(\tilde{f}_{kx}-f_x)} e^{j\pi(M_2N_2-1)(\tilde{f}_{ky}-f_y)} e^{j\frac{2\pi}{\lambda r}\tilde{\mathbf{a}}_k^T\overrightarrow{P_0Q_0}}.$$

It can be seen that $\alpha_A(f_x, f_y, t', kT)$ is actually the three dimensional image of the scatterer A at the kth pulse. The peak is located at $(\frac{\tilde{x}_k d_{rx}}{\lambda r}, \frac{\tilde{y}_k d_{ry}}{\lambda r}, \tau_A(kT))$, where the cross-range and down-range information of A are obtained. If

$s_{\tilde{m}\tilde{n}}(t', t)$ includes all the scatterers' back scattered information, $\alpha(f_x, f_y, t', kT)$ is then the three dimensional image of the target at slow time KT.

We will discuss how these 3D images can be coherently combined in the following section.

3.3 3D Images Alignment, Motion Compensation and Coherent Combination

The center of the three dimensional image at kth pulse is O_k and the O_k for different k may be different, so the 3D images are not aligned. Even though the O_k can be chosen as the same, because the target is moving during different pulses, the 3D images are also not aligned. Correlation criterion is usually used to align one-dimensional images in ISAR imaging. It can also be used to align the 3D images. According to our analysis, the width of the unambiguous window is $\frac{\lambda r}{d_x}$ ($\frac{\lambda r}{d_y}$). In order to increase the cross-range resolution, the radar parameters are usually designed such that the width of the unambiguous window is as small as possible. However, during the coherent processing period, the target may move through multiple unambiguous windows. This is shown in Fig.3.1. In this figure, the target moves towards the second unambiguous window and has just crossed the boundary between the first and second windows at the second pulse. The reference point O is located at the center of the first unambiguous window. The image obtained in the second pulse is cross-range wrapped. But in the range direction, there is no wrap. Based on this observation, the correlation of the images in the cross-range direction should be cyclic correlation, but in the range direction, the correlation is the conventional correlation.

Denote $\mathcal{A} = (f_x, f_y, t')$ the position variable of a scatterer, $\tilde{\mathcal{M}}_k = (f_{kx}, f_{ky}, \tau_k)|_{O_k}$ the coordinates of $\overrightarrow{O_0O_k}$ on the 3D image with O_0 as the origin. At first,

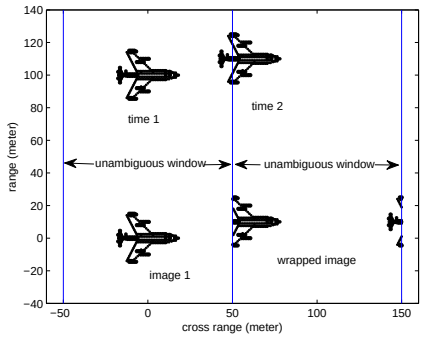

Figure 3.1: The image of the target is cross-range wrapped.

the image at kth instant should shift by $\tilde{\mathcal{M}}_k$, that is letting $\alpha(\mathcal{A}, kT) =: \alpha(\mathcal{A}+\tilde{\mathcal{M}}_k, kT)$, where if a pixel exceeds the cross-range unambiguous window during the shift, it should be wrapped to the other side. After this procedure, the 3D images have one common reference point O_0. The estimated movement parameters for kth pulse can be obtained as

$$\max_{\mathcal{V}_k} \quad \sum_{\mathcal{A}} |\alpha(\mathcal{A}, 0)||\alpha(\mathcal{A} - \mathcal{V}_k, kT)|, \tag{3.8}$$

where the shift in the cross-range direction is cyclic shift.

In order to increase the precision of alignment, the estimated $\mathcal{V}_k$ should be polynomial fitted to obtain a more precise estimation. But the cross-range movement parameters obtained using the cyclic correlation is wrapped to $[\frac{-\lambda r}{2d_x}, \frac{\lambda r}{2d_x}]([\frac{-\lambda r}{2d_y}, \frac{\lambda r}{2d_y}])$. It should be cross-range unwrapped first. Similar to phase unwrapping, cross-range unwrapping can be used to estimate the true cross-range position of each 3D image. It should be noted that the unwrapping process here only unwraps the wrapped cross range distance of the target relative to the first 3D image. If the first 3D image is wrapped, we should unwrap the first image at first or unwrap it after the above cross-range unwrapping procedure. This is easy to implement in image domain. Fig.3.12 shows one example of the wrapped cross-range and unwrapped cross-range distances.

After alignment, the 3D images should be coherently combined to increase the SNR and mitigate the cross-range sidelobes. Generally, as the Pulse Repetition Frequency (PRF) is low, the Doppler frequencies ($\frac{2P_0A'(kT)}{\lambda}$) of the scatterers are wrapped. They must be unwrapped before coherent combination. Furthermore, if wavefront disorder exists, there is phase noise which should also be compensated. This is called motion compensation in ISAR. We consider the case that there is an isolated scatterer. Denote O as an isolated scatterer on the target, the phase of $\tilde{s}_A$ can be compensated using the phase of scatterer O. Denote $\alpha_A(f_x, f_y, t', kT)$ the image at kth pulse after alignment. The image after alignment and motion compensation is (omit $\tilde{\alpha}(f_x, f_y)$ for simplicity):

$$\begin{aligned}
& \alpha_A(f_x, f_y, t', kT) \times e^{j\frac{4\pi}{\lambda}(P_0O(kT)-P_0O_k)} \\
= \;& e^{-j\frac{4\pi}{\lambda}(P_0A(kT)-P_0O(kT))}\delta\left(t'-\tau_A(0)\right)\tilde{\delta}(f_x-\tilde{f}_{0x}, f_y-\tilde{f}_{0y}) \\
= \;& e^{-j\frac{4\pi}{\lambda}|\mathbf{n}_0^T\overrightarrow{OA}(kT)|}\delta\left(t'-\tau_A(0)\right)\tilde{\delta}(f_x-\tilde{f}_{0x}, f_y-\tilde{f}_{0y}) \\
= \;& e^{-j\frac{4\pi}{\lambda}(\mathbf{w}^T\overrightarrow{OA}kT)}\delta\left(t'-\tau_A(0)\right)\tilde{\delta}(f_x-\tilde{f}_{0x}, f_y-\tilde{f}_{0y}) \\
= \;& e^{-j\frac{4\pi}{\lambda}(\mathbf{w}^T\tilde{\mathbf{a}}kT)}\delta\left(t'-\tau_A(0)\right)\tilde{\delta}(f_x-\tilde{f}_{0x}, f_y-\tilde{f}_{0y}),
\end{aligned} \tag{3.9}$$

where $\mathbf{w} = (\mathbf{v} - \mathbf{n}_0^T\mathbf{v}\mathbf{n}_0)/r - \Omega\hat{\omega}\mathbf{n}_0$, Ω is the rotation speed of the target around its self axis, $\hat{\omega}$ is a skew symmetric matrix [62] [12], $\mathbf{v}$ is the speed of the target, $\tilde{\mathbf{a}} = \overrightarrow{OA} - (\overrightarrow{OA}^T\mathbf{n}_0)\mathbf{n}_0$. It should be noted that the $\tilde{f}_{0x}$, $\tilde{f}_{0y}$ and $\tau_A(0)$ are now time independent or O_0 can be thought of as the origin of the 3D images. The candidate isolated scatterer O can be chosen as the scatterer with a high amplitude and low variance. Generally, the PRF is high enough to avoid frequency alias after motion compensation.

From (3.9) it can be seen that the 3D images in different instants can be combined coherently if the $\mathbf{w}$ is known. After coherent combination, the 3D image can be expressed as (3.10). The (3.10) is also the point spread function

of point A.

$$\begin{aligned}\alpha_A(f_x, f_y, t') = & \sum_k \tilde{\alpha}(f_x, f_y) e^{-j\frac{4\pi}{\lambda}(\mathbf{w}^T(\tilde{\mathbf{a}}-\mathbf{a})kT)} \delta\left(t' - \tau_A(0)\right) \tilde{\delta}(f_x - \tilde{f}_{0x}, f_y - \tilde{f}_{0y}) \\ = & \tilde{\alpha}(f_x, f_y)\delta\left(t' - \tau_A\right) \tilde{\delta}(f_x - \tilde{f}_{0x}, f_y - \tilde{f}_{0y}) \frac{sin(\frac{2\pi}{\lambda}\mathbf{w}^T(\tilde{\mathbf{a}}-\mathbf{a})KT)}{sin(\frac{2\pi}{\lambda}\mathbf{w}^T(\tilde{\mathbf{a}}-\mathbf{a})T)}.\end{aligned} \tag{3.10}$$

3.4 Point Spread Function Analysis

In this section we analyze the point spread function of combined MIMO array and ISAR processing. We assume that the scatterer is located on the center of the coordinate system.

Case 1: The MIMO array is a uniform linear array and located on the X axis. The target is located on the broadside direction. The direction of $\mathbf{w}$ is along the linear array. In this case we have $\mathbf{w} = [w_x, 0, 0]$ and

$$\alpha_A(x, y, t') = \tilde{\alpha}(x, y)\delta\left(t' - \tau_A\right) \frac{sin(\pi M_1 N_1 x/L)}{sin(\pi x/L)} \frac{sin(\frac{2\pi}{\lambda}w_x xKT)}{sin(\frac{2\pi}{\lambda}w_x xT)}, \tag{3.11}$$

where $L = \frac{\lambda r}{d_{rx}}$ is the unambiguous distance. When $\frac{\lambda}{2w_x KT} = L$, $sin(\pi x/L) = sin(\frac{2\pi}{\lambda}w_x xKT)$, which means the grating lobes of $\frac{sin(\pi M_1 N_1 x/L)}{sin(\pi x/L)}$ are canceled by the nulling points of $\frac{sin(\frac{2\pi}{\lambda}w_x xKT)}{sin(\frac{2\pi}{\lambda}w_x xT)}$. The grating lobes of $\frac{sin(\frac{2\pi}{\lambda}w_x xKT)}{sin(\frac{2\pi}{\lambda}w_x xT)}$ occurs at $x = \frac{\lambda}{2w_x KT}K = K\triangle x$, where $\triangle x$ is the cross range resolution of ISAR. Generally, $K\triangle x$ can be designed larger than the physical aperture of each antenna, such that the grating lobes of $\frac{sin(\frac{2\pi}{\lambda}w_x xKT)}{sin(\frac{2\pi}{\lambda}w_x xT)}$ are mitigated by the low sidelobes of the beam pattern of each physical antenna. For $L = 200m$, $M_1 N_1 = 6$ and $\triangle x = L$, the beam patterns of MIMO array, inverse synthetic aperture and MIMO combined with ISAR processing are shown in Fig.3.2. It can be seen that the MIMO combined ISAR beam pattern has narrower main lobe compared with ISAR beam pattern and has no grating lobes compared with MIMO beam pattern. $\frac{2}{\lambda}w_x KT = \frac{1}{L}$ means $rw_x KT = \frac{1}{2}d_{rx}$. That is the ISAR

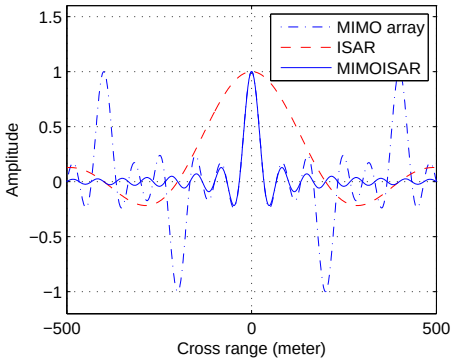

Figure 3.2: Beam pattern of linear MIMO array, ISAR and combined MIMO array and ISAR.

synthetic aperture is only half of d_{rx}. This can be explained as the synthetic aperture is due to round traveling propagation of the microwave. The total aperture is shown in Fig.3.3. This case 1 has been discussed by [30] and [31]. It should be noted that there is no separation capability in the Y direction.

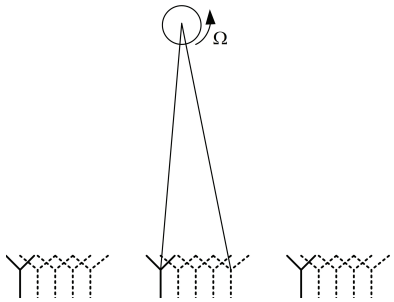

Figure 3.3: Synthetic aperture and linear MIMO array for a $\mathbf{w}$ along the linear array.

Case 2: The array is the same as case 1 and the target is located on the broadside direction. $\mathbf{w}$ is an arbitrary vector. Because $\mathbf{w} \perp \mathbf{n}_0$, we can denote $\mathbf{w}$ as $\mathbf{w} = [w_x, w_y, 0]$. The beam pattern due to ISAR processing can be expressed as $\frac{\sin(\frac{2\pi}{\lambda}(w_x x + w_y y)KT)}{\sin(\frac{2\pi}{\lambda}(w_x x + w_y y)T)}$. The zero points are located on lines $\frac{2}{\lambda}(w_x x + w_y y)KT = p$, where p is an integer. The zero lines do not coincide with the grating lobes lines of the MIMO beam pattern, so the grating lobes along the X direction cannot be canceled. For $L = 200m$, $M_1 N_1 = 5$, $\mathbf{w}$ is

along $[1, -1, 0]$ direction and $\frac{2}{\lambda}|w|KT = \frac{\sqrt{2}}{200}$, the beam pattern of MIMO array, inverse synthetic aperture and the combined MIMO and ISAR processing are show in Fig.3.4. From Fig.3.4 (c) we can see that although there are grating lobes in the X direction, the grating lobes are along the main lobe of the ISAR beam pattern. At the same time, the combined beam pattern has separation capability in the Y direction. This can be explained by the corresponding synthetic and physical array distribution as shown in Fig.3.5. The synthetic and physical array forms a two dimensional array. Because the two dimensional array is not a regular array and the synthetic aperture does not fill all the gaps between the MIMO array's inter-elements, there are grating lobes and the line along grating lobes are not perpendicular to the X axis.

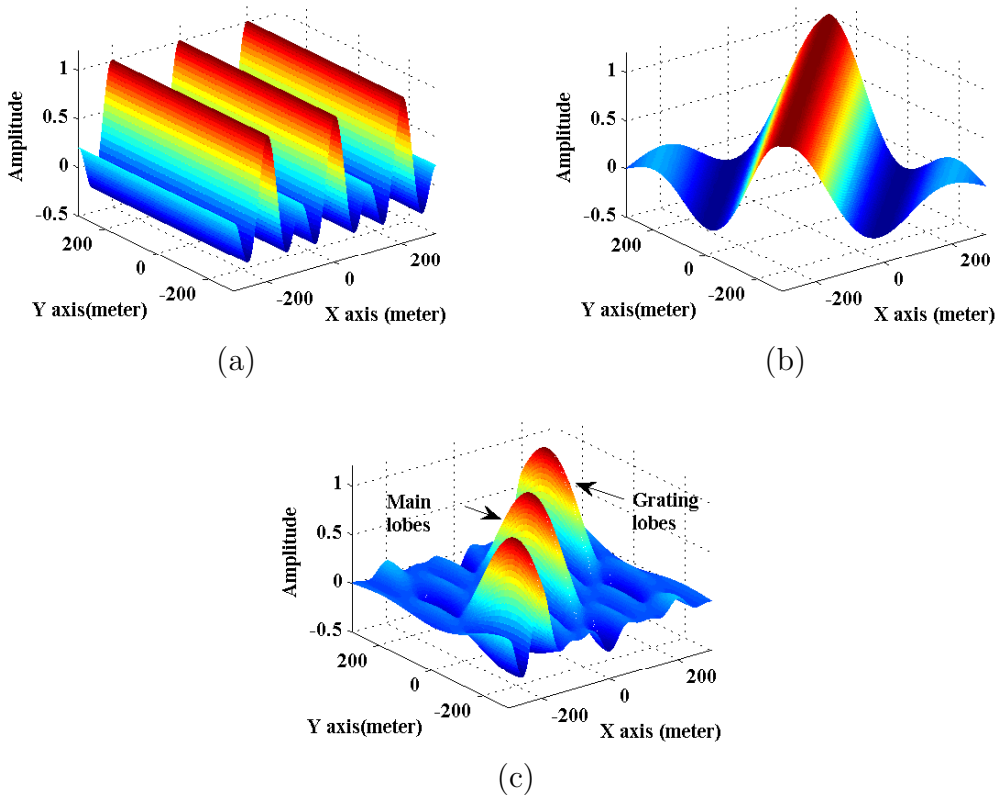

Figure 3.4: Beam pattern of (a) uniform linear MIMO array, (b) ISAR with $\mathbf{w}$ along $[1, -1, 0]$ direction, and (c) combined MIMO array and ISAR.

Case 3: The MIMO array is a rectangular array and the target is located on

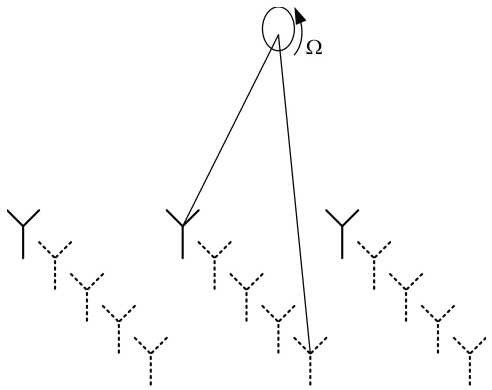

Figure 3.5: Synthetic aperture and MIMO array for an arbitrary rotation speed perpendicular to n_0.

the broadside direction. We assume the unambiguous distance is 200m. There are 10 virtual antennas on each direction. The $\mathbf{w}$ is along $[1, 0, 0]$ direction and the cross range resolution of ISAR is 100m (in this case, the ISAR synthetic aperture fill in the gap of MIMO array aperture in X direction). Fig.3.6 shows the MIMO array beam pattern, ISAR beam pattern and combined MIMO array and ISAR beam pattern. It can be seen that the MIMO array beam pattern has grating lobes. The ISAR beam pattern has wide mainlobe and has no separation capability in Y direction. The combined array has narrower main lobe compared with ISAR beampattern and only has grating lobes in Y direction. An important fact is that the combined beam pattern has lower sidelobes along the X direction as compared with MIMO array beam pattern. In these figures, we only show beampatterns above -40 dB.

Case 4: The MIMO array is a rectangular array and the target is located on a slant direction. The array configuration is the same as case 3. The target line of sight is $\mathbf{n}_0 = [1, -1, 1]/\sqrt{3}$, the $\mathbf{w}$ is along $\mathbf{w} = [1, -1.2, -2.2]$ direction. The ISAR cross range resolution is 100m. Because the combined beam patterns on the planes which are perpendicular to the $\mathbf{n}_0$ are the same, we only show the beam pattern on one such plane. Because the projections of X axis and Y axis on this plane are not orthogonal, we establish another new coordinate system

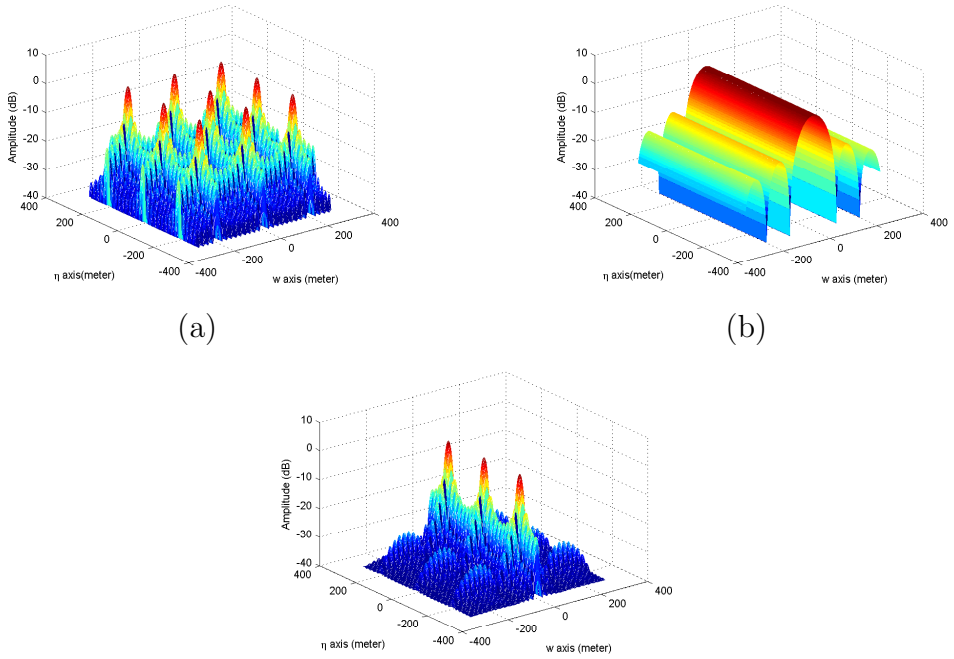

Figure 3.6: Beam pattern of (a) uniform square MIMO array, (b) ISAR with $\mathbf{w}$ along $[1, 0, 0]$ direction, and (c) combined MIMO array and ISAR.

on this plane. Denote $\mathbf{w}$ as one axis, $[\mathbf{w}, \eta, \mathbf{n}_0]$ form an orthogonal coordinate system. The beam patterns of MIMO array and combined MIMO and ISAR are shown in Fig.3.7. The performance is similar to case 3. For combined beam pattern, the grating lobes are only shown in η direction, the sidelobes in $\mathbf{w}$ direction are lower than that of MIMO array only beam pattern. In the derivation of (3.10) we uses the assumption of $\varphi_n(t') \otimes \tilde{\varphi}_m(t') = \delta_{mn}\delta(t')$. Unfortunately, in reality, this condition is difficult to satisfy. It can be written as $\varphi_n(t') \otimes \tilde{\varphi}_m(t') = \delta_{mn}\delta(t') + \xi_{mn}(t')$, where $\xi_{mn}(t')$ is random sidelobes, which cannot be mitigated using windowing technique. But the terms in (3.10) which influence cross-range property is $\tilde{\delta}(f_x - \tilde{f}_{0x}, f_y - \tilde{f}_{0y})$ and $\frac{sin(\frac{2\pi}{\lambda}\mathbf{w}^T(\tilde{\mathbf{a}}_0 - \mathbf{a})KT)}{sin(\frac{2\pi}{\lambda}\mathbf{w}^T(\tilde{\mathbf{a}}_0 - \mathbf{a})T)}$. $\frac{sin(\frac{2\pi}{\lambda}\mathbf{w}^T(\tilde{\mathbf{a}}_0 - \mathbf{a})KT)}{sin(\frac{2\pi}{\lambda}\mathbf{w}^T(\tilde{\mathbf{a}}_0 - \mathbf{a})T)}$ is a sinc function with amplitude of K, it can increase the SNR at $\tilde{\mathbf{a}}_0$ by $10log_{10}(K)$ dB, at the same time it mitigates the sidelobes in the cross-range direction ($\mathbf{w}$ direction).

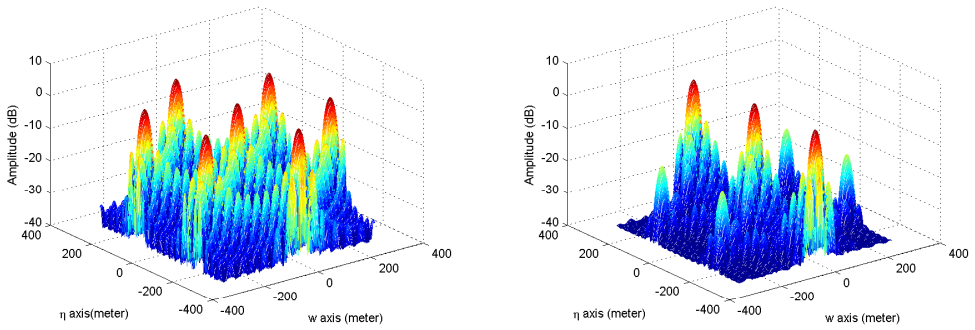

(a) (b)

Figure 3.7: Beam pattern of (a) uniform square MIMO array and (b) combined MIMO array and ISAR with $\mathbf{w}$ along $[1, -1.2, -2.2]$ direction.

3.5 Computation of Effective Rotation Vector

According to (3.9), $\mathbf{w}^T\tilde{\mathbf{a}}_0$ can be obtained by Fourier transform of $\alpha_A(\tilde{f}_{0x}, \tilde{f}_{0y}, \tau_A(0), kT)$ on k variable and denoted as f_d. At the same time, $\tilde{\mathbf{a}}_0$ can be obtained according to the information contained in $(\tilde{f}_{0x}, \tilde{f}_{0y}, \tau_A(0))$. It should be noted that $\tilde{\mathbf{a}}_0$ in $\mathbf{w}^T\tilde{\mathbf{a}}_0$ is relative to O (ISAR focusing point), $(\tilde{f}_{0x}, \tilde{f}_{0y}, \tau_A(0))$ is relative to O_0. O and O_0 may not be same. So in order to obtain $\tilde{\mathbf{a}}_0$, we should shift the 3D images such that O is the origin. We use $\tilde{\mathbf{a}}$ to replace $\tilde{\mathbf{a}}_0$ for simplicity in the following derivation. Then $\mathbf{w}$ can be estimated by minimum mean square error method:

$$\begin{aligned} \min_{\mathbf{w}} \quad & E \quad |f_d + \tfrac{2\mathbf{w}^T\tilde{\mathbf{a}}}{\lambda}|^2 \\ s.t. \quad & \mathbf{w}^T\mathbf{n}_0 = 0 \end{aligned} \tag{3.12}$$

The solution is

$$\mathbf{w} = -\frac{\lambda}{2}\mathbf{R}^{-1}\left(\mathbf{r}_{f_d\tilde{a}} - \frac{\mathbf{r}_{f_d\tilde{a}}^T\mathbf{R}^{-1}\mathbf{n}_0}{\mathbf{n}_0^T\mathbf{R}^{-1}\mathbf{n}_0}\mathbf{n}_0\right), \tag{3.13}$$

where $\mathbf{R} = E(\tilde{\mathbf{a}}\tilde{\mathbf{a}}^T)$, $\mathbf{r}_{f_d\tilde{a}} = E(f_d\tilde{\mathbf{a}})$, E is the expectation operator.

If isolated scatterer does not exist, some other motion compensation meth-

ods such as Rank One Phase Estimation (ROPE) algorithm, entropy minimization method and subspace method can be used [20]. But the phase obtained by ROPE and entropy minimization method is the estimation of the phase of one scatterer plus a linear phase term. A linear phase term changes the position of the image in cross-range direction, although it does not change the entropy of the image. The above $\mathbf{w}$ estimation method cannot be used in this case (without using isolated scatterer to do motion compensation). It should be revised as the following optimization procedure, where $\tilde{f}$ is the unknown frequency shift.

$$\begin{aligned} \min_{\mathbf{w},\tilde{f}} \quad & E|f_d - \tilde{f} + \tfrac{2\mathbf{w}^T\tilde{\mathbf{a}}}{\lambda}|^2 \\ s.t. \quad & \mathbf{w}^T\mathbf{n}_0 = 0. \end{aligned} \tag{3.14}$$

Let $g(\mathbf{w}, \tilde{f}, \mu) = E|f_d - \tilde{f} + \frac{2\mathbf{w}^T\tilde{\mathbf{a}}}{\lambda}|^2 + \mu\mathbf{w}^T\mathbf{n}_0$, then

$$\begin{aligned} g(\mathbf{w}, \tilde{f}, \mu) = \; & \tfrac{4}{\lambda^2}\mathbf{w}^T E(\tilde{\mathbf{a}}\tilde{\mathbf{a}}^T)\mathbf{w} + \tfrac{4}{\lambda}\mathbf{w}^T E\left(\tilde{\mathbf{a}}(f_d - \tilde{f})\right) \\ & -2E(f_d\tilde{f}) + E(f_d^2) + \tilde{f}^2 + \mu\mathbf{w}^T\mathbf{n}_0. \end{aligned} \tag{3.15}$$

Let $\frac{\partial g}{\partial \mathbf{w}} = 0$, we have

$$\frac{8}{\lambda^2}E(\tilde{\mathbf{a}}\tilde{\mathbf{a}}^T)\mathbf{w} + \frac{4}{\lambda}E\left(\tilde{\mathbf{a}}(f_d - \tilde{f})\right) + \mu\mathbf{n}_0 = 0. \tag{3.16}$$

Let $\frac{\partial g}{\partial \tilde{f}} = 0$, we have

$$\tilde{f} = E(f_d) + \frac{2}{\lambda}\mathbf{w}^T E(\tilde{\mathbf{a}}). \tag{3.17}$$

Substitute (3.17) into (3.16), we have

$$\frac{8}{\lambda^2}E(\tilde{\mathbf{a}}\tilde{\mathbf{a}}^T)\mathbf{w} - \frac{4}{\lambda}E(\tilde{\mathbf{a}})\left(E(f_d) + \frac{2}{\lambda}E(\tilde{\mathbf{a}})^T\mathbf{w}\right) + \frac{4}{\lambda}E(\tilde{\mathbf{a}}f_d) + \mu\mathbf{n}_0 = 0. \tag{3.18}$$

Denote $\bar{\mathbf{R}} = E(\tilde{\mathbf{a}}\tilde{\mathbf{a}}^T) - E(\tilde{\mathbf{a}})E(\tilde{\mathbf{a}})^T$, $\bar{\mathbf{a}} = E(\tilde{\mathbf{a}})$, $\bar{f}_d = E(f_d)$, we have

$$\mathbf{w} = -\frac{\lambda}{2}\bar{\mathbf{R}}^{-1}(\mathbf{r}_{f_d\tilde{a}} - \bar{\mathbf{a}}\bar{f}_d + \frac{\lambda}{4}\mu\mathbf{n}_0). \tag{3.19}$$

Using $\mathbf{n}_0^T\mathbf{w} = 0$, we have

$$\mu = \frac{4\mathbf{n}_0^T\bar{\mathbf{R}}^{-1}\left(\bar{\mathbf{a}}\bar{f}_d - \mathbf{r}_{f_d\tilde{a}}\right)}{\lambda\mathbf{n}_0^T\bar{\mathbf{R}}^{-1}\mathbf{n}_0}. \tag{3.20}$$

Assume that we have obtained the positions and Doppler frequencies of $\bar{K}$ scatterers from the 3D images of different pulses. Denote $\mathbf{1} = [1, 1, \ldots, 1]^T$, $\mathbf{f}_d = [f_{d1}, f_{d2}, \cdots, f_{d\bar{K}}]^T$ and $\mathbf{D} = [\tilde{\mathbf{a}}_1, \cdots, \tilde{\mathbf{a}}_{\bar{K}}]$. The expectation operators can be replaced by the mean of samples. That is $E(\tilde{\mathbf{a}}\tilde{\mathbf{a}}^T) =: \mathbf{D}\mathbf{D}^T/\bar{K}$, $E(\tilde{\mathbf{a}}) =: \mathbf{D} \times \mathbf{1}/\bar{K}$, $E(\tilde{\mathbf{a}}f_d) =: \mathbf{D} \times \mathbf{f}_d/\bar{K}$, $E(\tilde{\mathbf{a}}) =: \mathbf{D} \times \mathbf{1}/\bar{K}$, and $E(f_d) = \mathbf{f}_d^T\mathbf{1}/\bar{K}$.

After $\mathbf{w}$ is obtained, the multiple 3D images can be coherently combined. Then similar to Chapter 2, strong scatterers are selected. After coordinate transform, the coordinates of these scatterers are obtained and then the 3D image is obtained.

According to the description in last few sections, the MIMO radar 3D imaging technique can be described using the procedure in Fig.3.8.

3.6 Simulation Results

This section uses numerical examples to demonstrate the problems occurred in MIMO radar imaging using multiple snapshots and the merits obtained after using the methods proposed in this Chapter. The carrier frequency is 35G Hz. The transmitting code is random Binary Phase Shift Keying (BPSK) modulated signal with length $L = 512$ and bandwidth $B_s = 150M$ Hz.

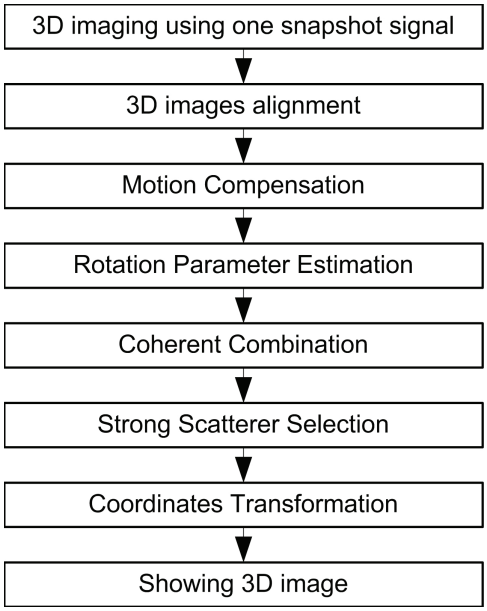

Figure 3.8: The total procedure of MIMO radar 3D imaging.

3.6.1 Simulation 1: Cross-Range Sidelobes Mitigation

Using multiple-snapshot signals, the 3D images can be coherently combined, resulting in increased SNR and lower sidelobes in the cross-range domain. In order to show clearly, the MIMO radar in this simulation contains $M = 10$ uniform linear transmitting antennas with inter-element distance of 85.7143 m and $N = 20$ uniform linear receiving antennas with inter-element distance of 4.2857 m. The unambiguous distance at $R = 50$ km is 100 m. The antennas are located along the X axis. The target with 8 scatterers is located 50 km away with line of sight [-0.8,1]. The speed of the target is [198.8,159] m/s. The time duration to collect the data is 0.16 s. During this time, the target moves about 40.7 m. The PRF is 300 and the number of discrete snapshot is 48. Because the virtual array is a one-dimensional array, the image obtained is a two-dimensional image. The transmit power of each antenna is $P_t = 4000$ w and the gain of each antenna is $G_t = 43.3$ dB. The effective area of each transmit and receive antenna is $A_r = 0.04\pi\ m^2$. The receiver noise temperature is

$T_0 = 290$ K, the noise figure is $F_n = 2.5$ dB. The RCS of each scatterer is $\alpha = 1\ m^2$. The SNR of each scatterer after array processing is 30 dB (does not consider time domain processing and the output SNR after only MIMO processing is $SNR = \frac{MNLP_tG_t\alpha A_r}{16\pi^2R^4K_bF_nT_0B_s}$, where $K_b = 1.38 \times 10^{-23}$ J/K is the Boltzmann constant, L is the length of the codes). Fig.3.9 (a) shows

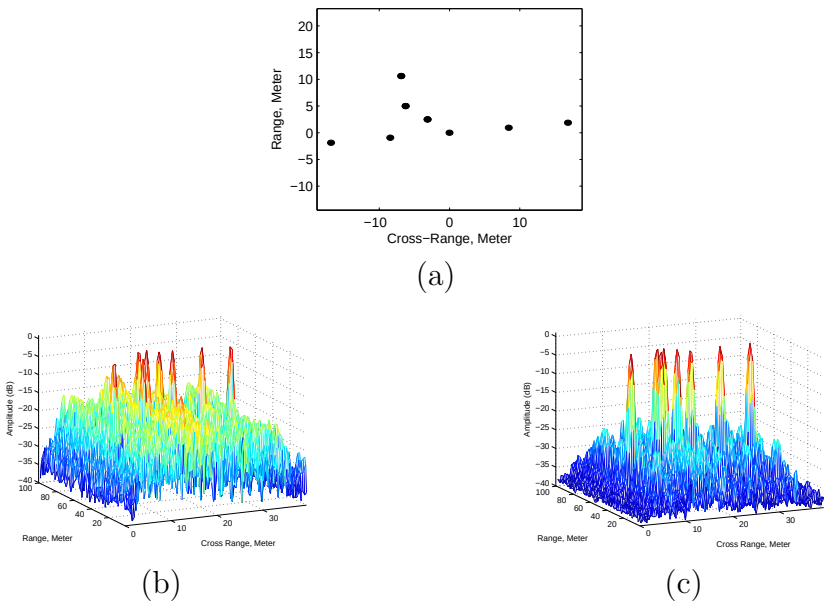

(a)

(b)

(c)

Figure 3.9: (a) Original 2D image of the target, (b)Reconstructed 2D image using one snapshot signals and (c) Reconstructed 2D image using multiple snapshots signals (simulation 1).

the original two-dimensional image of the target. Fig.3.9 (b) and (c) show the reconstructed images using one snapshot and multiple snapshots signals. From these two figures, we see that the reconstructed images reflect the distribution of the original scatterers. The cross-range sidelobes in Fig.3.9 (c) are lower than that in Fig.3.9 (b) due to time domain coherent processing. In order to show the results clearly, two-dimensional contour plot is also shown in Fig.3.10.

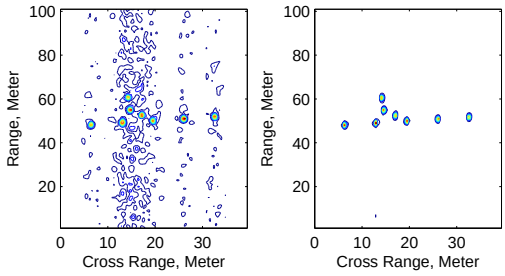

Figure 3.10: Contour plot of reconstructed 2D image using single and multiple snapshots signals (simulation 1).

3.6.2 Simulation 2: 3D Imaging of MIMO Radar Using Multiple Snapshots Signal

In this example, the MIMO radar under consideration contains a 8×8 square transmitting array with inter-element spacing of 107.1429 m and a 8×8 square receiving array with inter-element spacing of 13.3929 m. The target with 11 scatterers is located in the $\mathbf{n}_0 = [0.4402, 0.1761, 0.8805]$ direction and is 100 km from the radar. It moves uniformly in the X axis direction with speed $[133.9286, 0, 0]$ m/s. The unambiguous distance at 100 km is 64 m. The square roots of the RCS of the 11 scatterers are 1, 2, 3, ... , and 11 m. Fig.3.11 shows the original 3D image of the target (same as simulation 3 in Chapter 2). The antenna parameters are the same as that of simulation 1 except that the transmit power is 50 W. The SNR of the weakest scatterer after array processing is 12.2 dB (does not consider time domain processing). The PRF is 30 Hz and the coherent processing time is $T = 0.8$ s. During this period, the target moves 47 m along the direction of $\mathbf{n}_0$ and moves 96.2 m in the direction perpendicular to $\mathbf{n}_0$. The $(\mathbf{v} - (\mathbf{v}^T\mathbf{n}_0)\mathbf{n}_0) \times T = [86.3787, -8.3056, -41.5282]$ m. The target moves across the unambiguous window, therefore the 3D images of some snapshots are cross-range wrapped. Fig.3.12 shows the real cross-range position $(\mathbf{r}(t) - (\mathbf{r}(t)^T\mathbf{n}_0)\mathbf{n}_0)$ of the target, the measured cross-range wrapped position and the cross range unwrapped position with time, where

$\mathbf{r}(t)$ expresses the position of the target and we let the target be located in the $\mathbf{n}_0$ direction at time 0. It can be seen that the unwrapped position coincide with that of the real position.

The real $\mathbf{w} = (\mathbf{v} - (\mathbf{v}^T\mathbf{n}_0)\mathbf{n}_0)/r$ is $[1.0797, -0.1038, -0.5191] \times 10^{-3} m/s$. We choose $\delta v = 32$ dB and $\delta\zeta = 6$ dB. The estimated $\hat{\mathbf{w}}$ using our method is $[1.0704,\ -0.1225,\ -0.5093] \times\ 10^{-3} m/s$. The relative error $|\mathbf{w} - \hat{\mathbf{w}}|/|\mathbf{w}|$ is 0.0192. This is a small value. Fig.3.13 shows the reconstructed 3D image using one snapshot signal. Due to high cross-range sidelobes, some scatterers have not been constructed. Fig.3.14 shows the reconstructed 3D image using time domain information (estimated $\hat{\mathbf{w}}$). It can be seen that the quality of the 3D image in Fig.3.14 is better than that of Fig.3.13 although there are some false scatterers.

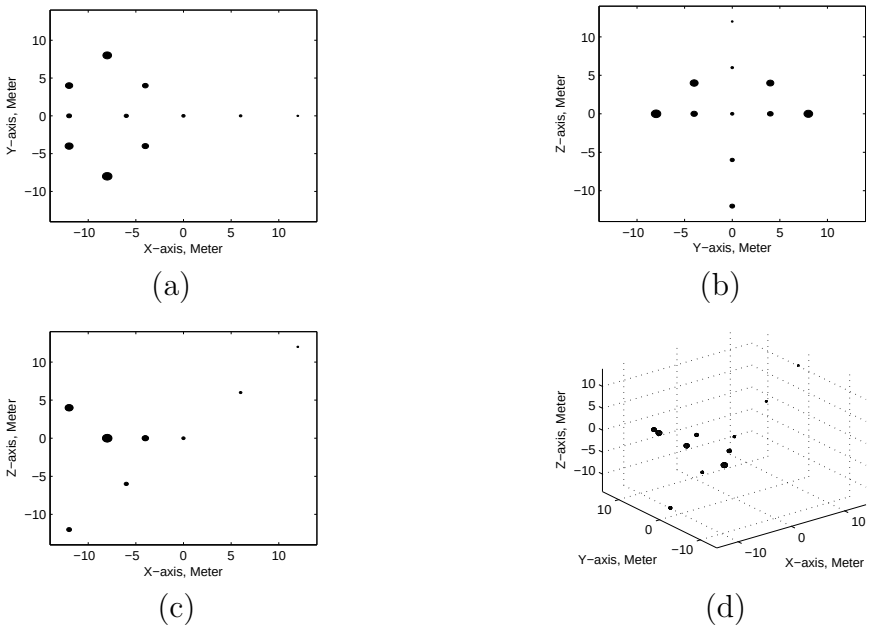

Figure 3.11: Three different projections and 3D view of the target model (simulation 2).

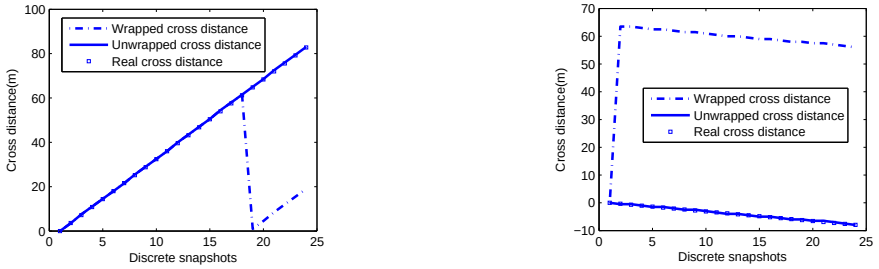

(a) (b)

Figure 3.12: Wrapped, unwrapped and real cross distance. (a) along the X axis, (b) along the Y axis (simulation 2)

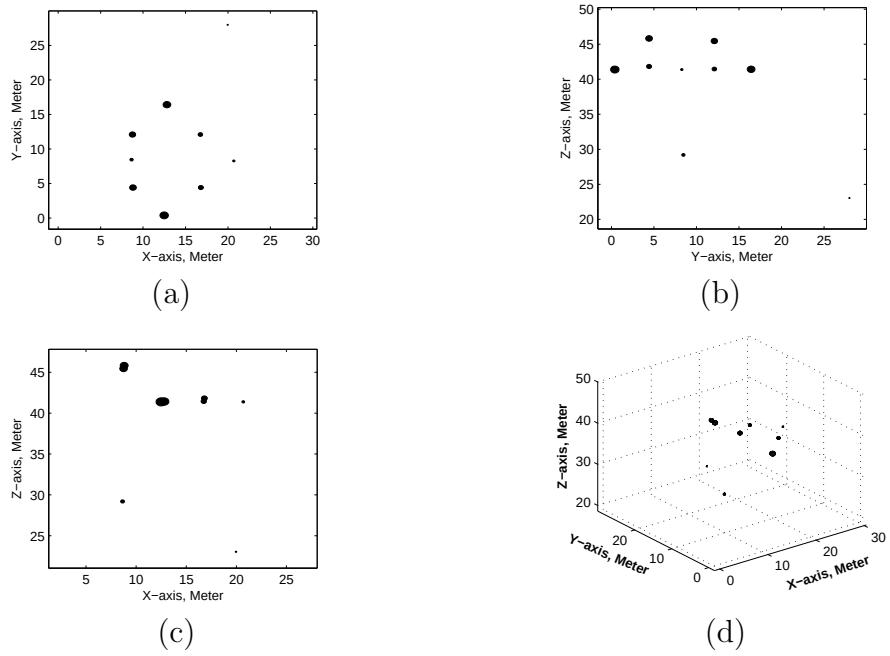

(a) (b) (c) (d)

Figure 3.13: Three different projections and 3D views of the image obtained by one snapshot MIMO array for δv=32 dB and $\delta\zeta$ = 6dB (simulation 2).

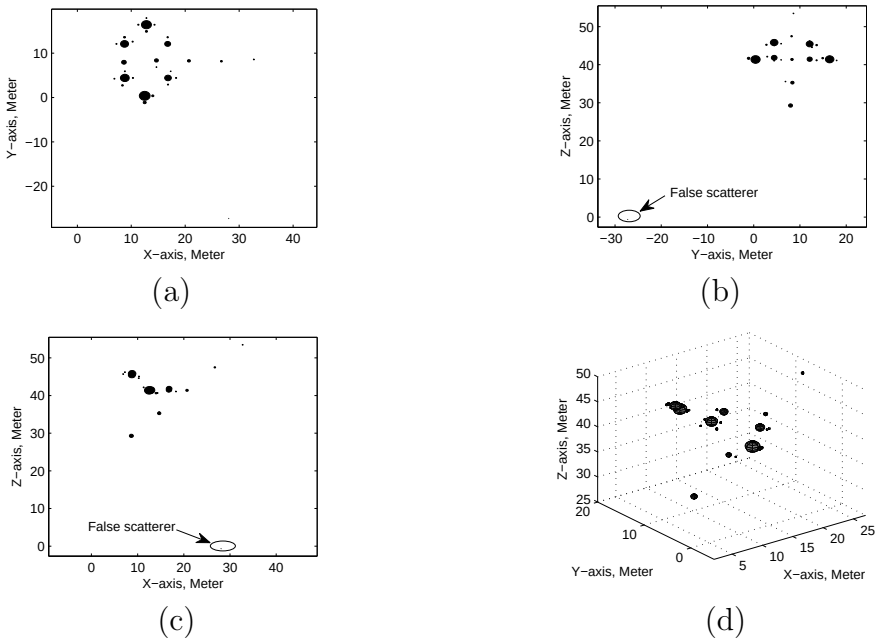

Figure 3.14: Three different projections and 3D views of the image obtained by multiple snapshots MIMO array for δv=32 dB and $\delta\zeta$ = 6dB (simulation 2).

3.6.3 Simulation3: 3D imaging of a Complex Target

In this example, we consider 3D imaging of a complex target. The target is comprises of 69 strong scatterers and is shown in Fig.3.15. The antenna parameters are the same as that of simulation 2. The target is located in the $\mathbf{n}_0 = [0.4082, 0.4082, 0.8165]$ direction and is 100 km from the radar. It moves uniformly in the [0.6917, 0.6917,0.2075] direction with speed $[109.1629, 109.1629, 32.7489]m/s$. The SNR of the weakest scatterer after array processing is 12.2 dB (does not consider time domain processing). The PRF is 30 Hz and the coherent processing time is $T = 1$ s. The real $\mathbf{w} = (\mathbf{v} - (\mathbf{v}^T\mathbf{n}_0)\mathbf{n}_0)/r$ is $[0.6186, 0.6186, -0.6186] \times 10^{-3}m/s$. We choose δv = 26 dB and $\delta\zeta$ = 9.5 dB when selecting strong scatterers to estimate the speed. These threshold values are set to ensure that we have higher probability in selecting the correct scatterers to further guarantee that the ro-

tation speed is estimated correctly. The estimated $\hat{\mathbf{w}}$ using our method is $[0.6116, 0.6095, -0.6105] \times 10^{-3} m/s$. The relative error $|\mathbf{w} - \hat{\mathbf{w}}|/|\mathbf{w}|$ is 0.0131. This is a small value. We also choose $\delta v = 32$ dB and $\delta\zeta = 6$ dB when selecting strong scatterers to form the 3D image. Fig.3.16 shows the reconstructed 3D image using one snapshot signal. Due to high cross-range sidelobes, some scatterers have not been reconstructed. Fig.3.17 shows the reconstructed 3D image using time domain information (estimated $\hat{\mathbf{w}}$). Similar to simulation 2, it can be seen that the quality of the 3D image in Fig.3.17 is better than that of Fig.3.16.

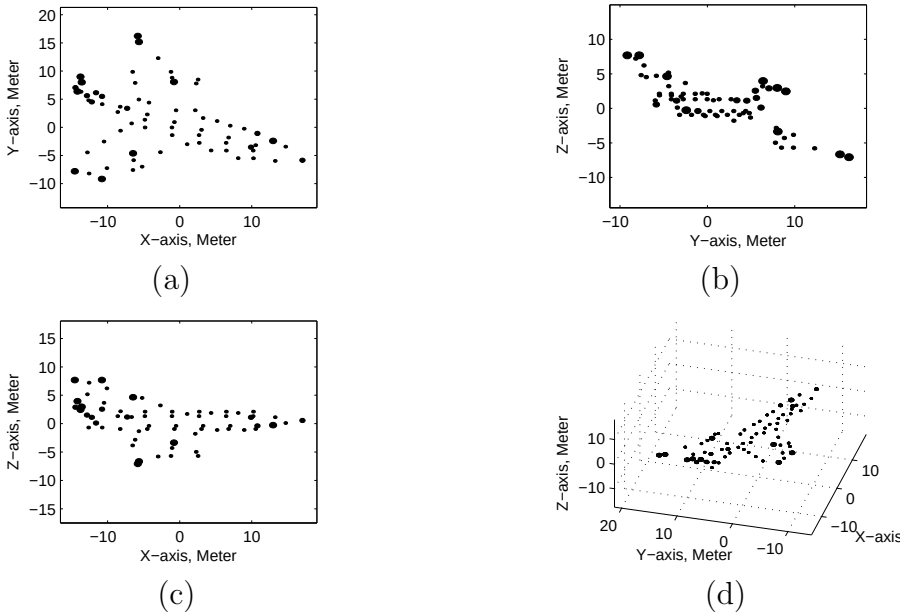

Figure 3.15: Three different projections and 3D view of the target model (simulation 3).

3.7 Conclusions

Compared with MIMO radar 3D imaging using single snapshot signal, using multiple snapshots can improve output SNR and mitigate cross-range sidelobes, resulting in improved image quality. For a faraway target, the cross-

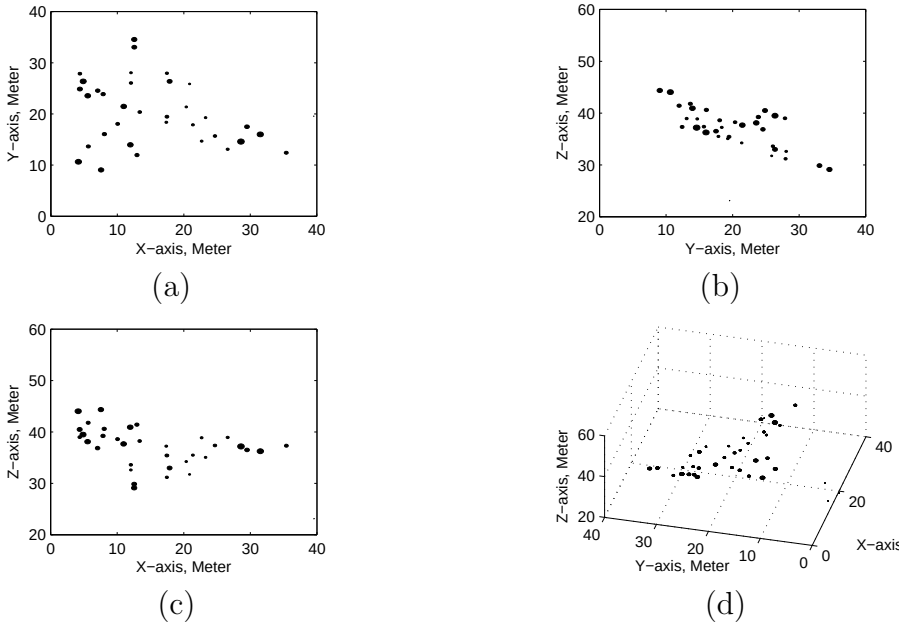

Figure 3.16: Three different projections and 3D views of the image obtained by MIMO array using one snapshot signal (δv=32 dB and $\delta\zeta$ = 6dB, simulation 3).

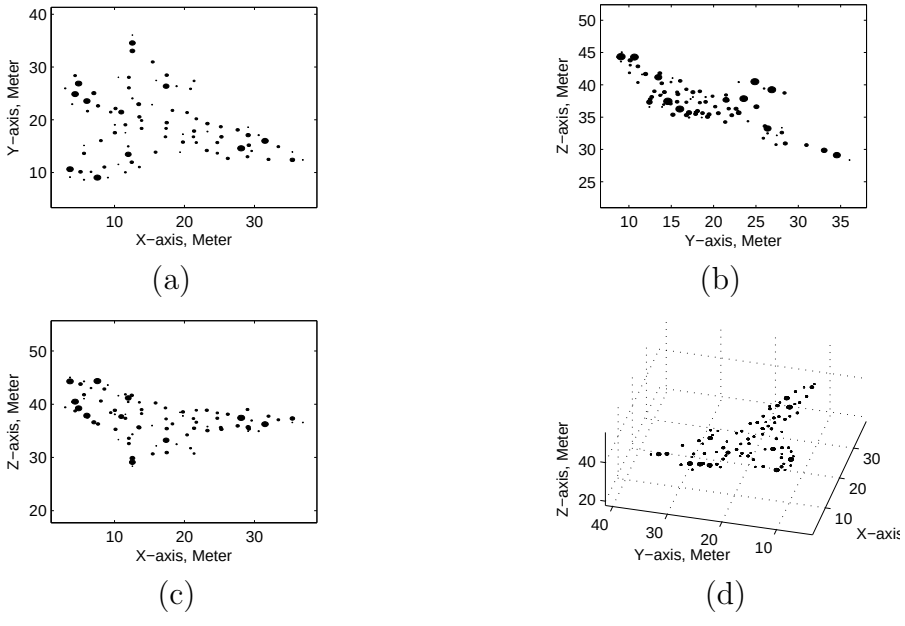

Figure 3.17: Three different projections and 3D views of the image obtained by MIMO array using multiple snapshots signals (δv=32 dB and $\delta\zeta$ = 6dB, simulation 3).

range distance of the target traveled may exceed the unambiguous window and therefore the 3D images may be wrapped in the cross-range domain. Cyclic correlation method is proposed to align the 3D images in cross-range direction. The three dimensional rotation speed is estimated using minimum mean square error criterion. The 3D images obtained in different snapshots are coherently combined to obtain an improved 3D image.

For multiple snapshots case, the computation load will increase. If the target does not move in a smooth manner, the approximation precision using one order polynomial function approximation will be affected. If there is no isolated scatterer, a more complex motion compensation method should be used. Non-smooth movement will also affect the precision of motion compensation.

Chapter 4

ℓ_1 ℓ_0 Norms Homotopy Sparse Signal Recovery Algorithms

4.1 Introduction

A target usually has only a few strong scatterers. These strong scatterers are often sparsely distributed. Sparse signal recovery algorithms can thus be used to improve image quality. This has been shown in two dimensional ISAR imaging [48]. So this Chapter discusses sparse signal recovery algorithm and the next chapter discusses its application on MIMO radar imaging.

Sparse signal recovery utilizes the *a prior* information of sparse property of the signal [32] [33]. A linear system can be expressed as

$$\mathbf{s} = \mathbf{\Psi}\boldsymbol{\alpha} + \mathbf{n}, \tag{4.1}$$

where $\mathbf{n}$ is the observation noise or/and model error. The dimension of $\mathbf{\Psi}$ is $M \times N$. When $M < N$, Eq.(4.1) is an under-determined system. When $\boldsymbol{\alpha}$ is a sparse signal, it can be solved by the following optimization criterion

$$\hat{\boldsymbol{\alpha}} = \arg\min ||\boldsymbol{\alpha}||_{sp} \quad \text{subject to} \, ||\mathbf{s} - \mathbf{\Psi}\boldsymbol{\alpha}||_2 < \varepsilon, \tag{4.2}$$

where $||\boldsymbol{\alpha}||_{sp}$ expresses sparse norm of $\boldsymbol{\alpha}$, ε is related with the variance of noise $\mathbf{n}$. Sparse property usually can be measured by $\ell_p(0 \leq p \leq 1)$ norm. Although ℓ_0 norm is better in describing sparsity of noise free case, sparse learning algorithms based on ℓ_0 norm are computationally complex, because it needs combinational optimization. So algorithms based on ℓ_1 norm, such as basis pursuit [34], ℓ_1-ℓ_s [35], etc, are more popular, because ℓ_1 norm is a convex function and minimization of a convex function on a convex set has unique solution. ℓ_1-magic program solves quadratically constrained ℓ_1 minimization by reformulating it as a second-order cone program and uses a log barrier algorithm [63]. However, it is computationally expensive. Hence many simpler algorithms, including the matching pursuit (MP) [36], orthogonal matching pursuit (OMP) [37] are proposed. It has also been shown that the performance using $0 < p < 1$ is better than using $p = 1$ [38] [39] [40]. So constrained ℓ_p norm minimization problem is another hot research topic, which is usually solved by steepest descent gradient projection (SDGP) [38] [39]. But because the derivative of α^p approximates to infinity when α approximates to zero, the step size should be designed carefully.

In order to obtain an approximate ℓ_0 norm solution, a smoothed pseudo norm function $F_\sigma(\boldsymbol{\alpha}) = N - \sum_{n=1}^{N} exp(-\frac{\alpha_n^2}{2\sigma^2})$ was used to replace the ℓ_0 norm in [41]. By letting σ varies from infinity to zero, a homotopy between ℓ_2 norm and ℓ_0 norm is formed and a smoothed ℓ_0 norm solution is obtained. It has been shown that the smoothed ℓ_0 norm method (simplified as SL0 in the followings) is two to three orders of magnitude faster than basis pursuit (based on interior-point linear programming solvers) and provides better estimation of the source than matching pursuit methods.

In this Chapter we propose a sequential order one negative exponential (SOONE) pseudo norm function $G_\sigma(\boldsymbol{\alpha}) = N - \sum_{n=1}^{N} exp(-|\alpha_i|/\sigma)$, where

when σ approaches infinity, $G_\sigma(\boldsymbol{\alpha})$ approximates to ℓ_1 norm (with difference of a ratio), and when σ approaches 0, $G_\sigma(\boldsymbol{\alpha})$ approximates to ℓ_0 norm. So a homotopy between ℓ_1 norm and ℓ_0 norm is formed (called $\ell_1\,\ell_0$ homotopy). Comparison among choosing $F_\sigma(\boldsymbol{\alpha})$, $G_\sigma(\boldsymbol{\alpha})$ and ℓ_p will be discussed in the next section.

In solving our optimization problem, the inverse of matrix $\boldsymbol{\Psi}\boldsymbol{\Psi}^H$ needs to be computed. In general, if the $\boldsymbol{\Psi}$ matrix is random, $\boldsymbol{\Psi}\boldsymbol{\Psi}^H$ usually will be well-conditioned. In real cases, such as MIMO radar 3D imaging discussed in this thesis, this matrix may be ill conditioned and the condition number may be as high as 10^{18}, and the original algorithm losses its robustness with increasing condition number. We propose using diagonal loading and singular value decomposition (SVD) to improve the robustness of this algorithm.

Some sparse signal recover algorithms are designed for real signal. In radar imaging, complex signals are used. In order to use these algorithms, a complex equation should be transformed to a real equation. In this case, if traditional algorithm is used directly, performance lose will be produced. $\ell_1\,\ell_0$ homotopy method is also be extended to process complex signal and block sparse signals.

This Chapter is organized as follows. Section 4.2 introduces the $\ell_1\,\ell_0$ norms homotopy sparse signal recovery algorithm. Comparison with iterative shrinkage threshold method is discussed in section 4.3. Robust implementation is discussed in section 4.4. Simulation results are presented in section 4.5. Finally, section 4.6 concludes this chapter.

4.2 $\ell_1\,\ell_0$ Norms Homotopy Sparse Signal Recover Algorithm

4.2.1 Fundamental of Sparse Signal Recovery

The sparsity of a vector can be characterized by the ℓ_p norm of the vector (where ℓ_p norm is defined as $\sum_{n=1}^{N}|\alpha_n|^p$ $(0 \leq p \leq 1)$, it is actually the power p of conventional ℓ_p norm. In order for simplification, literature denotes $\sum_{n=1}^{N}|\alpha_n|^p$ as ℓ_p norm). For $p = 0$, ℓ_0 is the number of the non-zero element. ℓ_p is a convex function for $p >= 1$, while for $0 < p < 1$, it is not a convex function. Fig.4.1 shows the mesh plot and contour plot of $\ell_{1/2}$ norm for two dimension case. It can be seen that the $\ell_{1/2}$ norm has smaller value at the origin and two axes. It can also be seen that the ℓ_p norm is concave in one quadrant. It is the concave property of ℓ_p norm $(0 < p < 1)$ in one quadrant that makes it more suitable to measure sparsity. The smaller the p, the deeper the channels in the two axes gets. The minimum points are more likely to be located on the axes. So, generally speaking, the smaller the value of p, the better the performance.

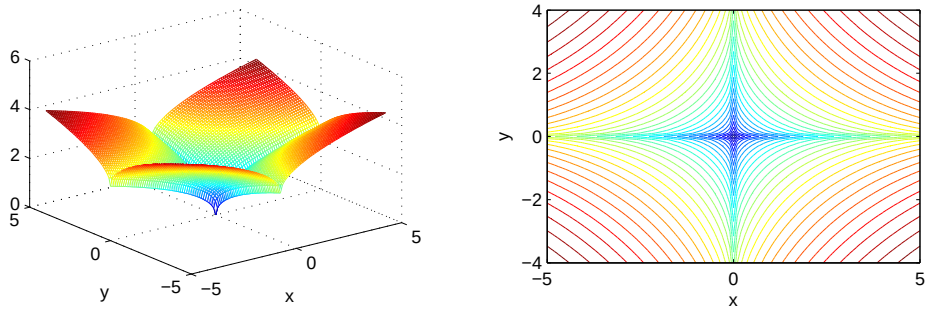

(a) (b)

Figure 4.1: (a) Mesh plot and (b) contour plot of two dimensional $\ell_{1/2}$ norm .

It is well know that if any $M \times M$ submatrix of $\boldsymbol{\Psi}$ is inverse, and the sparsity (number of non zero elements) of $\boldsymbol{\alpha}$ is not more than $\lfloor M/2 \rfloor$, then the

most sparse solution of a linear equation is unique.

In order to implement sparse signal recovery using ℓ_0 norm criterion, it requires combinational optimization, which is of non-deterministic polynomial time (NP) hard and computationally expensive. For $p = 1$, because $|\boldsymbol{\alpha}|^p$ is a convex function and convex optimization has matured algorithms, norm 1 based algorithms are popular. Many theory results on ℓ_1 norm based algorithms have relation with the Restricted Isometry Property (RIP) of the matrix $\boldsymbol{\Psi}$.

Definition 4.1: The restricted isometry constant (RIC) δ_k of a matrix $\boldsymbol{\Psi} \in \mathbb{C}^{M\times N}$ is the smallest number δ_k such that

$$(1-\delta_k)||\boldsymbol{\alpha}||_2^2 \leq ||\boldsymbol{\Psi}\boldsymbol{\alpha}||_2^2 \leq (1+\delta_k)||\boldsymbol{\alpha}||_2^2 \tag{4.3}$$

for all $||\boldsymbol{\alpha}||_0 \leq k$.

If $0 < \delta_k < 1$, matrix $\boldsymbol{\Psi}$ is said to satisfy the restricted isometry property condition. RIP means that the linear transform $\boldsymbol{\Psi}$ approximately preserves the lengths of k-sparse vectors, that is k-sparse vectors cannot be the null-space of $\boldsymbol{\Psi}$. The above restricted isometry property plays a fundamental role in the study of the recovery properties of compressive sensing.

Candès et al have shown that if $\boldsymbol{\Psi}$ satisfies the RIP with a RIC $\delta_{2k} < \sqrt{2}-1$, then the solution $\boldsymbol{\alpha}$ of equation (4.2) for $p = 1$ obeys [64]

$$||\boldsymbol{\alpha} - \boldsymbol{\alpha}^*|| \leq C_2\,\varepsilon + \frac{C_1}{\sqrt{k}}||\boldsymbol{\alpha} - \boldsymbol{\alpha}_k||_1 \tag{4.4}$$

where $\boldsymbol{\alpha}_k$ is the restriction of $\boldsymbol{\alpha}$ to its k largest entries, $C_1 = 2((1+(\sqrt{2}-1)\delta_{2k})/(1-(\sqrt{2}+1)\delta_{2k}))$ and $C_2 = (4\sqrt{1+\delta_{2k}})/(1-(\sqrt{2}+1)\delta_{2k})$.

This result implies that the reconstruction error by ℓ_1 minimization is finite. It is bounded by two terms. The first is the observation noise. With a decrease

of the noise, the reconstruction error becomes small. The second term is determined by the sparsity of the signal. If the sparsity of $\boldsymbol{\alpha}$ is less than or equal to k, the second term is zero, which means that the ℓ_1 minimization solution for noise free case can obtain the true solution.

However, the requirement of $\delta_{2k} < \sqrt{2} - 1$ restricts k to be a small value. The mathematic result is the most pessimistic. Usually, simulations provide realistic results.

Rick Chartrand pointed out that the performance based on ℓ_p $(0 < p < 1)$ norm is better than that based on ℓ_1 norm [38]. But due to its non-convex property, ℓ_p norm $(0 < p < 1)$ is described in the literature as intractable [38]. Even so, Rick Chartrand used a simple steepest descent gradient projection method to find the local minimizer. But the derivation of $\alpha^p (p < 1)$ is $p\alpha^{p-1}$ and approaches infinity when α approaches 0. So the gradient projection method should be designed carefully.

A function that has similar property with ℓ_p norm is the order one negative exponential function $G_\sigma(\boldsymbol{\alpha}) = N - \sum_{n=1}^{N} exp(-|\alpha_n|/\sigma)$, where σ is an auxiliary variable. The mesh plot and contour plot of $G_1(\boldsymbol{\alpha})$ for two dimensional case are shown in Fig.4.2. It can be seen that they are similar to Fig.4.1.

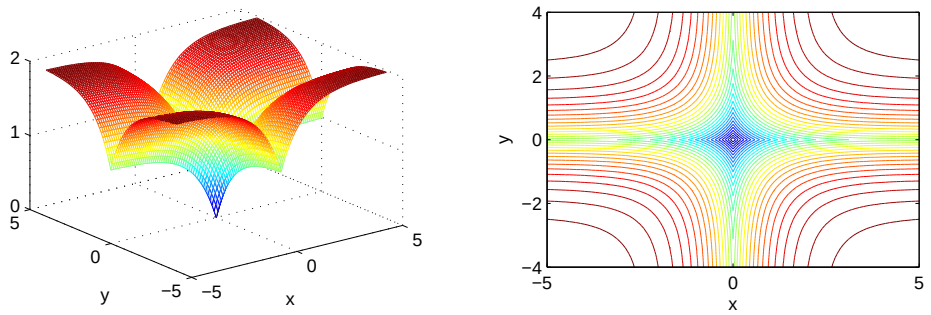

(a) (b)

Figure 4.2: (a) Mesh plot and (b) contour plot of two dimensional function $2 - e^{-|x|} - e^{-|y|}$.

Another similar negative exponential function defined by [41] is $f_\sigma(\alpha) =$

$1 - e^{-\alpha^2/2\sigma^2}$ (smoothed ℓ_0 norm method). Now let's compare the difference between choosing $f_\sigma(\alpha)$ and choosing $g_\sigma(\alpha) = 1 - exp(-\frac{|\alpha|}{\sigma})$. When $\sigma \to \infty$, $f_\sigma(\alpha) \to \alpha^2/(2\sigma^2)$, so function $F_\sigma(\boldsymbol{\alpha}) = \sum_{n=1}^{N} f_\sigma(\alpha_n)$ degenerates to ℓ_2 norm (with difference of a ratio); but $g_\sigma(\alpha) \to |\alpha|/\sigma$, therefore, $G_\sigma(\boldsymbol{\alpha})$ degenerates to ℓ_1 norm. So for large σ, the method based on the new cost function has higher probability to find sparse solution than that based on $F_\sigma(\boldsymbol{\alpha})$. From this discussion we have confident that the new method will be better than the smoothed ℓ_0 norm method.

The merit of this $G_\sigma(\boldsymbol{\alpha})$ function compared with ℓ_p norm is that the derivation of $-e^{-\alpha/\sigma}$ $(= \frac{1}{\sigma}e^{-\alpha/\sigma})$ does not approach infinity when α approaches 0. So it is easier to design gradient projection algorithm. On the other hand, for real signal with a few large values and many small values (not exactly 0), ℓ_0 norm is not a proper measure to describe the sparsity. By controlling the auxiliary variable σ, a suitable cost function can be built to improve the flexibility of the algorithm.

Therefore sparse signal recovery algorithm based on $G_\sigma(\boldsymbol{\alpha})$ function minimization can be described as:

$$\hat{\boldsymbol{\alpha}} = \lim_{\sigma \to \sigma_{min}} \arg\min G_\sigma(\boldsymbol{\alpha}) \quad \text{subject to} \, ||\mathbf{s} - \boldsymbol{\Psi}\boldsymbol{\alpha}||_2 < \varepsilon. \tag{4.5}$$

Many ℓ_1 based sparse signal recover methods assume that the vector and matrix are all real number. Denote $\mathbf{s} = \mathbf{s}_r + j\mathbf{s}_i$, $\boldsymbol{\Psi} = \boldsymbol{\Psi}_r + j\boldsymbol{\Psi}_i$, $\boldsymbol{\alpha} = \boldsymbol{\alpha}_r + j\boldsymbol{\alpha}_i$, $\mathbf{n} = \mathbf{n}_r + j\mathbf{n}_i$, $\mathbf{s}_2 = [\mathbf{s}_r^T, \mathbf{s}_i^T]^T$, $\boldsymbol{\Psi}_2 = \begin{pmatrix} \boldsymbol{\Psi}_r, & -\boldsymbol{\Psi}_i \\ \boldsymbol{\Psi}_i, & \boldsymbol{\Psi}_r \end{pmatrix}$, $\boldsymbol{\alpha}_2 = [\boldsymbol{\alpha}_r^T, \boldsymbol{\alpha}_i^T]^T$ and $\mathbf{n}_2 = [\mathbf{n}_r^T, \mathbf{n}_i^T]^T$. Eq. (4.1) can be expressed as

$$\mathbf{s}_2 = \boldsymbol{\Psi}_2\boldsymbol{\alpha}_2 + \mathbf{n}_2. \tag{4.6}$$

For symbol simplicity, we use $\mathbf{s}$, $\boldsymbol{\Psi}$, $\boldsymbol{\alpha}$ and $\mathbf{n}$ to express $\mathbf{s}_2$, $\boldsymbol{\Psi}_2$, $\boldsymbol{\alpha}_2$ and $\mathbf{n}_2$ in the following discussion and there should be no confusion.

4.2.2 Steepest Descent Gradient Projection Method

Steepest descent gradient method is usually used for finding local minimum point of non-constrained problem. For every searching step, the algorithm finds the steepest descent gradient direction and moves a small step. For constrained optimization problem, the new point along the steepest descent gradient direction may not belong to the feasible set, so the new iteration position should be projected into the feasible set. Gradient projection principle has been used in [41] and [38]. In this chapter we also use gradient projection method to solve Eq.(4.5). The entire algorithm consists of two loop layers. In the outer loop, σ is varied from a larger value to a smaller value. Gradient projection step is carried out in the inner loop. The algorithm structure can be described as follows [41] [65]:

- Initialization:

  1) define J, L, L_0, L_1.

  2) Let $\hat{\boldsymbol{\alpha}}_0$ be equal to the minimum ℓ_2 norm solution of $\mathbf{s} = \boldsymbol{\Psi}\boldsymbol{\alpha}$, obtained by $\hat{\boldsymbol{\alpha}}_0 = \boldsymbol{\Psi}^{\dagger}\mathbf{s}$, where $\boldsymbol{\Psi}^{\dagger}$ is the pseudo inverse of $\boldsymbol{\Psi}$.

  3) Choose a suitable decreasing sequence for $\{\sigma\}$, $[\sigma_1, \cdots, \sigma_J]$.

- for $j = 1, \cdots, J$:

  1) Minimize the function $G_{\sigma_j}(\boldsymbol{\alpha})$ on the feasible set $\boldsymbol{\alpha} = \{\boldsymbol{\alpha} : |\boldsymbol{\Psi}\boldsymbol{\alpha} - \mathbf{s}|_2 < \varepsilon\}$ using L iterations of the revised steepest descent gradient algorithm (followed by projection onto the feasible set):

  - Initialization: $\boldsymbol{\alpha} = \hat{\boldsymbol{\alpha}}_{j-1}$

- For $\ell = 1, \cdots, L$ (loop L times):

  a) Let $\boldsymbol{\delta}$ be gradient of $G_{\sigma_j}(\boldsymbol{\alpha})$ and $\mu = min(max(|\boldsymbol{\alpha}|)/L_0, \sigma_j/L_1)$.

  b) For every element of $\boldsymbol{\alpha}$, let $\alpha(n) \leftarrow \alpha(n) - \frac{\alpha(n)}{|\alpha(n)|} \times min(|\alpha(n)|, |\mu\sigma_j\delta(n)|)$.

  c) If $|\boldsymbol{\Psi\alpha} - \mathbf{s}|_2 > \varepsilon$, project $\boldsymbol{\alpha}$ back into the feasible set $\boldsymbol{\alpha}$: $\boldsymbol{\alpha} \leftarrow \boldsymbol{\alpha} + \boldsymbol{\Psi}^H(\boldsymbol{\Psi\Psi}^H)^{-1}(\mathbf{s} - \boldsymbol{\Psi\alpha})$

2) Set $\hat{\boldsymbol{\alpha}}_j = \boldsymbol{\alpha}$

- Final answer is $\hat{\boldsymbol{\alpha}} = \hat{\boldsymbol{\alpha}}_J$

When computing the gradient of $G_\sigma(\boldsymbol{\alpha})$, we take $\frac{\partial g_\sigma(\alpha)}{\partial \alpha} = 0$ at $\alpha = 0$. The above algorithm is also called gradient projection based on sequential order one negative exponential (GP-SOONE) function algorithm [65].

The above procedure is the same as [41], except for two points. The first is that the μ in [41] is a constant while μ here is varying with σ and $max(|\boldsymbol{\alpha}|)$. The second is by choosing the movement step as $\frac{\alpha(n)}{|\alpha(n)|} \times min(|\alpha(n)|, |\mu\sigma\delta(n)|)$, it ensures that step $\alpha(n) \leftarrow \alpha(n) - \frac{\alpha(n)}{|\alpha(n)|} \times min(|\alpha(n)|, |\mu\sigma\delta(n)|)$ does not change the sign of $\alpha(n)$ for real data and does not move over length of $\alpha(n)$ for complex data. In [41], μ is a constant, and by choosing $\mu \leqslant 1$, $\alpha \leftarrow \alpha - \mu\alpha e^{-\frac{\alpha^2}{2\sigma^2}}$ also does not change the sign of α.

The key of the above algorithm is steepest descent gradient searching plus projection on feasible set. A natural question is: is the above algorithm a descent algorithm in the feasible set? To answer this, we prove that if the steepest descent gradient search is the conventional method, that is $\boldsymbol{\alpha} \leftarrow \boldsymbol{\alpha} - \mu\sigma\boldsymbol{\delta}$, the algorithm is a descent algorithm in the feasible set. According

to the algorithm, the projection of $\boldsymbol{\alpha} - \mu\sigma\boldsymbol{\delta}$ onto the feasible set is

$$\begin{aligned} & \boldsymbol{\alpha} - \mu\sigma\boldsymbol{\delta} + \boldsymbol{\Psi}^H(\boldsymbol{\Psi}\boldsymbol{\Psi}^H)^{-1}(\mathbf{s} - \boldsymbol{\Psi}(\boldsymbol{\alpha} - \mu\sigma\boldsymbol{\delta})) \\ = \; & \boldsymbol{\alpha} - \mu\sigma[\mathbf{I} - \boldsymbol{\Psi}^H(\boldsymbol{\Psi}\boldsymbol{\Psi}^H)^{-1}\boldsymbol{\Psi}]\boldsymbol{\delta} \\ = \; & \boldsymbol{\alpha} - \mu\sigma\boldsymbol{\delta}_n, \end{aligned} \tag{4.7}$$

where $\boldsymbol{\delta}_n = [\mathbf{I} - \boldsymbol{\Psi}^H(\boldsymbol{\Psi}\boldsymbol{\Psi}^H)^{-1}\boldsymbol{\Psi}]\boldsymbol{\delta}$ is the projection of $\boldsymbol{\delta}$ onto the null subspace of matrix $\boldsymbol{\Psi}$ and we use $\mathbf{s} = \boldsymbol{\Psi}\boldsymbol{\alpha}$.

Denote $\mathbf{UDV}$ as the Singular Value Decomposition (SVD) of $\boldsymbol{\Psi}$, where $\mathbf{U}, \mathbf{V} = \begin{bmatrix} \mathbf{V}_1 \\ \mathbf{V}_2 \end{bmatrix}$ are the left and right singular vector matrices of $\boldsymbol{\Psi}$, $\mathbf{D} = [\mathbf{D}_1, \mathbf{0}]$ is the singular value matrix, $\mathbf{D}_1$ is the non-zero part of $\mathbf{D}$, and $\mathbf{V}_1$ corresponds to $\mathbf{D}_1$. We have

$$\begin{aligned} \boldsymbol{\delta}^H\boldsymbol{\delta}_n &= \boldsymbol{\delta}^H\boldsymbol{\delta} - \boldsymbol{\delta}^H\mathbf{V}^H\mathbf{D}^H\mathbf{U}^H(\mathbf{U}\mathbf{D}_1^{-2}\mathbf{U}^H)\mathbf{U}\mathbf{D}\mathbf{V}\boldsymbol{\delta} \\ &= \boldsymbol{\delta}^H\boldsymbol{\delta} - \boldsymbol{\delta}^H\mathbf{V}^H\begin{pmatrix} \mathbf{I}, & \mathbf{0} \\ \mathbf{0}, & \mathbf{0} \end{pmatrix}\mathbf{V}\boldsymbol{\delta} \\ &= \boldsymbol{\delta}^H\boldsymbol{\delta} - \Big(\mathbf{V}_1\boldsymbol{\delta}\Big)^H\Big(\mathbf{V}_1\boldsymbol{\delta}\Big) \geq 0. \end{aligned} \tag{4.8}$$

Because for any multi-variable function f, the directional derivative of f along any direction $\mathbf{v}$ is $D_{\mathbf{v}}f = \nabla f \cdot \mathbf{v}$, and $\boldsymbol{\delta}^H\boldsymbol{\delta}_n \geq 0$, so $G_\sigma(\boldsymbol{\alpha})$ decreases along $-\boldsymbol{\delta}_n$. Then we see that the above algorithm is a descent direction search algorithm on feasible set. For the algorithm in this Chapter, when $\alpha(n) \neq 0$, μ takes a very small value, such that $min(|\alpha(n)|, |\mu\sigma\delta(n)|) = \mu\sigma|\delta(n)|$. In this case, the revised algorithm is still a descent direction search algorithm on feasible set.

The projection step can also be explained as follows. After steepest descent search, we obtain an estimate $\boldsymbol{\alpha}$ of the true value $\boldsymbol{\alpha}_0$ and $\mathbf{s}-\boldsymbol{\Psi}\boldsymbol{\alpha}=\boldsymbol{\Psi}(\boldsymbol{\alpha}_0-\boldsymbol{\alpha})$. Because $\boldsymbol{\Psi}^H(\boldsymbol{\Psi}\boldsymbol{\Psi}^H)^{-1}$ is the pseudo inverse of $\boldsymbol{\Psi}$, so $\boldsymbol{\Psi}^H(\boldsymbol{\Psi}\boldsymbol{\Psi}^H)^{-1}(\mathbf{s}-\boldsymbol{\Psi}\boldsymbol{\alpha})$ is the minimum ℓ_2 norm estimate of $\boldsymbol{\alpha}_0-\boldsymbol{\alpha}$. After adding $\boldsymbol{\alpha}$, we obtain a more precise estimation of $\boldsymbol{\alpha}_0$.

Next we discuss the choice of certain parameters. Denote $\hat{\boldsymbol{\alpha}}_0=\boldsymbol{\Psi}^\dagger\mathbf{s}$ as the minimum ℓ_2 norm solution. In [41], σ_1 is chosen as $\sigma_1>4\max_n|\hat{\alpha}_0(n)|$, then $exp(-\hat{\alpha}_0(n)^2/2\sigma_1^2)>0.96\approx 1$ for all $1\le n\le N$, such that the shape of cost function $G_{\sigma_1}(\boldsymbol{\alpha})$ near $\hat{\boldsymbol{\alpha}}_0$ is similar to that of $\sigma_1\to\infty$. In this thesis, because we choose $g_\sigma(\alpha)=1-exp(\frac{-|\alpha|}{\sigma})$, σ_1 is chosen as $\sigma_1>16\max_n|\hat{\alpha}_0(n)|$, then $exp(-|\hat{\alpha}_0(n)|/\sigma_1)>0.93\approx 1$.

The choice of σ_J is also important. When $\sigma_J\to 0$, the cost function $G_\sigma(\boldsymbol{\alpha})$ approximates to ℓ_0 norm. ℓ_0 norm is not suitable to describe the sparsity of a vector with many small elements. For imaging application, there are many small scatterers. So we chose a σ_J which is not too small. In our algorithm, σ_J is chosen to be larger than $E(max(|\boldsymbol{\Psi}^\dagger\boldsymbol{n}|))$, where E expresses expectation. The reason of choosing this σ_J can be explained as follows. The feasible set $\{\boldsymbol{\alpha}:||\mathbf{s}-\boldsymbol{\Psi}\boldsymbol{\alpha}||_2<\varepsilon\}$ is not a subspace. In gradient projection algorithm, we project $\boldsymbol{\alpha}$ to subspace $\{\boldsymbol{\alpha}:\mathbf{s}=\boldsymbol{\Psi}\boldsymbol{\alpha}\}$. For noise case, because $\boldsymbol{\alpha}_0+\boldsymbol{\Psi}^\dagger\boldsymbol{n}$ is the solution of $\mathbf{s}=\boldsymbol{\Psi}\boldsymbol{\alpha}$ (where $\boldsymbol{\alpha}_0$ is the true sparse solution), $\boldsymbol{\alpha}_0+\boldsymbol{\Psi}^\dagger\boldsymbol{n}$ belongs to the feasible set and $\boldsymbol{\Psi}^\dagger\boldsymbol{n}$ has many small value elements. We assume $\boldsymbol{\alpha}_0+\boldsymbol{\Psi}^\dagger\boldsymbol{n}$ be one approximate solution and a searching point. When σ_J is much less than the element value of $|\boldsymbol{\Psi}^\dagger\boldsymbol{n}|$, the searching vector $exp(-|\boldsymbol{\alpha}_0+\boldsymbol{\Psi}^\dagger\boldsymbol{n}|/\sigma_J)$ approaches zero. The gradient projection algorithm will be locked in this solution. So σ_J need not be too small, it should be larger than $E(max(|\boldsymbol{\Psi}^\dagger\boldsymbol{n}))$.

Now let's consider the step size. Generally speaking, if the inner iterative number L is large enough, the step size can be small. In order to reduce the

computation load, L is usually chosen as a small number (in [41], L is chosen as 3). Actually, obtaining a precise solution in inner loop is not necessary. The aim of an inner loop is to provide an initial value for the next inner loop with smaller σ. For smooth convex optimization function, the gradient vector decreases gradually as the search variables approach local minimum point and equals to zero at the local minimum point. So the value of the gradient vector decides the speed towards the local minimum point. But for the local non-convex optimization function considered in this Chapter, at the local minimum point, the gradient may not exist. The derivative of $g_\sigma(\alpha)$ near the axes exists with a quantity of $1/\sigma$. When $\sigma \to 0$, it increases to ∞. So in our algorithm, the step size includes σ, which cancels the $1/\sigma$ in the gradient. At the same time, we choose $\mu = \min(\max(|\boldsymbol{\alpha}|)/L_0, \sigma/L_1)$. With the decrease of σ, the σ/L_1 term also decreases. The $\max(|\boldsymbol{\alpha}|)/L_0$ term adjusts the step size to match the amplitude of $\boldsymbol{\alpha}$ and avoid a big step size especially in the first few outer iterations where σ is much larger than $\boldsymbol{\alpha}$. L_0 and L_1 are two large numbers to control the step size. According to $\frac{d}{d\alpha}e^{-\frac{\alpha}{\sigma}} = -\frac{1}{\sigma}e^{-\frac{\alpha}{\sigma}}$, with the increase of $|\alpha|$, the absolute derivative value decreases. So the elements that converge quickly are the zero elements (or small value elements). With the decrease of σ, the large value elements converge more slowly. So the inner loop should guarantee the convergence of the bigger amplitude signals to avoid situations where the gradient values become small while the bigger elements have not converged. Certainly, there is no algorithm that guarantees the convergence in any case.

4.2.3 Block $\ell_1\,\ell_0$ Homotopy Algorithm

In some applications such as distributed MIMO radar parameters estimation, the sparse signal is block sparse with constant block size and regular positions.

Denote vector $\boldsymbol{\alpha} = [\alpha_1, \ldots, \alpha_L, \alpha_{L+1}, \cdots, \alpha_{2L}, \cdots, \alpha_N]$, where L is the block size, $N = PL$ is the multiple of L, P is an integer. For block sparse signal, $[\alpha_{pL+1}, \cdots, \alpha_{(p+1)L}]$ forms a block, which is a zero vector or not a zero vector (all of $[\alpha_{pL+1}, \cdots, \alpha_{(p+1)L}]$ are not zeros). The price function can be defined as

$$G_\sigma(\boldsymbol{\alpha}) = P - \sum_{p=0}^{P-1} exp\left(-\frac{\sqrt{\sum_{\ell=1}^{L} |\alpha_{pL+\ell}|^2}}{\sigma}\right). \tag{4.9}$$

Gradient projection can be used for the above price function.

The $\ell_1\,\ell_0$ homotopy method can process complex data equations and real data equations. If a real version algorithm is used to process complex data equation, the complex equation should be transformed to a real equation. Actually, the transformed real signal is a block signal because with high probability the real and imaginary number pair of a complex number takes on large value or small value at the same time. In the below steps we prove that the real version block $\ell_1\,\ell_0$ homotopy algorithm with block size of 2 is equivalent to complex version non-block algorithm.

For block size of 2 sparse signal α, the order one negative exponential function can be defined as $g_\sigma(\alpha_r, \alpha_i) = 1 - exp\left(-\frac{\sqrt{\alpha_r^2+\alpha_i^2}}{\sigma}\right)$, where α_r and α_i forms a block. A complex order one negative exponential function is defined as $g_\sigma(\alpha) = 1 - exp\left(-\frac{\sqrt{\alpha_r^2+\alpha_i^2}}{\sigma}\right)$, where $\alpha = \alpha_r + j\alpha_i$. Then the smoothed ℓ_0 norm of vector $\boldsymbol{\alpha}$ for block and complex cases are all the same as Eq.(4.9). The sparse signal recovery algorithm structures for all three cases (real no block, block size of 2, complex no block) are same. The only difference is the computation of gradient of $G_\sigma(\boldsymbol{\alpha})$. For block signal $\boldsymbol{\alpha}$, the derivative for component α_r is $\frac{\partial G}{\partial \alpha_r} = \frac{1}{\sigma}\frac{\alpha_r}{\sqrt{\alpha_r^2+\alpha_i^2}} exp(-\frac{\sqrt{\alpha_r^2+\alpha_i^2}}{\sigma})$. For a complex number α, we compute the derivative of G to the real part and imaginary part of α, then combine them to form a complex number, thus we have $\frac{\partial G}{\partial \alpha} = \frac{\partial G}{\partial \alpha_r} + j\frac{\partial G}{\partial \alpha_i} = \frac{1}{\sigma}\frac{\alpha}{|\alpha|} exp(-\frac{|\alpha|}{\sigma})$, it

has the same form when α is a real number. The parameter μ for two cases are also same if $max(|\boldsymbol{\alpha}|)$ is computed with block by block case.

We prove below that the above algorithms for real block signal with block size of 2 and complex signal are equivalent.

Lemma 1: Let $A = A_r + jA_i$ and $\mathbf{x} = \mathbf{x}_r + j\mathbf{x}_i$ be a complex matrix and a complex vector respectively. Define $\bar{A} = \begin{bmatrix} A_r & -A_i \\ A_i & A_r \end{bmatrix}$ and $\bar{\mathbf{x}} = \begin{bmatrix} \mathbf{x}_r \\ \mathbf{x}_i \end{bmatrix}$ be the real equivalent matrix of A and equivalent vector of $\mathbf{x}$. Then $A\mathbf{x}$ is equivalent to $\bar{A}\bar{\mathbf{x}}$.

Proof: Because $A\mathbf{x} = (A_r + jA_i)(\mathbf{x}_r + j\mathbf{x}_i) = A_r\mathbf{x}_r - A_i\mathbf{x}_i + j(A_r\mathbf{x}_i + A_i\mathbf{x}_r)$ and $\bar{A}\bar{\mathbf{x}} = \begin{bmatrix} A_r\mathbf{x}_r - A_i\mathbf{x}_i \\ A_i\mathbf{x}_r + A_r\mathbf{x}_i \end{bmatrix}$, so the lemma holds.

Lemma 2: The product of complex vectors $A = A_r + jA_i$ and $B = B_r + jB_i$ is equivalent to $\bar{A}\bar{B}$.

Lemma 3: $(A_r + jA_i)^H$ is equivalent to $\bar{A}^T$.

Lemma 4: The inverse of a block matrix $\begin{bmatrix} A & B \\ C & D \end{bmatrix}$ is expressed as

$$\begin{bmatrix} A & B \\ C & D \end{bmatrix}^{-1} = \begin{bmatrix} (A - BD^{-1}C)^{-1}, & -A^{-1}B(D - CA^{-1}B)^{-1} \\ -D^{-1}C(A - BD^{-1}C)^{-1}, & (D - CA^{-1}B)^{-1} \end{bmatrix} \tag{4.10}$$

where we assume that the inverses exist.

Lemma 5: The inverse of $\begin{bmatrix} C & -D \\ D & C \end{bmatrix}$ can be expressed as

$$\begin{bmatrix} C & -D \\ D & C \end{bmatrix}^{-1} = \begin{bmatrix} (C+DC^{-1}D)^{-1}, & C^{-1}D(C+DC^{-1}D)^{-1} \\ -C^{-1}D(C+DC^{-1}D)^{-1}, & (C+DC^{-1}D)^{-1} \end{bmatrix} \tag{4.11}$$

According to Lemma 4, it is easy to prove Lemma 5.

Lemma 6: The inverse of $C+jD$ is

$$(C+jD)^{-1} = (C+DC^{-1}D)^{-1} - jC^{-1}D(C+DC^{-1}D)^{-1}. \tag{4.12}$$

Proof: because $(C+jD)(C+jD)^{-1}(C+DC^{-1}D) = C+DC^{-1}D$, and

$$\begin{aligned} & (C+jD)((C+DC^{-1}D)^{-1} - jC^{-1}D(C+DC^{-1}D)^{-1})(C+DC^{-1}D) \\ = \;& (C+jD)(I-jC^{-1}D) \\ = \;& C+DC^{-1}D, \end{aligned}$$

so lemma 6 hold.

Lemma 7: $(C+jD)^{-1}$ is equivalent to $\begin{bmatrix} C & -D \\ D & C \end{bmatrix}^{-1}$

Theory: Let $\boldsymbol{\Psi}$, $\mathbf{s}$ and $\boldsymbol{\alpha}$ be complex matrix and vectors, $\bar{\boldsymbol{\Psi}}$, $\bar{\mathbf{s}}$ and $\bar{\boldsymbol{\alpha}}$ be the extended equivalent real matrix and vectors. Then $\boldsymbol{\alpha}+\boldsymbol{\Psi}^H(\boldsymbol{\Psi}\boldsymbol{\Psi}^H)^{-1}(\mathbf{s}-\boldsymbol{\Psi}\boldsymbol{\alpha})$ is equivalent to $\bar{\boldsymbol{\alpha}}+\bar{\boldsymbol{\Psi}}^T(\bar{\boldsymbol{\Psi}}\bar{\boldsymbol{\Psi}}^T)^{-1}(\bar{\mathbf{s}}-\bar{\boldsymbol{\Psi}}\bar{\boldsymbol{\alpha}})$. This means that the $\ell_1\,\ell_0$ algorithms for real block signal with block size of 2 and no-block complex signal are equivalent.

Proof: According to *Lemma 1*, $\mathbf{s}-\boldsymbol{\Psi}\boldsymbol{\alpha}$ is equivalent to $\bar{\mathbf{s}}-\bar{\boldsymbol{\Psi}}\bar{\boldsymbol{\alpha}}$. According to *Lemma 3* and *Lemma 2*, $\boldsymbol{\Psi}^H$ is equivalent to $\bar{\boldsymbol{\Psi}}^T$ and $\boldsymbol{\Psi}\boldsymbol{\Psi}^H$ is equivalent $\bar{\boldsymbol{\Psi}}\bar{\boldsymbol{\Psi}}^T$.

According to *Lemma 7*, $(\boldsymbol{\Psi}\boldsymbol{\Psi}^H)^{-1}$ is equivalent to $(\bar{\boldsymbol{\Psi}}\bar{\boldsymbol{\Psi}}^T)^{-1}$. So we have that $\boldsymbol{\alpha} + \boldsymbol{\Psi}^H(\boldsymbol{\Psi}\boldsymbol{\Psi}^H)^{-1}(\mathbf{s} - \boldsymbol{\Psi}\boldsymbol{\alpha})$ is equivalent to $\bar{\boldsymbol{\alpha}} + \bar{\boldsymbol{\Psi}}^H(\bar{\boldsymbol{\Psi}}\bar{\boldsymbol{\Psi}}^H)^{-1}(\bar{\mathbf{s}} - \bar{\boldsymbol{\Psi}}\bar{\boldsymbol{\alpha}})$. In addition to the real and complex version of steps a) and b) in the algorithm being equivalent, we have shown that the algorithm of real version with block size of 2 and complex version are equivalent.

For block sparse signal, no matter the block size is fixed or irregular, denote $\{\alpha_{i,j}\}$ the block signal, where i expresses block index, j expresses the element index in each block, we can define the smoothed ℓ_0 norm as $G_\sigma(\boldsymbol{\alpha}) = \sum_i \left(1 - exp\left(-\frac{\sqrt{\sum_j \alpha_{i,j}^2}}{\sigma}\right)\right)$. Block ℓ_0 norm ℓ_1 norm homotopy method can be built easily.

4.3 Comparison with Iterative Shrinkage Threshold Method

Iterative shrinkage threshold (IST) method is a kind of sparse signal recovery algorithms. The general procedure can be expressed as [66]

$$\boldsymbol{\alpha}_{i+1} = \eta_{t_i}(\boldsymbol{\alpha}_i + \kappa\boldsymbol{\Psi}^H\mathbf{r}_i); \quad \mathbf{r}_i = \mathbf{s} - \boldsymbol{\Psi}\boldsymbol{\alpha}_i. \tag{4.13}$$

Here κ is a relaxation parameter ($0 < \kappa < 1$), η_{t_i} denotes a scalar nonlinearity shrinkage operator; for soft thresholding $\eta_t^S(\alpha) = sign(\alpha)(|\alpha| - t)_+$. The selection of K maximum value elements in OMP and CoSaMp algorithms can be regarded as a special shrinkage operation. The $\ell_1\,\ell_0$ algorithm can also be regarded as a special form of IST method, where the $\boldsymbol{\Psi}^H\mathbf{r}_i$ in iterative shrinkage method is replaced by $\boldsymbol{\Psi}^H(\boldsymbol{\Psi}\boldsymbol{\Psi}^H)^{-1}\mathbf{r}_i$ in $\ell_1\,\ell_0$ algorithm. The increased computation to compute $(\boldsymbol{\Psi}\boldsymbol{\Psi}^H)^{-1}\mathbf{r}_i$ is only $O(M^2)$, but $\boldsymbol{\alpha}_{i+1} = \boldsymbol{\alpha}_i + \boldsymbol{\Psi}^H(\boldsymbol{\Psi}\boldsymbol{\Psi}^H)^{-1}\mathbf{r}_i$ satisfies $\boldsymbol{\Psi}\boldsymbol{\alpha}_{i+1} = \mathbf{s}$, however $\boldsymbol{\alpha}_i + \kappa\boldsymbol{\Psi}^H\mathbf{r}_i$ can only be regarded as one step

of steepest descend method to obtain the solution of $\mathbf{\Psi}\boldsymbol{\alpha}_{i+1} = \mathbf{s}$. The step $\alpha(n) \leftarrow \alpha(n) - \frac{\alpha(n)}{|\alpha(n)|} \times min(|\alpha(n)|, |\mu\sigma\delta(n)|)$ in $\ell_1\,\ell_0$ algorithm is a shrinkage operation (For real case, $\frac{\alpha(n)}{|\alpha(n)|} \times min(|\alpha(n)|, |\mu\sigma\delta(n)|)$ has the same sign with $\alpha(n)$ but with absolute value not larger than $|\alpha(n)|$; for complex case, $\frac{\alpha(n)}{|\alpha(n)|} \times min(|\alpha(n)|, |\mu\sigma\delta(n)|)$ has the same phase with $\alpha(n)$ but with absolute value not larger than $\alpha(n)$). The function of $\eta_t^S(\alpha)$, shrinkage in CoSaMp (OMP) and shrinkage in $\ell_1\,\ell_0$ are expressed in Fig.4.3. In $\eta_t^S(\alpha)$, the threshold t is chosen as 1. For CoSaMp (OMP), we assume that the K largest elements are larger than 1. For $\ell_1\,\ell_0$, two σ cases are shown. We assume the maximum value of the signal is 3. In Fig.4.3(c), $\sigma = 2$, $\mu = \sigma/2$. In Fig.4.3(d), $\sigma = 1$, $\mu = \sigma/2$. The solid curves express the quantity after shrinkage, while the dash curves express original quantity. It can be seen that the shrinkage quantities of $\ell_1\,\ell_0$ method are different for different α, at the same time with the decrease of σ, the shrinkage quantity decrease. With the proceeding of the iterations, if the estimate solution converges to the true solution, the shrinkage quantity should be decreased. It can be seen that the shrinkage character of $\ell_1\,\ell_0$ method fits the above heuristic requirement.

4.4 Robust Implementation

In real cases, the matrix $\mathbf{\Psi}\mathbf{\Psi}^H$ may be ill conditioned although its inverse does exist in theory. The condition number of $\mathbf{\Psi}\mathbf{\Psi}^H$ can be as high as over 10^{18}. So finding of $(\mathbf{\Psi}\mathbf{\Psi}^H)^{-1}$ directly will lead to no-convergence.

There are two methods to solve the ill condition problem. One is diagonal loading method and another is singular value decomposition method. For diagonal loading, a diagonal matrix $\rho\mathbf{I}$ is added to $\mathbf{\Psi}\mathbf{\Psi}^H$, and $(\mathbf{\Psi}\mathbf{\Psi}^H)^{-1}$ is replaced by $(\mathbf{\Psi}\mathbf{\Psi}^H + \rho\mathbf{I})^{-1}$. It is known that the larger the ρ, the more robust

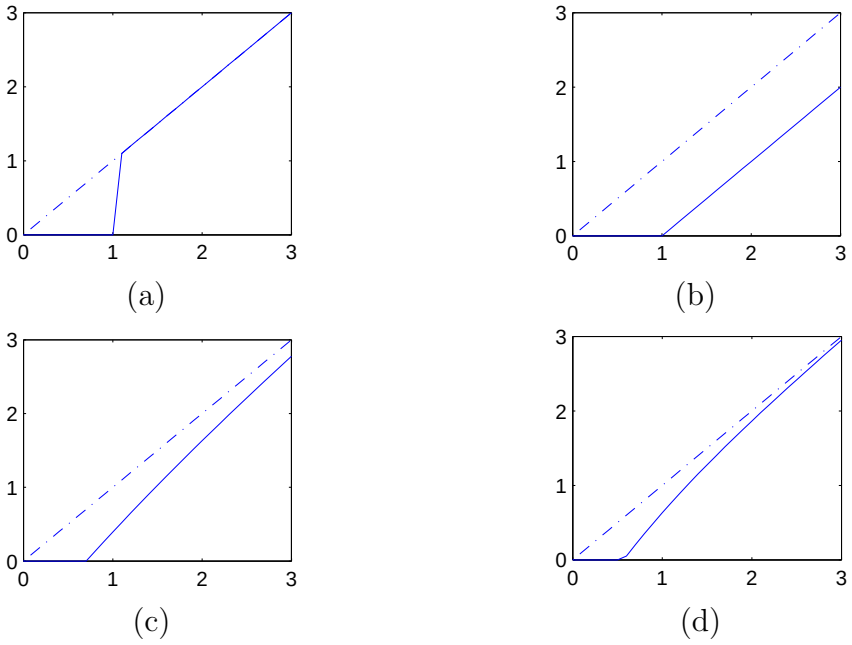

Figure 4.3: Shrinkage function for (a)CoSaMp, (b) Soft shrinkage ($t^* = 1$), (c) $\ell_1\,\ell_0$ ($\sigma = 2$, $\mu = \sigma/2$), (d) $\ell_1\,\ell_0$ ($\sigma = 1$, $\mu = \sigma/2$).

the algorithm, but the solution of the "modified" system also deviates further from the true solution. There is no good answer on how to choose the value of ρ. One suggested way is to compute the largest eigenvalue λ_1 of $\mathbf{\Psi}\mathbf{\Psi}^H$ and then to choose $\lambda_1 \times 10^{-4} < \rho < \lambda_1 \times 10^{-3}$.

Singular value decomposition is another method to improve the robustness of the original algorithm. Denote $\mathbf{\Psi} = \mathbf{UDV}$, where $\mathbf{U}$, $\mathbf{V}$ and $\mathbf{D}$ are the left singular matrix, the right singular matrix and the singular values matrix of $\mathbf{\Psi}$. Denote $\mathbf{U} = (\mathbf{U}_1\,\mathbf{U}_2)$, $\mathbf{D} = \begin{pmatrix} \mathbf{D}_1 & 0 & 0 \\ 0 & \mathbf{D}_2 & 0 \end{pmatrix}$ and $\mathbf{V} = \begin{pmatrix} \mathbf{V}_1 \\ \mathbf{V}_2 \end{pmatrix}$, where $\mathbf{D}_1$ includes the larger singular values, $\mathbf{D}_2$ includes the smaller singular values, $\mathbf{U}_1$ and $\mathbf{V}_1$ correspond to the larger singular values. Denote $\mathbf{\Psi}_1 = \mathbf{U}_1\mathbf{D}_1\mathbf{V}_1$, then the new robust algorithm is to replace $(\mathbf{\Psi}\mathbf{\Psi}^H)^{-1}$ with $\mathbf{U}_1\mathbf{D}_1^{-2}\mathbf{U}_1^H$.

We analyze the SVD-based algorithm below. In the SVD-based algorithm, the initial estimate of $\boldsymbol{\alpha}$ is

$$\begin{aligned}
\hat{\boldsymbol{\alpha}}_0 &= \boldsymbol{\Psi}^H(\mathbf{U}_1\mathbf{D}_1^{-2}\mathbf{U}_1^H)\mathbf{s} \\
&= (\mathbf{V}_1^H\mathbf{V}_2^H)\begin{pmatrix}\mathbf{D}_1 & 0\\ 0 & \mathbf{D}_2\\ 0 & 0\end{pmatrix}\begin{pmatrix}\mathbf{U}_1^H\\ \mathbf{U}_2^H\end{pmatrix}(\mathbf{U}_1\mathbf{D}_1^{-2}\mathbf{U}_1^H)\mathbf{s} \\
&= (\mathbf{V}_1^H\mathbf{V}_2^H)\begin{pmatrix}\mathbf{D}_1^{-1}\\ 0\end{pmatrix}\mathbf{U}_1^H\mathbf{s} \\
&= \mathbf{V}_1^H\mathbf{D}_1^{-1}\mathbf{U}_1^H\mathbf{s}.
\end{aligned} \tag{4.14}$$

We have

$$\begin{aligned}
\boldsymbol{\Psi}\hat{\boldsymbol{\alpha}}_0 &= (\mathbf{U}_1\mathbf{U}_2)\begin{pmatrix}\mathbf{D}_1 & 0 & 0\\ 0 & \mathbf{D}_2 & 0\end{pmatrix}\begin{pmatrix}\mathbf{V}_1\\ \mathbf{V}_2\end{pmatrix}\mathbf{V}_1^H\mathbf{D}_1^{-1}\mathbf{U}_1^H\mathbf{s} \\
&= \mathbf{U}_1\mathbf{U}_1^H\mathbf{s},
\end{aligned} \tag{4.15}$$

and

$$\boldsymbol{\Psi}_1\hat{\boldsymbol{\alpha}}_0 = \mathbf{U}_1\mathbf{D}_1\mathbf{V}_1\mathbf{V}_1^H\mathbf{D}_1^{-1}\mathbf{U}_1^H\mathbf{s} = \mathbf{U}_1\mathbf{U}_1^H\mathbf{s}, \tag{4.16}$$

which means that $\hat{\boldsymbol{\alpha}}_0$ is one solution of $\mathbf{s}_0 = \boldsymbol{\Psi}_1\boldsymbol{\alpha}$, where $\mathbf{s}_0 = \mathbf{U}_1\mathbf{U}_1^H\mathbf{s}$ is the projection of $\mathbf{s}$ on the span of $\mathbf{U}_1$.

Now we prove that the new projection $\boldsymbol{\alpha} \leftarrow \boldsymbol{\alpha} + \boldsymbol{\Psi}^H(\mathbf{U}_1\mathbf{D}_1^{-2}\mathbf{U}_1^H)(\mathbf{s} - \boldsymbol{\Psi}\boldsymbol{\alpha})$ projects $\boldsymbol{\alpha}$ in the revised feasible set $\{\boldsymbol{\alpha} : \boldsymbol{\Psi}_1\boldsymbol{\alpha} = \mathbf{s}_0\}$. Denote $\boldsymbol{\beta} = \boldsymbol{\alpha} + \boldsymbol{\Psi}^H(\mathbf{U}_1\mathbf{D}_1^{-2}\mathbf{U}_1^H)(\mathbf{s} - \boldsymbol{\Psi}\boldsymbol{\alpha})$. Because

$$\begin{aligned}
&\boldsymbol{\Psi}_1\boldsymbol{\Psi}^H(\mathbf{U}_1\mathbf{D}_1^{-2}\mathbf{U}_1^H) \\
= \;& \mathbf{U}_1\mathbf{D}_1\mathbf{V}_1(\mathbf{V}_1^H, \mathbf{V}_2^H)\begin{pmatrix}\mathbf{D}_1 & \\ & \mathbf{D}_2\\ 0 & 0\end{pmatrix}\begin{pmatrix}\mathbf{U}_1^H\\ \mathbf{U}_2^H\end{pmatrix}(\mathbf{U}_1\mathbf{D}_1^{-2}\mathbf{U}_1^H) \\
= \;& \mathbf{U}_1\mathbf{U}_1^H,
\end{aligned} \tag{4.17}$$

we have

$$\begin{aligned} & \boldsymbol{\Psi}_1\boldsymbol{\beta} \qquad (4.18)\\ = \; & \boldsymbol{\Psi}_1\boldsymbol{\alpha} - \mathbf{U}_1\mathbf{U}_1^H(\mathbf{U}_1,\mathbf{U}_2)\begin{pmatrix} \mathbf{D}_1 & 0 & 0 \\ 0 & \mathbf{D}_2 & 0 \end{pmatrix}\begin{pmatrix} \mathbf{V}_1 \\ \mathbf{V}_2 \end{pmatrix}\boldsymbol{\alpha} + \mathbf{U}_1\mathbf{U}_1^H\mathbf{s} \\ = \; & \boldsymbol{\Psi}_1\boldsymbol{\alpha} - \mathbf{U}_1\mathbf{D}_1\mathbf{V}_1\boldsymbol{\alpha} + \mathbf{s}_0 \\ = \; & \mathbf{s}_0. \end{aligned}$$

4.5 Simulation Results

4.5.1 Simulation 1: One Dimensional General Sparse Random Spikes Signals

In the first experiment, we compare $\ell_1\,\ell_0$ homotopy algorithm with OMP, smoothed ℓ_0 norm based method, Bayesian compressive sensing using Laplace prior, CoSaMp, ℓ_1-magic and ℓ_1-ℓ_s algorithms. The signal model is $\mathbf{s} = \boldsymbol{\Psi}\boldsymbol{\alpha}_0 + \mathbf{n}$. The dimension $(M \times N)$ of $\boldsymbol{\Psi}$ is 100×200. Each elements of $\boldsymbol{\Psi}$ is Gaussian distributed. The norm of each column of $\boldsymbol{\Psi}$ is normalized to 1. $\boldsymbol{\alpha}_0$ is a sparse signal, whose nonzero coefficients are uniform ± 1 random spikes signal (Because ℓ_1 magic and ℓ_1-ℓ_s program can only process real signal, in order to compare with them, real signal is used). The sparsity $p = K/M$, where K is the nonzero coefficient number of $\boldsymbol{\alpha}_0$, are from 0.1 to 0.4. $\mathbf{n}$ is independent Gaussian random vector with standard variance σ_n. The SNR is defined as $20log_{10}(1/\sigma_n)$. Four SNR cases (SNR=20, 25, 30, 35dB) are implemented. For OMP, Bayesian, ℓ_1-ℓ_s, ℓ_1-magic and CoSaMp methods, the simulation programs are downloaded from http://www.see.ed.ac.uk/tblumens/sparsify/, http://ivpl.eecs.northwestern.edu, http:// www.stanford.edu/boyd /l1-ls, http: // users. ece. gatech.edu/ justin/l1magic/ and http:// www. mathworks. com /matlabcentral/ fileexchange/32402- cosamp- and- omp- for- sparse- recovery/content/ CoSaMP.m, respectively. To evaluate the estimation quality, the mean absolute error (MAE) is used. The MAE is defined as $\frac{1}{N}||\boldsymbol{\alpha}_0 - \hat{\boldsymbol{\alpha}}||_1$,

where $\boldsymbol{\alpha}_0$ is the true solution and $\hat{\boldsymbol{\alpha}}$ is the estimate. This MAE computes the average error for every element. Another evaluation criterion is correct position estimation frequency, because after the positions of the nonzero components are known, the amplitudes of the nonzero components can be estimated by minimum least square criterion. So, after $\hat{\boldsymbol{\alpha}}$ has been obtained, triple-value decision will be made (if $\hat{\boldsymbol{\alpha}}(m) < -0.5$, let $\tilde{\boldsymbol{\alpha}}(m) = -1$, if $\hat{\boldsymbol{\alpha}}(m) > 0.5$, let $\tilde{\boldsymbol{\alpha}}(m) = +1$, else, let $\tilde{\boldsymbol{\alpha}}(m) = 0$). If $\boldsymbol{\alpha}_0 = \tilde{\boldsymbol{\alpha}}$, we say that the position estimation is correct, otherwise, it is not correct. For ℓ_1-ℓ_s method, $\min_{\boldsymbol{\alpha}} ||\boldsymbol{\Psi}\boldsymbol{\alpha} - \mathbf{s}||^2 + \lambda||\mathbf{s}||_1$ is solved. For situations of (SNR=20dB, $p = 0.15$), (SNR=25dB, $p = 0.275$), (SNR=30dB, $p = 0.35$) and (SNR=35dB, $p = 0.35$), optimal λ is computed by taking minimum MAE, then this obtained λ is applied to other sparsity p cases. The reason we choose $p = 0.15(0.275, 0.35)$ is that the correction rate is about 0.8 to 0.9 (if we choose a small correction rate, the "optimal" result may be meaningless). For CoSaMp method [49], we assume that the sparsity parameter K is known; the optimal "addK" parameter (the number of new entries to add each time) for minimum MAE for different SNR and "K" are shown in TABLE 4.1. For smoothed ℓ_0 method, $J = 25$, $L = 40$ and $\varepsilon = \sqrt{0.8M}\sigma_n$, $\sigma_J = E(max(|\boldsymbol{\Psi}^{\dagger}\mathbf{n}|))/\sqrt{2}$. For $\ell_1\,\ell_0$, $J = 25$, $L = 40$, $L_0 = 25$, $L_1 = 8$ and $\varepsilon = \sqrt{0.8M}\sigma_n$, $\sigma_J = E(max(|\boldsymbol{\Psi}^{\dagger}\mathbf{n}|))$. The experiment was repeated 500 times (with the same parameters, but for different randomly generated sources and coefficient matrices), the computation times, values of MAE and correct position estimation frequencies are averaged. Fig.4.4 shows the average computation times using different methods for 20dB SNR case. For other SNR cases, the computation times are similar to this case and are not shown. From this figure, we can see that the computation costs of OMP, CoSaMp, smoothed ℓ_0 norm based method and $\ell_1\,\ell_0$ are less than Bayesian with Laplace prior, ℓ_1-magic and ℓ_1-ℓ_s methods. The MAEs

Table 4.1: The optimal addK parameter in CoSaMp algorithm of simulation one

SNR	K=10	13	15	18	20	23	25	28	30	33
20dB	1	4	10	20	35	32	61	59	58	31
25dB	1	1	1	17	24	60	63	63	63	59
30dB	1	1	1	10	23	63	64	64	63	59
35dB	1	1	1	15	14	59	64	64	63	60

and correct position estimation frequencies for different methods, different p and different SNRs are shown in Fig.4.5 and Fig.4.6. We can see that with the increase of SNR, the performance of ℓ_1-ℓ_s and ℓ_1-magic methods improve faster than OMP, CoSaMp, smoothed ℓ_0 and Bayesian methods. CoSaMp method has good performance when p is small especially when SNR is low. The original CoSaMp program limits $p < \frac{1}{3}$, so $p > \frac{1}{3}$ cases are not shown. The performance of $\ell_1\,\ell_0$ method is competitive with other methods especially when SNR is high and p is large.

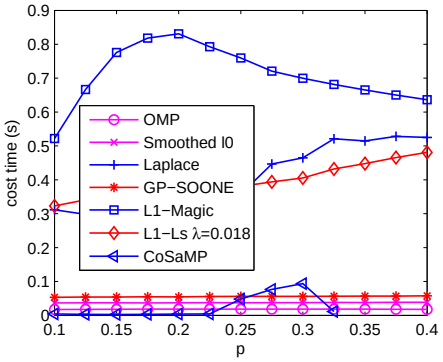

Figure 4.4: Computation costs of different methods.

4.5.2 Simulation 2: Comparison of Real Version and Complex Version $\ell_1\,\ell_0$ Algorithms

For a complex linear system, compared with real version algorithm, because the direct complex version ℓ_1 algorithm utilizes the block property of the signal,

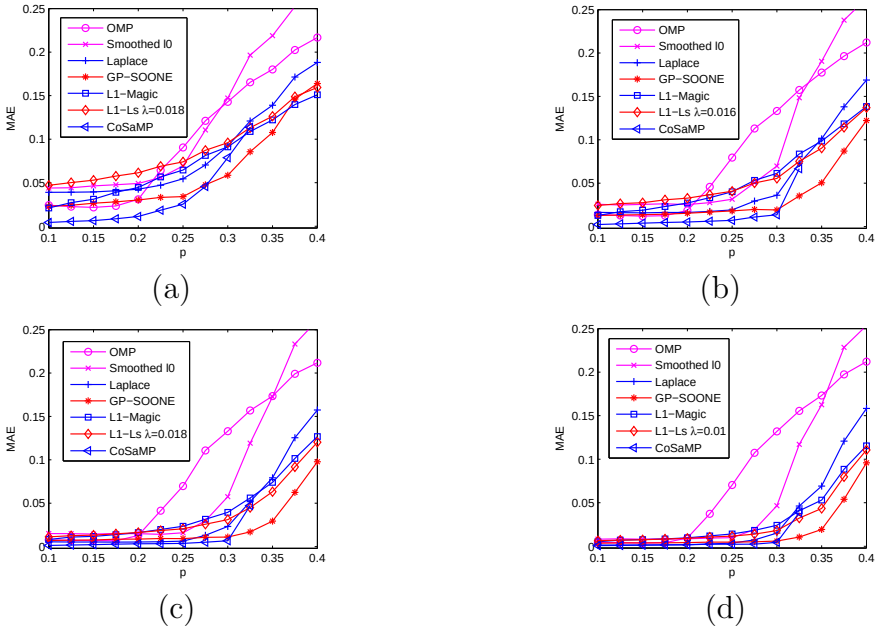

Figure 4.5: Minimum mean absolute value errors for different methods, different $p = K/M$ and different SNRs, (a) SNR=20dB, (b) SNR=25dB, (c) SNR=30dB, (d) SNR=35dB (simulation 1) .

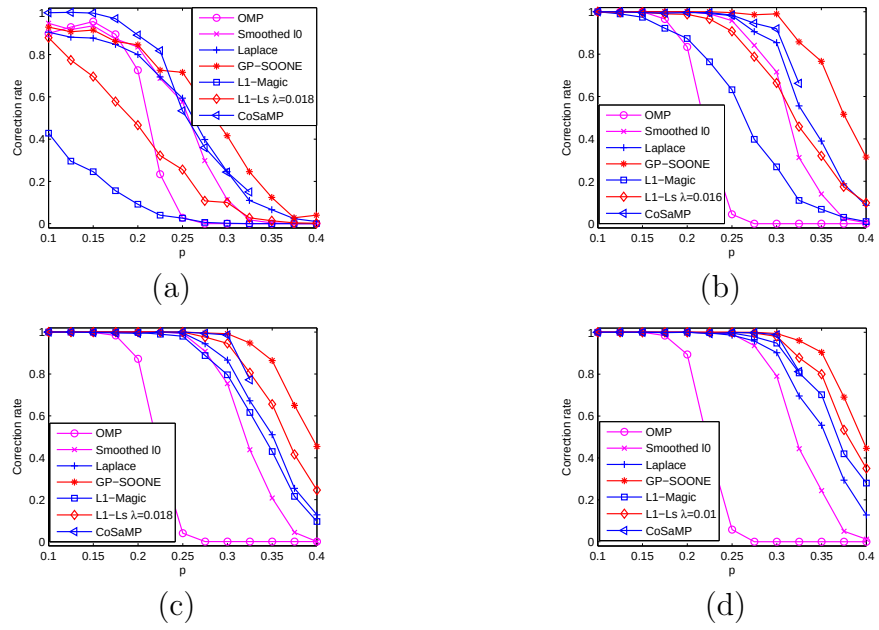

Figure 4.6: Correct position estimation frequencies for different methods, different $p = K/M$ and different SNRs, (a) SNR=20dB, (b) SNR=25dB, (c) SNR=30dB, (d) SNR=35dB (simulation 1).

it could have superior performance to real version algorithm. This simulation verifies this deduction.

The signal model is $\mathbf{s} = \mathbf{\Psi}\boldsymbol{\alpha}_0 + \mathbf{n}$. The dimension of $\mathbf{\Psi}$ $(M \times N)$ is 100×200. Each element of $\mathbf{\Psi}$ is complex Gaussian distributed and the norm of each column of $\mathbf{\Psi}$ is normalized to 1. The sparse signal $\boldsymbol{\alpha}_0$ is a complex random spike signal, where the real and imaginary parts of non-zero elements are 1 or -1 randomly. $\mathbf{n}$ is independent complex Gaussian random vector, and it's real and imaginary parts have standard variance σ_n. Four SNR cases (SNR=20dB, 25dB, 30dB and 35dB) are considered. The sparsity p takes values from 0.1 to 0.4 with step size of 0.025. For each p and SNR, 1000 times experiments are implemented. The parameters in the algorithm are chosen as $\varepsilon = \sqrt{M2\sigma^2 \times 1.3}$, outer loop and inner loop iteration times J and L are all chosen as 25, $L1 = L0 = 20$, σ_J is the maximum value of $\mathbf{\Psi}^{\dagger}\mathbf{n}$ for 100 times tests. The simulation results are shown in Fig.4.7 and Fig.4.8. It can be seen that the complex version algorithm is better than the real version algorithm.

4.5.3 Simulation 3: Recovery of One Dimensional Random Regular Block Sparse Spikes Signals

In this experiment, we compare $\ell_1\,\ell_0$ block sparse signal recovery algorithm (called BL1L0) with Block OMP (BOMP), Block CoSaMp (BCoSaMp) and block smoothed ℓ_0 norm method (called BSL0). The signal model is $\mathbf{s} = \mathbf{\Psi}\boldsymbol{\alpha}_0 + \mathbf{n}$, where all variables are real numbers. The dimension of $\mathbf{\Psi}$ is 80×160. Each elements of $\mathbf{\Psi}$ is Gaussian distributed and the norm of each column of $\mathbf{\Psi}$ is normalized to 1. $\boldsymbol{\alpha}_0$ is a block sparse signal with block size of 8, whose nonzero block coefficients are uniform ± 1 random spikes signal (the size of matrix and block are the same as [67]). $\mathbf{n}$ is independent Gaussian random vector with standard variance σ_n. The number of blocks is from 4 to 9. Four

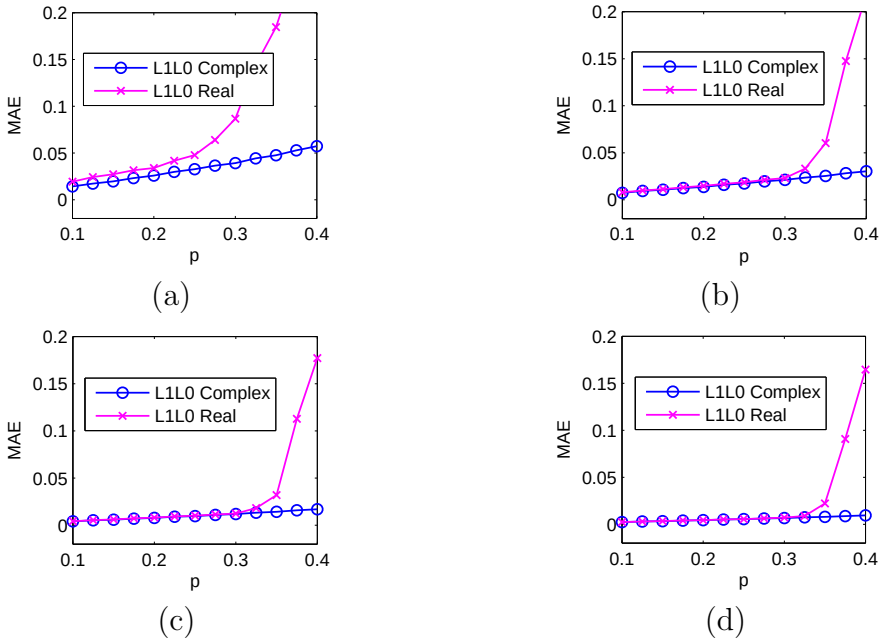

Figure 4.7: Minimum mean absolute value errors for different SNRs and p for real version and complex version $\ell_1\,\ell_0$ algorithms, (a) SNR=20dB, (b) SNR=25dB, (c) SNR=30dB, (d) SNR=35dB (simulation 2).

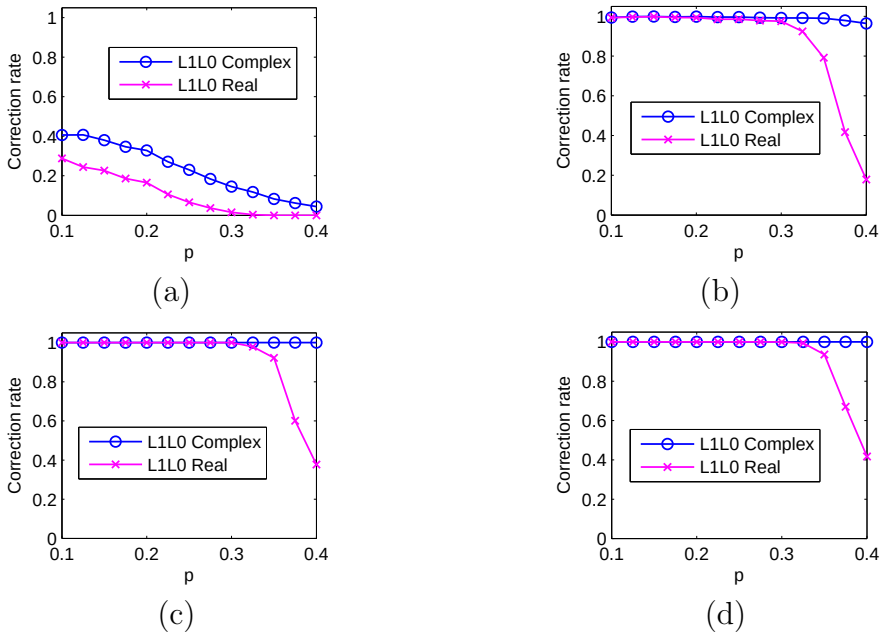

Figure 4.8: Correct position estimation frequencies for different SNRs for real version and complex version $\ell_1\,\ell_0$ algorithms, (a) SNR=20dB, (b) SNR=25dB, (c) SNR=30dB, (d) SNR=35dB (simulation 2).

SNR cases (SNR=20dB, 30dB, 40dB, 100dB) are implemented. For BOMP, and Block CoSaMp methods, the simulation programs are downloaded from http://www.codebus.net/d-E05O.html and http://dsp.rice.edu/software/model-based-compressive-sensing-toolbox-v11, respectively. For block smoothed ℓ_0 norm method and block $\ell_1\,\ell_0$ method, $J = 25$, $L = 20$, $L_0 = 20$, $L_1 = 20$, $\varepsilon = \sqrt{0.8M}\sigma_n$ and $\sigma_J = 0.1$. The oracle results, that the supports of the block sparse signals are known, are also computed. The experiment was repeated 1000 times, the computation times, values of MAE and correct position estimation frequencies are averaged. Fig.4.9 shows the average computation times using different methods for 20dB SNR case. For other SNR cases, the computation times are similar to this case and are not shown. We can see that the BCoSaMp method has the highest computation requirement, while BOMP method requires the least computation. For ISAR applications, the data size has the same quantity order as $\mathbf{\Psi}$ in this subchapter. The computation load of CS methods is not heavy. The MAEs and correct position estimation frequencies for different methods, different block sparsity and different SNRs are shown in Fig.4.10 and Fig.4.11. The performance from high to low are BL1L0, BSL0, BCoSaMp and BOMP respectively. With the increase of SNR, the performance of BL1L0 approaches the Oracle case.

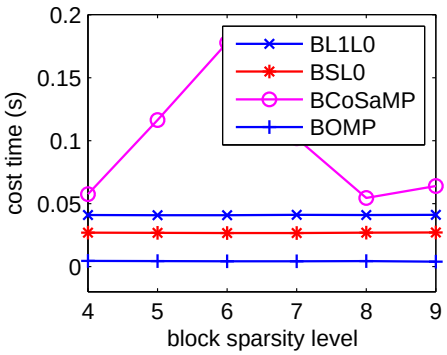

Figure 4.9: Computation costs of different methods (simulation 3).

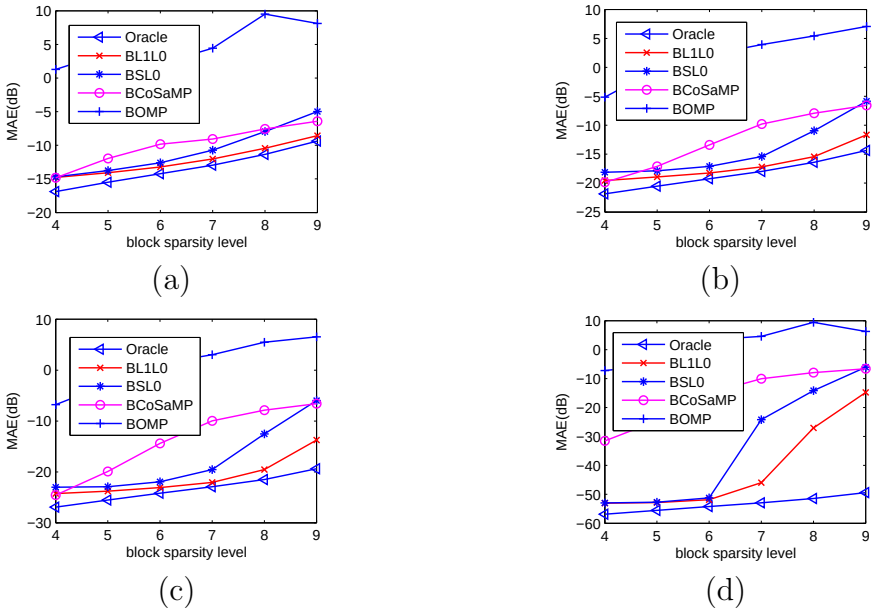

Figure 4.10: Minimum mean absolute value errors for different methods, different block sparsity and different SNRs, (a) SNR=20dB, (b) SNR=30dB, (c) SNR=40dB, (d) SNR=100dB (simulation 3).

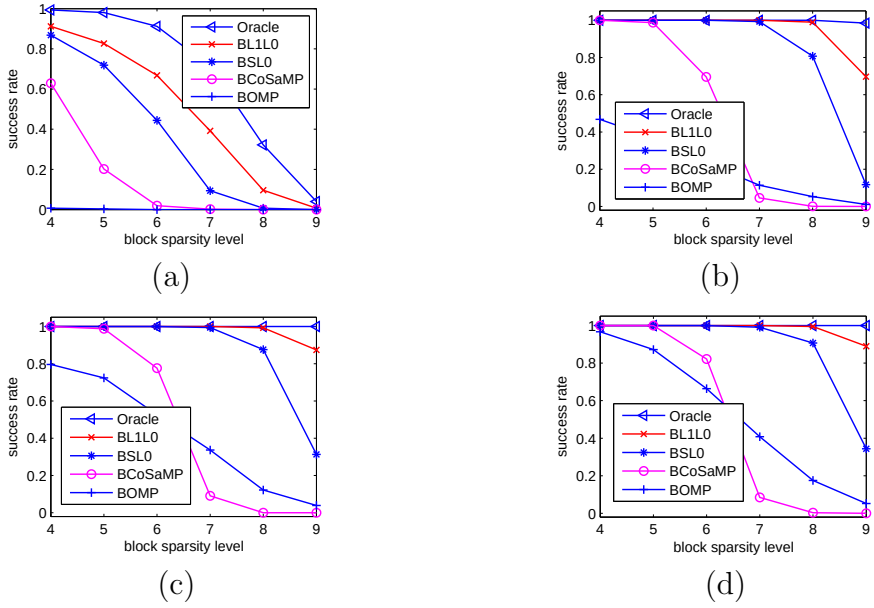

Figure 4.11: Correct position estimation frequencies for different methods, different block sparsity and different SNRs, (a) SNR=20dB, (b) SNR=30dB, (c) SNR=40dB, (d) SNR=100dB (simulation 3).

4.6 Conclusion

A new sequential order one negative exponential function which can describe the sparsity is proposed. Steepest descent gradient projection method is widely used in finding minimum point of optimization problem. It is faster than some popular sparse signal recovery algorithms. Similar to smoothed ℓ_0 method, a complex domain ℓ_1 ℓ_0 norms homotopy method using sequential order one negative exponential function as cost function was proposed. It has been proven that this complex domain algorithm is equivalent to a real domain block size of 2 algorithm, so its performance is better than non-block real domain algorithm. This ℓ_1 norm ℓ_0 norm homotopy method has been extended to block sparse signal case easily. From the simulation results, it can be seen that the performance of block ℓ_1 norm ℓ_0 norm homotopy method is better than block OMP, block CoSaMp and block smoothed ℓ_0 norm method.

In real applications, the coefficient matrix may be ill conditioned. Conventional ℓ_1-magic and smoothed ℓ_0 norm methods have not considered this problem. By employing either singular value decomposition and choosing the signal subspace corresponds to the larger singular values; or diagonal loading with the algorithm revised in this Chapter, the algorithm is more robust compared with the traditional algorithm.

Chapter 5

MIMO Radar Imaging Based on $\ell_1\,\ell_0$ Norms Homotopy Sparse Signal Recovery Algorithm

5.1 Introduction

In Chapter 2 and Chapter 3, collocated MIMO radar 3D imaging using conventional method was discussed. Due to non-orthogonality of the codes, high sidelobes are shown. Using time domain information can only suppress sidelobes in one direction. In Chapter 4, sparse signal recovery algorithms were discussed and a $\ell_1\,\ell_0$ homotopy algorithm was proposed. By using sparse signal recovery algorithms, sparse signal can be recovered with good performance. Fortunately, the strong scatterers of air targets are usually sparse. So in this Chapter, MIMO radar 3D imaging using sparse signal recovery algorithms are discussed.

MIMO radar includes both collocated MIMO radar and distributed MIMO radar. In section 5.2, collocated MIMO radar 3D imaging is discussed. Some targets may have large flat surfaces facing the radar. The area of these flat surfaces may be larger than a few sampling units (the imaging volume is divided as sampling units). In this case, a single "strong" scattered signal

from the entire flat surface could be considered as equivalent to be coming from a block of many scatterers each from a "sampling unit" on the surface. Then the scatterers forming a flat surface could be classified as block scatterers with similar amplitudes and the gradient of the reflectivity has high values at the edge of the surface. Total-variation (TV) (the sum of gradient) is usually used in 2D image processing (image de-noising, image de-blurring and image reconstruction) without de-blurring edges [68] [69]. In this Chapter, we also use the sequential order one negative exponential function to define the TV function (conventional TV is based on ℓ_1 or ℓ_2 norm) and Combine the Amplitude and TV volumes as another optimization cost function (denoted as CATV) to process the block scatterers.

In order to express the collocated MIMO radar 3D imaging with linear equation as done in section 5.2, the dimension of the coefficient matrix is large, which needs huge memory. In section 5.3, we discuss multi-dimensional linear equation (matrix equation) expression, which needs less memory. $\ell_1\,\ell_0$ homotopy sparse signal recovery algorithm based on multi-dimensional linear equation expression is also obtained.

In subsection 5.4, distributed MIMO radar 3D imaging is discussed. For distributed MIMO radar, the distances between the transmit antennas and the distances between the receive antennas are comparable with the distance between the target and the radar, it is difficult to maintain the coherent property of one target (or one scatterer) relative to different transmitters and different receivers. That is because the RCSs of a target (or a scatterer) corresponding to different transmit-receiver pairs are different. So coherent processing algorithms cannot be used to combine distributed MIMO radar data. On the other hand, diversity of the different transmitter-receiver pairs can be used to improve target detection [13]. Distributed MIMO radar has been used for

moving target detection [70] and parameters estimation [71]. But radar imaging using distributed MIMO radar has not been discussed. In this Chapter, a distributed MIMO radar configuration is proposed: a cluster of transmit antennas and a cluster of receive antennas form collocated arrays. In this case the RCSs of a strong scatterer corresponding to one particular collocated array are the same and thus virtual aperture can be formed to separate the strong scatterers. Different clusters of antennas are distributed.

The characteristics of distributed MIMO array for target parameters estimation and for target imaging are different. The RCSs of a target corresponding to different transmitter-receiver pairs is called a RCS vector below. For target parameters (positions, Dopplers) estimation, the elements of an RCS vector are different (independent). When linear equation (describing the relation between the received signal and the RCS) is formed, the RCSs of a target corresponding to different transmitter-receiver pairs are packed together and the whole vector describing the whole distribution of RCS of the estimation area are block sparse. For target imaging, the strong scatterers occur at the reflection, the dehidral, the trihidral, etc., which are sparse compared with the whole imaging volume. The positions of strong scatterers are dependent on the relative position of the viewing antenna and the target. A strong scatterer corresponding to one viewing antenna may not be a strong scatterer corresponding to another viewing antenna (the RCS vector of one scatterer may be a sparse vector). So when linear equation is formed, though the RCSs of a scatterer corresponding to different transmitter-receiver pairs are packed together, the vector describing the whole distribution of RCSs of the imaging area are not block sparse. The function of distributed MIMO radar imaging is to form different images of one target from different views, and to synthesis an image with abundance shape information.

5.2 Collocated MIMO Radar 3D Imaging Using Linear Equation $\ell_1\,\ell_0$ Homotopy Algorithm

5.2.1 Collocated MIMO Radar Signal Model

In Chapter 2 and Chapter 3, MIMO radar signal model of single snapshot and multiple snapshots are given, where the signals corresponding to different transmitting codes are separated by correlating the received signal with the transmitting codes. Because it is impossible to build orthogonal codes, high sidelobes of the codes decrease the image quality. In this Chapter, the signals corresponding to different transmitters need not be separated firstly. A linear equation for the received signal and the scatterers' RCSs is built, then sparse signal recovery algorithms can be used to solve the RCSs.

Let P_m, Q_n denote the positions of the mth transmit antenna and the nth receive antenna respectively. Similar to Chapter 2 and Chapter 3, after demodulation, the received back-scattered signal at receive antenna n from scatterer A can be expressed as

$$\tilde{s}_n(t) = \alpha_A \sum_{m=0}^{M-1} \varphi_m(t - T_m - \tau_{P_mA} - \tau_{Q_nA}) \times exp(-j2\pi f(\tau_{P_mA} + \tau_{Q_nA})), \quad (5.1)$$

where $\tau_{P_mA} = |P_mA|/c$, $\tau_{Q_nA} = |Q_nA|/c$. T_m is the pre-transmitting time of the mth transmitting code.

Like in Chapter 2 and Chapter 3, after adjusting the transmit code en-

velopes and the recording time, the receive signal can be expressed as

$$\begin{aligned} s_n(t) &= \tilde{s}_n(t - T_n) \\ &= \alpha_A \sum_{m=0}^{M-1} \varphi_m(t - T_m - T_n - \tau_{P_m A} - \tau_{Q_n A}) \times exp(-j2\pi f(\tau_{P_m A} + \tau_{Q_n A})) \\ &= \alpha_A \sum_{m=0}^{M-1} \varphi_m(t - \tau_{P_0 A} - \tau_{Q_0 A}) \times exp(-j2\pi f(\tau_{P_m A} + \tau_{Q_n A})). \end{aligned} \tag{5.2}$$

The above equation can be rewritten as a simple matrix form:

$$\mathbf{s}(t) = \alpha_A \mathbf{a}\mathbf{b}^T \mathbf{\Phi}(t - \tau_A), \tag{5.3}$$

where $\tau_A = \tau_{P_0 A} + \tau_{Q_0 A}$, $\mathbf{s}(t) = [s_0(t), s_1(t), \cdots, s_{N-1}(t)]^T$, $\mathbf{a} = [e^{-j2\pi f \tau_{Q_0 A}}, e^{-j2\pi f \tau_{Q_1 A}}, ..., e^{-j2\pi f \tau_{Q_{N-1} A}}]^T$, $\mathbf{b} = [e^{-j2\pi f \tau_{P_0 A}}, e^{-j2\pi f \tau_{P_1 A}}, ..., e^{-j2\pi f \tau_{P_{M-1} A}}]^T$ and

$$\mathbf{\Phi}(t) = \begin{bmatrix} \varphi_0(t) \\ \vdots \\ \varphi_{M-1}(t) \end{bmatrix}. \tag{5.4}$$

After time domain discrete sampling, the received signal can be expressed as a matrix $\mathbf{S}$. Let $\mathbf{s} = \text{vec}(\mathbf{S})$, $\mathbf{a}_A = \text{vec}(\mathbf{a}\mathbf{b}^T \mathbf{\Phi}(t - \tau_A))$, we have $\mathbf{s} = \mathbf{a}_A \alpha_A$. The imaging areas are divided as grids. Basis matrix $\mathbf{\Psi} = [\mathbf{a}_A, \cdots]$ and scatterer amplitudes vector $\boldsymbol{\alpha} = [\alpha_A, \cdots]^T$ are formed for all grids. If a strong scatterer is located in a grid, the amplitude of signal back-scattered from that scatterer is not zero. The received discrete signal $\mathbf{s}$ can be expressed as

$$\mathbf{s} = \mathbf{\Psi}\boldsymbol{\alpha} + \mathbf{n}, \tag{5.5}$$

where $\mathbf{n}$ expresses noise and errors induced by discretization.

5.2.2 Imaging Based on ℓ_2 Norm Minimization

The aim of imaging is to obtain the $\boldsymbol{\alpha}$. Assume the size of $\boldsymbol{\Psi}$ is $M_1 \times N_1$. M_1 is about $N \times (P + \triangle)$, where $\triangle$ is the width of the delay of the target (we assume the fast time sampling period is the subpulse duration T_0), P is the code length, N is the number of receive antennas. N_1 is the number of discrete grid points in the imaging volume. If $M_1 < N_1$, (this may occurs when there are fine grids on the imaging field or super resolution), and the rank of $\boldsymbol{\Psi}$ is M_1, then there are infinite vectors $\boldsymbol{\alpha}$ that satisfy the equation $\mathbf{s} = \boldsymbol{\Psi}\boldsymbol{\alpha}$, where the noise term $\mathbf{n}$ is omitted. The image of the target can be obtained by solving the following optimization problem

$$\min ||\boldsymbol{\alpha}||_2 \quad s.t. \quad \mathbf{s} = \boldsymbol{\Psi}\boldsymbol{\alpha}. \tag{5.6}$$

The solution is

$$\hat{\boldsymbol{\alpha}} = \boldsymbol{\Psi}^{\dagger}\mathbf{s}, \tag{5.7}$$

where $\boldsymbol{\Psi}^{\dagger} = \boldsymbol{\Psi}^H(\boldsymbol{\Psi}\boldsymbol{\Psi}^H)^{-1}$ is the pseudo inverse of $\boldsymbol{\Psi}$ [41]. If $\boldsymbol{\Psi}^{\dagger}$ is replaced by $\boldsymbol{\Psi}^H$, it becomes to the conventional correlation method discussed in Chapter 2.

5.2.3 Imaging Based on Combined Amplitude and Total variation Sparse Signal Recovery Algorithm

According to (1.5), strong scatterers occur at $\hat{\mathbf{r}}\cdot\hat{\mathbf{n}} = -1$ for monostatic radar or monostatic collocated MIMO radar. Positions satisfying the above condition are sparse compared with the whole imaging volume. So the sparse signal recovery algorithm can be used to recover the image. The $\ell_1\,\ell_0$ homotopy

based method can be described as

$$\hat{\boldsymbol{\alpha}} = \lim_{\sigma \to \sigma_{min}} \arg\min G_\sigma(\boldsymbol{\alpha}) \quad s.t. \quad ||\mathbf{s} - \boldsymbol{\Psi}\boldsymbol{\alpha}||_2 < \varepsilon. \tag{5.8}$$

If a larger planer patch is oriented perpendicular to the radar, all positions on this patch satisfy $\hat{\mathbf{r}} \cdot \hat{\mathbf{n}} = -1$. If the sampling unit is much less than the area of this patch, this patch should be considered as composed of many point scatterers with equal amplitudes. If we just use minimization of norm of amplitude as conventional radar signal processing does, this property is not utilized to our advantage. The characteristic of large planer patch is that high gradient value occurs only on the edge of the patch. So, gradient values are also sparse. In image processing, total-variation is used to describe the sum of gradients. For expression simplicity, $\boldsymbol{\alpha}$ is also used to express a two dimensional image. Denote $D_{i,j}\boldsymbol{\alpha} = \begin{pmatrix} \alpha_{i+1,j} - \alpha_{i,j} \\ \alpha_{i,j+1} - \alpha_{i,j} \end{pmatrix}$, then the ℓ_2-based isotropic TV and ℓ_1-based anisotropic TV are defined as [68]

$$TV_{iso}(\boldsymbol{\alpha}) = \Sigma_i \Sigma_j \sqrt{(\alpha_{i+1,j} - \alpha_{i,j})^2 + (\alpha_{i,j+1} - \alpha_{i,j})^2}, \tag{5.9}$$

and

$$TV_{aniso}(\boldsymbol{\alpha}) = \Sigma_i \Sigma_j (|\alpha_{i+1,j} - \alpha_{i,j}| + |\alpha_{i,j+1} - \alpha_{i,j}|), \tag{5.10}$$

respectively.

According to our definition of $G_\sigma(\boldsymbol{\alpha})$, we can define a new total-variation as

$$TV_\sigma(\boldsymbol{\alpha}) = -\Sigma_i \Sigma_j (e^{-|\alpha_{i+1,j} - \alpha_{i,j}|/\sigma} + e^{-|\alpha_{i,j+1} - \alpha_{i,j}|/\sigma}). \tag{5.11}$$

Then (5.8) can be revised as

$$\begin{aligned} \hat{\boldsymbol{\alpha}} \;=\; & \lim_{\sigma \to \sigma_{min}} \arg\min\{(1-\zeta)G_\sigma(\boldsymbol{\alpha}) + \zeta TV_\sigma(\boldsymbol{\alpha})\} \\ & \text{subject to } ||\mathbf{s} - \boldsymbol{\Psi}\boldsymbol{\alpha}||_2 < \varepsilon, \end{aligned} \tag{5.12}$$

where ζ is a tradeoff factor. A bigger ζ emphasizes the edges, and a smaller ζ emphasizes the isolated scatterers. For radar imaging, because a broadside patch has the same range unit, $TV(\cdot)$ operator is done on same range unit data.

5.2.4 Linear Equation Based Simulation Results

In simulation 1, simulation 2 and simulation 3, the center frequency is $f_0 = 10\,G$ Hz. Random BPSK modulated codes with code length 100 are chosen as the transmitting codes. The bandwidth is 150M Hz, which corresponds to range resolution of 1 m.

Simulation 1: Two Dimensional Imaging of a Target with Scatterers on the Grid Points

In many publications, the scatterers are chosen as located on the grid points. In this case, there is no model error. In this simulation, we also assume that the scatterers are ideal, isolated and located on the grid points.

Eight transmit and eight receive antennas are evenly located on X axis with inter-element distances of 187.5 m and 23.4375 m, respectively. This means that we consider imaging in two-dimension. The target is located in $[0, 1]$ direction, the distance between the target and the radar is 50 km. The target is composed of 20 discrete point scatterers with amplitudes from 0.5 to 10. The amplitudes and positions of the original target is shown in Fig.5.1(a). The output SNR is defined as $SNR = 10log_{10}(\frac{\alpha^2 MNP}{\sigma_n^2})$, where P is the length of the code. The output SNR of the smallest scatterer is 30dB. According to the MIMO radar parameters, the range and cross-range resolutions at the target position using conventional method are all 1 m. In our imaging algorithm, the distance between sampling grid points at X and Y axes are all 0.25 m.

The scan range is $[-1, 21.75]$ m $\times$ $[-1, 21.75]$ m. So the dimensions of the complex coefficient matrix $\mathbf{\Psi}$ and real matrix $\mathbf{\Psi}_2$ are 984×8464 and 1968×16928 respectively. The condition number output of $\mathbf{\Psi}_2\mathbf{\Psi}_2^H$ using Matlab is infinite. Diagonal loading of $\rho = 100$ is used in methods needed to compute $(\mathbf{\Psi_2\Psi_2}^H)^{-1}$. For ℓ_1-ℓ_s method, cases of $\lambda = 1, 2, \cdots, 20$ are implemented. The performance for $\lambda = 10, 11, \cdots, 20$ are similar and better than that of $\lambda = 1, 2, \cdots, 9$. For CoSaMp method, non-zero element number K is chosen as $K = 16, 17, \cdots, 26$, $addK$ is chosen as K and $2K$. The best results occurs at $K = 20$ and $addK = K$. When a smaller K is chosen, weak scatterers may not be imaged. When a larger K is chosen, more sidelobes appear. For smoothed ℓ_0 method, $\sigma_{min} = 0.05$, $J = 40$, $L = 25$ and $\varepsilon = \sqrt{0.8M_1}\sigma_n$. For $\ell_1\,\ell_0$ method, $\sigma_{min} = 0.2$, $J = 40$, $L = 25$, $L_0 = 20$, $L_1 = 20$ and $\varepsilon = \sqrt{0.8M_1}\sigma_n$. Images using ℓ_1-magic, OMP, CoSaMp ($k = 20$, $addK = k$), ℓ_1-ℓ_s ($\lambda = 20$), Bayesian method with Laplace prior, smoothed ℓ_0 and $\ell_1\,\ell_0$ methods are shown in Fig.5.1(b),(c), (d), (e), (f), (g) and (h). Because the coefficient matrix $\mathbf{\Psi}_2\mathbf{\Psi}_2^H$ is nearly singular, the ℓ_1-magic algorithm ends with "matrix ill-conditioned" and the image performance is poor. The performance of OMP is also not satisfactory. CoSaMp, ℓ_1-ℓ_s, Bayesian, Smoothed ℓ_0 norm and $\ell_1\,\ell_0$ methods are better. The Matlab computation times are 2.95s (Bayesian), 20s (CoSaMp), 92s (Smoothed ℓ_0), 102s ($\ell_1\,\ell_0$), 177s (OMP), 555.7s (ℓ_1-ℓ_s) and 720s (ℓ_1-magic). Because these programs are not optimized and subfunctions and multiple-loops in Matlab affect the computation time, these computation times are not absolute quantities to judge the computation complexity of each algorithm. They are just a useful reference.

The scatterers in this example are not block scatterers, TV term should not be used. But because this information is not known *a prior*, we check how TV term would affect the imaging quality. Using σ_J= 0.05, 0.1, 0.2 and 0.5, ζ=

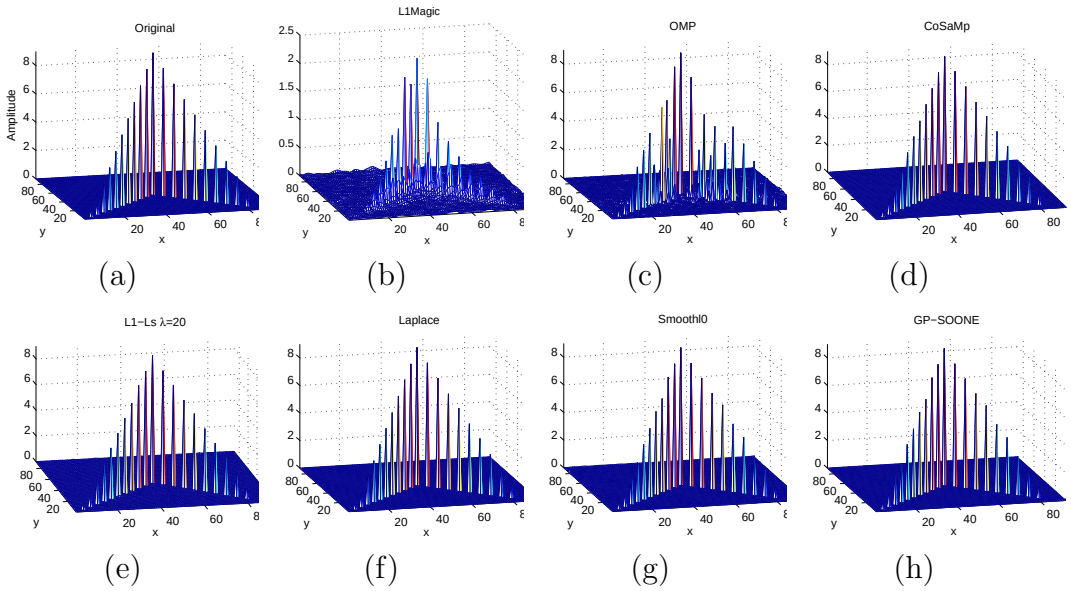

Figure 5.1: (a) Original image of the target. Reconstructed image using (b)ℓ_1-magic; (c) OMP algorithm; (d) CoSaMp ($k = 21$, $addK = k$); (e) $\ell_1 - \ell_s$ ($\lambda = 20$); (f) Bayesian method with Laplace prior; (g) Smoothed ℓ_0 algorithm and (h) GP-SOONE($\ell_1\,\ell_0$).

0.1, 0.2, 0.3, and 0.4, the images using diagonal loading $\ell_1\,\ell_0$-CATV method ($J = 40$, $L = 25$, $L_0 = 25$, $L_1 = 8$, $\rho = 100$) are shown in Fig.5.2. We can see that with increasing of σ_J, there are less noise sparks, but scatterers with smaller amplitudes may be omitted because the importance of small scatterers decreases in the cost function with the increase of σ_J. Because there are no block scatterers, increasing ζ means redundantly loading the cost function and resulting in degraded performance. Some scatterers show flat top phenomenon which is expected by using TV constrained.

Simulation 2: Two Dimensional Imaging of a Target with Scatterers not Located on the Grid Points

In this simulation, some scatterers of the target are not located on the grid points. We use this as a much more realistic situation to demonstrate the performance of sparse signal recovery algorithm. The parameters of the radar are

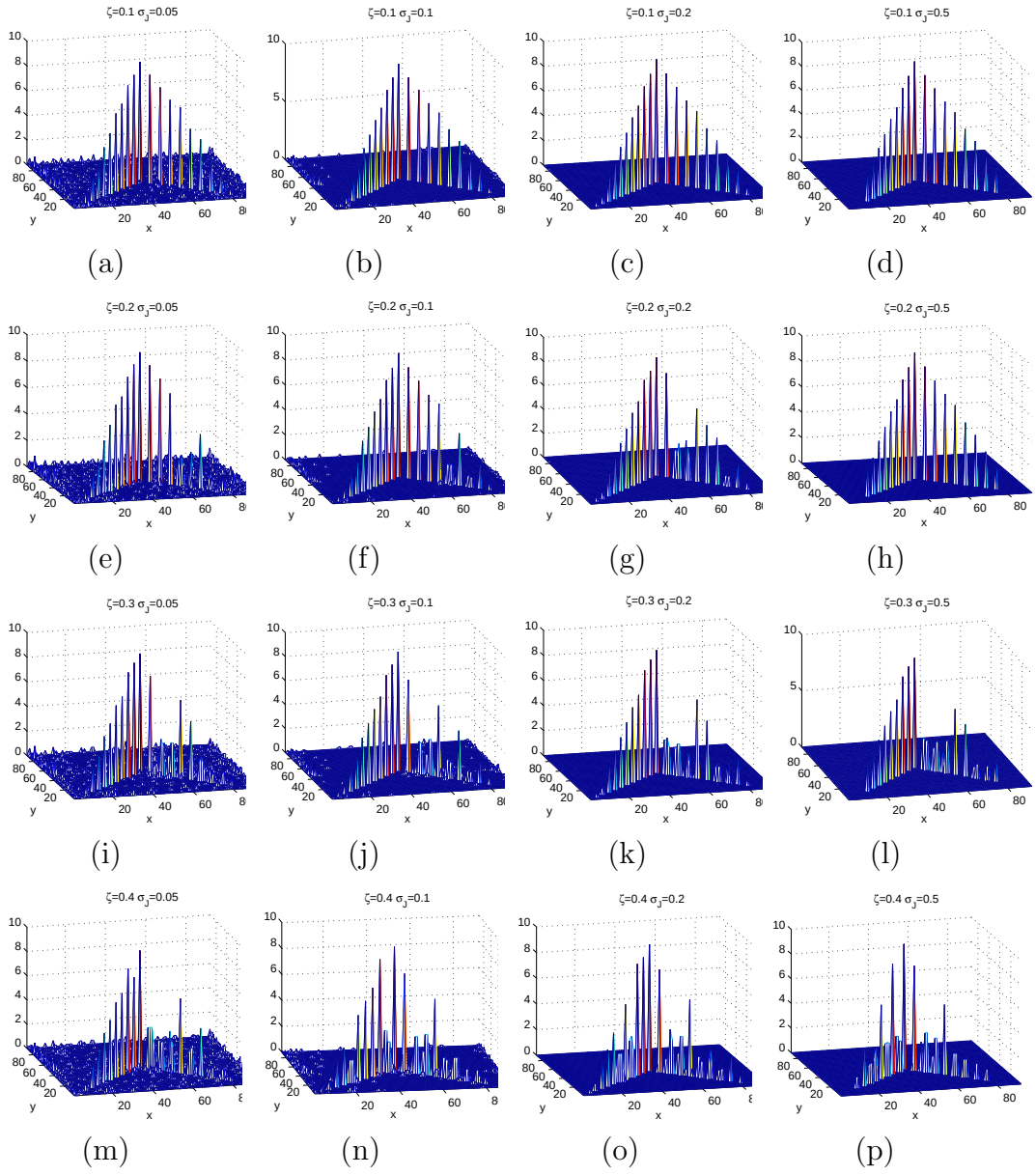

Figure 5.2: Reconstructed image using SOONE-CATV cost function and diagonal loading gradient projection optimization method for $\zeta = 0.1, 0.2, 0.3$ and 0.4 (from top to bottom) and $\sigma_J = 0.05, 0.1, 0.2$ and 0.5 (from left to right).

the same as that of simulation 1. The target composed of 14 scatterers with amplitudes all equal to 1 are shown in Fig.5.3. The target is located in [1,1] direction and the distance between the target and the radar is 50 km. The relative positions of the scatterers are (0,0), (4,0), (2.5,2.5), (6.5,2.5), (0.5,5), (4.5,5), (2,6.5), (6,6.5), (9,1.25), (12,1.25), (9.25,5), (12.25,5), (9.25,8.25) and (12.25,8.25)(m,m). The sampling distance between grid points at two dimensions are all 1 m. The size of the matrix $\mathbf{\Psi}_2$ is 2192×2738, and the condition number of $\mathbf{\Psi}_2\mathbf{\Psi}_2^H$ is 4.33×10^{12}. $\rho = 100$ is chosen as the diagonal loading factor. The SNR is 30dB. For ℓ_1-ℓ_s method, λ from 1 to 10 with step 1, from 10 to 100 with step 10, from 100 to 3000 with step 100 are implemented. The performance for λ from 2000 to 3000 are similar and better than other cases, thus the image of $\lambda = 2000$ is shown. For CoSaMp method, number of nonzero elements K from 9 to 33 with step 1, $addK = K$ and $addK = 2K$ are implemented, where the performance for K from 17 to 33 are similar, thus image when $K = 20$, $addK = K$ is shown. For smoothed ℓ_0 method, the parameters are $J = 40$, $L = 25$, $\sigma_{min} = 0.05$. In $\ell_1\,\ell_0$ method, we use $\zeta = 0$ (no TV term) and the other parameters are $J = 40$, $L = 25$, $L_0 = 20$ and $L_1 = 20$, $\sigma_{min} = 0.06$. ε for smoothed ℓ_0 method and $\ell_1\,\ell_0$ are all chosen as $\sigma_n\sqrt{3M_1}$ (a little larger ε is chosen because model error increases the observation error). The contour plots and mesh plots of the reconstructed images using different methods are shown in Fig.5.4. It can be seen that the performance using minimum ℓ_2 norm, OMP, ℓ_1-magic and Bayesian with Laplace prior methods are poor. For ℓ_1-magic, it may be due to the ill condition matrix. Smoothed ℓ_0, ℓ_1-ℓ_s, $\ell_1\,\ell_0$ and CoSaMp are better. It can also be seen that the scatterers with small distances from the sampling grids have better reconstruction performance.

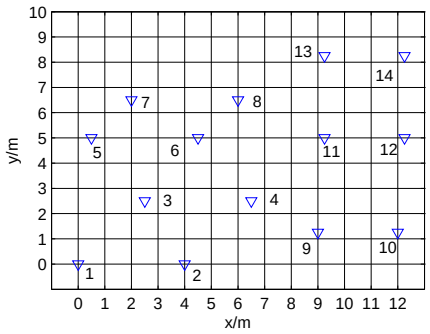

Figure 5.3: The original image of the target in simulation 2

Simulation 3: Three Dimensional Imaging Case

In the above simulations, similar to many papers found in the literature, scatterers are all assumed to be ideal and isolated. In order to show the superiority of our algorithm, we carry out imaging process on no ideal point objects, namely, 4 thin metal plates with dimension $1 \times 1\ m^2$ as shown in Fig.5.5(a).

The imaging radar consists of a 4×4 transmit square antenna array and a 4×4 receive square antenna array located near the origin and on the XZ plane. The target is 50 km away from the radar and on the Y axis. The faces of the four plates are perpendicular to the Y axis. The distances between the adjacent transmit antennas and the adjacent receive antennas are 375 m and 93.75 m, respectively. The unambiguous distance is then 16 meters and the cross-range resolution for conventional radar with the same aperture of this MIMO radar is 1 meter. The sampling distance in X, Y and Z directions are all 0.25 m. The imaging range in X, Y and Z directions are 8.5, 7.5 and 7.5 m respectively. Then the discrete sampling point in X, Y and Z directions are 34, 31 and 30 respectively and the dimension of $\mathbf{\Psi}_2$ is 3936×63240.

The SNR is 30 dB, then the noise variance is $\sigma_n = 0.0807$. Only strong scatterers are selected to form the 3D image. For strong scatterers selection, $\delta v = 32dB$, $\delta\zeta = 6dB$ are chosen. For ℓ_1-ℓ_s method, cases of λ from 1 to 81 step

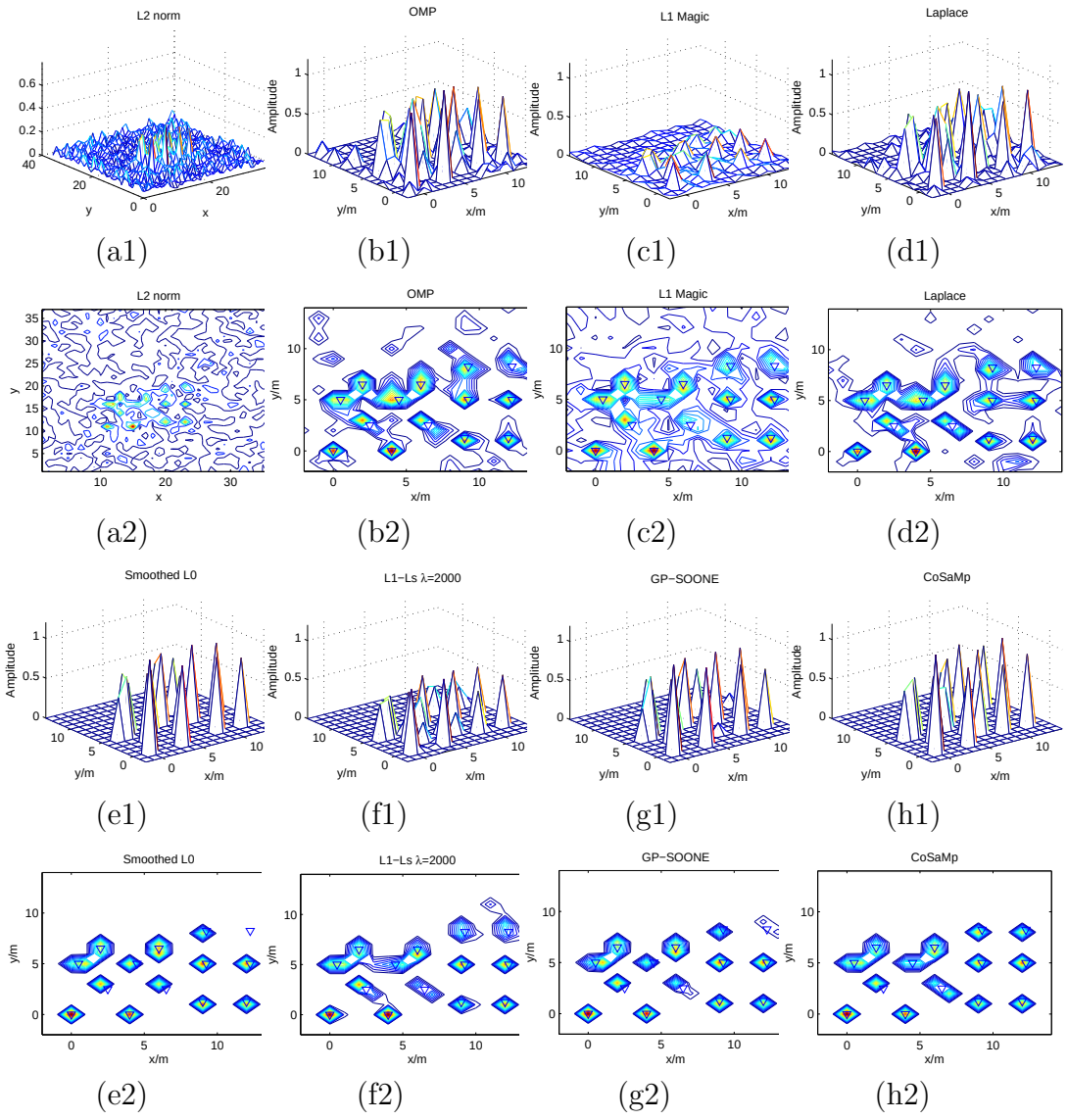

Figure 5.4: Mesh plot and contour plot of reconstructed images using (a1, a2) ℓ_2 norm minimization, (b1, b2) OMP, (c1, c2) ℓ_1-magic, (d1, d2) Bayesian method with Laplace prior, (e1, e2) Smoothed ℓ_0 algorithm ($\sigma_{min} = 0.05$, $J = 40$, $L = 25$), (f1,f2) ℓ_1-ℓ_s ($\lambda = 2000$), (g1,g2) $\ell_1\,\ell_0$ (GP-SOONE) ($\sigma_{min} = 0.06$, $J = 40$, $L = 25$, $L_0 = 20$ and $L_1 = 20$) and (h1,h2) CoSaMp ($K = 20$, $addK = 1K$) (simulation 2).

10, from 100 to 1000 step 100 are implemented and case of $\lambda = 81$ is the best. For CoSaMp method, cases of $K = 32, 36, \cdots, 84$ step 4, $addK = 2K$ and K are implemented and the performance of these cases are not good and $K = 40$, $addK = 2K$ case is the best and shown. ℓ_1-magic method exits with "matrix must be positive definite" and no result output. For smoothed ℓ_0 norm method and $\ell_1\,\ell_0$ method ($\zeta = 0$), σ_J is chosen as 0.004, outer loop number and inner loop number are 25 and 40 respectively, $\varepsilon = \sigma_n\sqrt{2N(P+\triangle)} = 5.06$ (N=16, $P + \triangle = 123$ is the time domain length of the signal). For $\ell_1\,\ell_0$, $L_0 = 25$ and $L_1 = 8$. SVD is used to improve the robustness and 1053 large eigenvectors are used to compute the pseudo inverse of $\mathbf{\Psi_2\Psi_2}^H$. The images reconstructed using these methods are shown in Fig.5.5.

It can be seen that the minimum ℓ_2 norm and OMP methods have high sidelobes. The reconstructed patches using minimum ℓ_2 norm method are small due to the solution are minimum in ℓ_2 norm. The images using smoothed ℓ_0 norm, Bayesian, CoSaMp and $\ell_1\,\ell_0$ methods have low sidelobes, but the shapes of the 4 square patches changed slightly. The performance using ℓ_1-ℓ_s method is best with optimal parameter λ chosen.

The results of $\ell_1\,\ell_0$ of Fig.5.5(f) could be improved by incorporating CATV. Fig.5.6 shows the reconstructed images where amplitude and total variation are used as cost function. The trade-off parameter ζ is chosen as 0.1, 0.2, 0.3 and 0.4, and the σ_J is chosen as 0.001, 0.002, 0.004 and 0.006 respectively. Other simulation conditions are the same as the above that without total variation term. It can be seen that with the increase of ζ, the four square patches keep their shapes better. With the increase of σ_J, there are fewer sidelobes, but small scatterers may be omitted though this does not appear in Fig.5.6, because there are no small scatterers in this simulation. In a wide range of ζ the performance using CATV objective function is better than that

using only amplitude objective function.

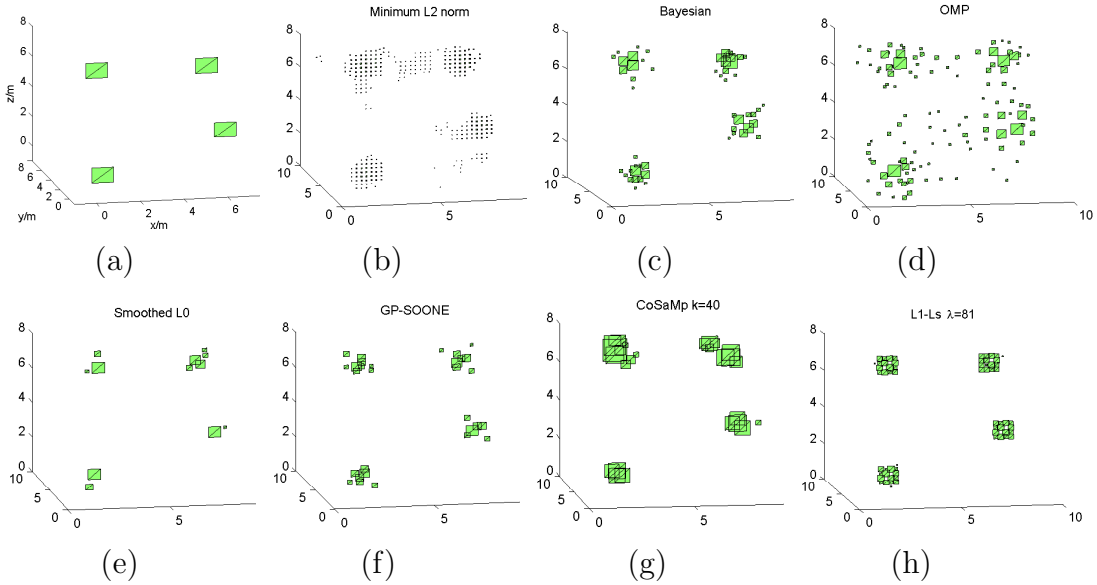

Figure 5.5: (a) Original image of the target. Reconstructed images using (b) ℓ_2 norm minimization, (c) Bayesian method with Laplace prior, (d) OMP, (e) Smoothed ℓ_0 algorithm ($\sigma_J = 0.004, J = 25, L = 40$), (f) $\ell_1\,\ell_0$ (GP-SOONE) ($\zeta = 0$, $\sigma_J = 0.004, J = 25, L = 40, L_0 = 25, L_1 = 8$), (g) CoSaMp (k=40, addK=2k) and (h) ℓ_1-ℓ_s ($\lambda = 81$) (simulation 3).

Simulation 4: Experiment of ISAR Imaging Using Real Data

In this section, a set of real data of the Yak-42 aircraft is used to demonstrate the performance of sparse signal recovery algorithms. The detailed target and data descriptions are provided in [48] and the references therein. Some related radar parameters are listed as follows: the carrier frequency is 10 GHz with signal bandwidth of 400 MHz, corresponding to a range resolution of 0.375 m. The pulse repetition frequency is 100 Hz, i.e., 64 pulses within dwell time [-0.32, 0.32]s are used in this experiment. For every range cell, the signal in Doppler domain is sparse. So sparse signal recovery algorithms are used in every range cell (the coefficient matrix $\mathbf{\Psi}$ is a discrete complex sine matrix, and $\mathbf{\Psi}\mathbf{\Psi}^H$ is not singular). Same as [48], the noise level is estimated from the range profile, that is using range cells from 1 to 25 to estimate the noise

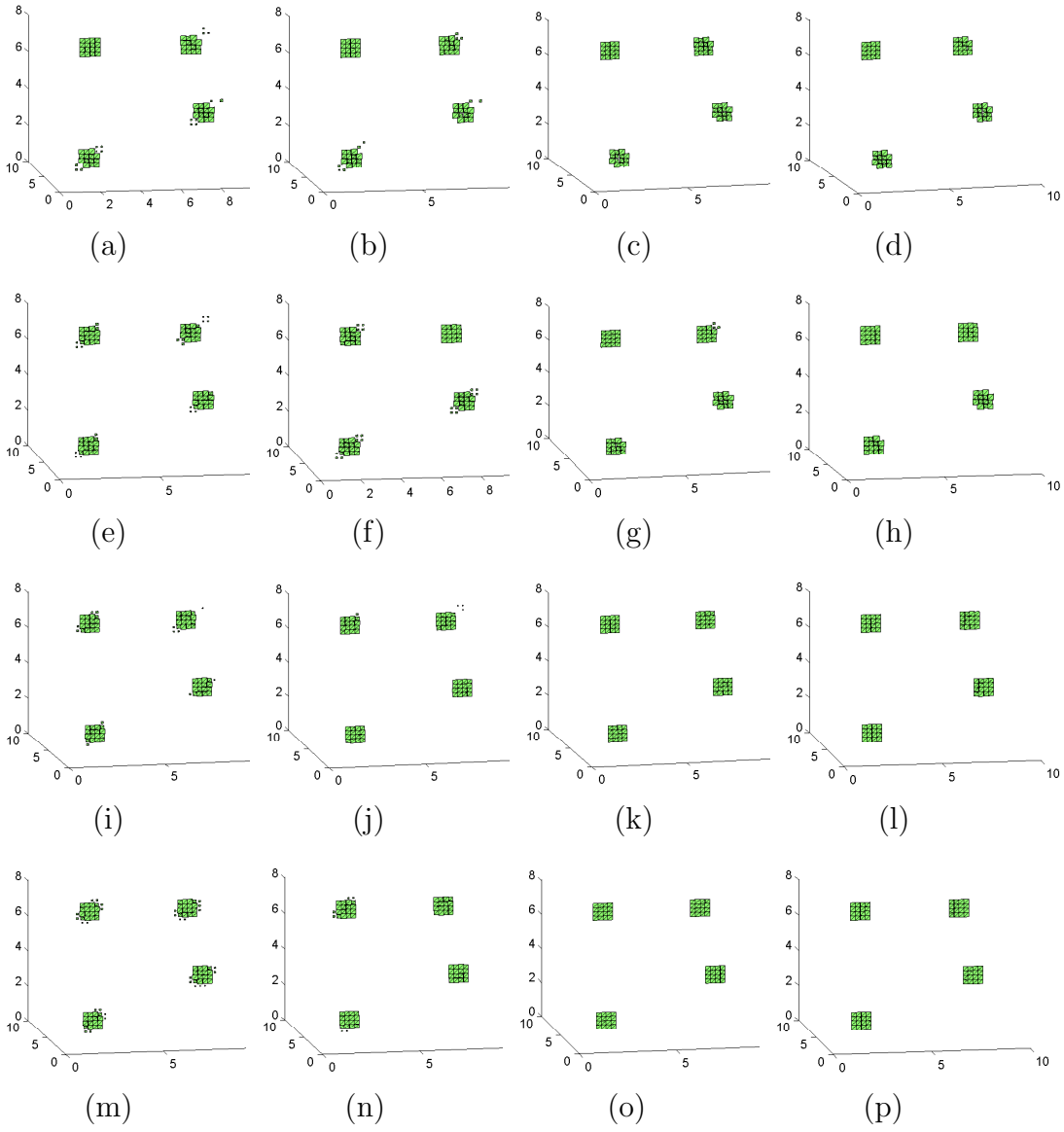

Figure 5.6: Reconstructed images using combined amplitude and total variation objective function with SOONE form and gradient projection optimization method for $\zeta = 0.1, 0.2, 0.3$ and 0.4 (from top to bottom) and $\sigma_J = 0.001, 0.002, 0.004$ and 0.006 (from left to right)(simulation 3).

variance. Two cases of 32-snapshot and 64-snapshot are implemented. For CoSaMp method, cases that the expected sparsity K chosen from 3 to 8 and the $addK$ parameter chosen as K and $2K$ are implemented and the best results occurs at $K = 5$ and $addK = K$. Performance of $K = 3$ and $addK = 2K$ case is similar. For ℓ_1-ℓ_s method, λ is chosen as 0.008, 0.009, 0.01, 0.02, 0.03. The ISAR images are similar but case of $\lambda = 0.03$ is best. ISAR images using FFT, Bayesian, Smoothed ℓ_0 ($\sigma_J = 200$, J=25, L=40, $\varepsilon = \sigma_n\sqrt{2N}$, $N = 32, 64$), OMP, ℓ_1-ℓ_s ($\lambda = 0.03$), CoSaMp ($K = 5$, $addK = K$) , ℓ_1-magic and $\ell_1\,\ell_0$ ($\sigma_J = 565$, J=25, L=40, $L_0 = 25$, $L_1 = 8$, $\varepsilon = \sigma_n\sqrt{2N}$, $N = 32, 64$) methods are shown in Fig.5.7. From these images, we can see that the resolution of ISAR image using FFT method is coarse due to less signal length, and has high sidelobes (windowing can reduce sidelobes but the cost is a coarser resolution). All images using sparse signal recovery methods are better than FFT method. For CoSaMp method, it is dependent on the choice of sparsity K and $addK$. For 32 snapshots case, more sidelobes appear. Images using OMP method have a little high sidelobes. $\ell_1\,\ell_0$ method has competitive performance. The time of 32 snapshots is only one eighth of the original 256 snapshots acquirement time. So using sparse signal recovery algorithms, it is possible to image maneuvering target in a short time duration, then the approximation of uniform rotation is adequate.

5.2. COLLOCATED MIMO RADAR 3D IMAGING USING LINEAR EQUATION $\ell_1\,\ell_0$ HOMOTOPY ALGORITHM

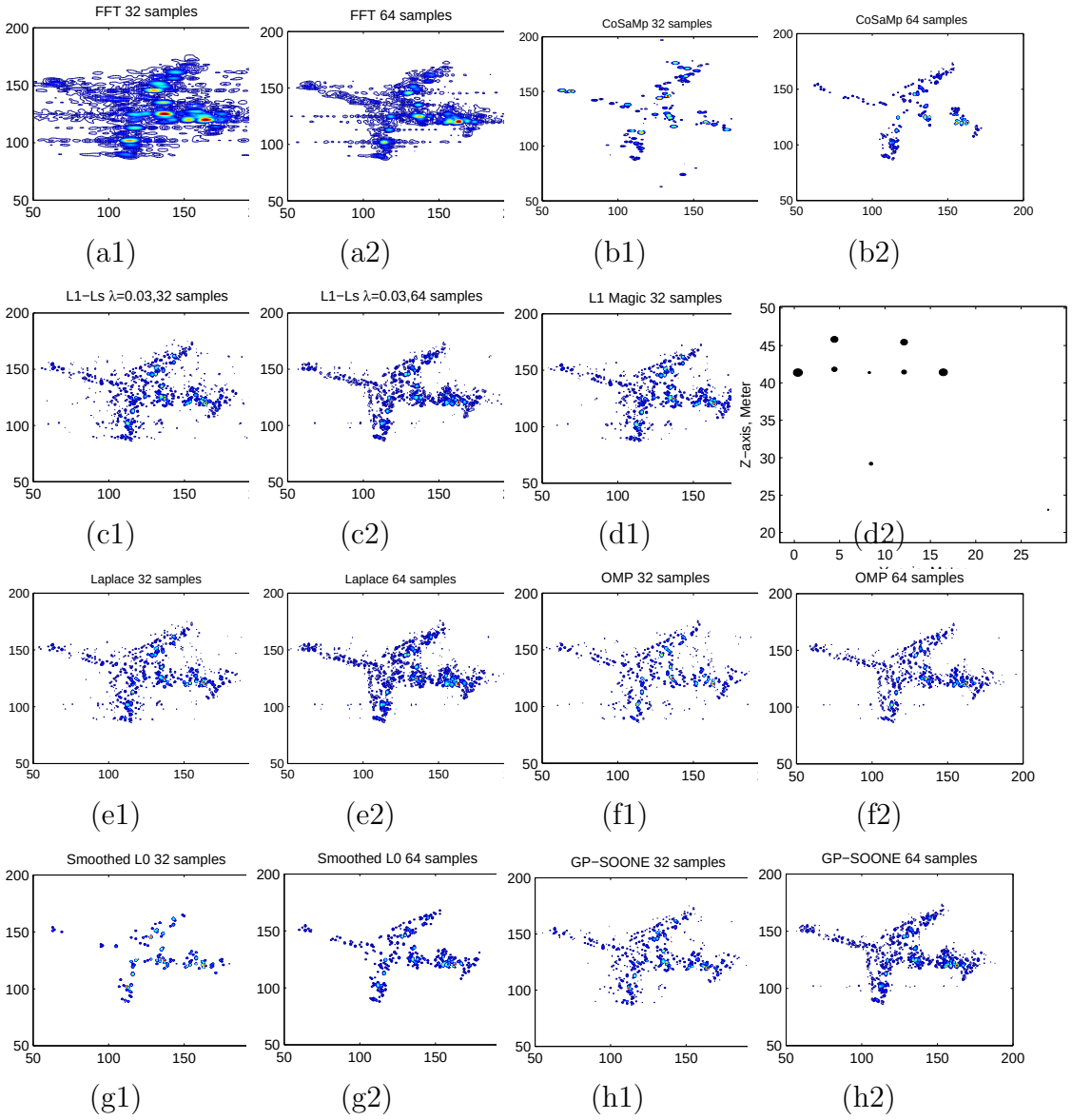

Figure 5.7: Reconstructed images using 32 and 64 snapshots, (a1,a2)FFT method, (b1,b2) CoSaMp ($k = 5$, $addK = k$), (c1,c2)ℓ_1-ℓ_s, $\lambda = 0.03$, (d1,d2)ℓ_1-magic, (e1,e2) Bayesian method with Laplace prior, (f1,f2) OMP, (g1,g2) Smoothed ℓ_0 algorithm, and (h1,h2) $\ell_1\,\ell_0$ (GP-SOONE)($\zeta = 0$) (simulation 4).

5.3 Collocated MIMO Radar 3D Imaging Using Multi-Dimensional Linear Equation $\ell_1\,\ell_0$ Homotopy Algorithm

Conventional sparse signal recovery algorithms solve a linear equation. For MIMO radar imaging, as shown in Eq.(5.5), the dimension of the coefficient matrix is $M_1 \times N_1$, where M_1 is the product between the number of the receive antenna and the time domain signal length, N_1 is the number of discrete sampling points of the imaging area. For a three dimensional imaging volume, the dimension of the coefficient matrix is huge. This occupies great memory and costs huge computation. In this section, the signal is expressed as a multi-dimensional equation form, the memory and the computation are saved.

According to Eq.(5.3), the signal received can be expressed as

$$\mathbf{s}(t) = \alpha_A \mathbf{a}\mathbf{b}^T \mathbf{\Phi}(t - \tau_A), \tag{5.13}$$

where

$$\mathbf{a} = [e^{-j2\pi f \tau_{Q_0 A}}, e^{-j2\pi f \tau_{Q_1 A}}, ..., e^{-j2\pi f \tau_{Q_{N-1} A}}]^T$$

and

$$\mathbf{b} = [e^{-j2\pi f \tau_{P_0 A}}, e^{-j2\pi f \tau_{P_1 A}}, ..., e^{-j2\pi f \tau_{P_{M-1} A}}]^T.$$

Denote

$$\mathbf{a}_0 = [e^{-j2\pi f \tau_{Q_0 O}}, e^{-j2\pi f \tau_{Q_1 O}}, ..., e^{-j2\pi f \tau_{Q_{N-1} O}}]^T$$

and

$$\mathbf{b}_0 = [e^{-j2\pi f \tau_{P_0 O}}, e^{-j2\pi f \tau_{P_1 O}}, ..., e^{-j2\pi f \tau_{P_{M-1} O}}]^T,$$

where O is the reference point. After phase compensation using $\mathbf{a}_0$, we also use $\mathbf{s}(t)$ to express $\mathbf{s}(t) \odot \mathbf{a}_0^*$ for symbol simplicity, where $\odot$ expresses element

wise product, the received signal can be expressed as

$$\mathbf{s}(t) = \alpha_A(\mathbf{a} \odot \mathbf{a}_0^*)(\mathbf{b} \odot \mathbf{b}_0^*)^T(\mathbf{b}_0 \odot \mathbf{\Phi}(t - \tau_A)), \tag{5.14}$$

If the transmit codes are phase compensated before transmitting, that is the transmitting codes are $\mathbf{b}_0^* \odot \mathbf{\Phi}(t)$, the above equation can be expressed as

$$\mathbf{s}(t) = \alpha_A \hat{\mathbf{a}}\hat{\mathbf{b}}^T\mathbf{\Phi}(t - \tau_A). \tag{5.15}$$

According to Eq.(2.8),the n^{th} element of $\hat{\mathbf{a}}$ can be expressed as $e^{j2\pi\tilde{\mathbf{a}}^T\overrightarrow{Q_0Q_n}/r\lambda}$, the m^{th} element of $\hat{\mathbf{b}}$ can be expressed as $exp(j2\pi\tilde{\mathbf{a}}^T\overrightarrow{P_0P_m}/r\lambda)$. It is possible to express $\mathbf{s}(t)$ as a separable function form. In details, three MIMO radar configurations are discussed as followings.

5.3.1 One Dimensional MIMO Radar 2D Imaging

The geometry of a linear MIMO radar is shown in Fig.5.8, where M transmit antennas and N receive antennas are evenly deployed on the X axis. Y is the range axis. The inter-element distances between transmit antennas and between receive antennas are d_t and d_r respectively. Note that the unambiguous distances in X axis is $L = \frac{\lambda}{d_r}r$. Denote $\tilde{x}$ the coordinate of $\tilde{\mathbf{a}}$ on X axis. The receive signal from scatterer A is now a two dimensional matrix. The receive signal at the n^{th} receive antenna can be expressed as

$$\mathbf{s}_n(t) = \alpha_A e^{j\frac{2\pi\tilde{x}nd_r}{\lambda r}} \times \sum_m e^{j\frac{2\pi\tilde{x}md_t}{\lambda r}}\boldsymbol{\varphi}_m(t - \tau_A). \tag{5.16}$$

We assume that the inter-element distance of transmit antennas is larger than the inter-element distance of receive antennas and $d_t = Pd_r$. Then $e^{j\frac{2\pi\tilde{x}md_t}{\lambda r}} = e^{j\frac{2\pi\tilde{x}mP}{L}}$. In $[0, L)$, $e^{j\frac{2\pi\tilde{x}mP}{L}}$ is a period function for $\tilde{x}$ with period of L/P. Define

$c_{\tilde{x}}(t) =: \sum_m e^{j\frac{2\pi\tilde{x}md_t}{\lambda r}}\boldsymbol{\varphi}_m(t)$, then $c_{\tilde{x}}(t)$ is also a period function on $\tilde{x}$. Function $c_{\tilde{x}}(t)$ can be regarded as a synthetic code at $\tilde{x}$.

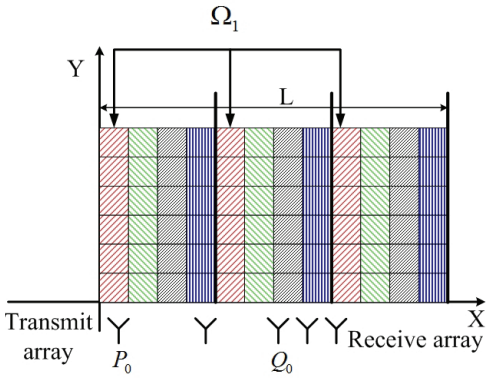

Figure 5.8: Imaging field division for One Dimensional MIMO array radar.

In Fig.5.8, the unambiguous window $[0, L)$ is divided as P parts, where we assume that $P = N = 3$. Usually, P is not larger than N, otherwise grating lobes will appear. In each part $(i\frac{L}{P}, (i+1)\frac{L}{P})$, we assume that it is divided as M_1 strips, where M_1 is larger than or equal to M. Then there are PM_1 strips in the imaging region. The value of M_1 is decided by the cross-range resolution of the image expected by the designer. In Fig.5.8 M_1 is chosen as 4. So there are M_1 independent synthetic codes. Denote $\triangle$ the sampling distance in X axis, m_1 is an integer, we have $\tilde{x} = m_1\triangle$ and $L = PM_1\triangle$. The imaging region can also be divided as M_1 sets corresponding to different synthetic code. Denote Ω_{m_1} the index set of the m_1^{th} set which is defined as $\Omega_{m_1} = \{(pM_1 + m_1) : p = 0, 1, \cdots, P-1, m_1 \in [0, M_1 - 1]\}$. For every Ω_{m_1}, there is only one synthetic code $c_{m_1}(t) = \sum_m e^{j\frac{2\pi m_1 m}{M_1}}\varphi_m(t)$.

From now, the imaging region has been divided as M_1 sets $\{\Omega_{m_1}, m_1 = 0, 1, \cdots, M_1 - 1\}$. Denote $\mathbf{a}_m = [1, e^{j\frac{2\pi m}{PM_1}}, \cdots, e^{j\frac{2\pi m(N-1)}{PM_1}}]^T$, $c_{m,\tau} = c_m(t-\tau)$, then the signal received from the scatterer located at $(m\triangle, \tau)$ can be expressed as

$$\mathbf{s}_{m,\tau}(t) = \alpha\mathbf{a}_m c_{m,\tau}. \tag{5.17}$$

Note that $\mathbf{a}_m$ is a column vector while $c_{m,\tau}$ is a function. The character of the above expression is that $\mathbf{a}_m$ is only related with the cross range index m and has no relation with delay τ. $c_{m,\tau}$ in set $\Omega_{m\ mod\ M_1}$ is only related with τ and has no relation with cross range index. Denote $\mathbf{A}_{m_1} = [\mathbf{a}_{m_1}, \mathbf{a}_{m_1+M_1}, \cdots, \mathbf{a}_{m_1+(P-1)M_1}]$, $c_{m_1}(k)$ the discrete sampling of $c_{m_1}(t)$, and

$$\mathbf{C}_{m_1} = \begin{bmatrix} c_{m_1}(1) & c_{m_1}(2) & \cdots & c_{m_1}(K) & 0 & 0 & 0 \\ 0 & c_{m_1}(1) & c_{m_1}(2) & \cdots & c_{m_1}(K) & 0 & 0 \\ \vdots & \vdots & \vdots & \vdots & \vdots & \vdots & \vdots \\ 0 & \cdots & 0 & c_{m_1}(1) & c_{m_1}(2) & \cdots & c_{m_1}(K) \end{bmatrix}, \quad (5.18)$$

where K is the length of code $\mathbf{c}_{m_1}$, the length of the rows of $\mathbf{C}_{m_1}$ is the number of range units of the region Ω_{m_1}. Then the two dimensional discrete signal received from region Ω_{m_1} can be expressed as

$$\mathbf{S}_{m_1} = \mathbf{A}_{m_1}\boldsymbol{\alpha}_{m_1}\mathbf{C}_{m_1}, \quad (5.19)$$

where $\boldsymbol{\alpha}_{m_1}$ is the scatterer reflection matrix on region Ω_{m_1}. Then the signal received from the entire imaging region can be expressed as

$$\mathbf{S} = \sum_{m_1=0}^{M_1-1} \mathbf{A}_{m_1}\boldsymbol{\alpha}_{m_1}\mathbf{C}_{m_1}. \quad (5.20)$$

Denote $\mathbf{A} = [\mathbf{A}_1, \mathbf{A}_2, \cdots, \mathbf{A}_{M_1}]$, $\boldsymbol{\alpha} = diag(\boldsymbol{\alpha}_1, \cdots, \boldsymbol{\alpha}_{M_1})$ and $\mathbf{C} = \left[\mathbf{C}_0^T, \mathbf{C}_1^T, \cdots, \mathbf{C}_{M_1}^T\right]^T$, then $\mathbf{S}$ can be expressed as

$$\mathbf{S} = \mathbf{A}\boldsymbol{\alpha}\mathbf{C}. \quad (5.21)$$

In the above expression, the matrix $\mathbf{A}$ is not the conventional Fourier matrix. By adjusting the orders of the columns of matrix $\mathbf{A}$, $\mathbf{A}$ can be the conventional Fourier matrix. Then FFT can be used in computing of $\boldsymbol{\alpha}$.

Denote $\bar{\mathbf{A}} = [\mathbf{a}_0, \mathbf{a}_1, \cdots, \mathbf{a}_{PM_1-1}]$ the conventional Fourier matrix, where

$$\mathbf{a}_m = \left[1, e^{j\frac{2\pi m}{PM_1}}, \cdots, e^{j\frac{2\pi m(N-1)}{PM_1}}\right]^T.$$

The natural order reflection coefficient matrix $\boldsymbol{\alpha}$ is

$$\boldsymbol{\alpha} = \begin{bmatrix} \alpha_{1,1} & \alpha_{1,2} & \cdots \\ \alpha_{2,1} & \alpha_{2,2} & \cdots \\ \alpha_{3,1} & \alpha_{3,2} & \cdots \\ \alpha_{4,1} & \alpha_{4,2} & \cdots \\ \alpha_{5,1} & \alpha_{5,2} & \cdots \\ \alpha_{6,1} & \alpha_{6,2} & \cdots \\ \alpha_{7,1} & \alpha_{7,2} & \cdots \\ \alpha_{8,1} & \alpha_{8,2} & \cdots \\ \vdots & \vdots & \vdots \end{bmatrix}, \tag{5.22}$$

where row expresses cross range, column expresses down range. According to the parameters of the MIMO radar shown in Fig. 5.8, a new matrix $\bar{\boldsymbol{\alpha}}$ is defined as

$$\bar{\boldsymbol{\alpha}} = \begin{bmatrix} \alpha_{1,1} & 0 & 0 & 0 & \alpha_{1,2} & 0 & 0 & 0 & \cdots \\ 0 & \alpha_{2,1} & 0 & 0 & 0 & \alpha_{2,2} & 0 & 0 & \cdots \\ 0 & 0 & \alpha_{3,1} & 0 & 0 & 0 & \alpha_{3,2} & 0 & \cdots \\ 0 & 0 & 0 & \alpha_{4,1} & 0 & 0 & 0 & \alpha_{4,2} & \cdots \\ \alpha_{5,1} & 0 & 0 & 0 & \alpha_{5,2} & 0 & 0 & 0 & \cdots \\ 0 & \alpha_{6,1} & 0 & 0 & 0 & \alpha_{6,2} & 0 & 0 & \cdots \\ 0 & 0 & \alpha_{7,1} & 0 & 0 & 0 & \alpha_{7,2} & 0 & \cdots \\ 0 & 0 & 0 & \alpha_{8,1} & 0 & 0 & 0 & \alpha_{8,2} & \cdots \\ \vdots & \vdots & \vdots & \vdots & \vdots & \vdots & \vdots & \vdots & \end{bmatrix}, \tag{5.23}$$

and a new code matrix is defined as:

$$\bar{\mathbf{C}} = \begin{bmatrix} c_0(1) & c_0(2) & \cdots & c_0(K) & 0 & 0 & 0 \\ c_1(1) & c_1(2) & \cdots & c_1(K) & 0 & 0 & 0 \\ c_2(1) & c_2(2) & \cdots & c_2(K) & 0 & 0 & 0 \\ c_3(1) & c_3(2) & \cdots & c_3(K) & 0 & 0 & 0 \\ 0 & c_0(1) & c_0(2) & \cdots & c_0(K) & 0 & 0 \\ 0 & c_1(1) & c_1(2) & \cdots & c_1(K) & 0 & 0 \\ 0 & c_2(1) & c_2(2) & \cdots & c_2(K) & 0 & 0 \\ 0 & c_3(1) & c_3(2) & \cdots & c_3(K) & 0 & 0 \\ \cdots & \cdots & \cdots & \cdots & \cdots & \cdots & \cdots \end{bmatrix}. \tag{5.24}$$

Then we have

$$\mathbf{S} = \bar{\mathbf{A}}\bar{\boldsymbol{\alpha}}\bar{\mathbf{C}}. \tag{5.25}$$

Eq.(5.21) and Eq.(5.25) are multi-dimensional linear equations (tensor equations).

5.3.2 Cross-Array MIMO Radar 3D Imaging

The geometry of cross-array MIMO radar is shown in Fig.2.3. Note that the unambiguous distances in X and Y axes are $L_x = \frac{\lambda}{d_x}r$ and $L_y = \frac{\lambda}{d_y}r$ respectively. Denote $\tilde{x}, \tilde{y}$ the coordinates of $\tilde{\mathbf{a}}$ on XY coordinate system. According to Eq.(5.16), the signal $\mathbf{s}(t)$ can be expressed as

$$\mathbf{s}(t) = \alpha_A \begin{pmatrix} 1 \\ e^{j2\pi\tilde{x}d_x/(\lambda r)} \\ \vdots \\ e^{j2\pi\tilde{x}(N-1)d_x/(\lambda r)} \end{pmatrix} \begin{pmatrix} 1 \\ e^{j2\pi\tilde{y}d_y/(\lambda r)} \\ \vdots \\ e^{j2\pi\tilde{y}(M-1)d_y/(\lambda r)} \end{pmatrix}^T \boldsymbol{\Phi}(t-\tau_A). \tag{5.26}$$

We assume that L_x and L_y are divided into $\tilde{N}$ and $\tilde{M}$ divisions. $(\tilde{x},\tilde{y}) =: (\tilde{n}\frac{L_x}{\tilde{N}}, \tilde{m}\frac{L_y}{\tilde{M}})$. Then $\mathbf{s}(t)$ can be expressed as

$$\mathbf{s}(t) = \alpha_A \begin{pmatrix} 1 \\ e^{j2\pi\frac{\tilde{n}}{\tilde{N}}} \\ \vdots \\ e^{j2\pi(N-1)\frac{\tilde{n}}{\tilde{N}}} \end{pmatrix} \begin{pmatrix} 1 \\ e^{j2\pi\frac{\tilde{m}}{\tilde{M}}} \\ \vdots \\ e^{j2\pi(M-1)\frac{\tilde{m}}{\tilde{M}}} \end{pmatrix}^T \mathbf{\Phi}(t-\tau_A). \tag{5.27}$$

Denote $\mathbf{c}_{\tilde{m}}(t) = [1, e^{j2\pi\frac{\tilde{m}}{\tilde{M}}}, \cdots, e^{j2\pi(M-1)\frac{\tilde{m}}{\tilde{M}}}]\mathbf{\Phi}(t)$, we can see that scatterers with the same coordinate $\tilde{m}$ (on Y axis) have the same synthetic code $\mathbf{c}_{\tilde{m}}(t)$. So the imaging volume can be divided as $\tilde{M}$ parts along the Y direction. This is shown in Fig.5.9.

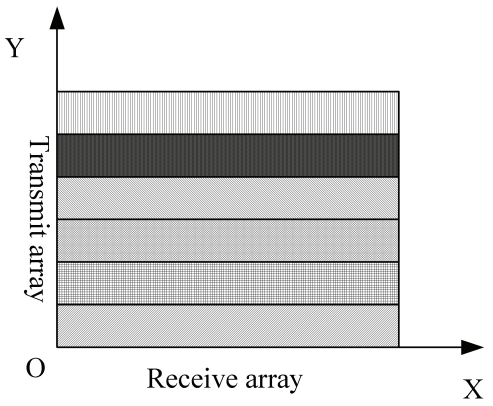

Figure 5.9: Imaging field division for cross array MIMO radar.

We assume that there are L range units. Denote $\boldsymbol{\alpha}_{\tilde{m}} = \{\alpha_{n,l}\}$ the scatterers' reflectivity matrix at $\tilde{m}$th region(Y axis), where n and l express the index in X and range directions. Denote

$$A = \begin{pmatrix} 1 & 1 & 1 & 1 \\ 1 & e^{j2\pi\frac{1}{\tilde{N}}} & \cdots & e^{j2\pi\frac{\tilde{N}-1}{\tilde{N}}} \\ \vdots & \vdots & \vdots & \vdots \\ 1 & e^{j2\pi(N-1)\frac{1}{\tilde{N}}} & \cdots & e^{j2\pi(N-1)\frac{\tilde{N}-1}{\tilde{N}}} \end{pmatrix}. \tag{5.28}$$

For simplicity, let $\mathbf{c}_{\tilde{m}}$ express the discrete version of $\mathbf{c}_{\tilde{m}}(t)$. Demote

$$\mathbf{C}_{\tilde{m}} = \begin{bmatrix} c_{\tilde{m}}(1) & c_{\tilde{m}}(2) & \cdots & c_{\tilde{m}}(K) & 0 & 0 & 0 \\ 0 & c_{\tilde{m}}(1) & c_{\tilde{m}}(2) & \cdots & c_{\tilde{m}}(K) & 0 & 0 \\ \vdots & \vdots & \vdots & \vdots & \vdots & \vdots & \vdots \\ 0 & \cdots & 0 & c_{\tilde{m}}(1) & c_{\tilde{m}}(2) & \cdots & c_{\tilde{m}}(K) \end{bmatrix}. \tag{5.29}$$

The discrete receive signal can be expressed as

$$\mathbf{S} = \sum_{\tilde{m}=1}^{\tilde{M}} \mathbf{A}\boldsymbol{\alpha}_{\tilde{m}}\mathbf{C}_{\tilde{m}}. \tag{5.30}$$

Denote $\bar{\boldsymbol{\alpha}} = [\boldsymbol{\alpha}_1, \boldsymbol{\alpha}_2, \cdots, \boldsymbol{\alpha}_{\tilde{M}}]$, $\bar{\mathbf{C}} = [\mathbf{C}_1^T, \mathbf{C}_2^T, \cdots, \mathbf{C}_{\tilde{M}}^T]^T$, $\mathbf{S}$ can be expressed as

$$\mathbf{S} = \mathbf{A}\bar{\boldsymbol{\alpha}}\bar{\mathbf{C}}. \tag{5.31}$$

5.3.3 Square-Array MIMO Radar 3D Imaging

The geometry of square-array MIMO radar is shown in Fig.2.4. The dimensions of 2D transmit array and receive array are $M_1 \times M_2$ and $N_1 \times N_2$. Note that the unambiguous distances in X and Y axes are $L_x = \frac{\lambda}{d_{rx}}r$ and $L_y = \frac{\lambda}{d_{ry}}r$ respectively. The receive signal is now a three dimensional matrix and denoted as $\mathbf{S}(t)$. The $\mathbf{S}(t)$ received at the (n_1, n_2)th receive antenna can be expressed as

$$\mathbf{S}_{n_1,n_2}(t) = \alpha_A e^{j2\pi(\tilde{x}n_1 d_{rx} + \tilde{y}n_2 d_{ry})/\lambda r} \times \sum_{m_1,m_2} e^{j2\pi(\tilde{x}m_1 d_{tx} + \tilde{y}m_2 d_{ty})/\lambda r}\boldsymbol{\varphi}_{m1,m2}(t - \tau_A). \tag{5.32}$$

We assume that the inter-element distance of transmit array is larger than the inter-element distance of receive array and $d_{tx} = Pd_{rx}$, $d_{ty} = Qd_{ry}$, $P \leq N_1$ and $Q \leq N_2$. Then $e^{j2\pi(\tilde{x}m_1 d_{tx} + \tilde{y}m_2 d_{ty})/\lambda r} = e^{j2\pi(\tilde{x}m_1 P/L_x + \tilde{y}m_2 Q/L_y)}$, which is a

period function in X and Y directions with periods of L_x/P and L_y/Q. Then $\sum_{m_1,m_2} e^{j2\pi(\tilde{x}m_1 d_{tx}+\tilde{y}m_2 d_{ty})/\lambda r}\boldsymbol{\varphi}_{m1,m2}(t)$ is also a period function which is shown in Fig.5.10.

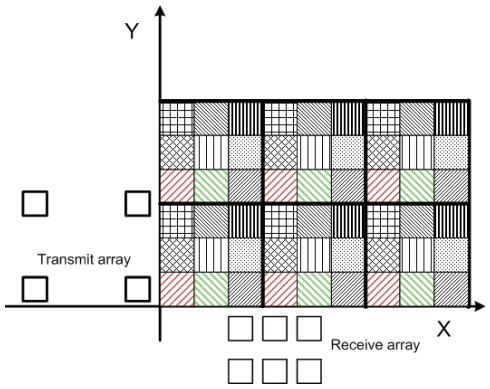

Figure 5.10: Imaging field division for Square array MIMO radar.

In this figure, we assume that $P = 3$ and $Q = 2$. It can be seen that the imaging region is divided as 6 parts. There are P and Q divisions in the X and Y directions. Generally, we assume that a sub-square is divided as M_x and M_y parts in the X and Y directions. So the imaging region is also divided as $M_x \times M_y$ parts $\Omega_{m_x,m_y} = \{(pM_x + m_x, qM_y + m_y) : p = 0, 1, \cdots, P-1, q = 0, 1, \cdots, Q-1, m_x \in [0, M_x - 1], m_y \in [0, M_y - 1]\}$, where (m_x, m_y) is the index of the sub-square. For every Ω_{m_x,m_y}, there is only one synthetic code $c_{m_x,m_y}(t) = \sum_{m_1,m_2} e^{j2\pi(m_x m_1/M_x + m_y m_2/M_y)}\boldsymbol{\varphi}_{m1,m2}(t)$. In Fig.5.10, $M_x = M_y = 3$, there are 9 synthetic codes.

From now, the imaging region has been divided as $M_x \times M_y$ parts Ω_{m_x,m_y}. For simplicity, if m_x (m_y) is larger than M_x (M_y), in expression of Ω_{m_x,m_y}, Ω_{m_x,m_y} is equivalent to $\Omega_{m_x\ Mod\ M_x, m_y\ Mod\ M_y}$.

Denote

$$\mathbf{a}_{x,m_x} = [1, e^{j2\pi m_x/(PM_x)}, \cdots, e^{j2\pi m_x(N_1-1)/(PM_x)}]^T,$$

$$\mathbf{a}_{y,m_y} = [1, e^{j2\pi m_y/(QM_y)}, \cdots, e^{j2\pi m_y(N_2-1)/(QM_y)}]^T,$$

where $m_x \in [0, M_xP), m_y \in [0, M_yQ)$. Then the three dimensional signal received from the scatterer located at (m_x, m_y, τ) can be expressed as

$$\mathbf{S}_{m_x,m_y,\tau}(t) = \alpha \mathbf{a}_{x,m_x} \otimes \mathbf{a}_{y,m_y} \otimes \mathbf{c}_{m_x,m_y}(t-\tau). \tag{5.33}$$

The character of the above expression is that $\mathbf{a}_{m_x}$ is only related with m_x, $\mathbf{a}_{m_y}$ is only related with m_y. In region Ω_{m_x,m_y}, $\mathbf{c}_{m_x,m_y}(t-\tau)$ is only related with τ. Denote

$\mathbf{A}_{x,m_x} = [\mathbf{a}_{x,m_x}, \mathbf{a}_{x,m_x+M_x}, \cdots, \mathbf{a}_{x,m_x+(P-1)M_x}]$, $\mathbf{A}_{y,m_y} = [\mathbf{a}_{y,m_y}, \mathbf{a}_{y,m_y+M_y}, \cdots, \mathbf{a}_{y,m_y+(Q-1)M_y}]$, $c_{m_x,m_y}(k)$ the discrete version of $c_{m_x,m_y}(t)$,

$$\mathbf{C}_{m_x,m_y} = \begin{bmatrix} c_{m_x,m_y}(1) & c_{m_x,m_y}(2) & \cdots & c_{m_x,m_y}(K) & 0 & 0 & 0 \\ 0 & c_{m_x,m_y}(1) & c_{m_x,m_y}(2) & \cdots & c_{m_x,m_y}(K) & 0 & 0 \\ \vdots & \vdots & \vdots & \vdots & \vdots & \vdots & \vdots \\ 0 & \cdots & 0 & c_{m_x,m_y}(1) & c_{m_x,m_y}(2) & \cdots & c_{m_x,m_y}(K) \end{bmatrix}. \tag{5.34}$$

Signal received from region Ω_{m_x,m_y} can be expressed as

$$\mathbf{S}_{m_x,m_y} = \boldsymbol{\alpha}_{m_x,m_y} \times_1 \mathbf{A}_{x,m_x} \times_2 \mathbf{A}_{y,m_y} \times_3 \mathbf{C}_{m_x,m_y}, \tag{5.35}$$

where $\boldsymbol{\alpha}_{m_x,m_y}$ is the reflectivity matrix, $\times_i$ expresses product in the i^{th} dimension. Signal received from all region can be expressed as

$$\mathbf{S} = \sum_{m_x=0}^{M_x-1} \sum_{m_y=0}^{M_y-1} \boldsymbol{\alpha}_{m_x,m_y} \times_1 \mathbf{A}_{x,m_x} \times_2 \mathbf{A}_{y,m_y} \times_3 \mathbf{C}_{m_x,m_y}. \tag{5.36}$$

In order to express $\mathbf{S}$ as a single multi-dimensional linear equation, $\boldsymbol{\alpha}_{m_x,m_y}$ can be rearranged as shown in Fig.5.11

That is $\boldsymbol{\alpha}_{m_x,m_y}$ is pushed to rear and keep the cross range coordinate static.

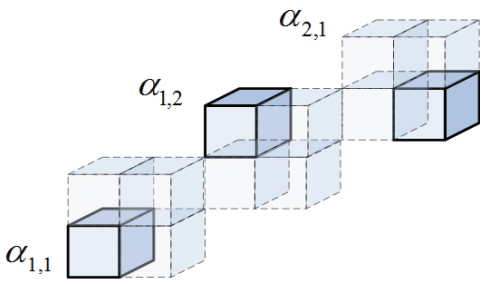

Figure 5.11: Rearrangement of reflectivity matrix.

One $\boldsymbol{\alpha}_{m_x,m_y}$ occupies only one segment and the new $\boldsymbol{\alpha}$ occupies $M_x \times M_y \times L_2$ range length, where L_2 is the range length of the imaging region.

Denote $\mathbf{A}_x = [\mathbf{A}_{x,0}, \mathbf{A}_{x,1}, \cdots, \mathbf{A}_{x,M_x-1}]$, $\mathbf{A}_y = [\mathbf{A}_{y,0}, \mathbf{A}_{y,1}, \cdots, \mathbf{A}_{y,M_y-1}]$ and

$$\mathbf{C} = \begin{bmatrix} \mathbf{c}_{0,0} \\ \mathbf{c}_{0,1} \\ \vdots \\ \mathbf{c}_{M_x-1,M_y-1} \end{bmatrix}. \tag{5.37}$$

where the order of $\mathbf{c}_{m_x,m_y}$ are the same as that of $\boldsymbol{\alpha}_{m_x,m_y}$, then $\mathbf{S}$ can be expressed as

$$\mathbf{S} = \boldsymbol{\alpha} \times_1 \mathbf{A}_x \times_2 \mathbf{A}_y \times_3 \mathbf{C} \tag{5.38}$$

If linear equation is used to express the imaging system, the dimension of the coefficient matrix is $N_1N_2(K+L_2)\times PM_xQM_YL_2$, where K is the length of the code. However the dimensions of $\mathbf{A}_x$, $\mathbf{A}_y$ and $\mathbf{C}$ are $N_1 \times PM_x$, $N_2 \times QM_y$ and $M_xM_yL_2 \times (L_2 + K)$. It can be seen that the memory needs by tensor equation is great less than that of linear system.

5.3.4 Multi-Dimensional Linear Equation $\ell_1\,\ell_0$ Norms Homotopy Sparse Signal Recover Algorithm

Similar to $\ell_1\,\ell_0$ norms homotopy algorithm for linear equations, $\ell_1\,\ell_0$ norms homotopy algorithm for multi-dimensional linear equations (MD $\ell_1\,\ell_0$) can be designed. Define $G_\sigma(\boldsymbol{\alpha}) = \sum_m \sum_n \sum_k g_\sigma(\alpha(m,n,k))$. The sparse signal recovery criterion can be described as:

$$\hat{\boldsymbol{\alpha}} = \lim_{\sigma \to \sigma_{min}} \arg\min G_\sigma(\boldsymbol{\alpha}) \quad \text{subject to} \, ||\mathbf{S} - \boldsymbol{\alpha} \times_1 \mathbf{A}_x \times_2 \mathbf{A}_y \times_3 \mathbf{C}||_F < \varepsilon. \tag{5.39}$$

where $||\cdot||_F$ is the Frobenius norm of a tensor. The MD $\ell_1\,\ell_0$ algorithm can be expressed as:

Multi-Dimensional Linear Equations $\ell_1\,\ell_0$ Norms Homotopy (MD $\ell_1\,\ell_0$) Algorithm

---

- Initialization:

  1) Define L_0, L_1.

  2) Let $\hat{\boldsymbol{\alpha}}_0$ be equal to the minimum Frobenius norm solution of (5.38), obtained by $\hat{\boldsymbol{\alpha}}_0 = \mathbf{S} \times_1 \mathbf{A}_x^\dagger \times_2 \mathbf{A}_y^\dagger \times_3 \mathbf{C}^\dagger$.

  3) Choose a suitable decreasing sequence for $\{\sigma\}$, $[\sigma_1, \cdots, \sigma_J]$.

- for $j = 1, \cdots, J$:

  1) Minimize the function $G_{\sigma_j}(\boldsymbol{\alpha})$ on the feasible set $\{\boldsymbol{\alpha} : ||\mathbf{S} - \boldsymbol{\alpha} \times_1 \mathbf{A}_x \times_2 \mathbf{A}_y \times_3 \mathbf{C}||_F < \varepsilon\}$ using L iterations of the revised steepest descent gradient algorithm (followed by projection onto the feasible set):

- Initialization: $\boldsymbol{\alpha} = \hat{\boldsymbol{\alpha}}_{j-1}$

- For $\ell = 1, \cdots, L$ (loop L times):

  a) Let $\boldsymbol{\delta}$ be gradient of $G_{\sigma_j}(\boldsymbol{\alpha})$ and $\mu = min(max(|\boldsymbol{\alpha}|)/L_0, \sigma_j/L_1)$.

  b) For every element of $\boldsymbol{\alpha}$, let
  $\alpha(m,n,k) \leftarrow \alpha(m,n,k) - \frac{\alpha(m,n,k)}{|\alpha(m,n,k)|} \times min(|\alpha(m,n,k)|, |\mu\sigma_j\delta(m,n,k)|)$.

  c) For $\boldsymbol{\alpha}$ such as in Eq.(5.23) and Fig.5.11, we let the $\boldsymbol{\alpha}$ satisfy the structure of Eq.(5.23) and Fig.5.11.

  d) If $||\mathbf{S} - \boldsymbol{\alpha} \times_1 \mathbf{A}_x \times_2 \mathbf{A}_y \times_3 \mathbf{C}||_F > \varepsilon$, project $\boldsymbol{\alpha}$ back into the feasible set:
  $\boldsymbol{\alpha} \leftarrow \boldsymbol{\alpha} + (\mathbf{S} - \boldsymbol{\alpha} \times_1 \mathbf{A}_x \times_2 \mathbf{A}_y \times_3 \mathbf{C}) \times_1 \mathbf{A}_x^{\dagger} \times_2 \mathbf{A}_y^{\dagger} \times_3 \mathbf{C}^{\dagger}$

2) Set $\hat{\boldsymbol{\alpha}}_j = \boldsymbol{\alpha}$

- Final answer is $\hat{\boldsymbol{\alpha}} = \hat{\boldsymbol{\alpha}}_J$

5.3.5 Multi-Dimensional Linear Equations Based Simulation Results

Simulation 1: 2D Imaging Using One Dimensional MIMO Array

In this simulation, the simulation conditions are the same as that of simulation 1 of section 5.2.4 except that the distance between the sampling grid points at X and Y axes are all 0.5 m. The dimension of $\mathbf{A}$ and $\mathbf{C}$ are 8×128 and 736×124. (For the sampling distance of 0.25, same as simulation 1 of section 5.2.4, the dimension of $\mathbf{A}$ and $\mathbf{C}$ are 8×256 and 2944×124). The dimension is less than 984×8464 in simulation 1 of section 5.2.4. The image obtained is shown in Fig.5.12. It can be seen that the performance is similar to that of simulation 1 of section 5.2.4, where linear equation model is used.

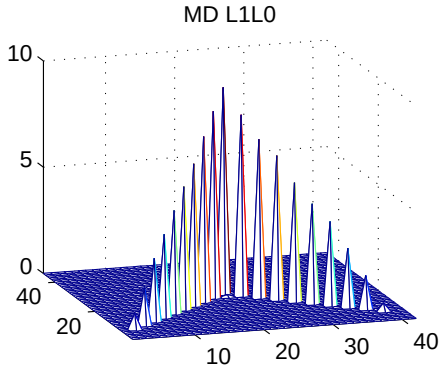

Figure 5.12: Reconstructed image using multi-dimensional linear equations signal model(simulation 1).

Simulation 2: 3D Imaging Using Two Dimensional Cross MIMO Array

The simulation conditions are the same as that of simulation 3 of section 5.2.4 except that the MIMO array is a 16×16 cross array, while in simulation 3 of section 5.2.4 the transmit MIMO array and receive MIMO array are all 4×4 square array. The total number of transmit antennas and receive antennas for two cases are the same. The inter-element distances of the transmit array and the receive array are all 93.75 m. The unambiguous distance are divided as 64 divisions. The dimensions of the coefficient matrices of $\mathbf{A}$ and $\bar{\mathbf{C}}$ are 16×64 and 3200×125, which are less than the dimension 1968×31620 of $\mathbf{\Psi}$ in simulation 3 of section 5.2.4. Parameters in the multi-dimensional linear equations $\ell_1\,\ell_0$ homotopy algorithm are $\varepsilon^2 = 0, \sigma_J = 0.003, J = 25, L = 40, L_0 = 20, L_1 = 20$. The images using minimum ℓ_2 norm criterion and using MD $\ell_1\,\ell_0$ homotopy algorithm are shown in Fig.5.13 It can be seen that the image using minimum ℓ_2 norm criterion has high sidelobes and the performance using multi-dimensional linear equations is similar to that of using linear equations as shown in Fig.5.5(f).

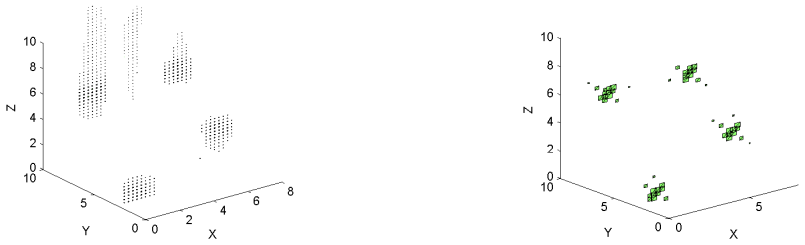

(a) (b)

Figure 5.13: Reconstructed images using cross array MIMO radar multi-dimensional linear equations signal model. (a) minimum ℓ_2 norm method, (b) MD $\ell_1\,\ell_0$ homotopy algorithm, $\varepsilon^2 = 0, \sigma_J = 0.003, J = 25, L = 40, L_0 = 20, L_1 = 20$.

5.4 Distributed MIMO Radar 3D Imaging Using Sparse Signal Recovery Algorithm

In the last section, collocated MIMO radar signal model fitting to sparse signal recovery algorithm was derived. In the following subsection, distributed MIMO radar signal model is derived.

5.4.1 Distributed MIMO Radar Signal Model

The distributed MIMO radar imaging geometry is shown in Fig.5.14.

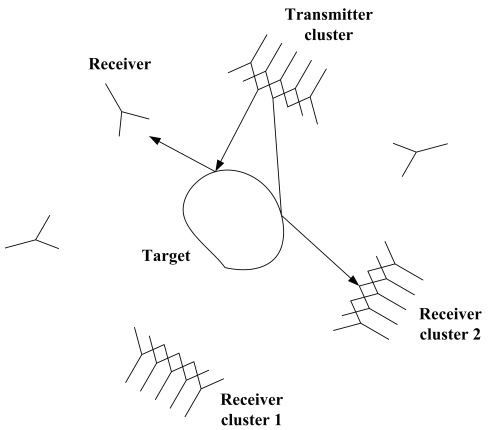

Figure 5.14: Geometry of distributed MIMO radar.

Let $\mathbf{H}_0$ denote the magnetic field from one transmitter, $\mathbf{r}'$ denote one point

on the surface ∂D of a target, where the outwardly directed unit normal to ∂D at $\mathbf{r}'$ is denoted as $\hat{\mathbf{n}}$. The incident magnetic field at $\mathbf{r}'$ is then $\mathbf{H}_{inc} = \mathbf{H}_0 exp(-j2\pi r_1/\lambda)/r_1$, where r_1 is the distance from the transmitter to $\mathbf{r}'$. In the far field, using physical optics approximation, the induced current $\mathbf{J}$ on a conducing surface can be approximately expressed as [15]

$$\mathbf{J}(\mathbf{r}^{'}) = \begin{cases} 2\hat{\mathbf{n}} \times \mathbf{H}_{inc}(\mathbf{r}') & if \quad \hat{\mathbf{r}}_1 \cdot \hat{\mathbf{n}} < 0 \\ 0 & otherwise, \end{cases} \tag{5.40}$$

where $\hat{\mathbf{r}}_1$ is the transmitter line of sight unit vector.

Let the receive antenna be located at $\mathbf{r}$. The distance between $\mathbf{r}$ and $\mathbf{r}'$ is r_2. The vector potential $\mathbf{A}(\mathbf{r})$ due to the presence of the electric current density $\mathbf{J}(\mathbf{r}^{'})$ is [16]

$$\mathbf{A}(\mathbf{r}) = \iiint \frac{e^{-j2\pi r_2/\lambda}}{4\pi r_2} \mu_0 \mathbf{J}(\mathbf{r}')d\mathbf{r}', \tag{5.41}$$

where μ_0 is the permeability of free space. The scattered magnetic field at $\mathbf{r}$ is

$$\mathbf{H}(\mathbf{r}) = \nabla \times \iiint \frac{e^{-j2\pi r_2/\lambda}}{4\pi r_2} \mathbf{J}(\mathbf{r}')d\mathbf{r}'. \tag{5.42}$$

Denote $\hat{\mathbf{r}}_2$ as the receiver to the target line of sight unit vector. ∇ operator can be approximated as $-j\frac{2\pi}{\lambda}\hat{\mathbf{r}}_2$ in the far field. The scattered magnetic field can then be simplified as

$$\mathbf{H}(\mathbf{r}) = \xi \iint_{\Omega} \hat{\mathbf{r}}_2 \times (\hat{\mathbf{n}} \times \hat{\mathbf{H}}_0) e^{\frac{-j2\pi(r_1+r_2)}{\lambda}} dS \tag{5.43}$$

where Ω is the integration area, $\Omega = \{\partial D, \hat{\mathbf{r}}_1 \cdot \hat{\mathbf{n}} < 0, \hat{\mathbf{r}}_2 \cdot \hat{\mathbf{n}} < 0\}$, $\xi = \frac{-jH_0}{\lambda r_1 r_2}$ is a constant, $\hat{\mathbf{H}}_0 = \frac{\mathbf{H}_0}{||\mathbf{H}_0||}$. The equation in (5.43) is a bistatic radar signal model. Denote $\hat{\mathbf{m}}$ the polarization unit vector of the receive antenna, the received signal at $\hat{\mathbf{m}}$ direction is then $H(\mathbf{r}) = \mathbf{H}(\mathbf{r}) \cdot \hat{\mathbf{m}}$. $H(\mathbf{r})$ can be approximated using the principle of stationary phase, then we have

$$H(\mathbf{r}) = \frac{-jH_0}{\lambda\tilde{r}_1\tilde{r}_2}\sum_m \alpha_m e^{-\frac{j2\pi(r_{1,m}+r_{2,m})}{\lambda}} + o(\tilde{r}_1^{-1}\tilde{r}_2^{-1}), \tag{5.44}$$

where the sum is over all points $\mathbf{r}_m^{'}$ on ∂D, and $\mathbf{r}_m^{'}$ is the tangential point between ∂D and an ellipse with the transmitter and the receiver be two focuses. $r_{1,m}$ and $r_{2,m}$ are the distances between the transmitter and $\mathbf{r}_m^{'}$, the distance between the receiver and $\mathbf{r}_m^{'}$, respectively. $\tilde{r}_1$ and $\tilde{r}_2$ are the distances between the transmitter, the receiver and the target center respectively. α_m denotes the contribution to the integral in (5.43) of the local neighborhood $N_{r_m^{'}} \subset \partial D$ of $\mathbf{r}_m^{'}$, where the signals have approximately the same phase.

For the special case of a monostatic radar, because $\hat{\mathbf{r}}_2 \times (\hat{\mathbf{n}} \times \hat{\mathbf{H}}_0) = \hat{\mathbf{n}}(\hat{\mathbf{r}}_2 \cdot \hat{\mathbf{H}}_0) - (\hat{\mathbf{r}}_2 \cdot \hat{\mathbf{n}})\hat{\mathbf{H}}_0$, $\hat{\mathbf{m}} = \hat{\mathbf{H}}_0$ and $\hat{\mathbf{r}}_2 \cdot \hat{\mathbf{H}}_0 = 0$, we have $\hat{\mathbf{m}} \cdot \left(\hat{\mathbf{r}}_2 \times (\hat{\mathbf{n}} \times \hat{\mathbf{H}}_0)\right) = -(\hat{\mathbf{r}}_2 \cdot \hat{\mathbf{n}})$. At point $\mathbf{r}_m^{'}$, $(\hat{\mathbf{r}}_2 \cdot \hat{\mathbf{n}}) = -1$. If the surface near $\mathbf{r}_m'$ is a planar patch, α_m is the geometric area of this patch. So, α_m can be regarded as an "effective area".

But for the bistatic radar case, usually $\hat{\mathbf{m}} \cdot \left(\hat{\mathbf{r}}_2 \times (\hat{\mathbf{n}} \times \hat{\mathbf{H}}_0)\right)$ will be less than 1. Even for a planar patch, α_m will also be less than the geometric area. $-jH_0/(\lambda\tilde{r}_1\tilde{r}_2)$ is a constant and can be combined into α_m to simplify the expression. After α_m has been estimated, the patch can be established.

In the above derivation, we assume a bistatic radar working at a single frequency. Now we derive the signal model of a distributed wideband MIMO radar imaging system. Let L be the one dimensional size of a patch on the surface of the target. If the patch is regarded as an antenna, its beam width in this dimension is about $\frac{\lambda}{L}$. Let the distance between two antennas in this dimension be d, if $r\frac{\lambda}{L} < d$, the signal amplitudes received by these two antennas from this patch can be regarded as different. If $r\frac{\lambda}{L} >> d$, the signal amplitudes received by these two antennas from this patch can be regarded as

the same, and these two antennas can be regarded as collocated and belong to one antenna cluster. We assume that there are M_T transmitter clusters and N_R receiver clusters. The antennas in each cluster are collocated. For the i^{th} transmitter cluster, there are M_i transmitting antennas. For the j^{th} receiver cluster, there are N_j receiving antennas.

Let $\mathbf{w}_{i,i'}$ be the transmitting code envelope function at i'^{th} transmitter of i^{th} cluster, $\tau^t_{i,i'}$ be the delay from $(i,i')^{th}$ transmitter to k^{th} scatterer, $\tau^r_{j,j'}$ be the delay from k^{th} scatterer to $(j,j')^{th}$ receiver. We first consider that there is only one scatterer k. In order to express the equations in a concise form, we omit the relation with k when there is no confusion. After mixing, the received back-scattered signal at $(j,j')^{th}$ receiver can be expressed as

$$\mathbf{s}_{j,j'} = \sum_{i=1}^{M_T} \alpha_{i,j} \sum_{i'=1}^{M_i} \mathbf{w}_{i,i'}(t - \tau^t_{i,i'} - \tau^r_{j,j'}) e^{-j2\pi f(\tau^t_{i,i'} + \tau^r_{j,j'})} \tag{5.45}$$

where $\alpha_{i,j}$ is the reflection coefficient between transmitter cluster i, scatterer k and receiver cluster j (note that $\alpha_{i,j}$ is independent of $i^{'}$ and $j^{'}$). Define

$$\boldsymbol{\varphi}_{i,j,j'} = \sum_{i'=1}^{M_i} \mathbf{w}_{i,i'}(t - \tau^t_{i,i'} - \tau^r_{j,j'}) e^{-j2\pi f(\tau^t_{i,i'} + \tau^r_{j,j'})}, \tag{5.46}$$

we have

$$\mathbf{s}_{j,j'} = \sum_{i=1}^{M_T} \alpha_{i,j} \boldsymbol{\varphi}_{i,j,j'}. \tag{5.47}$$

Define $\boldsymbol{\Phi}_{j,j'} = [\boldsymbol{\varphi}_{1,j,j'}, \cdots, \boldsymbol{\varphi}_{M_T,j,j'}]$, $\boldsymbol{\alpha}^k_j = [\alpha_{1,j}, \cdots, \alpha_{M_T,j}]^T$, then $\mathbf{s}_{j,j'}$ can be simply expressed as

$$\mathbf{s}_{j,j'} = \boldsymbol{\Phi}_{j,j'} \boldsymbol{\alpha}^k_j. \tag{5.48}$$

Define $\mathbf{s}_j = [\mathbf{s}^T_{j,1}, \cdots, \mathbf{s}^T_{j,N_j}]^T$, $\boldsymbol{\Phi}^k_j = [{\boldsymbol{\Phi}_{j,1}}^T, \cdots, {\boldsymbol{\Phi}_{j,N_j}}^T]^T$, we have

$$\mathbf{s}_j = \boldsymbol{\Phi}^k_j \boldsymbol{\alpha}^k_j. \tag{5.49}$$

Here we use a superscript k to emphasize that $\boldsymbol{\Phi}^k_j$ and $\boldsymbol{\alpha}^k_j$ are related to

scatterer k. Assume that the imaging area is divided into K grids. Define $\mathbf{\Phi}_j = [\mathbf{\Phi}_j^1, \cdots, \mathbf{\Phi}_j^K]$, $\boldsymbol{\alpha}_j = [\boldsymbol{\alpha}_j^{1^T}, \cdots, \boldsymbol{\alpha}_j^{K^T}]^T$, the total signal model is

$$\mathbf{s}_j = \mathbf{\Phi}_j \boldsymbol{\alpha}_j + \mathbf{n}, \quad j = 1, \cdots, N_R, \tag{5.50}$$

where $\mathbf{n}$ is the noise and modeling error. The dimensions of $\mathbf{s}_j$, $\mathbf{\Phi}_j$ and $\boldsymbol{\alpha}_j$ are $LN_j \times 1$, $LN_j \times M_T K$ and $M_T K \times 1$, respectively, where L is the length of signal collected in fast time.

So far we have obtained N_R linear equations. Because $\boldsymbol{\alpha}_j$ is only related to $\mathbf{s}_j$, and independent of $\mathbf{s}_i, i \neq j$, there is no need to stack $\mathbf{s}_j$ and $\boldsymbol{\alpha}_j$ to form a bigger $\mathbf{s}$ and a bigger $\boldsymbol{\alpha}$. It means that one receiver cluster and all transmitter clusters form an imaging system, another receiver cluster and all transmitter clusters form another imaging system. All of the $\boldsymbol{\alpha}_j$ obtained are combined to form the image of the target. From the definition of $\alpha_{i,j}$, we see that for one scatterer there are $M_T \times N_R$ amplitudes corresponding to $M_T \times N_R$ transmitter-receiver cluster pairs. So after the $\{\alpha_{i,j}\}$ has been obtained, the maximum value of $\{\alpha_{i,j}\}$ can be selected to form the image of the target. Eq. (5.50) can also be solved by $\ell_1\,\ell_0$ homotopy method.

5.4.2 Antennas Configuration and Signal Property

According to the analysis of high frequency signal model in section 5.4.1, the strong scatterers are mainly coming from the reflection surface (relative to the transmitter and the receiver) of the target. So the distribution of transmitters and receivers should be such that the reflection patches are covered as much as possible. Now we consider two special imaging geometries: (a) two distributed antennas operate as receivers and a collocated array as transmitter; (b) two distributed antennas operate as transmitters and a collocated array as receiver.

The number of antennas in the above two cases are the same. According to section 5.4.1, the signal model of (a) for two receivers are

$$\mathbf{s}_{a1} = \left(\sum_{i'=1}^{M_1} \mathbf{w}_{i'} (t - \tau_{i'}^t - \tau_1^r) e^{-j2\pi f(\tau_{i'}^t + \tau_1^r)} \right) \alpha_{a,1,1} \tag{5.51}$$

and

$$\mathbf{s}_{a2} = \left(\sum_{i'=1}^{M_1} \mathbf{w}_{i'} (t - \tau_{i'}^t - \tau_2^r) e^{-j2\pi f(\tau_{i'}^t + \tau_2^r)} \right) \alpha_{a,1,2}, \tag{5.52}$$

here we assume that there is only one scatterer, $\alpha_{a,1,1}$ and $\alpha_{a,1,2}$ are the reflection coefficients of this scatterer for different transmitter-receiver pairs, where the first subscript expresses transmitter and the second subscript expresses receiver. The signal model of (b) for two transmitters can be expressed as:

$$\mathbf{s}_b = \begin{bmatrix} \mathbf{w}_1(t - \tau_1^t - \tau_1^r) e^{-j2\pi f(\tau_1^t + \tau_1^r)} & , & \mathbf{w}_2(t - \tau_2^t - \tau_1^r) e^{-j2\pi f(\tau_2^t + \tau_1^r)} \\ \vdots & , & \vdots \\ \mathbf{w}_1(t - \tau_1^t - \tau_{N_1}^r) e^{-j2\pi f(\tau_1^t + \tau_{N_1}^r)} & , & \mathbf{w}_2(t - \tau_2^t - \tau_{N_1}^r) e^{-j2\pi f(\tau_2^t + \tau_{N_1}^r)} \end{bmatrix} \begin{bmatrix} \alpha_{b,1,1} \\ \alpha_{b,2,1} \end{bmatrix} \tag{5.53}$$

where $\mathbf{s}_b = \left[\mathbf{s}_1^T, \cdots, \mathbf{s}_{N_1}^T \right]^T$, $\alpha_{b,1,1}$ and $\alpha_{b,2,1}$ are the reflection coefficients of this scatterer for different transmitter-receiver pairs.

Because Eq. (5.51), (5.52) are two independent equations, the solution of $\alpha_{a,1,1}$ does not affect $\alpha_{a,1,2}$, which means that the solutions of this kind of system are easier to be obtained. However, from equation (5.53), it shows that $\alpha_{b,1,1}$ and $\alpha_{b,2,1}$ are coupled, which means that the solution of $\alpha_{b,1,1}$ affects $\alpha_{b,2,1}$. It is relatively difficult to solve this system compared with case (a). The dimensions of $\mathbf{s}_{a1}$ and $\mathbf{s}_{a2}$ are only L, but the dimension of $\mathbf{s}_b$ is as long as LN_1, where L is the length of signal in time domain, N_1 is the number of antennas of the receive array ($N_1 = M_1$).

The property of the coefficient matrix is very important in imaging system configuration and algorithm design. For MIMO radar configuration, it is diffi-

cult to derive an analytic expression of the point spread function (correlation between columns of coefficient matrix $\mathbf{\Phi}_j$). But numerical solution can be obtained by simulations. Let the carrier frequency be 2 GHz, 18-element linear transmitter array with inter-element distance of 300 m, is located at (0,-200) km along the X axis. One receiver is located at (200,0) km. Eighteen random BPSK codes with length of 100 are transmitted. The range resolution is one meter. Fig.5.15 shows the point spread function for a limited range when the origin is the center point of the point spread function. It can be seen that though there is only one receiver, but because 18 transmitters transmit independent codes, a nail shape point spread function is also obtained. Because the phase centers of the transmitters and the receiver are located at (0,-200) km and (200,0) km, the cross-range direction is along the 45^o direction, as seen from Fig. 5.15. High sidelobes are also produced due to the small number of transmitters.

For case (b), we need to consider point spread function for one transmitter-receiver-array pair and the cross-correlation between different transmitter-receiver-array pairs. When a transmitter is located at $(200, 0)$ m, the receiver array is at (0,-200) km and along the X direction, the point spread function at origin is shown in Fig.5.16. Because the dimension of the basis vector of case (b) is longer than that of case (a), the sidelobes of case (b) is lower than case (a). The second transmitter is located at $(-153209.8, -128556.5427)$ m. The basis function of first transmitter-receiver-array pair is chosen as come from the origin. The cross correlation between the first and second transmitter-receiver-array pairs near the origin is shown in Fig.5.17. It can be seen that the cross correlations have small values compared with the auto-correlation at the origin.

If there is only one receiver at case (a) and there is only one transmitter

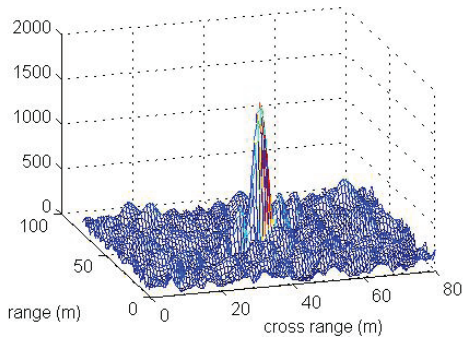

Figure 5.15: The point spread function of case (a) where a linear transmitting antenna array is located at (0, -200)km and along the x axis, a receiver is located at (200,0)km.

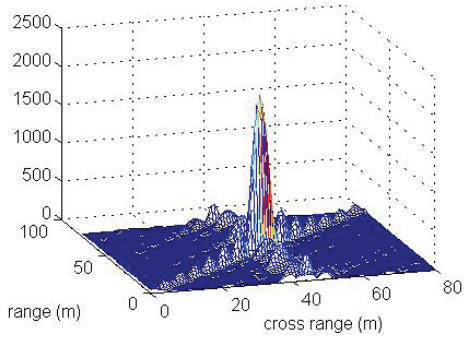

Figure 5.16: The point spread function of one transmitter-receiver pair of case (b) where a linear receiving antenna array is located at (0, -200)km and along the x axis, a transmitter is located at (200,0)km.

in case (b), the performance of (b) will be better than case (a), because the dimension of the coefficient matrix of case (b) is longer than that of case (a) and the sidelobes of case (b) is lower than case (a).

However, with the increase of number of receivers in case (a) and transmitters in case (b) simultaneously , the dimension of the coefficient matrix of case (a) does not change, but the number of columns of coefficient matrix of case (b) increases linearly with the increase of transmitters while the number of rows keep to a constant. This means the interference between different transmitter-receiver pairs increase.

So for limited number of antennas, the number of transmitters and receivers

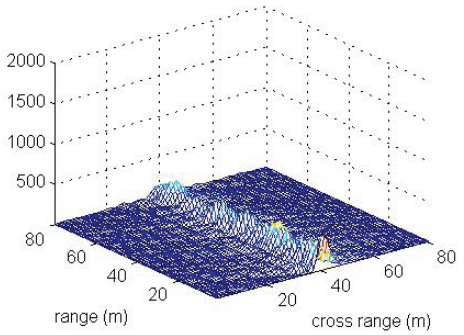

Figure 5.17: The cross correlation of case (b) where a linear receiving antenna array is located at (0, -200)km and along the x axis, the two transmitters are located at (200,0)km and $(-153209.8, -128556.5427)$ m, respectively. The signal corresponding to transmitter one at (200,0)km is come from the origin. The signal corresponding to the second transmitter varies with different positions.

should be balanced bearing in mind that one transmitter-receiver-array pair is sufficient to obtain the desired resolution.

5.4.3 Simulation of Imaging of a Two Dimensional Circle

In this subsection, we present a simulation of two dimensional imaging results using distributed MIMO radar. The carrier frequency is 1 GHz, and the signal bandwidth is 300M Hz. The target is a metal plate with radius of 5 m and located at the center of XY plane. Three transmit antenna arrays, each with 8 antennas with inter-element-distance of 750 m and arranged in an arc shape facing toward the origin, are located at (20 km, 200^o), (20 km, 270^o) and (20 km, 350^o). Two receive antenna arrays, each with 8 antennas with inter-element-distance of 93.75 m, are located at (20 km, 230^o) and (20 km, 320^o). Twenty four BPSK signals with length of 100 are used as transmitting codes. When generating data, the circle is divided with step size of $\lambda/10$. The imaging sampling grid intervals in X and Y directions are all chosen as 0.06 m. The

image using conventional correlation method is shown in Fig.5.18. It can be seen that high sidelobes occurs. Fig.5.19 shows the reconstructed images using three transmitter arrays and only one receiver array. The images are obtained by $\ell_1\,\ell_0$ method with parameters $\sigma_J = 0.005$, $\varepsilon^2 = 3$, $J = 25$, $L = 25$, $L_1 = 20$ and $L_0 = 20$. Fig.5.19(a) is the image using the first receiver, Fig.5.19(b) is the image using the second receiver. It can be seen that different antennas observe the target from different views and obtain different images. If there is only one transmitter array, the receiver can only observe a narrower scene. Fig.5.20 shows the reconstructed images using OMP method with assumed number of nonzero element of $K = 4, 6, 7, 9$. The matlab program of OMP is downloaded from http://www.mathworks.com/matlabcentral/fileexchange/authors /30530 contributed by Dr. Stephen Becker. For smoothed ℓ_0 and $\ell_1\,\ell_0$ methods, we choose $J = 25$, $L = 25$. Parameters of L_0 and L_1 in $\ell_1\,\ell_0$ method are all chosen as 20. For smoothed ℓ_0 norm method, cases of $\sigma_J = 0.0001$, 0.0002, 0.0005, and 0.001, $\varepsilon^2 = 3$ are imaged and shown in Fig.5.21. For $\ell_1\,\ell_0$ method, cases of $\sigma_J = 0.001$, 0.002, 0.005, and 0.01, $\varepsilon^2 = 3$ are imaged and shown in Fig.5.22. From these simulations we can see that using distributed MIMO radar, more shape information of the target can be obtained. For OMP method, with the increase of the assumed sparsity, more shape information are observed, however more noises are appeared. For SL0 and $\ell_1\,\ell_0$ methods, with the decrease of σ_J, more noises are observed. Compared with OMP, SL0 and $\ell_1\,\ell_0$ with other parameters, $\ell_1\,\ell_0$ method for $\sigma_J = 0.005$ has best performance.

5.5 Conclusion

Because the strong scatterers are sparse, a $\ell_1\,\ell_0$ homotopy sparse signal recovery algorithm is used to improve the image quality. For a target with large

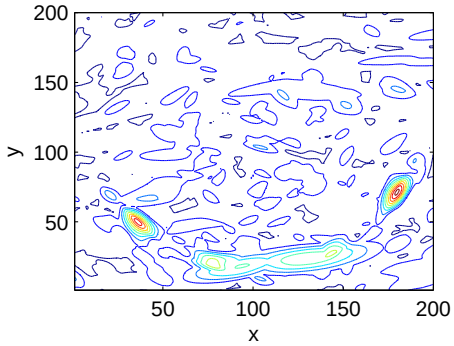

Figure 5.18: Target's image using conventional correlation method.

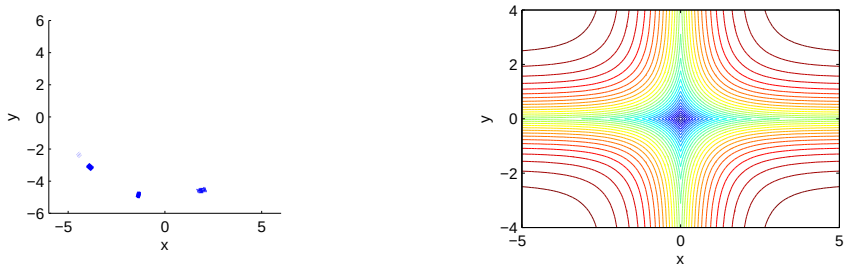

(a) (b)

Figure 5.19: Reconstructed images using distributed MIMO radar with only one collocated antenna array receiver configuration and complex $\ell_1\,\ell_0$ homotopy sparse signal recovery algorithm. $\sigma_J = 0.005, \varepsilon^2 = 3$. (a) First receiver, (b) Second receiver.

patches towards the radar, the total variations of the reflections are large value at the edge of the patches, a combined amplitude and total variation objective function is proposed.

The dimension of the coefficient matrix of the linear system for MIMO radar imaging is large. It requires huge memory. In order to save memory, multi-dimensional linear equations based signal model is derived. $\ell_1\,\ell_0$ homotopy sparse signal recovery algorithm for multi-dimensional linear equations signal model is also presented.

Conventional mono-static radar observes the target from one view direction and can only obtain part information of a target. Distributed radar observes the target from multiple view directions, more information of the target can

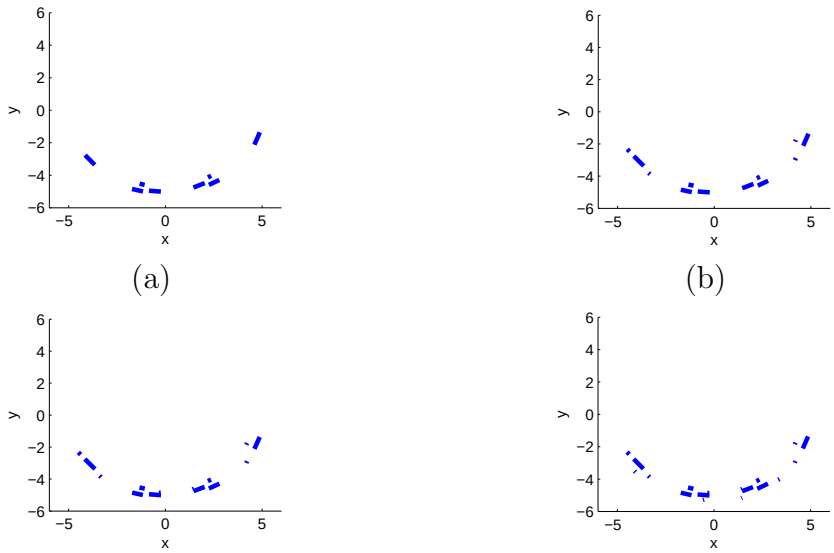

Figure 5.20: Reconstructed images using distributed MIMO radar and OMP method assuming sparsity of (a)K=4, (b) K=6, (c) K=7, (d) K=9.

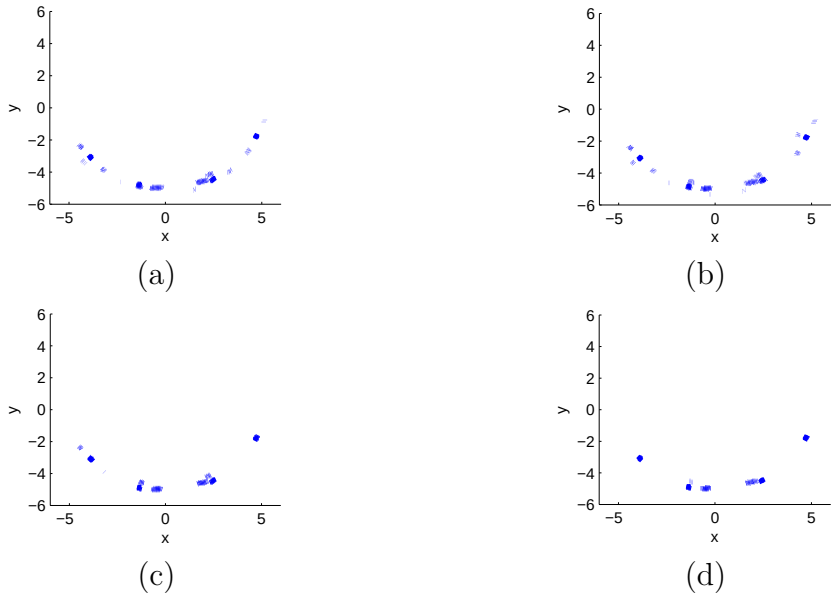

Figure 5.21: Reconstructed image using distributed MIMO radar and complex smoothed ℓ_0 norm method. $\varepsilon^2 = 3$, (a) $\sigma_J = 0.0001$, (b) $\sigma_J = 0.0002$,(c) $\sigma_J = 0.0005$, (d) $\sigma_J = 0.001$.

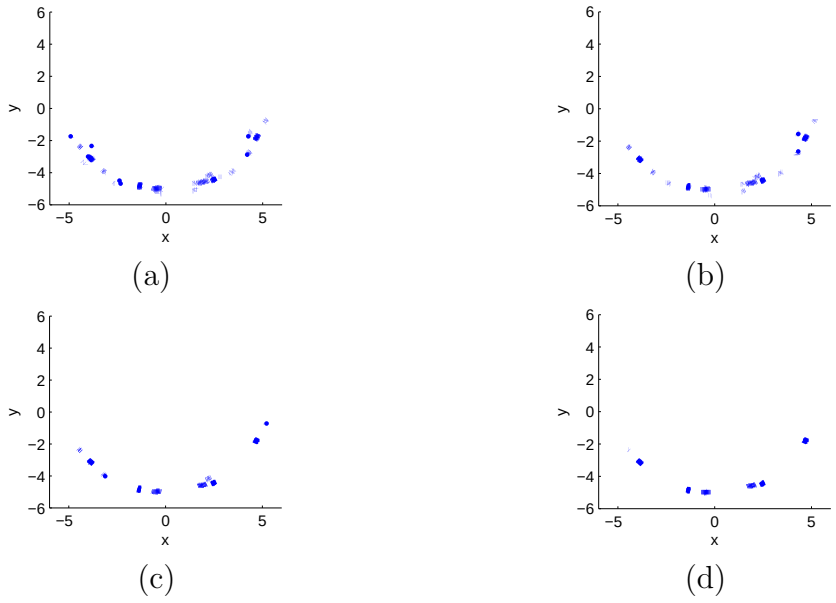

Figure 5.22: Reconstructed image using distributed MIMO radar and complex $\ell_1\,\ell_0$ norms homotopy method. $\varepsilon^2 = 3$, (a) $\sigma_J = 0.001$, (b) $\sigma_J = 0.002$,(c) $\sigma_J = 0.005$, (d) $\sigma_J = 0.01$.

thus be obtained. The distributed MIMO radar imaging signal model is derived in this Chapter. The conditions that antennas can be regarded as a cluster of antennas and coherent property be preserved are discussed. Due to the sparsity of strong scatterers, the image can be obtained by sparse signal recovery algorithms. Because every point is observed from all transmitter-receiver pairs, there are many images for one point of the target. The maximum value is chosen to form the image.

Simulation results show that the image quality has been improved using sparse signal recovery algorithms and the proposed $\ell_1\,\ell_0$ homotopy method has competitive performance.

Chapter 6

Bistatic ISAR Imaging Incorporating Interferometric 3D Imaging Technique

6.1 Introduction

For collocated ISAR, the transmitter and receiver are located on the same place. The transmitter transmit high power microwave energy, which can be easily detected and the radar is easy be destroyed. For bistatic radar, the transmitter and the receiver are located on two different positions, the transmitter can be far away from the enemy field to avoid being attacked. In addition, the bistatic receiver is passive and thus electromagnetically invisible to the third party and can be near the target. On the other hand, the bistatic receiver observe the target from different directions. The scattering mechanism is different from monostatic radar. So the bistatic ISAR image is different from the monostatic ISAR image [72]. BiISAR provides complementary information of the target. Because of these advantages, BiISAR has been studied by many

researchers recently [73] [74]. The major processing steps of BiISAR are similar to the ISAR. It includes range compression, motion compensation and cross-range Fourier transform. Because of the similarity, some researchers surmise that from signal processing aspect the bistatic radar can be replaced by a monostatic equivalent radar [73] . For applications of ranging and range-speed estimation, this simplification is sufficient and adequate. However, for general BiISAR imaging, this simplification is neither sufficient nor adequate, because the information used in BiISAR to image the target in the cross-range direction is the difference in Doppler frequencies, and not the Doppler frequency itself. For BiISAR, the gradient of iso-Doppler frequency planes characterizes this difference in Doppler frequencies. For a moving target, generally, the gradient direction of the iso-Doppler planes is not perpendicular to the range direction. This fact is different from monostatic ISAR.

In ISAR and BiISAR imagings, the ISAR and BiISAR images are the projections of the target on a plane with the direction of range and direction of gradient of Doppler frequencies as the two axes. Because the two axes are not perpendicular in BiISAR case, the BiISAR image is sheared. This distortion has not been analyzed before, although distortion of point spread function (PSF) had been discussed in [75] and the simulations of [76] had showed the shear of BiISAR image.

The shear of the BiISAR image makes it difficult for use in target identification application. In order to correct the shear of BiISAR image, we propose using interferometric techniques. Interferometric techniques have been widely used in interferometric SAR and interferometric ISAR 3D imaging [9], [77]. For interferometric ISAR, three antennas are usually used to measure the two cross-range coordinates of a scatterer. In addition to the range information, 3D image can be obtained. But because the range directions of monostatic

ISAR and BiISAR are different, the coordinate transformation of interferometric BiISAR is different from that of monostatic interferometric ISAR. The coordinate transformation formula of BiISAR is given in this Chapter.

This Chapter is organized as follows. In section 6.2, the bistatic radar signal model and BiISAR imaging algorithm are discussed. Interferometric 3D imaging is discussed in section 6.3. Simulation results are demonstrated in section 6.4 and we conclude our works in section 6.5.

6.2 The Bistatic Radar Signal Model and Bi-ISAR Imaging Algorithm

The geometry of the bistatic ISAR imaging and the bistatic interferometric 3D imaging is shown in Fig.6.1, where T is the transmitter, R, R1 and R2 are three receivers. The origin of the global coordinate system is R. R1 and R2 are located on X axis and Y axis respectively. $|\mathbf{RR}_1| = |\mathbf{RR}_2| = d$. The target is located in the far field. A local coordinate system (O, X, Y, Z) parallel to the global coordinate system is used to describe the positions of the scatterers on the target at time 0. Scatterer A_i located at (x_i, y_i, z_i) is expressed as $\overrightarrow{OA_i}$. The target moves with speed $\mathbf{v}$ and rotates with speed Ω around its rotation axis ω. The line between T and R is called baseline. The angle $\angle OTR$ and $\angle ORT$ are denoted as α and γ. The bistatic angle $\angle TOR$ is denoted as β. E is the intersection between the bistatic bisector line and TR.

Let t and t' express "slow" and "fast" time. Fast time is sampled at the ADC rate of the receiver, and slow time is sampled at the pulse repetition frequency (PRF) of the system. The transmitted signal from antenna T be $u(t+t'-n\tilde{T})\exp(j2\pi f(t+t'))$, where $u(t)$ is 1 for $|t| < T_0/2$ and 0 for others. T_0 is the pulse width. Because pulse compression of BiISAR is the same as

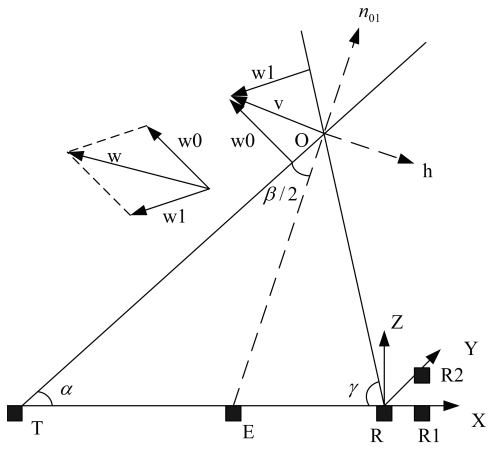

Figure 6.1: Geometry of the bistatic radar and the target.

that in ISAR, we do not discuss pulse compression. Hence we assume $u(t)$ be a short pulse or $u(t)$ can be regarded as the pulse after pulse compression. $\tilde{T}$ is the pulse repetition interval, f is the carrier frequency. Denote $\{A_i\}$ as the scatterers on the target. As the aim of this Chapter is to demonstrate and mitigate the shearing of BISAR image, we also assume that the reflection coefficient of each individual scatterer equals to one for expression simplicity. The demodulated backscattered (or side scattered) signals from the target received at antenna R is

$$\begin{aligned} s_R(t', t) = \quad & \textstyle\sum_i u(t + t' - n\tilde{T} - \tau_{TA_i}(t) - \tau_{A_iR}(t)) \\ & \times exp\left(-j2\pi f(\tau_{TA_i}(t) + \tau_{A_iR}(t))\right), \end{aligned} \tag{6.1}$$

where $\tau_{TA_i}(t)$ and $\tau_{A_iR}(t)$ are the delays from T to A_i and from A_i to R. $|s_R(t', n\tilde{T})|$ is the one-dimensional range profile of the target in slow time $t = n\tilde{T}$.

The techniques of range alignment in bistatic ISAR are similar to that of monostatic ISAR imaging. After range alignment, the signal received can be

expressed as

$$s_R(t',t) = \sum_i u(t' - \tau_{TA_i}(0) - \tau_{A_iR}(0)) exp\left(-j2\pi f(\tau_{TA_i}(t) + \tau_{A_iR}(t))\right). \quad (6.2)$$

The scatterers in the range direction have been separated. In order to separate the scatterers in the cross-range direction, the phase information should be used. Similar to monostatic ISAR motion compensation, the motion of the target which is common for all scatterers should be compensated, because the useful information are the difference in Doppler frequencies, and not the Doppler frequencies themselves. All the motion compensation methods used in monostatic ISAR can be used in BiISAR.

We assume that the target moves uniformly with velocity $\mathbf{v}$ and rotates uniformly around axis $\omega = [\omega_x, \omega_y, \omega_z]$ with rotation speed Ω. Let O also denote the rotation center of the target. The instantaneous velocity of scatterer A_i due to rotation of the target is $\Omega \bigotimes \overrightarrow{OA_i}$ where $\bigotimes$ expresses cross-product. Define a skew symmetric matrix

$$\hat{\omega} = \begin{pmatrix} 0 & -\omega_z & \omega_y \\ \omega_z & 0 & -\omega_x \\ -\omega_y & \omega_x & 0 \end{pmatrix}, \quad (6.3)$$

then the rotation matrix can be denoted as $\mathcal{R}(t) = \mathcal{I} + sin(\Omega t)\hat{\omega} + (1 - cos(\Omega t))\hat{\omega}^2$ [62], where $\mathcal{I}$ is the identity matrix. The position of vector $\overrightarrow{OA_i}$ at time t is $\mathcal{R}(t)\overrightarrow{OA_i}$. Let O be the focusing center. After the phase of O has been compensated, the received signal can be expressed as

$$s_R(t',t) = \sum_i u(t' - \tau_{TA_i}(0) - \tau_{A_iR}(0)) e^{-j2\pi f(\tau_{TA_i}(t) + \tau_{A_iR}(t) - \tau_{TO}(t) - \tau_{OR}(t))} \quad (6.4)$$

where

$$\begin{aligned}
& (\tau_{TA_i}(t) - \tau_{TO}(t))c \\
= \;& ||\mathbf{r_0} + \mathbf{v}t + \mathcal{R}(t)\overrightarrow{OA_i}|| - ||\mathbf{r}_0 + \mathbf{v}t|| \\
\approx \;& TA_i - TO + ((\mathbf{v} - \mathbf{n}_0^T\mathbf{v}\mathbf{n}_0)/r_0 - \Omega\hat{\omega}\mathbf{n}_0)^T\overrightarrow{OA_i}t \\
= \;& TA_i - TO + \mathbf{w_0}^T\overrightarrow{OA_i}t, \qquad (6.5)
\end{aligned}$$

where $\mathbf{r}_0 = \overrightarrow{TO}(0)$, $r_0 = |\mathbf{r}_0|$, $TA_i = |\overrightarrow{TA_i}(0)|$, $TO = r_0$, $\mathbf{n}_0 = \mathbf{r}_0/|r_0| = (n_{0x}, n_{0y}, n_{0z})$ is the transmit antenna line of sight unit vector, $\mathbf{w_0} = (\mathbf{v} - \mathbf{n}_0^T\mathbf{v}\mathbf{n}_0)/r_0 - \Omega\hat{\omega}\mathbf{n}_0$ is the synthetic vector which represents the effects induced by the target's translational and rotational motions. $\mathbf{w_0}$ is perpendicular to $\mathbf{n}_0$. For the detailed derivation, please refer to [12].

Similarly, we have

$$\begin{aligned}
& (\tau_{A_iR}(t) - \tau_{OR}(t))c \\
= \;& ||\mathbf{r_1} + \mathbf{v}t + \mathcal{R}(t)\overrightarrow{OA_i}|| - ||\mathbf{r_1} + \mathbf{v}t|| \\
\approx \;& A_iR - OR + ((\mathbf{v} - \mathbf{n}_1^T\mathbf{v}\mathbf{n}_1)/r_1 - \Omega\hat{\omega}\mathbf{n}_1)^T\overrightarrow{OA_i}t \\
= \;& A_iR - OR + \mathbf{w_1}^T\overrightarrow{OA_i}t, \qquad (6.6)
\end{aligned}$$

where $\mathbf{r}_1 = \overrightarrow{RO}(0)$, $r_1 = |\mathbf{r}_1| = OR$, $A_iR = |\overrightarrow{A_iR}(0)|$, $\mathbf{n}_1 = \mathbf{r}_1/r_1 = (n_{1x}, n_{1y}, n_{1z})$ is the receive antenna line of sight unit vector, $\mathbf{w_1} = (\mathbf{v} - \mathbf{n}_1^T\mathbf{v}\mathbf{n}_1)/r_1 - \Omega\hat{\omega}\mathbf{n}_1$.

Substitute (6.5) and (6.6) into (6.4), we have

$$s_R(t', t) \approx \sum_i u(t' - \tau_{A_i}(0))e^{-j2\pi\frac{TA_i + A_iR - TO - OR}{\lambda}}e^{-j\frac{2\pi}{\lambda}(\mathbf{w}_0 + \mathbf{w}_1)^T\overrightarrow{OA_i}t}, \qquad (6.7)$$

where $\tau_{A_i}(0) = \tau_{TA_i}(0) + \tau_{RA_i}(0)$. From Eq.(6.7) we can see that the frequency of scatterer A_i is proportional to the projection of $\overrightarrow{OA_i}$ on vector

$\mathbf{w}_0 + \mathbf{w}_1$, scatterers on the $\mathbf{w}_0 + \mathbf{w}_1$ direction can be separated by Fourier transform of $s_R(t', t)$ on variable t. Denote T_p as the time duration of signal for Fourier transform and $\mathbf{w} = \mathbf{w}_0 + \mathbf{w}_1$. In order to show the image in cross-range clearly, we define another orthogonal coordinate system $(\mathbf{h}, \mathbf{q}, \mathbf{n}_{01})$, where $\mathbf{n}_{01} = \frac{\mathbf{n}_0+\mathbf{n}_1}{|\mathbf{n}_0+\mathbf{n}_1|}$, $\mathbf{h}$ is perpendicular to $\mathbf{n}_{01}$ and located on plane expanded by $\mathbf{n}_{01}$ and $\mathbf{w}$, $\mathbf{q} = \mathbf{n}_{01} \bigotimes \mathbf{h}$. In this coordinate system, $\mathbf{w} = w_1\mathbf{h} + w_3\mathbf{n}_{01}$ (Generally, $\mathbf{w}$ is not perpendicular to $\mathbf{n}_{01}$, so $w_3 \neq 0$). $\overrightarrow{OA_i}$ can be expressed as $\overrightarrow{OA_i} = a_{ih}\mathbf{h} + a_{iq}\mathbf{q} + a_{in_{01}}\mathbf{n}_{01}$. The Fourier transform of $s_R(t', t)$ on variable t can be expressed as

$$\begin{aligned} S_R(t', f) &= \int_{-T_p/2}^{T_p/2} s_R(t', t) e^{-j2\pi ft} dt \\ &= T_p \sum_i u(t' - \tau_{A_i}(0)) e^{-j2\pi \frac{TA_i + A_iR - TO - OR}{\lambda}} sinc\left(\left(f + \frac{\mathbf{w}^T\overrightarrow{OA_i}}{\lambda}\right)T_p\right) \\ &= T_p \sum_i u(t' - \tau_{A_i}(0)) e^{-j2\pi \frac{TA_i + A_iR - TO - OR}{\lambda}} sinc\left(\left(f + \frac{w_1 a_{ih} + w_3 a_{in_{01}}}{\lambda}\right)T_p\right). \end{aligned} \tag{6.8}$$

Some researchers surmise that the bistatic ISAR imaging system is equivalent to a monostatic ISAR imaging system with the transmitter and receiver all located at E (Fig.6.1) [73]. The followings will show that this simplification is inadequate in BiISAR imaging. We compare the ISAR and BiISAR images as follows. After envelope alignment and motion compensation, the signal received from the so called "equivalent" monostatic radar E can be expressed as

$$\begin{aligned} s_E(t', t) &= \sum_i u(t' - \tau_{EA_i}(0)) e^{-j2\pi(\tau_{EA_i}(t) - \tau_{EO}(t))} \\ &\approx \alpha \sum_i u(t' - \tau_{EA_i}(0)) e^{-j\frac{4\pi}{\lambda}(\frac{\mathbf{v} - \mathbf{v}^T\mathbf{n}_{01}\mathbf{n}_{01}}{r_{01}} - \Omega\hat{\omega}\mathbf{n}_{01})^T\overrightarrow{OA_i}t}, \end{aligned} \tag{6.9}$$

where $r_{01} = EO$, and $\alpha = exp(-j\frac{4\pi}{\lambda}(EA_i(0) - EO(0)))$ is a useless initial

phase term and can be omitted. Define $\mathbf{w}_E = 2(\frac{\mathbf{v}-\mathbf{v}^T\mathbf{n}_{01}\mathbf{n}_{01}}{r_{01}} - \Omega\hat{\omega}\mathbf{n}_{01})$. It is easy to prove that $\mathbf{w}_E$ is perpendicular to $\mathbf{n}_{01}$. Generally, $\mathbf{w} \neq \mathbf{w}_E$ and we have expression $\mathbf{w}_E = w_{e1}\mathbf{h} + w_{e2}\mathbf{q}$. The Fourier transform of $s_E(t', t)$ on variable t can be expressed as

$$\begin{aligned} S_E(t', f) &= \int_{-T_p/2}^{T_p/2} s_E(t', t)e^{-j2\pi ft}dt \\ &\approx T_p \sum_i u(t' - \tau_{EA_i}(0))sinc\left(\left(f + \frac{\mathbf{w}_E^T\overrightarrow{OA_i}}{\lambda}\right)T_p\right) \\ &= T_p \sum_i u(t' - \tau_{EA_i}(0))sinc\left(\left(f + \frac{w_{e1}a_{ih} + w_{e2}a_{iq}}{\lambda}\right)T_p\right). \end{aligned} \tag{6.10}$$

We first compare the ISAR and BiISAR images in range resolution. Let O be the reference point. The relative delay between A_i and O in BiISAR is

$$\begin{aligned} & \tau_{A_i}(0) - \tau_O(0) \\ = \ & \tau_{TA_i}(0) - \tau_{TO}(0) + \tau_{A_iR}(0) - \tau_{OR}(0) \\ \approx \ & \frac{\overrightarrow{OA_i}^T\mathbf{n}_0}{c} + \frac{\overrightarrow{OA_i}^T\mathbf{n}_1}{c} \\ = \ & \frac{|\mathbf{n}_0 + \mathbf{n}_1|}{c}\overrightarrow{OA_i}^T\mathbf{n}_{01} \\ = \ & \frac{2a_{in_{01}}}{c}\cos(\frac{\beta}{2}) \end{aligned} \tag{6.11}$$

where $\cos(\frac{\beta}{2}) = \frac{|\mathbf{n}_0+\mathbf{n}_1|}{2}$.

The relative delay between A_i and O in ISAR is

$$\tau_{EA_i}(0) - \tau_{EO}(0) \approx \frac{2\overrightarrow{OA_i}^T\mathbf{n}_{01}}{c} = \frac{2a_{in_{01}}}{c}. \tag{6.12}$$

From (6.11) and (6.12) we can see that the relative delay in BiISAR is $\cos(\frac{\beta}{2})$ times that of the relative delay in monostatic ISAR. For the two imaging systems, the delay resolutions are all T_0. So the range resolutions of BiISAR

and ISAR are

$$\delta r_{Bi} = \frac{cT_0}{2}\frac{1}{\cos(\beta/2)}, \tag{6.13}$$

and

$$\delta r_{Mo} = \frac{cT_0}{2}. \tag{6.14}$$

So the range resolution of BiISAR is $1/\cos(\frac{\beta}{2})$ times as that of ISAR.

Now we analyze the image in cross-range direction. According to (6.8), in the cross range direction, the scatterer A_i is located on $f = -\frac{w_1 a_{ih} + w_3 a_{in_{01}}}{\lambda}$. Denote $\tau = \tau_{A_i}(0) - \tau_O(0)$, we have

$$\begin{pmatrix} f \\ \tau \end{pmatrix}_{BiISAR} = \begin{pmatrix} -\frac{w_1}{\lambda} & -\frac{w_3}{\lambda} \\ 0 & \frac{2\cos(\beta/2)}{c} \end{pmatrix} \begin{pmatrix} a_{ih} \\ a_{in_{01}} \end{pmatrix}. \tag{6.15}$$

We can see that the above coordinate transformation means a shear proportional to the $a_{in_{01}}$ coordinate. This is shown in Fig.6.2. The $\bigcirc$, $\triangle$ and $+$ in Fig.6.2(a) express the scatterers on the target. $(\mathbf{n}_{01}, \mathbf{h})$ expresses the range and horizontal axes. The BiISAR image (shown in range-Doppler plane) is as shown in Fig.6.2(b). Obviously, the bistatic ISAR image is a sheared version of the target.

The shear character can also be explained as follows. Because the BiISAR image is the projection of the scatterers on axes of $\mathbf{n}_{01}$ and $\mathbf{w}$, but the $\mathbf{n}_{01}$ and $\mathbf{w}$ are not perpendicular. Hence, when we show the BiISAR image using two orthogonal axes (stretching the $\mathbf{n}_{01}$ and $\mathbf{w}$ such that they are orthogonal), shear of the original shape occurs.

But for monostatic ISAR, in the cross-range direction, the scatterer is

located on $f = -\frac{w_{e1}a_{ih}+w_{e2}a_{iq}}{\lambda}$. Denote $\tau = \tau_{EA_i}(0) - \tau_{EO}(0)$, we have

$$\begin{pmatrix} f \\ \tau \end{pmatrix}_{ISAR} = \begin{pmatrix} -\frac{w_{e1}}{\lambda} & -\frac{w_{e2}}{\lambda} & 0 \\ 0 & 0 & \frac{2}{c} \end{pmatrix} \begin{pmatrix} a_{ih} \\ a_{iq} \\ a_{in_{01}} \end{pmatrix}. \tag{6.16}$$

It can be seen that the cross range coordinate is independent on the range coordinate. The ISAR image is a scaling of the shape of the target on $(\mathbf{w}_E, \mathbf{n}_{01})$ plane.

From (6.8) and (6.10) we can see that the iso-Doppler plane is perpendicular to $\mathbf{w}(\mathbf{w}_E)$. If the $\mathbf{n}_{01}$ and the $\mathbf{w}$ are perpendicular, the iso-Doppler planes and the iso-range planes are perpendicular. In other words, for monostatic ISAR, the iso-Doppler planes and the iso-range planes are perpendicular. But for bistatic ISAR, the iso-Doppler planes and the iso-range planes are not perpendicular in general.

6.2.1 Special Case

If there is no translational motion, that is to say the target only rotates around it's axis, then $\mathbf{w} = -2\Omega\hat{\omega}\mathbf{n}_{01}\cos(\beta/2)$, $\mathbf{w}_E = -2\Omega\hat{\omega}\mathbf{n}_{01}$. We can see that $\mathbf{w} = \cos(\beta/2)\mathbf{w}_E$. So the bistatic ISAR image is the same as the monostatic ISAR image except there is a range and cross range scaling of $\cos(\beta/2)$.

6.2.2 Range Migration

It is well known that the range migration of the target is severe on the side of the cross-range direction for monostatic ISAR imaging. For bistatic ISAR, according to (6.5) and (6.6), $\frac{d((\tau_{TA_i}(t)-\tau_{TO}(t)+\tau_{A_iR}(t)-\tau_{OR}(t))c)}{dt} \approx \mathbf{w}^T\overrightarrow{OA_i}$ means that the range migration is severe on the two tips of the target along $\mathbf{w}$ direc-

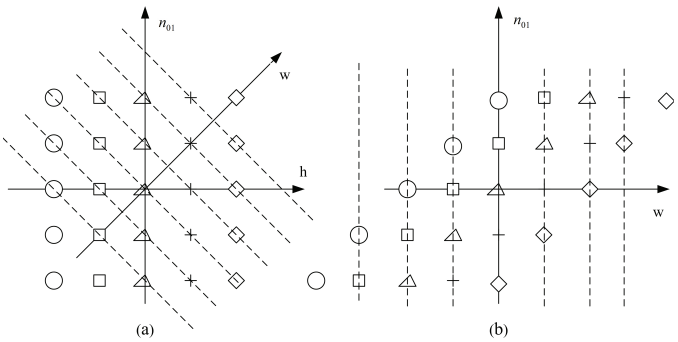

Figure 6.2: The bistatic ISAR image of a target ((a) is the target, (b) is the image).

tion. But due to the shear property of the BiISAR image, the range migration degradation also shows up at the two sides of the cross-range direction of the BiISAR image. In order to mitigate range migration, the following equation must be satisfied:

$$|\mathbf{w}|OA_M T_p < \delta r_{Bi}/2 \tag{6.17}$$

where OA_M is the maximum distance of the target along the $\mathbf{w}$ direction from the focusing center.

6.3 Interferometric 3D imaging

Through comparing the phase difference of a scatterer between two antennas, the cross-range position of the scatterer along the baseline of the two antennas can be obtained. By placing three receive antennas as a triangle, the two cross-range positions of scatterers can be obtained and can form a 3D image of the target (combined with pulse compression technique) [9] [77]. Similarly, three-antenna configuration can also be used in bistatic radar to form 3D image. The three-antenna configuration is shown in Fig.6.1, where R, R_1 and R_2 are three receive antennas. We denote R as the origin of the coordinate, and the R_1 and R_2 are located on the $\mathbf{X}$ and $\mathbf{Y}$ axis respectively. The distances between R

and R_1, R and R_2 are d. After range alignment of $s_{R_1}(t',t)$ itself and aligning $s_{R_1}(t',t)$ with $s_R(t',t)$, the received signal of R_1 can be expressed as

$$s_{R_1}(t',t) = \sum_i u(t' - \tau_{TA_i}(0) - \tau_{A_iR}(0)) e^{-j2\pi f(\tau_{TA_i}(t)+\tau_{A_iR_1}(t))}. \tag{6.18}$$

Similar to signal of $s_R(t',t)$, the phase of O point is also used to do motion compensation. After motion compensation, $s_{R_1}(t',t)$ can be expressed as

$$\begin{aligned} s_{R_1}(t',t) = & \sum_i u(t' - \tau_{TA_i}(0) - \tau_{A_iR}(0)) e^{-j2\pi f(\tau_{TA_i}(t)+\tau_{A_iR_1}(t)-\tau_{TO}(t)-\tau_{OR_1}(t))} \\ \approx & \sum_i u(t' - \tau_{A_i}(0)) e^{-j2\pi \frac{TA_i+A_iR_1-TO-OR_1}{\lambda}} e^{-j\frac{2\pi}{\lambda}(\mathbf{w}_0+\mathbf{w}_1)^T\overrightarrow{OA_i}t}. \end{aligned} \tag{6.19}$$

The ISAR image of antenna R_1 can be expressed as

$$\begin{aligned} S_{R_1}(t',f) = & \int_{-T_p/2}^{T_p/2} s_{R_1}(t',t) e^{-j2\pi ft} dt \\ = & T_p \sum_i u(t' - \tau_{A_i}(0)) e^{-j2\pi \frac{TA_i+A_iR_1-TO-OR_1}{\lambda}} sinc\left(\left(f + \frac{\mathbf{w}^T\overrightarrow{OA_i}}{\lambda}\right)T_p\right). \end{aligned} \tag{6.20}$$

It can be seen that the ISAR images $S_R(t',f)$ and $S_{R_1}(t',f)$ are aligned in range and cross-range directions. The difference is the phase of each scatterer. For scatterer A, we can compute the phase difference between S_R and S_{R_1} to obtain the cross-range position of A. Denote $\mathbf{a} = \overrightarrow{OA} = (x,y,z)$ on the (O,X,Y,Z) coordinate system (the position of a general scatterer), and $\mathbf{d}_1 = \overrightarrow{RR_1}$, we have

$$\begin{aligned} & S_{R_1}(A) \times S_R(A)^* \\ = & exp\Big(j2\pi \frac{AR - AR_1 + OR_1 - OR}{\lambda}\Big) \\ \approx & exp\Big(j2\pi \frac{(\mathbf{a} - \mathbf{n}_1^T\mathbf{a}\mathbf{n}_1)^T\mathbf{d}_1}{\lambda r_1}\Big) \\ = & exp\Big(j2\pi \frac{\tilde{\mathbf{a}}^T\mathbf{d}_1}{\lambda r_1}\Big) \\ = & exp\Big(j2\pi \frac{\tilde{x}d}{\lambda r_1}\Big), \end{aligned} \tag{6.21}$$

where $\tilde{\mathbf{a}} = \mathbf{a} - \mathbf{n}_1^T\mathbf{a}\mathbf{n}_1 = (\tilde{x}, \tilde{y}, \tilde{z})$. Similarly, we can obtain the BiISAR image on antenna R2 and compute

$$\begin{aligned} & S_{R_2}(A) \times S_R(A)^* \\ = \; & exp\Big(j2\pi\frac{AR - AR_2 + OR_2 - OR}{\lambda}\Big) \\ \approx \; & exp\Big(j2\pi\frac{(\mathbf{a} - \mathbf{n}_1^T\mathbf{a}\mathbf{n}_1)^T\mathbf{d}_2}{\lambda r_1}\Big) \\ = \; & exp\Big(j2\pi\frac{\tilde{\mathbf{a}}^T\mathbf{d}_2}{\lambda r_1}\Big) \\ = \; & exp\Big(j2\pi\frac{\tilde{y}d}{\lambda r_1}\Big). \end{aligned} \tag{6.22}$$

For the approximation in (6.21) and (6.22), please refer to the lemma of section 2.1. Define φ_1 and φ_2 the phases of $S_{R_1}(A) \times S_R(A)^*$ and $S_{R_2}(A) \times S_R(A)^*$ respectively, then we have

$$\tilde{x} = \frac{\lambda\varphi_1 r_1}{2\pi d}, \tag{6.23}$$

$$\tilde{y} = \frac{\lambda\varphi_2 r_1}{2\pi d}. \tag{6.24}$$

Denote $r_{n_{01}} = \mathbf{a}^T\mathbf{n}_{01}$ as the range projection of $\mathbf{a}$ on the range direction, where $\mathbf{n}_{01} = (n_{01x}, n_{01y}, n_{01z})$. We have the following equations

$$\begin{cases} \mathbf{a} - (\mathbf{a}^T\mathbf{n}_1)\mathbf{n}_1|_x = \tilde{\mathbf{a}}|_x = \tilde{x} \\ \mathbf{a} - (\mathbf{a}^T\mathbf{n}_1)\mathbf{n}_1|_y = \tilde{\mathbf{a}}|_y = \tilde{y} \\ \mathbf{a}^T\mathbf{n}_{01} = r_{n_{01}}. \end{cases} \tag{6.25}$$

There are three unknown variables in $\mathbf{a} = (x, y, z)$ and three equations. So we can determine $\mathbf{a}$ by solving the above linear equations simultaneously. The

above equations can also be expressed as

$$\begin{pmatrix} 1-n_{1x}^2, & -n_{1x}n_{1y}, & -n_{1x}n_{1z} \\ -n_{1x}n_{1y}, & 1-n_{1y}^2, & -n_{1y}n_{1z} \\ n_{01x}, & n_{01y}, & n_{01z} \end{pmatrix} \begin{pmatrix} x \\ y \\ z \end{pmatrix} = \begin{pmatrix} \tilde{x} \\ \tilde{y} \\ r_{n_{01}} \end{pmatrix}. \tag{6.26}$$

For special coordinate system, the above equation can be further simplified. For example, if we choose to have the target locates on the XZ plane of the coordinate system, then $n_{1y} = 0$, $n_{01y} = 0$ and $y = \tilde{y}$ hold. Equation (6.26) can then be simplified as

$$\begin{pmatrix} 1-n_{1x}^2, & -n_{1x}n_{1z} \\ n_{01x}, & n_{01z} \end{pmatrix} \begin{pmatrix} x \\ z \end{pmatrix} = \begin{pmatrix} \tilde{x} \\ r_{n_{01}} \end{pmatrix}. \tag{6.27}$$

6.4 Simulation results

In this section, we use simulations to verify the correctness of our analysis on shear of BiISAR image and the performance of the proposed interferometric 3D imaging algorithm. The transmitted signal is a linear chirp signal with bandwidth of 150 MHz and carrier frequency of 35 GHz. The sampling rate is 1.2 GHz. The chirp pulse duration is 1 microsecond and the chirp rate is 1.5×10^{14} Hz^2. The transmitter T and three receivers R, R1 and R2 are located at $[-50, 0, 0] \times 10^3$ m, $[50, 0, 0] \times 10^3$ m, $[50, 0, 0] \times 10^3 + [d, 0, 0]$ m and $[50, 0, 0] \times 10^3 + [0, d, 0]$ m respectively, where $d = 11.4998$ m in simulation 1 and $d = 9.9683$ m in simulation 3. The Pulse Repetition Frequency (PRF) is 128 Hz and the coherent processing time T_p is 1 second. The discrete Fourier transform point in the cross range is 512.

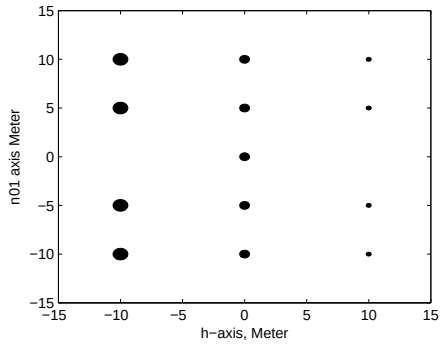

Figure 6.3: Target model (simulation 1).

6.4.1 Simulation 1: Distortion of BiISAR Image

In this simulation, we show the distortion of BiISAR image due to bistatic radar geometry and the movement of the target. The so called monostatic equivalent antenna is located at $[7.8835, 0, 0] \times 10^3$ m. The target is located at $[20, 0, 60] \times 10^3$ m. In this case, $\alpha = 40.6°$, $\gamma = 63.43°$ and bistatic angle $\beta = 75.96°$. $1/\cos(\beta/2) = 1.2687$. The target moves uniformly with speed $[335.35, 0, 335.35]$ m/s. The target is composed of 13 scatterers. All the scatterers are located on the XZ plane. Fig.6.3 shows the original target model (in order to show the shear clearly, we choose a regular shape target). The target forms a rectangle in $\mathbf{h}$ and $\mathbf{n}_{01}$ coordinate system. Fig.6.4 and Fig.6.5 show the monostatic radar ISAR image and the bistatic radar BiISAR image. It can be seen that the ISAR image keeps the shape of the target but the BiISAR image shears proportional to the range. The ISAR and BiISAR images are different. The range resolutions of BiISAR image is worse than that of ISAR image. These concur with our analysis. Because the $\mathbf{w}$ is along the positive $\mathbf{h}$ axis direction, the relative Doppler on the right part of the target is negative, so the ISAR image on the cross-range direction is a reverse version of the target model. Fig.6.6 shows the projection of the reconstructed 3D image on the $(\mathbf{h}, \mathbf{n}_{01})$ plane. It can be seen that it is similar to the original target model.

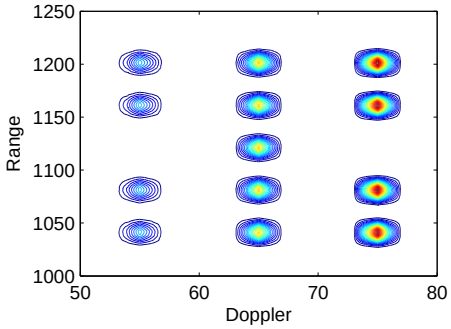

Figure 6.4: ISAR image of monostatic radar on the so called equivalent position (simulation 1).

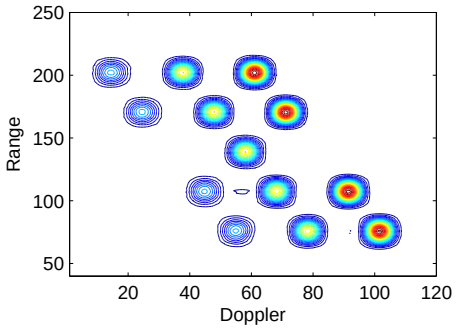

Figure 6.5: BiISAR image using bistatic radar (simulation 1).

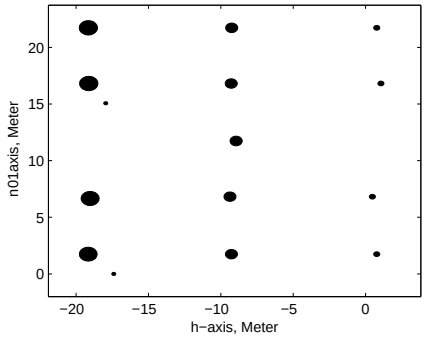

Figure 6.6: Reconstructed projection image on XZ plane using interferometric technique (simulation 1).

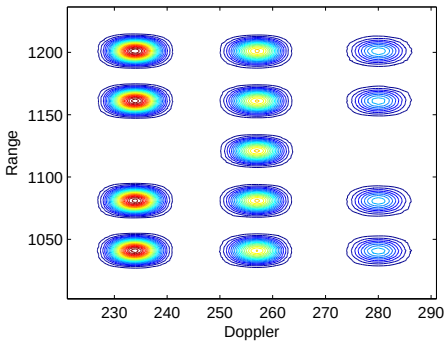

Figure 6.7: ISAR image of monostatic radar on the so called equivalent position (simulation 2).

6.4.2 Simulation 2: BiISAR Image with Only Rotation Movement

In this simulation, we show the ISAR and BiISAR images when the target rotates around its axis and does not move. According to the analysis, the shape of ISAR and BiISAR are similar but with different resolutions in range and cross-range. The target model is the same as that in simulation 1 but the target rotates an angle such that the target is also a rectangle in the new $(\mathbf{h}, \mathbf{n}_{01})$ coordinate. The target is located at $[55, 0, 60] \times 10^3$ m. Then the bistatic angle is different from simulation 1. The target rotates around axis $[1, 1, 1]$ and with rotation speed 0.0043 rad/s. The duration to collect data is 1 second and then the cross-range resolution of ISAR is 1 m. The geometry of the bistatic radar is the same as that of simulation 1. Fig.6.7 and Fig.6.8 show the ISAR and BiISAR images. Again concurring with our analysis, the ISAR and BiISAR images are similar. The range and cross-range resolutions of BiISAR image are worse than that of ISAR image.

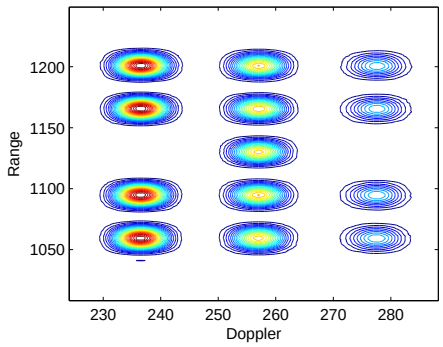

Figure 6.8: BiISAR image of the bistatic radar (simulation 2).

6.4.3 Simulation 3: 3D Imaging using Interferometric Technique

In this simulation, we show the 3D image of interferometric bistatic radar. The coordinates of the transmitter and the receivers are the same as that in simulation 1. The target is located at $[-55, 0, 50] \times 10^3\ m$. In this case, $\alpha = 95.71°$, $\gamma = 25.46°$ and bistatic angle $\beta = 58.83°$. The target is composed of 13 strong scatterers. During 1 second data collection time, the target moves uniformly with speed $[384.48, -256.32, -640.80]\ m/s$ and rotates uniformly around axis $[0.1, -1, 0]$ with speed $8.57 \times 10^{-4}\ rad/s$. Fig.6.9 shows the target model on three projected planes and the whole 3D model. Fig.6.10 and Fig.6.11 show the ISAR image and the BiISAR image. It can be seen that due to the translational motion as well as rotational motion, the difference between these two images are not as severe as that shown in simulation 1, where only translational motion exists. At the same time, the similarity between these two images are not as high as that in simulation 2, where only rotational motion exists. Fig.6.12 shows the three projected image and the 3D image reconstructed using interferometric bistatic radar. It is close to the original target model.

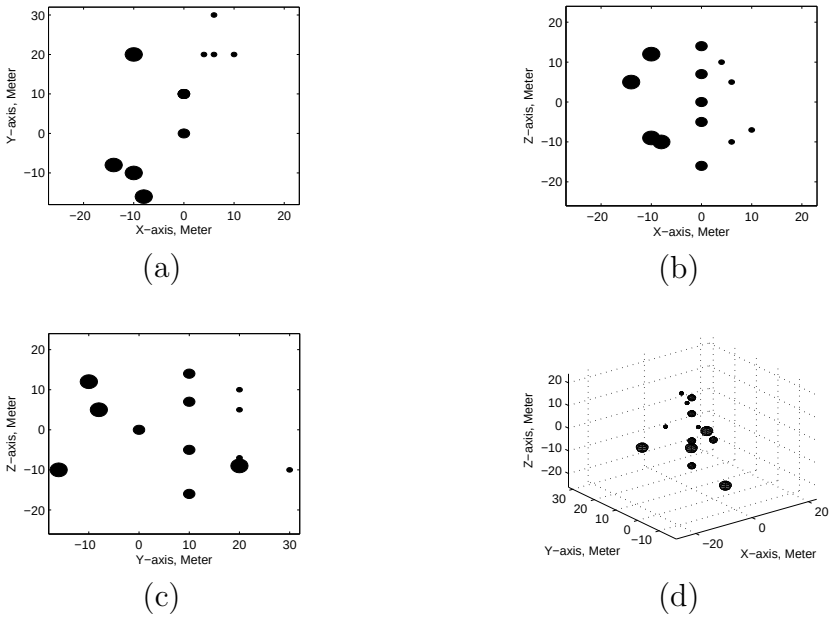

Figure 6.9: Three different projected views and the 3-D model of the target (simulation 3).

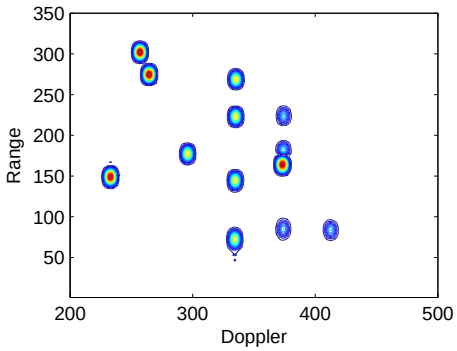

Figure 6.10: ISAR image of monostatic radar on the so called equivalent position (simulation 3).

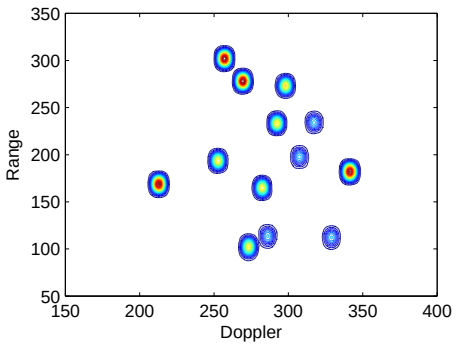

Figure 6.11: BiISAR image of the bistatic radar (simulation 3).

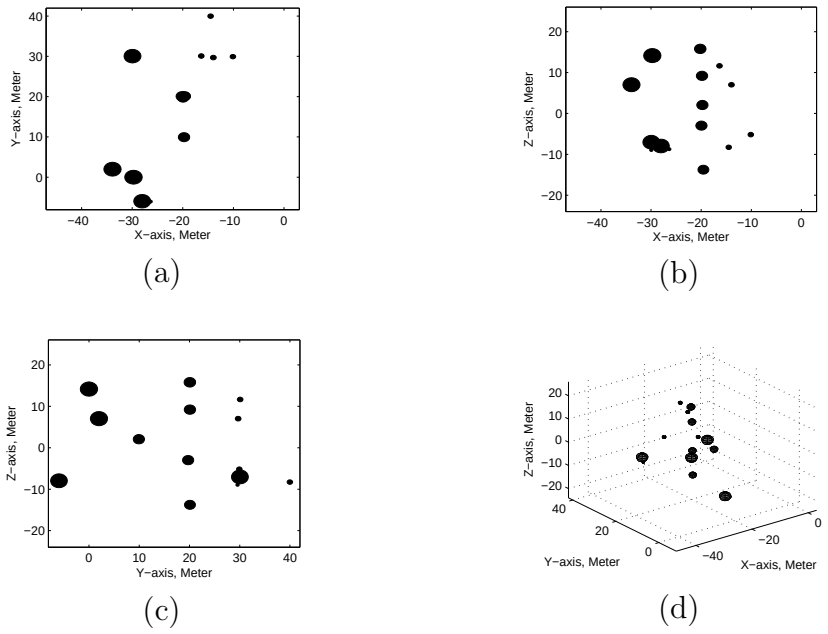

Figure 6.12: Three different projected views and the 3-D image of the target using interferometric bistatic radar (simulation 3).

6.5 Conclusions

Monostatic ISAR image explores the back scattering character of a target. For bistatic radar, the transmitter and the receiver observe the target from different views. So BiISAR image is complementary to ISAR image. The range resolution and Doppler resolution of bistatic radar are a ratio of that of monostatic radar. Although bistatic radar and monostatic radar share common signal processing procedures, we show that bistatic radar could not be simply replaced by a monostatic radar from the standpoint of radar imaging. Our analysis shows that the BiISAR image is the projection of the target on range and Doppler-gradient axes. Because the range direction and the Doppler-gradient direction are not perpendicular, the BiISAR image is a sheared version of the target when projected on the range and cross-range plane. Thus bistatic ISAR cannot be equivalent to any monostatic radar system in general. Three-antenna receiver interferometric configuration is proposed to correct this

shear and to obtain 3D image of a target. Simulation results have validated our analysis and shown the viability of the proposed 3D imaging algorithm.

Chapter 7

Conclusions and Future Works

7.1 Research Purposes and Results

The aims of this study were to develop MIMO radar three dimensional imaging algorithms and to improve image quality using sparse signal recovery algorithms. In Chapter 2, an algorithm of MIMO radar 3D imaging using one snapshot signals was developed. Under the assumption of orthogonal coding, after signal separation, phase compensation and signal order arrangement processes, a large virtual aperture was formed, which improved the spatial resolution using fewer number of antennas. An equation describing the signals from a slant range target was obtained. Based on this equation, a slant range target could be imaged, while conventional interferometric method proposed assumes that the target is located at the broadside of the three-antenna receivers. In reality, the codes are not orthogonal. If the length of the codes is short, high sidelobes occur, and this affects the image quality. So zero correlation zone codes were proposed to overcome the high sidelobes problem for isolated target. In Chapter 3, an algorithm of MIMO radar 3D imaging using multiple snapshots signals was discussed. The space time mathematic

equation fit for slant range target has been derived and the total 3D imaging procedure has been proposed. In order to improve the SNR and increase the separation ability by coherently combine the space-time signals, a method to extract the effective rotation vector has been proposed.

The scatterers of a target are usually distributed sparsely on the target's surface. This information was used to improve the image quality. An ℓ_1 norm and ℓ_0 norm homotopy was built by proposing a sequential order one negative exponential function. By varying a parameter from infinity to zero, a near ℓ_0 norm criterion could be obtained. Compared with other sparse signal recovery algorithms such as, OMP, CoSaMp, Bayesian method with Laplace priori, ℓ_1 magic, L1-Ls, and smoothed ℓ_0 norm, our algorithm has superior performance for high SNR and low sparsity signals. Furthermore, our method is easily extended to block sparse and complex signal cases. Because when a complex linear equation is transformed to a real linear equation, the conventional complex sparse signal becomes block size of 2 real sparse signal. The equivalence between block size of 2 real sparse signal recovery and complex sparse signal recovery using our ℓ_1 ℓ_0 norms homotopy method has been proven. This means that complex signal based algorithm is better than real signal based algorithm (not using block property) using our method. These results were reported in Chapter 4.

The collocated MIMO radar 3D imaging signal model can be described as a (one-dimensional) linear equation or a multi-dimensional linear equation. Application of linear equation based ℓ_1 ℓ_0 homotopy sparse signal recovery algorithm on collocated MIMO radar 3D imaging was discussed in the first part of Chapter 5. Although it can improve the image quality compared with conventional correlation method, it needs huge memory. Multi-dimensional linear equation based method has compact expression, occupies less memory and

has similar performance compared to linear equation based method. A distributed MIMO radar 3D imaging technique was also discussed. By analysis, the distributed MIMO radar system is divided into a few subimaging systems. All the transmitting arrays and one collocated receiving array constitute a subimaging system. After the images have been obtained by all subimaging systems, they are combined to form the final image. Sparse signal recovery algorithms were also used to improve the image quality.

In Chapter 6, bistatic ISAR imaging technique was discussed. We proved that the bistatic ISAR image is a sheared version of the projection image of the target on range-Doppler plane. This phenomenon limits the application of bistatic ISAR image on target identification. In order to solve this problem, a three receive antennas interferometric 3D imaging technique was proposed to obtain the non-sheared 3D image of the target. Our results rectified the errors of some researchers that the bistatic image is equivalent to the monostatic ISAR image obtained by an equivalent antenna located on bisector angle.

7.2 Significance, Limitations and Future Works

Our results extend the availability of 3D imaging to slant range target. The space-time equation derived provides a basis for any future imaging methods development. The $\ell_1\,\ell_0$ homotopy sparse signal recovery algorithm has potentially important applications on image processing, communication signal processing, etc. For one snapshot case, in order to obtain high cross-range resolution, the distances between different antennas should be large enough. This may cause problems on synchronization between different antennas. The way to solve this problem is beyond the scope of this thesis. The whole beampattern is the product of the standard beampattern of one antenna and the

array beam pattern. Because the size of each antenna is small, which corresponds to a large width beam pattern, if the unambiguous window is less than the one antenna beampattern width, grating lobes occur. If there is only one target in the beam, the MIMO radar structure discussed in this thesis can work. However, if multiple targets are located in the beam of one antenna and cover one unambiguous window of the MIMO array, ambiguity occurs when only one snapshot signal is used to form the image. Multiple targets imaging should be a research topic in the future.

Sparse signal recovery on multiple snapshots MIMO radar 3D imaging has not been discussed in this study due to the limited time duration. Combining advanced sparse signal recovery algorithm with multiple snapshots signal could improve the image quality. Theoretic analysis of our proposed ℓ_1 ℓ_0 homotopy method has not been discussed. The conditions under which our algorithm converges to the ℓ_0 norm solution is also not known. This is a future research topic.

Conventional CS imaging methods divide the imaging field as grids. The scatterers may not be just located on the grids. Gridless method is another future research topic.

Bibliography

[1] D. L. Mensa, *High Resolution Radar Cross-Section Imaging.* Artech House, 1991.

[2] D. A. Ausherman, A. Kozma, J. L. Walker, H. M. Jones, and E. C. Poggio, "Developments in radar imaging," *IEEE Trans. Aerosp. Electron. Syst.*, vol. 4, pp. 363–400, Jul. 1984.

[3] C. C. Chen and H. C. Andrews, "Target-motion-induced radar imaging," *IEEE Trans. Aerosp. Electron. Syst.*, vol. 16, pp. 2–14, Jan. 1980.

[4] J. Walker, "Range-doppler imaging of rotating objects," *IEEE Trans. Aerosp. Electron. Syst.*, vol. 16, no. 1, pp. 23–52, 1980.

[5] B. D. Steinberg, "Microwave imaging of aircraft," *Proceedings of the IEEE*, vol. 76, no. 12, pp. 1578–1592, 1988.

[6] G. Delisle and H. Wu, "Moving target imaging and trajectory computation using isar," *IEEE Trans. Aerosp. Electron. Syst.*, vol. 30, no. 3, pp. 887–899, 1994.

[7] H. Wu, D. Grenier, G. Delisle, and D. Fang, "Translational motion compensation in isar image processing," *IEEE Trans. Image Process.*, vol. 4, no. 11, pp. 1561–1571, 1995.

[8] X. Xu and R. Narayanan, "Three-dimensional interferometric isar imaging for target scattering diagnosis and modeling," *IEEE Trans. Image Process.*, vol. 10, no. 7, pp. 1094–1102, 2001.

[9] G. Wang, X. Xia, and V. Chen, "Three-dimensional isar imaging of maneuvering targets using three receivers," *IEEE Trans. Image Process.*, vol. 10, no. 3, pp. 436–447, 2001.

[10] Q. Zhang, T. S. Yeo, G. Du, and S. Zhang, "Estimation of three-dimensional motion parameters in interferometric isar imaging," *IEEE Trans. Geosci. Remote Sens.*, vol. 42, no. 2, pp. 292–300, 2004.

[11] C. Ma, T. S. Yeo, Q. Zhang, H. Tan, and J. Wang, "Three-dimensional isar imaging based on antenna array," *IEEE Trans. Geosci. Remote Sens.*, vol. 46, no. 2, pp. 504–515, 2008.

[12] C. Ma, T. S. Yeo, C. S. Tan, and H. S. Tan, "Sparse array 3-d isar imaging based on maximum likelihood estimation and clean technique," *IEEE Trans. Image Process.*, vol. 19, no. 8, pp. 2127–2142, 2010.

[13] A. Haimovich, R. Blum, and L. Cimini, "Mimo radar with widely separated antennas," *IEEE Signal Processing Magazine*, vol. 25, no. 1, pp. 116–129, 2008.

[14] J. Li and P. Stoica, "Mimo radar with colocated antennas," *IEEE Signal Processing Magazine*, vol. 24, no. 5, pp. 106–114, 2007.

[15] B. Borden, "Mathematical problems in radar inverse scattering," *Inverse Problems*, vol. 18, pp. R1–R28, 2002.

[16] M. Cheney and B. Borden, *Fundamentals of Radar Imaging.* SIAM, Philadelphia, 2009.

[17] G. Y. Wang and Z. Bao, "Isar imaging of maneuvering targets based on chirplet decomposition," *Opt. Eng.*, vol. 38, pp. 1534–1541, 1999.

[18] V. C. Chen and Q. S., "Joint time -frequency transform for radar range doppler imaging," *IEEE Trans. Aerosp. Electron. Syst.*, vol. 34, no. 2, pp. 486–499, 1998.

[19] W. Ye, T. S. Yeo, and Z. Bao, "Weighted least-squares estimation of phase errors for sar/isar autofocus," *IEEE Trans. Geosci. Remote Sens.*, vol. 37, no. 5, pp. 2487–2494, 1999.

[20] P. Cao, M. Xing, G. Sun, Y. Li, and Z. Bao, "Minimum entropy via subspace for isar autofocus," *IEEE Geosci. Remote Sens. Lett.*, vol. 7, no. 1, pp. 205–209, 2010.

[21] L. C. Graham, "Synthetic interferometer radar for topographic mapping," *Proceedings of the IEEE*, vol. 62, no. 6, pp. 763–768, 1974.

[22] Q. Zhang, C. Ma, T. Zhang, and S. H. Zhang, "Research on radar three dimensional imaging techniques based on interferometric techniques," *Journal of Electronic and Information*, vol. 23, pp. 890–898, 2001.

[23] J. Tsao and B. Steinberg, "Reduction of sidelobe and speckle artifacts in microwave imaging: the clean technique," *IEEE Trans. Antennas Propag.*, vol. 36, no. 4, pp. 543–556, 1988.

[24] J. Li and P. Stoica, *MIMO radar signal processing.* Wiley Online Library, 2009.

[25] W. Wang, "Space-time coding mimo-ofdm sar for high-resolution imaging," *IEEE Trans. Geosci. Remote Sens.*, vol. 49, no. 8, pp. 3094–3104, 2011.

[26] X. Zhuge and A. G. Yarovoy, "A sparse aperture mimo-sar-based uwb imaging system for concealed weapon detection," *IEEE Trans. Geosci. Remote Sens.*, vol. 49, no. 1, pp. 509–518, 2011.

[27] D. Wang, X. Ma, and Y. Su, "Two-dimensional imaging via a narrowband mimo radar system with two perpendicular linear arrays," *IEEE Trans. Image Process.*, vol. 19, no. 5, pp. 1269–1279, 2010.

[28] D. Wang, X. Ma, A. Chen, and Y. Su, "High-resolution imaging using a wideband mimo radar system with two distributed arrays," *IEEE Trans. Image Process.*, vol. 19, no. 5, pp. 1280–1289, 2010.

[29] C. Ma, T. S. Yeo, C. S. Tan, and Z. Liu, "Three-dimensional imaging of targets using colocated mimo radar," *IEEE Trans. Geosci. Remote Sens.*, vol. 49, no. 8, pp. 3009–3021, 2011.

[30] Y. Zhu, Y. Su, and W. Yu, "An isar imaging method based on mimo technique," *IEEE Trans. Geosci. Remote Sens.*, vol. 48, no. 8, pp. 3290–3299, 2010.

[31] D. Pastina, M. Bucciarelli, and P. Lombardo, "Multistatic and mimo distributed isar for enhanced cross-range resolution of rotating targets," *IEEE Trans. Geosci. Remote Sens.*, vol. 48, no. 8, pp. 3300–3317, 2010.

[32] D. Donoho, "Compressed sensing," *IEEE Trans. Inf. Theory*, vol. 52, no. 4, pp. 1289–1306, 2006.

[33] E. Candès, J. Romberg, and T. Tao, "Robust uncertainty principles: Exact signal reconstruction from highly incomplete frequency information," *IEEE Trans. Inf. Theory*, vol. 52, no. 2, pp. 489–509, 2006.

[34] S. Chen, D. Donoho, and M. Saunders, "Atomic decomposition by basis pursuit," *SIAM review*, pp. 129–159, 2001.

[35] S.-J. Kim, K. Koh, M. Lustig, S. Boyd, and D. Gorinevsky, "A method for large-scale ℓ_1-regularized least squares," *IEEE Journal on Selected Topics in Signal Processing*, vol. 1, no. 4, pp. 606–617, 2007.

[36] S. Mallat and Z. Zhang, "Matching pursuits with time-frequency dictionaries," *IEEE Trans. Signal Process.*, vol. 41, no. 12, pp. 3397–3415, 1993.

[37] J. A. Tropp and A. C. Gilbert, "Signal recovery from random measurements via orthogonal matching pursuit," *IEEE Transactions on Information Theory*, vol. 53, no. 12, pp. 4655–4666, 2007.

[38] R. Chartrand, "Exact reconstruction of sparse signals via nonconvex minimization," *IEEE Signal Process. Lett.*, vol. 14, no. 10, pp. 707–710, 2007.

[39] R. Saab, R. Chartrand, and Yilmaz, "Stable sparse approximations via nonconvex optimization," in *IEEE International Conference on Acoustics, Speech and Signal Processing.*, 2008, pp. 3885–3888.

[40] M. Wang, W. Xu, and A. Tang, "On the performance of sparse revovery via ℓ_p-minimization$(0 \leq p \leq 1)$," *IEEE Trans. Inf. Theory*, vol. 57, no. 11, pp. 7255–7278, 2011.

[41] H. Mohimani, M. Babaie-Zadeh, and C. Jutten, "A fast approach for overcomplete sparse decomposition based on smoothed ℓ_0 norm," *IEEE Trans. Signal Process.*, vol. 57, no. 1, pp. 289–301, 2009.

[42] R. Roy and T. Kailath, "Esprit-estimation of signal parameters via rotational invariance techniques," *IEEE Transactions on Acoustics, Speech and Signal Processing*, vol. 37, no. 7, pp. 984–995, 1989.

[43] Y. Hua and T. K. Sarkar, "Matrix pencil method for estimating parameters of exponentially damped/undamped sinusoids in noise," *IEEE Transactions on Acoustics, Speech and Signal Processing*, vol. 38, no. 5, pp. 814–824, 1990.

[44] V. Chandrasekaran, B. Recht, P. A. Parrilo, and A. S. Willsky, "The convex geometry of linear inverse problems," *Foundations of Computational Mathematics*, vol. 12, no. 6, pp. 805–849, 2012.

[45] G. Tang, B. N. Bhaskar, P. Shah, and B. Recht, "Compressive sensing off the grid," *IEEE Trans. Inf. Theory*, vol. 59, no. 11, pp. 7465–7490, 2013.

[46] L. Hu, Z. Shi, J. Zhou, and Q. Fu, "Compressed sensing of complex sinusoids: An approach based on dictionary refinement," *IEEE Transactions on Signal Processing*, vol. 60, no. 7, pp. 3809–3822, 2012.

[47] J. Fang, J. Li, Y. Shen, H. Li, and S. Li, "Super-resolution compressed sensing: An iterative reweighted algorithm for joint parameter learning and sparse signal recovery," *IEEE Signal Processing Letters*, vol. 21, no. 6, pp. 761–765, 2014.

[48] L. Zhang, M. Xing, C. W. Qiu, J. Li, , and Z. Bao, "Achieving higher resolution isar imaging with limited pulses via compressed sampling," *IEEE Geosci. Remote Sens. Lett.*, vol. 6, no. 3, pp. 567–571, 2009.

[49] D. Needell and J. Tropp, "Cosamp: Iterative signal recovery from incomplete and inaccurate samples," *Applied and Computational Harmonic Analysis*, vol. 26, no. 3, pp. 301–321, 2009.

[50] S. D. Babacan, R. Molina, and A. K. Katsaggelos, "Bayesian compressive sensing using laplace priors," *IEEE Trans. Image Process.*, vol. 19, no. 1, pp. 53–63, 2010.

[51] M. Cheney and B. Borden, "Imaging moving targets from scattered waves," *Inverse Problems*, vol. 24, no. 3, pp. 1–22, 2008.

[52] Z. Bao, G. Y. Wang, and L. Luo, "Inverse synthetic aperture radar imaging of maneuvering targets," *Opt. Eng.*, vol. 37, pp. 1582–1588, 1998.

[53] J. Li, R. Wu, and V. C. Chen, "Robust autofocus algorithm for isar imaging of moving targets," *IEEE Trans. Aerosp. Electron. Syst.*, vol. 37, no. 3, pp. 1056–1069, 2001.

[54] M. Soumekh, "Automatic aircraft landing using interferometric inverse synthetic aperture radar imaging," *IEEE Trans. Image Process.*, vol. 5, no. 9, pp. 1335–1345, 1996.

[55] C. Ma, T. S. Yeo, H. S. Tan, J. Wang, and B. X. Chen, "Three-dimensional isar imaging using a two-dimensional sparse antenna array," *IEEE Trans. Geosci. Remote Sens.*, vol. 5, no. 3, pp. 378–382, 2008.

[56] G. Duan, D. Wang, X. Ma, and Y. Su, "Three-dimensional imaging via wideband mimo radar system," *IEEE Geosci. Remote Sens. Lett.*, vol. 7, no. 3, pp. 445–449, 2010.

[57] H. Deng, "Polyphase code design for orthogonal netted radar systems," *IEEE Trans. Signal Process.*, vol. 52, no. 11, pp. 3126–3135, 2004.

[58] M. D. Xing, Z. Bao, and Y. M. Zheng, "Range alignment using global optimization criterion in isar imaging," *ACTA Electronica Sinica*, vol. 29, no. 12A, pp. 1807–1811, 2001.

[59] D. Chu, "Polyphase codes with good periodic correlation properties (corresp.)," *IEEE Trans. Inf. Theory*, vol. 18, no. 4, pp. 531–532, 1972.

[60] N. Suehiro, "A signal design without co-channel interference for approximately synchronized cdma systems," *IEEE J. Sel. Areas Commun.*, vol. 12, no. 5, pp. 837–841, 1994.

[61] P.P.Vaidyanathan and P. Pal, "Mimo radar, simo radar, and ifir radar: a comparison," in *IEEE 2009 Conference Record of the Forty-Third Asilomar Conference on Signals, Systems and Computers*, 2009, pp. 160–167.

[62] V. Chen, F. Li, S. Ho, and H. Wechsler, "Micro-doppler effect in radar: phenomenon, model, and simulation study," *IEEE Trans. Aerosp. Electron. Syst.*, vol. 42, no. 1, pp. 2–21, 2006.

[63] E. Candes and J. Romberg, "ℓ_1-magic : Recovery of sparse signals via convex programming," 2005.

[64] Y. C. Eldar and G. Kutyniok, *Compressive Sensing Theory and Application*. Cambridge University Press, 2012.

[65] C. Ma, T. S. Yeo, Y. Zhao, and J. Feng, "Mimo radar 3d imaging based on combined amplitude and total variation cost function with sequential order one negative exponential form," vol. 23, no. 5, pp. 2168–2183, 2014.

[66] A. Maleki and D. L. Donoho, "Optimally tuned iterative reconstruction algorithms for compressed sensing," *IEEE Journal of Selected Topics in Signal Processing*, vol. 4, no. 2, pp. 330–341, 2010.

[67] Y. Eldar, P. Kuppinger, and H. Bolcskei, "Block-sparse signals: Uncertainty relations and efficient recovery," *IEEE Trans. Signal Process.*, vol. 58, no. 6, pp. 3042–3054, 2010.

[68] W. Zuo and Z. Lin, "A generalized accelerated proximal gradient approach for total-variation-based image restoration," *IEEE Trans. Image Process.*, vol. 20, no. 10, pp. 2748–2759, 2011.

[69] T. F. Chan, S. Osher, and J. Shen, "The digital **TV** filter and nonlinear denoising," *IEEE Trans. Image Process.*, vol. 10, no. 2, pp. 231–241, 2001.

[70] P. Wang, H. Li, and B. Himed, "A parametric moving target detection for distributed mimo radar in non-homogeneous environment," *IEEE Trans. Signal Process.*, vol. 61, no. 9, pp. 2282–2294, 2013.

[71] S. Gogineni and A. Nehorai, "Target estimation using sparse modeling for distributed mimo radar," *IEEE Trans. Signal Process.*, vol. 59, no. 11, pp. 5315–5325, 2011.

[72] R. J. Burkholder, I. J. Gupta, and J. T. Johnson, "Comparison of monostatic and bistatic radar images," *Antennas Propagat. Mag.*, vol. 45, no. 3, pp. 41–50, 2003.

[73] Z. B. Zhu, Y. B. Zhang, and Z. Y. Tang, "Bistatic inverse synthetic aperture radar imaging," *IEEE International Radar Conference*, pp. 354–358, 2005.

[74] X. R. Bai, F. zhou, M. D. Xing, and Z. Bao, "Scaling the 3-d image of spinning space debris via bistatic inverse synthetic aperture radar," *IEEE Geosci. Remote Sens. Lett.*, vol. 7, no. 3, pp. 430–434, 2010.

[75] M. Martorella, J. Palmer, J. Homer, B. Littleton, and I. Longstaff, "On bistatic inverse synthetic aperture radar," *IEEE Trans. Aerosp. Electron. Syst.*, vol. 43, no. 3, pp. 1125–1134, 2007.

[76] Kolev and N. Zhelev, "Bistatic isar target simulation," *7th European Conference on Synthetic Aperture Radar (EUSAR)*, pp. 1–4, 2008.

[77] J. A. Given and W. R. Schmidt, "Generalized isar-part ii: interferometric techniques for three-dimensional location of scatterers," *IEEE Trans. Image Process.*, vol. 14, no. 11, pp. 1792–1797, 2005.